Particle-based Simulation of the Selective Laser Melting Process

Von der Fakultät für Maschinenbau
der Gottfried Wilhelm Leibniz Universität Hannover

zur Erlangung des akademischen Grades
Doktor-Ingenieur

genehmigte Dissertation
von

M. Sc. Jan-Philipp Fürstenau (geb. Haun)

geboren am 31.03.1989 in Gehrden

2020

Herausgeber:
Prof. Dr.-Ing. habil. Dr. h.c. mult. Dr.-Ing. E. h Peter Wriggers

Verwaltung:
Institut für Kontinuumsmechanik
Gottfried Wilhelm Leibniz Universität Hannover
An der Universität 1
30823 Garbsen

Tel: +49 511 762 3220
Fax: +49 511 762 5496
Web: www.ikm.uni-hannover.de

© M. Sc. Jan-Philipp Fürstenau
Institut für Kontinuumsmechanik
Gottfried Wilhelm Leibniz Universität Hannover
An der Universität 1
30823 Garbsen

Alle Rechte, insbesondere das der Übersetzung in fremde Sprachen, vorbehalten. Ohne Genehmigung des Autors ist es nicht gestattet, dieses Heft ganz oder teilweise auf photomechanischem, elektronischem oder sonstigem Wege zu vervielfältigen.

ISBN 978-3-941302-37-2

1. Referent: Prof. Dr.-Ing. habil. Dr. h.c. mult. Dr.-Ing. E. h Peter Wriggers
2. Referent: Prof. Dr.-Ing. Matthias Teschner

Tag der Promotion: 23.11.2020

*W*e can only see a short distance
ahead, but we can see plenty
there that needs to be done.

- Alan Turing (1912 - 1954),
computer scientist,
deciphered the Enigma

Zusammenfassung

Die Additive Fertigung (AM, *engl.* Additive Manufacturing) erfreut sich auf industrieller Ebene wachsender Beliebtheit, da auf diese Weise Bauteile deutlich freier gestaltet werden können als mit konventionellen Methoden. Mit additiver Fertigung lassen sich beispielsweise topologieoptimierte Bauteile oder Bauteile mit innerer Struktur, wie Kühlkanälen, abbilden. Das am weitesten verbreitete Verfahren hierbei ist das Selektive Laserstrahlschmelzen (SLM, *engl.* Selective Laser Melting), ein Verfahren bei dem ein Pulverbett schichtweise aufgebracht und aufgeschmolzen wird um das Bauteil generativ zu erzeugen. Zum Zeitpunkt dieser Arbeit sind Bauteile, die mit additiven Fertigungsmethoden hergestellt sind, jedoch deutlich teurer als konventionell gefertigte Bauteile. Dies liegt zu einem großen Teil an einer vergleichsweise hohen Ausschussrate, die bei der Preiskalkulation berücksichtigt wird. Die Quellen für schlechte Bauteilqualität liegen dabei sowohl auf Bauteilebene, wo thermischer Verzug zu Ausschuss führt, als auch auf Pulverebene, wo mangelhaftes Aufschmelzen oder ein instabiler Schmelzpool das Gefüge des Bauteils negativ beeinflussen.

In dieser Arbeit wird die Entwicklung des Schmelzpools auf Pulverebene näher betrachtet, um die Schmelzpoolgeometrie sowie die Abkühlung vorherzusagen. Um die Strömungsverhältnisse im Schmelzpool vorherzusagen wird die netzfreie Smoothed Particle Hydrodynamics (SPH) Methode verwendet. Mit dieser lässt sich das Aufschmelzen des festen Pulvers sowie die sich schnell verändernden freien Oberflächen der Schmelze auf numerisch effiziente Weise darstellen. Dies ergibt sich daraus, dass bei solchen mehrphasigen Systemen (festes Pulver - flüssige Schmelze - gasförmige Atmosphäre) die Beschreibung der Grenzflächen auf Basis der Partikelverteilung stattfindet, ohne dass eine zusätzliche Oberflächenvernetzung oder -erkennung notwendig wird. Durch Vernachlässigung der Gasphase und der mechanischen Verformung im Pulverbett entsteht eine leistungsfähige Methode, die die entscheidenden thermischen und fluidmechanischen Phänomene bei der Schmelzpoolentwicklung erfasst. Der zweite Schwerpunkt liegt auf der Implementierung der inkompressiblen SPH-Methode (ISPH). Durch die implizite Berechnung des Druckes der Partikel ergeben sich deutliche Vorteile in Fragen der Stabilität und Rechenzeit im Vergleich zur expliziten, schwach kompressiblen SPH-Methode (WCSPH, *engl.* Weakly Compressible SPH), die in dieser Arbeit beleuchtet werden. Möglich ist dies, durch die auf Grafikkarte (GPU, *engl.* Graphics Processing Unit) parallelisierte Lösung des Gleichungssystems auf Basis der PARALUTION Bibliothek und des DualSPHysics Frameworks.

Die Leistungsfähigkeit des vorgestellten Frameworks wird anhand von akademischen Beispielen aus der Fluiddynamik sowie am Beispiel des SLM-Pulverbetts dargestellt. Es finden Abgleiche mit experimentellen und simulativen Ergebnissen statt. Trotz einer Auflösung von 3 Mikrometern liegt die Simulationsdauer eines Laserübergangs (0,8 mm Länge) mit der inkompressiblen SPH-Methode bei nur 3,5 bis 11,3 Stunden, simuliert auf einer Mittelklasse-Grafikkarte (NVIDIA GTX 1660 Ti).

Schlagworte: Additive Fertigung, Selektives Laserstrahlschmelzen, Inkompressible Smoothed Particle Hydrodynamics Methode, GPU Parallelisierung, Semiimplizit, Netzfrei, Freie Oberfläche, Oberflächenkräfte

Abstract

Additive manufacturing (AM) is becoming increasingly popular on an industrial level, as it allows for components to be designed much more freely than with conventional methods. For example, additive manufacturing can be used to produce topologically optimized parts or components with internal structures such as cooling channels. The most widely used process is Selective Laser Melting (SLM), a process in which a powder bed is applied and melted layer by layer to create the component generatively. At the time of this work, components manufactured with additive manufacturing methods are, however, significantly more expensive than conventionally manufactured components. This is in large extent due to a comparatively high scrap rate, which is taken into account in the price calculation. The sources for poor part quality are on the part level, where thermal distortion leads to scrap, as well as on powder level, where incomplete melting or an unstable melt pool can affect the inner structure of the component in a negative way.

In this thesis, the development of the melt pool at the powder level is considered in detail in order to predict the melt pool geometry as well as the cooling. In order to predict flow conditions in the melt pool, the mesh-free Smoothed Particle Hydrodynamics (SPH) method is used. With this method, the melting of the solid powder and the rapidly changing free surfaces of the melt pool can be represented in a numerically efficient way. This follows from the fact that in such multi-phase systems (solid powder - liquid melt - gaseous atmosphere) the description of the interfaces is based on the particle distribution without the need for additional surface meshing or detection. By neglecting the gas phase and the mechanical deformation in the powder bed, a performant method is created, which captures the decisive thermal and fluid mechanical phenomena during melt pool development. The second focus is the implementation of the incompressible SPH method (ISPH). The implicit calculation of the particle pressures results in significant advantages in terms of stability and computing time compared to the explicit, weakly compressible SPH method (WCSPH), which are discussed in this thesis. This is possible due to the parallel solution of the equation system on a graphics card (GPU, Graphics Processing Unit) based on the PARALUTION library and the DualSPHysics Framework.

The performance of the presented framework will be demonstrated on academic examples from fluid dynamics as well as on the example of the SLM powder bed. Comparisons with experimental and simulative results are carried out. Despite a resolution of 3 micrometers, the simulation time of a laser transition (0.8 mm length) with the incompressible SPH method is only 3.5 to 11.3 hours, simulated on a mid-range graphics card (NVIDIA GTX 1660 Ti).

Keywords: additive manufacturing, selective laser melting, incompressible Smoothed Particle Hydrodynamics Method, GPU parallelization, semi-implicit, mesh-free, free surface, surface forces

Acknowledgements

At this point I want to take the opportunity to thank those people without whom this work would not have been possible. First and foremost, I would like to thank Professor Wriggers, who gave me the greatest possible freedom in choosing the topic and in working on it. His guidance and the associated freedoms are largely responsible for the friendly and productive atmosphere at the institute, which cannot be taken for granted. I have always enjoyed both the work and the lectures at the institute, and participating in several international conferences has been a highlight for me. I also want to thank my second examiner, Professor Teschner, for the inspiration that led me to study the incompressible SPH method and for his support in implementing it.

I extend my gratitude to my two supervisors, Dr. Bircan Avci and Dr. Christian Weißenfels, for their mentoring and the stimulating discussions while I was working on my thesis. Dr. Avci first introduced me to the topic of particle simulation and gave me the best possible start in the subject. Dr. Weißenfels gave me an industrially relevant problem with the SLM process that takes advantage of SPH.

There was always a pleasant working atmosphere at the institute with equally helpful, smart and nice colleagues. Special mention should be made here of Dr. Henning Wessels, who helped me out with his extensive knowledge in the field of SLM simulation whenever I needed it and always provided motivation when progress stalled. Likewise, I would like to mention Jens Bsdok and Dr. Malte Hothan, who helped me with so many hardware and software problems, without whom my work with GPU technology would have lost much of its momentum. But I would also like to thank all the other colleagues who cannot find a place here. Whenever I had a problem, be it scientific, organizational or otherwise, I could count on a listening ear and willing help. I will always remember the time at the institute as very inspiring and very enjoyable.

Finally, I would like to sincerely thank my family, who have always encouraged and supported me so that I could dedicate myself to my work. In particular, I would like to thank my wife Katrina, whom I always know is by my side and who, along with our children, is my source of motivation. Without your love and support, I would not have come this far.

Hannover, January 2021 Jan-Philipp Fürstenau

Contents

List of Symbols **xi**

List of Abbreviations **xv**

1 Introduction **1**
- 1.1 The SLM process 2
- 1.2 Simulating the SLM process 4
- 1.3 Simulative approach of this thesis 7

2 Physical Phenomena and Governing Equations **11**
- 2.1 Physical phenomena 11
  - 2.1.1 Heat transfer 11
  - 2.1.2 Thermal expansion 13
  - 2.1.3 Surface tension 14
  - 2.1.4 Phase change 16
  - 2.1.5 Evaporation 16
  - 2.1.6 Material defects 17
  - 2.1.7 Residual stresses 18
  - 2.1.8 Summary 18
- 2.2 Balance equations 19
  - 2.2.1 Continuity equation 19
  - 2.2.2 Momentum equation 20
  - 2.2.3 Energy equation 21
- 2.3 Boundary conditions 22
  - 2.3.1 Momentum equation 22
  - 2.3.2 Energy equation 23
- 2.4 Constitutive equations 23
  - 2.4.1 Fluid stresses 24
  - 2.4.2 Tait equation 24
  - 2.4.3 Recoil pressure 25
  - 2.4.4 Heat source modeling 26
  - 2.4.5 Heat loss modeling 28
- 2.5 Order of magnitude analysis 30

3 Smoothed Particle Hydrodynamics 33
- 3.1 SPH - the basic ideas 33
  - 3.1.1 Lagrangian and Eulerian desription 33
  - 3.1.2 Particle-based methods 35
  - 3.1.3 SPH kernel interpolation 36
  - 3.1.4 First Order Derivative 39
  - 3.1.5 Second Order Derivative 42
- 3.2 Modeling of the balance equations 43
  - 3.2.1 Balance of momentum 43
  - 3.2.2 Surface Forces 45
  - 3.2.3 Continuity equation - WCSPH 50
  - 3.2.4 Continuity equation - ISPH 50
  - 3.2.5 Energy equation 53

4 Implementation Details 55
- 4.1 Time stepping schemes 55
  - 4.1.1 WCSPH 55
  - 4.1.2 ISPH 56
  - 4.1.3 Energy equation 57
  - 4.1.4 Time step limitations 57
  - 4.1.5 Shifting 58
- 4.2 GPU programming details 59
  - 4.2.1 Programming basics 60
  - 4.2.2 Memory usage 64
  - 4.2.3 Matrix assembly 66
- 4.3 Post-processing 68

5 CFD Validation 71
- 5.1 Lid-driven cavity flow 71
- 5.2 Bubble collision 76

6 Selective Laser Melting 81
- 6.1 Mechanical modeling 82
  - 6.1.1 Resolution 83
  - 6.1.2 Smoothing length 85
  - 6.1.3 Viscosity 89
- 6.2 Thermal modeling 94
  - 6.2.1 Powder conductivity 94
  - 6.2.2 Substrate depth 99
  - 6.2.3 Laser modeling 100
- 6.3 Physical phenomena 103
- 6.4 Validation / Simulation Series 115

7 Conclusions 125

A Solution Procedures **129**
A.1 Weakly compressible SPH 129
A.2 Incompressible SPH 130

B Temperature Variable Material Parameters **133**

C Supplementary Test Data **137**
C.1 Powder conductivity 137
C.2 Laser modeling 138
C.3 Validation / Simulation series 140

Bibliography **143**

List of Figures **152**

List of Tables **159**

CURRICULUM VITAE **163**

List of Symbols

Operators

$\mathbf{1}$	unit tensor
δ	denoting virtual quantity
Δ	denoting linearized quantity
$\langle \bullet \rangle$	discretization of $(\bullet)$
$(\hat{\bullet})$	denoting normalized quantity
$(\tilde{\bullet})$	denoting a corrected kernel (gradient) or smoothed quantity
$\frac{d(\bullet)}{dt}$, $(\dot{\bullet})$	time derivative of $(\bullet)$
$\nabla(\bullet)$	gradient of $(\bullet)$
$\nabla_S(\bullet)$	surface/ tangential gradient of $(\bullet)$
$\nabla \cdot (\bullet)$	divergence of $(\bullet)$
$\nabla^2(\bullet)$, $\nabla \cdot (\nabla(\bullet))$	second spatial derivative of $(\bullet)$
$(\bullet)'$	first derivative of $(\bullet)$
$(\bullet)''$	second derivative of $(\bullet)$
$\int_\Omega (\bullet) dv$	volumetric integral of $(\bullet)$
$\int_\Gamma (\bullet) da$	surface integral of $(\bullet)$
$(\bullet) \cdot (\bullet)$	dot product of two vectors
$(\bullet) : (\bullet)$	double dot product of two tensors
$(\bullet)_b$	denotes $(\bullet)$ to be a boundary value
$(\bullet)_i$	$(\bullet)$ is a variable of the currently observed particle i
$(\bullet)_j$	$(\bullet)$ is a variable of a neighbor of the currently observed particle
$(\bullet)_m$	molar value
$(\bullet)_{int}$	denotes $(\bullet)$ to be an internal value
$(\bullet)_{ext}$	denotes $(\bullet)$ to be an external value
$(\bullet)^m$	variable in the context of melting
$(\bullet)^t$	$(\bullet)$ is a variable of the last time step
$(\bullet)^{t+\Delta t}$	$(\bullet)$ is a variable of the time step beeing computed
$(\bullet)^v$	variable in the context of vaporization
$(\bullet)^*$	variable of the predictive intermediate step

Latin symbols

$\mathbf{a}^g$	acceleration due to gravity
$\mathbf{a}^S$	acceleration due to surface forces
A, $\mathbf{A}$	a general value for derivations
A_{ij}	ISPH matrix entry for row i and column j
b_i	ISPH source term for particle i
$\mathbf{b}$	body force vector
B, b	impact parameter for bubble collision
$\mathbf{d}$	symmetric strain rate tensor
c	color function
c_0	numerical speed of sound
c_I	laser volume filling
C	shifting constant
d	characteristic length
da	surface increment
dv	volume increment
dx	distance increment / particle spacing
D_{laser}	laser diameter
E	total energy
E_V	volumetric energy density
$\mathbf{f}$	force density vector
$\mathbf{F}$	force vector
$\mathbf{g}$	gravity vector
h	smoothing length
h_c	convective heat transfer coefficient
H	hatch spacing
I	Laser intensity function
k	thermal conductivity
K	kinetic energy
L	layer height
m	mass
$\mathbf{n}$	normal vector
$\mathcal{O}$	denoting order of (error, magnitude, etc.)
p	(gauge) pressure
p_0	atmospheric pressure
p^{rec}	recoil pressure
P_{ext}	external power
P_{int}	internal power
P_{laser}	laser power
$\mathbf{q}$	heat flux vector
$\mathbf{q}_{ext}$	external heat flux vector
$\mathbf{q}_{int}$	internal heat flux vector

Q	heat
r	volumetric thermal source/ loss term
r_{laser}	laser radius
R	gas constant
$\mathbf{R}$	shifting direction
Re	Reynolds number
s	transition region width
t	time
$\mathbf{t}$	surface force vector
T	temperature
T_0	reference temperature
T'	deviation from reference temperature
$\mathbf{t}$	surface force vector
u	local inner energy
U	global inner energy
$\mathbf{v}$	velocity vector
V	volume
v_{laser}	laser speed
W	SPH kernel
We	Weber number
z	depth
Z	laser depth

Greek symbols

α	Courant number for time stepping
$\alpha_{\mathbf{v}}$	weighting factor for velocity source term
α_ρ	weighting factor for density source term
β	thermal expansion coefficient
β_{laser}	extinction coefficient
γ	surface tension coefficient
Γ	body surface
Γ_D	body surface under Dirichlet boundary condition
Γ_N	body surface under Neumann boundary condition
δ	Dirac delta function
δ_p	powder porosity
δ_S	denoting transition region
$\delta\mathbf{r}$	shifting vector
ΔH	phase change enthalpy
Δt	time step size
ΔV	volumetric expansion ratio
Δt	time step size
ϵ	surface emissivity
ζ	extinction coefficient
η	correction factor preventing divergence of second order derivative
θ	contact angle
κ	surface curvature
μ	dynamic viscosity
ν	kinematic viscosity
ξ	viscosity calibration factor
ρ	density
ρ_0	rest density
σ	Stefan-Boltzmann constant
$\boldsymbol{\sigma}$	Cauchy stress tensor
τ	adiabatic exponent
$\boldsymbol{\tau}$	viscous stress tensor
ϕ	evaporation (or sticking) coefficient

List of Abbreviations

ALE	Arbitrary Lagrangian Eulerian
AM	Additive Manufacturing
AMG	Algebraic Multi Grid
BiCGStab	Bi-Conjugate Gradient Stabilized
CALPHAD	CALculation of PHase Diagram
CFD	Computational Fluid Dynamics
CPU	Central Processing Unit
CSF	Continuous Surface Force
CSR	Compressed Sparse Row format
CUDA	Compute Unified Device Architecture
DEM	Discrete Element Method
DIN	Deutsches Institut für Normung
DSD/ST	Deforming-Spatial-Domain/Space-Time
EBM	Electron Beam Melting
FEM	Finite Element Method
FV	Finite Volume
GMRES	Generalized Minimal Residual Method
GPU	Grafical Processing Unit
GPGPU	General Purpose Grafical Processing Unit
IDR	Induced Dimension Reduction
ISPH	Incompressible Smoothed Particle Hydrodynamics
IISPH	’Implicit Incompressible Smoothed Particle Hydrodynamics’
LBM	Lattice Boltzmann Method
MD	Molecular Dynamics
MLS	Moving Least Squares
MPM	Material Point Method
OTM	Optimal Transportation Method
PFEM	Particle Finite Elements Method
PBF	Powder Bed Fusion
SIMT	Single Instruction Multiple Threads
SPH	Smoothed Particle Hydrodynamics
SPHERIC	SPH rEsearch and engineeRing International Community
SLM	Selective Laser Melting
VoF	Volume of Fluid
WCSPH	Weakly Compressible Smoothed Particle Hydrodynamics

Chapter 1

Introduction

This thesis treats the simulation of the Selective Laser Melting (SLM) process. SLM is an Additive Manufacturing (AM) process for the generative manufacturing of metal parts. Additive manufacturing is the youngest group of manufacturing processes. In contrast to AM processes, there are the original forming, shaping, cutting, joining, coating and changing of material properties as classical manufacturing processes according to DIN 8580 (2003). AM made its first steps in the early 1980s, when the first AM processes were invented. At that time the AM processes were called Rapid Prototyping. The novelty of the AM processes was, that a part is generated by adding up material layer-wise. While today there is a variety of materials that can be processed additively, the first AM processes all dealt with the printing of plastics. The Fraunhofer Institute of Laser Technology developed the Selective Laser Melting (SLM) process in 1995, resulting in the first patent on an AM process for metal parts (MEINERS ET AL. (1998-02-12)). In 2003 the MCP-HEK Tooling GmbH (today SLM Solutions Group) launched the first commercial SLM machine and protected the name SLM. Since then the SLM process evolved from a niche product towards a process method to generate complex structures in several fields of engineering (e.g. aerospace, medical and automotive engineering) (SLM SOLUTIONS GROUP AG (2016)). This evolution is made possible through the recurring sequence of improvement of the process and exploration of new applications. In the Wohlers Report (WOHLERS ET AL. (2018)), the sales of AM machines for metal parts increased by 80 % within one year. Today, there exist several companies, who are using various names for their SLM process, because of the protected term SLM (a general and unprotected name is Powder Bed Fusion (PBF)). In 2020 the four largest global suppliers of SLM machines and services are:

1. Electro-Optical Systems (EOS) GmbH, Krailing,
2. Concept Laser GmbH, a GE Additive company, Lichtenfels,
3. SLM Solutions Group AG, Lübeck,
4. Trumpf GmbH, Ditzingen.

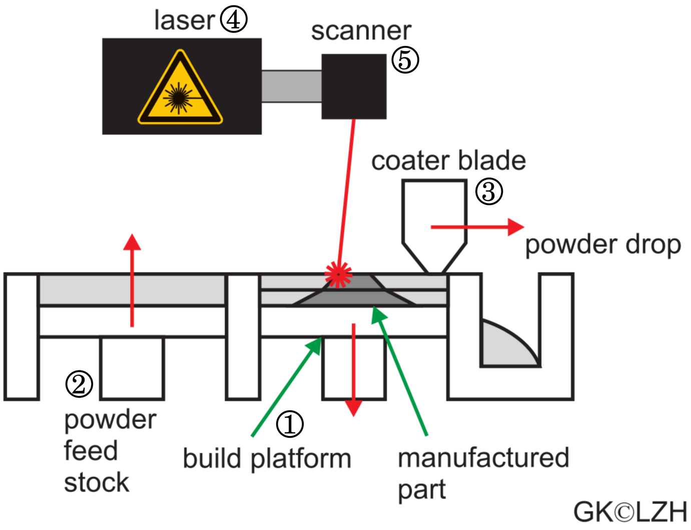

Figure 1.1. Basic components of a SLM machine, visualizing the SLM process. Adapted from GIESEKE ET AL. (2016).

1.1 The SLM process

In the SLM process, powder layers are completely melted to produce components with a particularly high density (up to 99.9 %) which lead to mechanical properties similar to those of casted components (GIESEKE ET AL. (2016)). The SLM process consists of four essential steps (see Fig. 1.1):

1. Lowering of the build platform (1) by the layer height to make space for a new powder layer,
2. Deliver new powder by raising the powder feed stock (2),
3. Distribute the new powder as a thin layer with the help of the coater blade (3) (or roller),
4. Selectively melt the powder by a laser (4) positioned by a scanner system (5).

Advantages

The SLM process has several advantages compared to classical manufacturing processes from DIN 8580 (2003). The most important ones are the geometrical flexibility and material flexibility (GIESEKE ET AL. (2016)):
Geometrical flexibility: Like many other AM processes, SLM offers a unique flexibility, especially for the generation of undercuts or custom shaped internal geometries. With metallic materials, this can be used to generate custom shaped cooling channels for e.g. production tools or engines (see Fig. 1.2).
Material flexibility: In contrast to many other AM processes, SLM machines are basically capable of processing a wide range of materials such as metals, ceramics or plastics. The

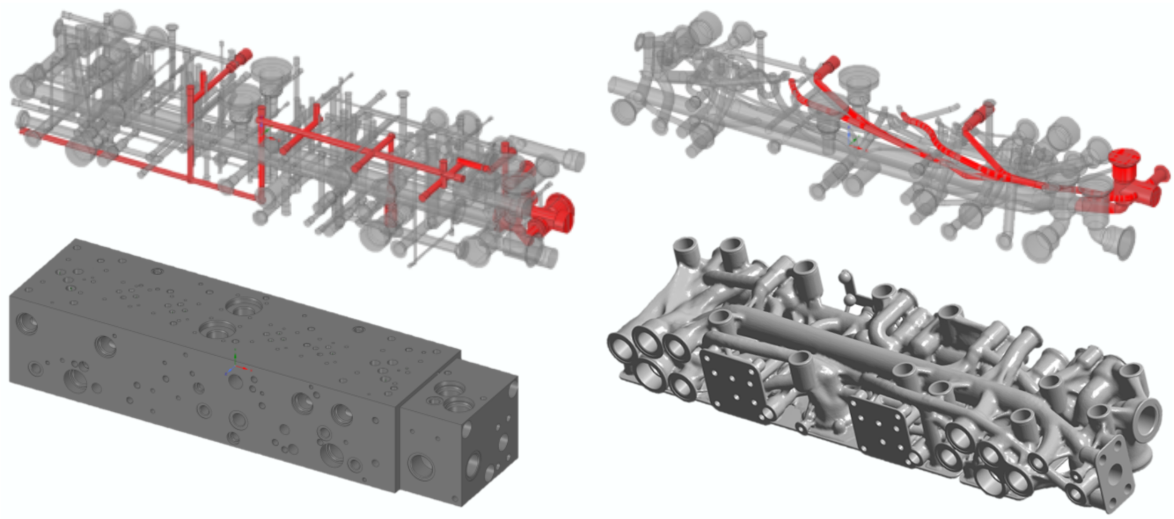

Figure 1.2. Left: inner and outer geometry of a classic hydraulic block, manufactured as a solid component with connected bores; right: inner and outer geometry of a flow-optimised hydraulic block, manufactured as an additive metal component. Courtesy of S.M.I.L.E. - FEM GmbH.

only requirement is the availability of a powder with usable particle size and an energy source providing sufficient power.

Disadvantages

The disadvantages of the SLM process can be summarized in three categories: speed, residual stress, resources (GEBHARDT (2016)):
Speed: Common to all AM processes is that the production speed is low compared to classical production processes. In contrast to e.g. shaping, cutting or joining the build time is directly proportional to the filled volume of the final part. In this way, the process speed limits AM processes to light or small structures. Solutions for higher process speeds in SLM are the use of stronger lasers for higher laser speeds or the use of multiple lasers. However, with increasing laser power and laser speed, the quality can be compromised.
Residual stress: For the SLM process the use of support structures is a necessity. Support structures are applied to support the component during the production. This is necessary because the component expands and contracts under the effect of the laser, which creates deformations that can lead to detachment from the build platform or collisions with the coater blade. The use of support structures is especially necessary for overhangs. The support structures act in two ways: First, the supports hold the solidified part in place and prevent the thermal stresses from deforming the component. Second, the support structures dissipate heat from the melting area, which is why they can be used to control cooling. However, fixing the component against thermal deformation introduces residual stresses that can weaken the final part and should be prevented.
Resources: A pool of molten metal reacts with the atmosphere resulting in metal oxide, which is mostly brittle and unusable. Just like in the welding process the area around the melt pool has to be filled with a passive gas. For the comparatively time consuming process

of SLM the gas is not permanently delivered towards the melt pool, like in the welding process. Instead of this, the whole build chamber is flooded with gas, which expects the air-tightness of the chamber.

In the Laser Sintering process of plastics, the chamber is preheated slightly below the melting temperature of the plastic to use low power lasers. For most metals this is not applicable but pre-heating up to 550 $^{\circ}C$ is state-of-the-art, as it improves the quality of the resulting parts. Unfortunately the preheating of the chamber is very energy intensive. However, the unmelted powder can be recycled, and energy-intensive post-processing, such as heat treatment or grinding, is only required to change the material properties and to create functional surfaces.

1.2 Simulating the SLM process

According to YADROITSEV (2008) more than 130 parameters influence the quality of SLM fabricated parts. Melting and consolidation occur within milliseconds. The thermal cycles and the melt pool dynamics affect the quality of the surface and the inner structure of finished parts, but are difficult to investigate experimentally. Consequently, the parameter sets for SLM-generated components are based more on experience and experiments than on an understanding of the underlying physical processes. Often at least one test or scrap part is produced before the desired geometries can be generated within acceptable tolerances. At this point, simulations can help to improve the process and make it more reliable in order to reduce scrap and thus lower the price per printed part. When laser or material parameters are calibrated experimentally, the preparation of the machine can be intensive, depending on the varied parameters. On top of that the printed samples have to be cleaned, cut and polished to measure the print quality (called micrographs). Instead of that, a number of tests can be performed using a calibrated numerical model without further preparation and post-processing time. The evaluations can also be automated to test more parameter combinations and perform more precise calibrations. This way higher machine efficiencies as much as a deeper insight into the physical process can be reached. Regarding the pointed out disadvantages of SLM, numerical simulations can help to handle most of them. With a pre-build virtual twin of a desired part, the laser speed and power can be tweaked and preprogrammed to increase the speed and quality of the real build process. Predicting the deformation and cooling of the component during the process can help to improve the design to reduce stress and the necessary supports. Optimizing the process parameters by simulation can, for example, evaluate the advantages of preheating the chamber and thus help to save resources.

For the simulation of SLM, two different scales are in the center of interest, the part scale and the powder scale. Both scales are explained in the following subsections.

Powder scale simulation

The powder scale simulation is the lowest level to simulate for the SLM process. The powder bed is fully resolved, leading to a resolution below 5 μm. Thus, the dimensions of the simulated space around the melt track are commonly smaller than 1-3 mm. In this work, the simulated cases have the dimensions of 1 mm x 0.3 mm x 200 μm. The purpose of powder scale models is to capture the melt pool dynamics and the energy input of the laser. For this reason, coupled thermo-fluiddynamic simulations are carried out. Especially the hydrodynamic aspects of the melt pool are a challenge: the melt pool is a low viscous liquid, which is limited on the one side by a free surface under high surface tension and on the other side by melting and solidifying boundaries.

On the powder scale, the input parameters of the simulation are powder distribution, powder material properties and laser source parameters. From this point a variety of tests can be performed to evaluate the influence of:

- powder particle size, shape, distribution and compaction,
- powder materials, alloys or material blends,
- influences of the substrate below the powder layer,
- the effect of laser power, power distribution, laser speed or the use of multiple laser sources resulting in a common melt pool,
- for larger testing areas, also the hatch spacing can be analyzed.

The melt pool behavior on the powder scale is driven by surface tension and recoil pressure. The thermodynamics are mostly affected by the thermal conduction which is constrained by the geometry. Here, the powder particles with their small contact areas lead to a low thermal conductivity while the melt pool enlarges the contact area by oozing between the unmolten particles. To cover these effects, a fully coupled, fully resolved model has to be set up. The desired results of powder scale simulations are the melt pool geometries, where width, depth and surface roughness of the solidified pool can be evaluated as much as the obtainable density of the final tracks. This data can be gathered to create process maps of optimal process parameters or to feed it into machine learning models (so-called surrogate models). Furthermore, from powder scale models the total energy absorbed, the distribution of temperature and its time history are valuable input parameters for part scale models.

Part scale simulation

When simulating part scale models the whole part is represented, leading to dimensions between millimeters and meters. Currently one of the largest commercially available metal printers allows for maximum dimensions of 0.8 m x 0.5 m x 0.4 m (X LINE 2000R from Concept Laser, a GE Additive company). To predict the behavior of parts of that size, physical phenomena have to be neglected or simplified (e.g. homogenization). The need for simplification requests more complex inputs. While on the powder scale the laser and the melt pool are explicitly represented, this would lead to extensive computing times on the part scale. Instead of that, the material is added layer-stack wise with a prescribed temperature. As mentioned before, the temperature of the solidified track can vary depending on several parameters. To cope with that, the temperature data and the geometry of the track from the powder scale model can be included.

The benefit of such a part scale model is a prediction of the overall thermo-mechanical behavior. For the production process a part scale model becomes useful to calculate:

- temperatures and cooling rates on the whole part,
- thermal stresses inside the part from inhomogeneous cooling,
- deformations of the part based on the stresses,
- evolution of the microstructures inside the printed material.

All these results have a direct effect on the dimensional accuracy and strength of the final component. The main factors influencing the above quantities are the powder material, the geometry to be printed and the distribution of support structures. All these parameters can be optimized with regard to: minimum warpage, minimum material consumption and controlled growth of microstructures.

Simulation approaches

Several approaches to simulate SLM are available in literature and commercial codes, starting with the more widespread part scale simulation tools. For the simulation on the part scale, grid based methods like the Finite Element Method (FEM) or Finite Volume (FV) method are mostly used. When simulating the layer wise generation of a part the underlying mesh can be chosen coarse to represent cold powder or evenly heated areas. A mesh refinement has to be performed in areas with high temperature gradients or where the geometry requires such. A FEM formulation with local refinement is presented in RIEDLBAUER ET AL. (2017). Another academic approach is the Diablo framework from the Lawrence Livermore National Laboratory (HODGE ET AL. (2014) and HODGE ET AL. (2016)). Their department focuses on the understanding of the SLM process using numerics and experiments. In recent years, several simulation tools for modeling the component and powder scale have been presented together with studies on the effects of laser heat sources. An overview of the research is given in KING ET AL. (2015a). To calculate the microstructures during solidification, the use of a so-called CALPHAD method (CALculation of PHase Diagram) can be applied. This method can be applied to any continuous method of calculating the thermo-dynamically consistent material properties like performed by NEUGEBAUER ET AL. (2014) and SMITH ET AL. (2016). On the commercial side, ANSYS, Inc. launched several products under the collective term additive manufacturing simulation in early 2018. With these products, all the part-scale simulation capabilities are provided which were mentioned before. Additionally the thermal distortions can be compensated by automatically altering the geometry to be printed.

When speaking of powder scale modeling, two different steps of the process can be accounted for. First of all, the powder coating can be predicted in several ways. With varying particle sizes, the distribution has to be performed either with a particle based simulation or with a space filling algorithm. Most wide-spread is the Discrete Element Method (DEM). With this physically simple, particle-based simulation the deployment with the coater blade or roller can be simulated explicitly. This way the compaction is close to reality and gives information on the packing density. With a space filling algorithm, the packing density is a direct control parameter, but the distribution can be different from a compaction driven

packing. Additionally, space filling algorithms become more complicated when accounting for heterogeneous particle size distributions or non-spherical particles. For many DEM frameworks non-spherical particles are representable, but general shapes often have to be approximated by particle agglomerates or analytical objects. To mention are the academic code Pasimodo by FLEISSNER (2012) from the TU Stuttgart applying agglomerates or the work of WELLMANN ET AL. (2008) using super ellipsoids as DEM particles. The commercial software Rocky DEM from ESSS allows for arbitrarily shaped powder particles with facets, which can be used to generate more sophisticating powder beds.
The second part of the powder scale modeling is the laser-powder interaction, on which this work focuses. As already mentioned, the main challenge consists in the stable capturing of the melt pool geometry, including volume and mass conservation in the presence of violent motion. To give an idea of that motion, velocities of up to 2 m/s were observed in the test cases in this work within a simulation space of about 0.06 mm^3. To cover the powder scale process, several methods from the field of fluid mechanics were applied. On the Eulerian side, AMMER ET AL. (2014) presented a Lattice-Boltzmann Method (LBM) simulationg the melt pool behavior for Electron Beam Melting (EBM), which is similar to SLM. The FV method could also be applied within OpenFOAM by YAN ET AL. (2015). A drawback of the mesh based methods, describing the whole simulation space by a prescribed grid, is that the solid phase has to be included in the framework. This is often realized as a highly viscous fluid (YAN ET AL. (2017)). Additional methods like level-sets or phase fields have to be applied to capture the interfaces between solid, liquid and gaseous phase. The commercial software FLOW-3D by Flow Science, Inc. applies the Volume of Fluid (VoF) method onto a FV framework to capture free surface flow processes. In recent years their group focused on AM, presenting both powder scale steps in their code besides the representations of several other AM processes (FLOW SCIENCE, INC. (2017)). Again, in the Lawrence Livermore National Laboratory an Arbitrary Lagrangian Eulerian (ALE) formulation (KHAIRALLAH & ANDERSON (2014) and KHAIRALLAH ET AL. (2016)) was developed to solve the melt pool dynamics. With their approach, test cases similar to the ones from this work were simulated. Based on the high computation times, their works were restricted to high laser speeds. For a purely Lagrangian representation of the melt pool dynamics, recently an explicit SPH approach was presented by RUSSELL ET AL. (2018) solving 2D test cases, giving the stimulus to this work. To get a complete overview of the state of the art of SLM simulation methods at powder level the publication of COOK & MURPHY (2019) is recommended. This publication also mentions the most important research groups dealing with SLM powder simulation.

1.3 Simulative approach of this thesis

The Smoothed Particle Hydrodynamics (SPH) method is a constantly evolving method for the simulation of fluids and solids. Developed by GINGOLD & MONAGHAN (1977) and LUCY (1977) simultaneously for astrophysical problems, SPH became more popular in the late 1990s when, computational power got cheap enough to simulate several thousands of particles in reasonable time. Since then, SPH has continued to develop, opening up new areas of application. Important improvements from various academic disciplines such as mathematics, astrophysics, engineering and information technology contributed to this development. Worth to mention for this work are: the Wendland kernel function from WENDLAND (1995), the zeroth- and first-order kernel correction by SHEPARD (1968) and RANDLES & LIBERSKY (1996), the Incompressible SPH (ISPH) projection scheme by CUMMINS & RUDMAN (1999), the surface-corrected shifting scheme by LIND ET AL. (2012), the Continuous Surface Force model by MORRIS (2000) and the open-source, GPU-based DualSPHysics Framework by CRESPO ET AL. (2015). These publications represent the foundation for this thesis. To get an overview on the state of SPH, the 'SPH rEsearch and engineeRing International Community' (SPHERIC) references, all popular frameworks (commercial and academic), informs about conferences and offers an overview of publications on the topic.

For the simulation of the SLM process on the powder scale, SPH was found to be a promising tool. In contrast to the Eulerian and ALE methods mentioned before, in SPH the solid and gaseous phase do not have to be represented explicitly. This is because, explicit and semi-implicit SPH algorithms allow for rapidly changing free surfaces and boundaries. In this work, the surrounding gas phase is neglected and therefore not discretized with particles. This results in lower memory consumption and lower computation times. For the solid phase only the thermal variables are calculated as much as the pressure close to the fluid phase as it is common for solid boundaries. This again saves memory when the solid stresses do not have to be stored and reduces computation times again as the interactions are reduced. Surely, taking the effects of fully modeled gas and solid phase into account, opens new possibilities for the simulation. Namely these are:

- trapping of air inside the meltpool, creating pores,
- convective heat transfer through the gas phase,
- evaporation of metal into the gas phase,
- creation of stresses and voids from thermal expansion of the solid.

This means, that in the present framework the keyholing effect due to gas-liquid interaction has to be neglected. Also the thermal expansion and generation of residual stresses in the melt pool region is not represented in this thesis. Anyhow, an upside of SPH is that the missing parts can be brought into the formulation, which has been done in literature already. In the SPH-based simulations of laser welding by HU & EBERHARD (2017), the solid phase is fully discretized with solid SPH particles, giving the reaction forces and deformations of the unmolten material. The full representation of the gas phase in form of a multi phase problem with density ratios around 1/7000 is still a topic of high complexity. MOKOS ET AL. (2017) presented a solution for the instabilities resulting from high density gradients in explicit, Weakly Compressible SPH (WCSPH). Although their solution made the problems calculable, the density ratio reduces the time step size significantly.

This thesis consists of six further chapters. In the second chapter the central phenomena of the SLM process are described in detail, concluding in the governing equations. The third chapter continues with the numerical method of SPH in general and the discretization of the previously described phenomena in detail. In the fourth chapter numerical details on the implementation are explained. The fifth chapter deals with academic, fluid mechanical validation cases. In the sixth chapter the modeling of the SLM process and potential uncertainties are discussed. Finally, this chapter presents a validation example based on experimental results from the literature, which also illustrates possibilities for advanced analyses. The seventh and last chapter summarizes the results and provides thinking impulses for further research.

Chapter 2

Physical Phenomena and Governing Equations

This chapter highlights the physical phenomena in the 2.1 section, followed by the governing equations in section 2.2 and the corresponding boundary conditions and constitutive equations in sections 2.3 and 2.4. At the end of this chapter an order of magnitude analysis is performed (section 2.5) to distinguish the phenomena with a large influence on the melt pool dynamics from those with a small influence.

2.1 Physical phenomena

As already described in section 1.2, there are two different simulation approaches. These are the powder scale simulation and the part scale simulation. They differ in their objective, their input and resulting parameters and the phenomena that can be represented. These phenomena are shown in table 2.1, as well as their simulability on both scales. This table also serves as a table of contents for the following subsections.

2.1.1 Heat transfer

When the light of the laser hits the powder, the light is not absorbed in total at the topmost powder layer. Instead of this, the light is partly reflected which does not give energy to the melt pool. Other amounts of the light miss the topmost powder particles and and are absorbed in the lower layers. The amount of absorbed light depends on the geometry of the irradiated area and the absorptivity. Both are permanently changing in the SLM process as the melt pool moves and changes its geometry as much as its absorptivity. On the one hand, the absorptivity of iron for example is changing from 0.36 for solid to 0.32 for liquid iron (HU & EBERHARD (2017)). On the other hand the changing geometry has an even lager impact. In KING ET AL. (2015b) a ray tracing algorithm was used to analyze the absorptivity of the initial powder layer of several materials. Starting from an absorptivity of 0.34 for stainless steel the absorptivity of a powder substrate combination was calculated to be 0.6. This number is surprisingly high and results from multiple reflections. When the powder melts and a more even surface without gaps is formed, more light is reflected again and

Phenomenon	Effect	Powder scale	Part scale
Heat transfer	- absorption, conduction - reflection, convection, radiation	X X	(X) /
Thermal expansion	- solid and fluid mechanical effect, results in solid expansion and fluid buoyancy	(X)	X
Surface tension	- cohesion effects resulting in surface tension and Marangoni convection	X	/
Phase change	- latent heat - change of mechanical properties	X X	X (X)
Evaporation	- melt pool indentation by recoil pressure - evaporative cooling	X X	/ /
Material defects	- encapsulation of gas from high recoil pressure/ voids from shrinkage	X	/
Residual stress & microstructure	- solid mechanical effects resulting from cyclic heating and thermal gradients	(X)	X

Table 2.1. List of representable phenomena in powder and partial scale. Phenomena that can be represented on a certain scale are marked with 'X'. Phenomena that cannot be displayed are marked with a '/'. The representability of phenomena marked with '(X)' is limited. The table is based on FÜRSTENAU ET AL. (2020b).

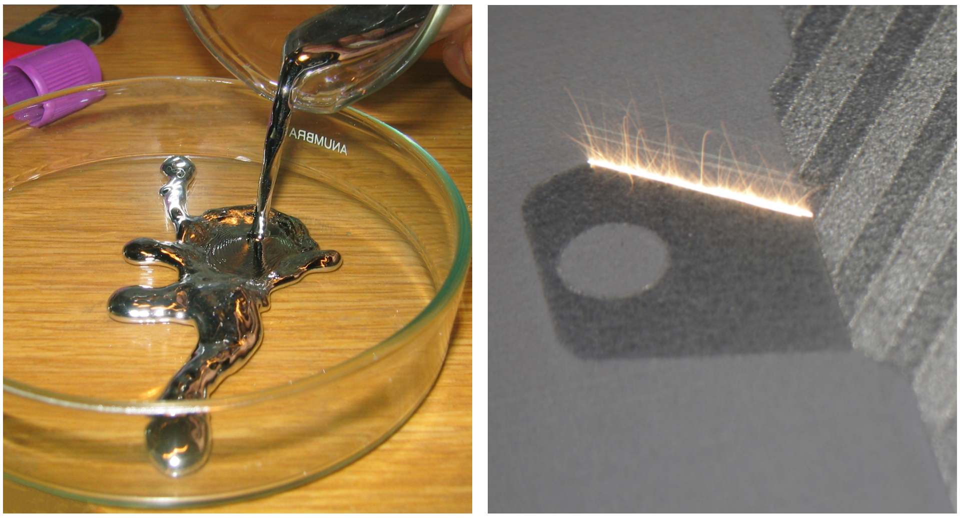

Figure 2.1. left: Photograph of mercury being poured onto a glas surface at room temperature by WIKIMEDIA COMMONS: BIONERD (2008). The strong effect of surface tension is visible, being still smaller than molten steel by a factor around 3.5; right: Photograph of the first line of a new layer being irradiated in the SLM process. The spatter of molten particles caused by vaporization is clearly visbile. Courtesy of Gorden Reh, Institute of Product Development (IPeG), Leibniz Universität Hannover.

the absorptivity will reduce. To simulate the heat absorption of the melt pool a volumetric distribution of energy can be applied like in GUSAROV & KRUTH (2005) or GANERIWALA & ZOHDI (2016). These models are simple, consisting of only few parameters and are representing a low computational effort in terms of memory consumption and additional computations. The necessary parameters can be fitted to experimental data quiet fast.

Alternatively a ray tracing algorithm can be used, giving more exact results when looking at reflective effects or geometrical irregularities (KHAIRALLAH ET AL. (2016)). The ray tracing algorithm has equivalently many parameters but demands to store thousands of rays with position and velocity, leading to a significant increase of computational effort. A ray tracing algorithm for the application on mesh-free methods has recently been presented in WESSELS ET AL. (2019). Nevertheless, in this work a volumetric heat source with a constant absorptivity is applied, for its computational simplicity.

The conduction, convection and radiation of the metal belong to the topic of heat transfer of the melt pool. The heat conduction is a well-studied phenomenon representable in SPH, based on the work of CLEARY (1998). What has to be taken into account is the geometry of the simulated cases. The heat conduction between the powder particles is dominated by the gas in the gaps leading to a reduced conductivity compared to solid steel by a factor around 100 (GUSAROV ET AL. (2009)). The reason for this are the small contact areas between the spheres (or the spheres and the substrate). To account for the reduced heat conductivity, the resolution has to be sufficiently small. With coarse resolution the small contact areas cant be realized, resulting in an overestimation of conductivity. Thus, fine resolutions are a necessity and not driven by the fluid- but the thermodynamics. If the geometrical effects cannot be represented by the discretization, the values of the heat conductivity can be reduced for the lose powder. This is a common procedure for part scale simulations. Convection and radiation both represent thermal losses at the free surface. The thermal gradient between gas and metal convects heat into the gas phase. The radiation becomes relevant at high temperatures. Then the energy is lost in form of visible light (glowing like in figure 2.1) or as infrared light. Both effects are low, compared to conduction.

Further details on the thermal losses are presented in section 2.4.5. To test the influence of the spatial discretization on the thermal conductivity of the powder tests are performed in section 6.2.1. Finally the effect of the radiative and convective cooling is captured in 6.3. Another important source of cooling besides heat conduction is the (partial) evaporation of the metal, being introduced in section 2.1.5.

2.1.2 Thermal expansion

All solid materials expand when the temperature increases. The reason for this is at the atomic level and thus eludes modeling. Nevertheless the effects of thermal expansion can be modeled. For this purpose, there are thermal expansion coefficients for linearized thermal expansion as well as measurement curves for the representation of non-linear thermal expansion. The thermal expansion has the same effect on the solid phase as on the liquid phase.

In the solid phase, the thermal expansion and subsequent cooling shrinkage leads to the internal stresses of the final component. On the other hand, it can lead to the formation of

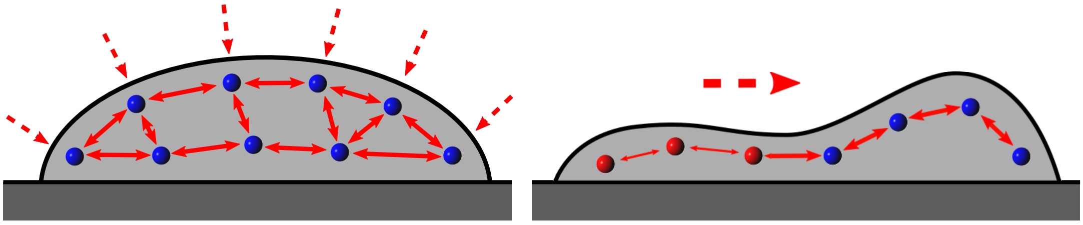

Figure 2.2. left: visualization of the molecular forces forces inside a fluid body (solid arrow) and the apparent surface tension force (dotted arrows); right: visualization of the Marangoni convection. The red particles have a higher temperature and thus a lower cohesive force than colder blue particles (arrow thickness). The dotted arrow shows the apparent Marangoni force.

voids during cooling inside the melt pool if the stresses become too large or the bonding forces too small. This is especially the case if the laser power is too low. An extensive experimental study was conducted by YAKOUT ET AL. (2018). Since the solid phase is not calculated in this work, the thermal expansion cannot be captured.

In the liquid phase the thermal expansion causes a decrease in density. This leads to an expansion of the liquid and natural convection within the melt pool. In RUSSELL ET AL. (2018) the phenomenon of natural convection in the SLM process was considered in a WC-SPH framework, but no estimate or comparison of the effect of convection on the melt pool dynamics was made. In this work the thermal expansion of the fluid is neglected. Reason for this is that the expansion of the particles in SPH is a cumbersome topic, especially when accounting for ISPH. The negligence of the expansion also avoids the imbalance between a non-expanding solid and an expanding liquid. Instead of the real expansion of the particles a buoyancy term is included as a body force to account for the natural convection.

2.1.3 Surface tension

According to KING ET AL. (2015b), the melt pool dynamics in SLM are dominated by two principles: surface tension and recoil pressure. The most important effect here is the surface tension. This is what characterizes the SLM process as soon as the metal changes to a liquid state. The surface tension is not a simple force but consists of multiple phenomena resulting from molecular cohesion and adhesion. On the one hand the normal surface tension and on the other hand the tangential Marangoni convection based on the gradients of the surface tension. Surface tension in general results from cohesion effects within the liquid, which are greater than the adhesion effects to the surrounding material. For molten metals, the coefficients of surface tension are in the order of 1-2 N/m, which are the highest possible values occurring in nature. The effect of the high surface tension is shown in figure 2.1. In addition to the high surface tension coefficient, the surface force increases with curvature, which is anti proportional to the radius. For powder particle sizes of 10-40 μm, large surface tension effects can therefore be observed. Therefore, the surface tension is the driving force for the SLM process. An example is given in KHAIRALLAH & ANDERSON (2014) where a single laser track is analyzed in one case under the influence of surface tension and in another

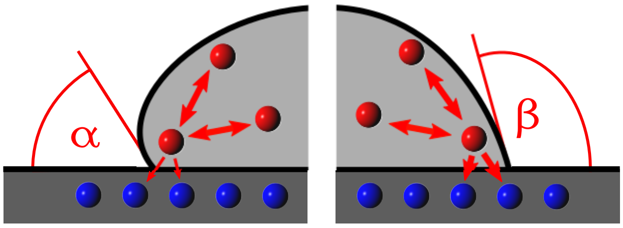

Figure 2.3. Visualization of the wetting effect; left: the low adhesive force (arrow thickness) between fluid particles (red) and substrate particles (blue) results in an acute contact angle; right: the higher adhesive force leads to an obtuse contact angle.

case only under gravity. The case without surface tension showed almost no generation of a melt pool because the metal cools faster than it can be moved by gravity. This means that an SLM process without surface tension would not be possible. In contrast, the surface tension is also responsible for the so-called balling effect, in which the minimization of the surface leads to the undesired formation of spherical melt pools. In YADROITSEV ET AL. (2010) the instability of the melt pool leading to balling is described with a Plateau-Rayleigh instability to predict this behavior. Usually, Plateau-Rayleigh instability describes the decay of liquid jets under the influence of surface tension. A visualization of the surface tension effect is shown in figure 2.2 [left].

The second effect emerging from surface tension is the Marangoni convection. Marangoni convection results from differences in surface tension. Most metals have a temperature-dependent decreasing surface tension (and some an increasing one). From this physical property, a force tangential to the surface is generated, pointing from hotter to colder regions. This effect leads to a starvation of the pool directly below the laser. A visualization can be found in figure 2.2 [right]. The effect of the Marangoni convection is presented in FÜRSTENAU ET AL. (2020b), where simulations with and without Marangoni convection are compared. The effect of the Marangoni convection was found to have a large impact on the final melt track.

The third surface tension related effect is wetting. When multiple phases come into contact, the surface tension coefficient for every pairing differs. The result is a contact angle θ which can be calculated based on the surface tension coefficients:

$$\cos\theta = \frac{\gamma_{sg} - \gamma_{sl}}{\gamma_{lg}}, \tag{2.1}$$

with γ_{sg}, γ_{sl} and γ_{lg} being the surface tension coefficients for the solid-gas, solid-liquid and liquid-gas pairing. The contact angle is visualized in figure 2.3. This effect was implemented for SPH by KUNZ ET AL. (2018) for multi phase flows. In this thesis the effect was neglected, as the model depends on all three phases being modeled explicitly. By neglecting the gas phase, this requirement is not met. Instead of this, the solid and liquid phase are handled as one material for the surface tension. Anyways, the wetting behavior could be adjusted by changing the surface tension coefficient for the unmolten material.

In section 6.3 the influence of surface tension and Marangoni convection are treated separately and their effects are shown. For the analysis of the Marangoni convection both the temperature dependent increase and decrease of the surface tension are depicted.

2.1.4 Phase change

Based on the heat input of the laser, the metal powder changes its properties in a continuous way. When the internal energy accumulates towards the melting point the solid material gets weaker and more viscoelastic. When reaching the melting point, the metal does not start to flow immediately, because it is still a mixture of solid and liquid shares. When reaching the melting point the so-called latent heat is absorbed. Latent heat is the internal energy necessary to change the low energy state of the solid material to the higher energy state of a liquid. The same happens during the phase change between liquid and gas. While the latent heat is absorbed, the temperature stays nearly constant, such that a direct association between temperature and phase change is difficult to realize. During the phase change the fluid is in the so-called mushy region, where the flow properties are dominated by the ratio of fluid and solid shares. The effect of the mushy region is captured in mesh-based methods by a porous medium approach (COOK & MURPHY (2019)) but is mostly ignored in particle based methods (see distinction in section 3.1). For example in HU & EBERHARD (2017) the particles are treated as solid particles during the phase change and are released as liquid particles after the phase change is completed. The reason for this is that the distinction between liquid and mushy matter in the mesh-based methods is only associated with changing material properties. In particle-based simulation, a completely different treatment of solid and liquid particles takes place. For the representation of partly liquid and partly solid particles no model has been established in the literature so far. In the SLM process, the negligence of the the mushy behavior appears legit as the laser heating is short-termed and influence of the mushy region is expected to be small. However, the effect of the latent heat plays an important role in the SLM process. The stored latent heat prevents the molten pool from overheating too quickly under the laser and keeps the temperature of the molten pool stable over a longer period of time during cooling. Especially the increased cooling time has an effect on the geometry of the resolidified melt. In this work the latent heat is fully modeled, unlike in e.g. HU & EBERHARD (2017) or RUSSELL ET AL. (2018), where the apparent heat approach is used. A comparison of the models is carried out in FÜRSTENAU ET AL. (2020b). In the publication it was shown that the apparent heat approach can lead to unphysical deviations combined with an explicit time integration scheme like used here.

2.1.5 Evaporation

Evaporation is the second phase change from liquid to gaseous metal. There are two phenomena caused by evaporation influencing the SLM process: recoil pressure and evaporative cooling. The recoil pressure is the most important effect that drives the melt pool which is not related to surface tension. During the SLM process the laser heats the particles in an irregular manner, based on the inhomogeneous heat conduction and the dynamics of the flow. Thus, some portions of the powder overheat during the irradiation, reaching the vaporization temperature. At this point, partial vaporization happens, leading to a quick expansion at the surface. The amount of vaporizing metal is low, which was calculated by KHAIRALLAH ET AL. (2016). The visible result of the expansion is the spattering shown in Fig. 2.1. The effect of recoil pressure from partial vaporization can be approximated by a pressure term based on the Clausius-Clapeyron equation, which was applied e.g. by KHAIRALLAH ET AL.

(2016). The derivation of the evaporative cooling and recoil pressure from the Clausius-Clapeyron equation is found in section 2.4.3 and 2.4.5. A free surface implementation of the recoil pressure for deep penetration welding has been applied by HU ET AL. (2016) for weakly compressible SPH. When applying low laser powers, like it is done in most academic experiments, like in CHILDS ET AL. (2005) or YADROITSEV ET AL. (2010), the appearance of recoil pressure is unlikely and its effect on the melt pool is negligible. But for the simulation of high laser powers, like appearing in industrial applications, the utilization of recoil pressure is inevitable. The implemented formulation of recoil pressure is described in section 3.2.2.

The evaporation of the high-energy portions of the melt pool leads to a significant cooling despite the low mass fraction. The resulting cooling is higher than the cooling by convection and radiation and should therefore be modeled. In section 2.4.5 the applied formulation is derived from the Hertz-Knudsen model.

2.1.6 Material defects

Material defects in SLM are usually the encapsulation of gases within the melt pool, leading to pores in the final product. The gases occur for two different reasons. Firstly, as the packing density of nearly spherical particles never reaches 100 $\%$, there is always gas between the powder particles. The common powder packing density is around 55 $\%$ according to KING ET AL. (2015b). This gas must escape from the molten metal, which it does by flowing around the molten metal or flowing through the melt as gas bubbles. Both paths are only slightly disturbed by the liquid metal for three reasons:

- the buoyant force of the gas is large based on a density ratio around 1/7000,
- the high surface tension of the metal keeps the gas from dissolving,
- the low viscosity of gas and liquid metal result in a low friction.

The most likely reason for trapped gas in the pool is that the melt pool is cooling down too quickly. The other source of gas is generated by overheating of the material. Especially with alloys, the generation of small pores based on trapped gases is a topic of concern according to ABOULKHAIR ET AL. (2014). An overheating problem arising with every type of powder is the keyholing effect. When the surface of the melt pool vaporizes, the recoil pressure opens up a so-called keyhole, ranging down to the unmolten material. This effect can be observed in KHAIRALLAH ET AL. (2016) and HU ET AL. (2016). The reflux of the melt pool leads to a trapping of gas and a fast cooling of the pool when reaching the bottom of the keyhole. In ABOULKHAIR ET AL. (2014) it was found that the keyhole pores can be avoided by two strategies: by slower laser speeds and lower powers or by remelting the pool by either a small hatch spacing or by scanning the solidified track again. They found that keyholes must be avoided, as they also tend to trap unmelted powder particles in SLM, which reduces the overall loading capacity.

For this thesis and the academic codes reviewed, the process of trapping unmolten particles is not reproduceable, as the powder particles are always expected to be immobile. In this work, the pore generation processes cannot be captured, as the gaseous phase is neglected (unlike in KHAIRALLAH ET AL. (2016)). This means, that no pressure force keeps the pores from collapsing and thus the keyholing process, will not lead to lasting pores.

2.1.7 Residual stresses

Residual stresses occur through the thermal expansion of the metal. When the melt pool undergoes solidification, the solid material does not stop shrinking. Until room temperature the metal part shrinks about 2 $\%$ based on the parameters by WESSELS ET AL. (2018). This shrinkage leads to residual stresses deforming the final part. In classical production techniques like molding, the cooling happens in a controlled way for the whole part, leading to less stresses. Alternatively, the parts are tempered to reduce internal stresses after the production. Within a SLM machine a controlled cooling is hardly possible, although there are controlling strategies through planning of the laser patterns and the positioning of support structures.

The microstructure of the solidified metal is also affected by the cooling rate. Like for the residual stresses, a controlled cooling rate leads to the desired grain growth in the solid metal. As mentioned in the introduction the CALPHAD methods can be introduced to a simulation tool to predict the local material composition and grain size based on the thermal history. While during the SLM process, the cooling is hard to control, post-treatments like tempering can improve the properties of the final part.

Residual stresses and the crystallization in the solid phase are influenced by several phenomena, which are hard to distinguish. High cooling rates, can affect the results as much as sharp thermal gradients or the cyclic heating. The first two effects, could be tracked down on the powder scale, because they are observable in short-termed simulations. The cyclic heating on the other hand is not only appearing when several lines within one layer are irradiated. When a new layer is processed, the underlying layer is remelted to weld the layers together. This means that for a complete simulation of the process the cooling time has to be simulated as much as the addition of further layers. On the powder scale simulation times of that size are not realizable yet, such that these long-lasting phenomena are mostly restricted to the part scale as pointed out in table 2.1. In this work, both phenomena have to be neglected to circumvent the simulation of the solid phase.

2.1.8 Summary

In summary, all the effects mentioned in this section affect the SLM process in several ways. In this work, the focus is on the melt pool dynamics and their effect on the final melt geometry. With this focus the following points can be concluded:

- there is a range of laser powers and laser speeds with which stable and uniform melt pools and thus parts of high quality can be produced. The bandwidth is defined by the physical effects, which mostly take place at the powder level,
- most of the effects can be related to the ratio of laser speed to laser power, which is part of the so-called volumetric energy density E_V:

$$E_V = \frac{P_{laser}}{v_{laser} H L}, \tag{2.2}$$

with P_{laser}, v_{laser}, H and L being laser power, laser speed, hatch spacing and layer height. As in single track experiments and simulation no hatching exist, this is oftentimes replaced by the applied laser diameter D_{laser}, as done in this work.

- if the energy density is low, rapid cooling and partial melting of the powder leads to uneven melt tracks and the generation of pores and voids,
- if the energy density is high, temperature peaks in the material lead to partial evaporation. This results in energy losses and spattering. With increasing E_V this leads to unwanted keyhole formation, and thus to gas trapping in the melt.
- another important parameter of the SLM process is the energy loss of the pool. Here, four phenomena are appearing: conduction, evaporation, radiation and convection. Since the cooling time is an important result that affects the melt pool and the surrounding material, the correct representation of the cooling is essential.

In this work the generation of pores and the evolution of residual stresses from sections 2.1.6 and 2.1.7 are not captured, since the solid and the gaseous phase are not simulated. Without the simulation of the solid and gaseous phase, however, the uniformity of the melt pool surface and its edges, the temperature, width and depth of the melt and the duration of the liquid state can be recorded. This allows far-reaching conclusions to be drawn about the quality of the resulting melt track. In addition, these results are easily comparable with measurements, while the measurement of pores, residual stresses and microstructures is difficult.

2.2 Balance equations

In order to describe the melt pool dynamics at the powder scale of the SLM process, the thermo-mechanical balance equations have to be solved. As pointed out in the introduction, the mechanical equilibrium of the solid phase is not calculated in this work. In the following, the continuity equation for an incompressible liquid, the momentum equation and the energy equation are depicted.

2.2.1 Continuity equation

The continuity equation derives from the mass conservation law. Mass conservation for incompressible liquids describes the change in density within a unit cell (or particle/ element):

$$\frac{d\rho}{dt} = -\rho \nabla \cdot \mathbf{v}. \tag{2.3}$$

Here, ρ, t and $\mathbf{v}$ are the density, time and velocity. The equation is valid if no sources or sinks for the mass are expected, leading to an increase or decrease of mass in the system (LANDAU & LIFŠIC (1987)). In this work, weakly compressible and incompressible SPH are included. For the weakly compressible approach, equation (3.47) is evaluated explicitly, allowing for slight deviations (≤ 1 %) of the density from the rest density ρ_0. The current density ρ is then fed into a constitutive equation (2.28) calculating the material answer in form of pressure p. In the incompressible regime, the density is expected to be constant. Excluding the density from equation (3.47) leads to:

$$0 = \nabla \cdot \mathbf{v}. \tag{2.4}$$

The pressure, which is needed to maintain this state of no compression is calculated by a system of equations implicitly. In mesh-based methods, the use of a monolithical approach calculating velocity and pressure within one system of equations is commonly applied. In ISPH this is not the case. Here, the Pressure-Poisson Equation is applied within a fractional step approach according to CUMMINS & RUDMAN (1999). The method is described in detail in section 3.2.4. Finally, it has to be mentioned that both the WCSPH and the ISPH approach neglect thermal expansion when calculating the density. Buoyancy due to temperature differences is only considered within the gravitational acceleration (3.29). This is a common procedure in simulation of the SLM process (COOK & MURPHY (2019)).

2.2.2 Momentum equation

The momentum equilibrium calculates the change in momentum based on the resulting forces acting on a body. According to Newton's second law of motion, the change in momentum of a body of mass m is calculated as

$$m\frac{d\mathbf{v}}{dt} = \mathbf{F}, \tag{2.5}$$

where $\mathbf{F}$ is the resulting force acting on the body. From a hydromechanical viewpoint the use of an integral description of the volume is beneficial, summing up several portions of fluid handling their properties in an averaged way. This takes the mass and force out of the equation, being replaced by the density and force density $\mathbf{f}$:

$$\int_\Omega \rho\frac{d\mathbf{v}}{dt}dv = \int_\Omega \mathbf{f}dv, \tag{2.6}$$

with dv being an incremental volume and Ω describing the bulk of the fluid body. The resulting force can consist of two parts, namely body forces $\mathbf{b}$ and surface forces $\mathbf{t}$. Body forces act from the inside of a body, being dependent on the mass or density like gravitational or centripetal forces. Surface forces represent the interactions of the fluid bodies with each other and are dependent on the surface area and its shape. Having both included, equation (2.6) reads:

$$\int_\Omega \rho\frac{d\mathbf{v}}{dt}dv = \int_\Omega \mathbf{b}dv + \int_\Gamma \mathbf{t}da, \tag{2.7}$$

where da is a surface increment and Γ describes the surface of the fluid body. Afterwards the surface force is introduced $\mathbf{t} = \boldsymbol{\sigma}\cdot\mathbf{n}$, consisting of the Cauchy stress tensor $\boldsymbol{\sigma}$ and the surface normal $\mathbf{n}$. With surface force being plugged into equation (2.7), the divergence theorem can be applied. This results in the commonly known integral form of the momentum balance equation being completely integrated over the volume:

$$\int_\Omega \rho\frac{d\mathbf{v}}{dt}dv = \int_\Omega \mathbf{b} + \nabla\cdot\boldsymbol{\sigma}dv. \tag{2.8}$$

When the formulation is expected to be fulfilled in every point of the body, the equation can be transformed into the differential form, being characteristic for fluid dynamics:

$$\rho\frac{d\mathbf{v}}{dt} = \mathbf{b} + \nabla\cdot\boldsymbol{\sigma}. \tag{2.9}$$

2.2.3 Energy equation

To model the thermal behavior of the problem the first law of thermodynamics is applied to calculate the internal energy. The first law of thermodynamics describes the total energy E of the system to be conserved, leading to

$$\frac{dE}{dt} = P_{ext} + Q. \tag{2.10}$$

Here P_{ext} and Q are the mechanical power due to external forces and the heat. To split the mechanical power from the internal energy the mechanical energy is subtracted from the total energy. With the temporal change of the kinetic energy being defined as $\frac{d}{dt}K = P_{ext} - P_{int}$, the difference of external and internal mechanical power. The result of the subtraction is the internal energy:

$$\frac{dU}{dt} = \frac{dE}{dt} - \frac{dK}{dt} = P_{int} + Q. \tag{2.11}$$

The internal mechanical power can be depicted by the Cauchy stress tensor $\boldsymbol{\sigma}$ and the symmetric strain rate tensor $\mathbf{d}$ being the symmetric part of the velocity gradient $\mathbf{d} = \frac{1}{2}\left(\nabla\mathbf{v} + (\nabla\mathbf{v})^T\right)$. By combining the Cauchy stress tensor from equation 2.25 and the symmetric strain rate tensor the internal mechanical power reads

$$P_{int} = \boldsymbol{\sigma} : \mathbf{d} = -\mathbf{1}p : \mathbf{d} + \boldsymbol{\tau} : \mathbf{d}. \tag{2.12}$$

Due to the incompressible assumption, the first part is becoming zero as there is no internal volumetric work without a corresponding external work. The remaining part is the generation of internal energy through viscous heating. In general, this term is not zero, which is why it is represented for example in HU ET AL. (2016) or RUSSELL ET AL. (2018). However, the influence of viscous heating can be assumed to be very small compared to the laser power and due to the short time span between melting and solidification. The additional calculations and the storing of the strain rate tensor and the viscous stresses represents a significant additional effort in terms of calculations and memory consumption. For this reason, the viscous heating is also neglected, which reduces the equation of internal energy to the following term:

$$\frac{dU}{dt} = Q. \tag{2.13}$$

In this formulation, the external heat flux can be represented either by a surface heat flux $\mathbf{q}$ or by a volumetric source term r. This leads to the following integral description:

$$\int_\Omega \rho\dot{u}dv = -\int_\Gamma \mathbf{q}\cdot\mathbf{n}da + \int_\Omega \rho r dv. \tag{2.14}$$

By applying again the divergence theorem, the local form of the balance of internal energy can be derived as

$$\rho \dot{u} = \nabla \cdot \mathbf{q} + \rho r. \tag{2.15}$$

To account for the internal heat conduction the heat flux is split into an internal and external part $\nabla \cdot \mathbf{q} = \nabla \cdot \mathbf{q}_{int} + \nabla \cdot \mathbf{q}_{ext}$ and Fourier's law of heat conduction $\nabla \cdot \mathbf{q}_{int} = -\nabla \cdot (k \nabla T)$ is applied, where k is the thermal conductivity of the liquid. With Fourier's law the final formulation for the energy equation in this work reads:

$$\rho \frac{du}{dt} = -\nabla \cdot (k \nabla T) + \nabla \cdot \mathbf{q}_{ext} + \rho r. \tag{2.16}$$

Due to the assumptions made, the balance of internal energy u is identical with the balance of enthalpy, which in the literature is often used directly for the simulation of SLM processes (COOK & MURPHY (2019)). Since viscous heating is neglected and thus the mechanical and thermal part of the internal energy is decoupled, the process direction must only be considered for heat conduction. The other processes are not dissipative and therefore entropy neutral. Fourier's law obeys the second law of thermodynamics, because it grants that internal energy always flows from areas of high temperature to areas of low temperature.

2.3 Boundary conditions

The boundary conditions of the equation systems fulfill two purposes. On the one hand, they allow the interaction of the observed body with its environment, e.g. via incoming and outgoing heat flows, fixations and external forces. On the other hand, they oftentimes enable the solvability of the governing equations, and provide the existence of a unique solution.

2.3.1 Momentum equation

The fluid domain is outlined by Dirichlet boundaries Γ_D on which the velocity is prescribed

$$\mathbf{v} = \mathbf{v}_b \qquad on \qquad \Gamma_D, \tag{2.17}$$

or Neumann boundaries Γ_N where the forces are defined,

$$\boldsymbol{\sigma} \cdot \mathbf{n} = \mathbf{t}_b \qquad on \qquad \Gamma_N. \tag{2.18}$$

Surface tension and recoil pressure are variable Neumann boundaries depending on further parameters like curvature κ and temperature T. They are applied in the following way

$$\boldsymbol{\sigma} \cdot \mathbf{n} = -\gamma(T)\,\kappa\,\mathbf{n} + \nabla_S\,\gamma(T) - p^{rec}(T)\,\mathbf{n} \qquad on \qquad \Gamma_N. \tag{2.19}$$

here, the $\nabla_S \gamma(T)$ term models the Marangoni force which is the surface (or tangential) derivative of the surface tension coefficient.

2.3.2 Energy equation

In the internal energy balance (2.16) there exist three possible ways of exchanging energy with the environment:

- as a boundary temperature T,
- as a heat flux $\mathbf{q}_{ext}$,
- or as a volumetric source term r.

For the modeling of these thermal boundaries, again Dirichlet and Neumann boundaries are used in literature. On the Dirichlet boundary the temperature is prescribed,

$$T = T_b \qquad on \qquad \Gamma_D. \tag{2.20}$$

For the Neumann variant of the boundary, the heat flux $\mathbf{q}_b$ can be prescribed

$$\mathbf{q}_{ext} = \mathbf{q}_b \qquad on \qquad \Gamma_N. \tag{2.21}$$

A common application in literature are adiabatic boundaries to the sides of the powder to model the low conductive powder bed:

$$\mathbf{q}_{ext} = 0 \qquad on \qquad \Gamma_N, \tag{2.22}$$

this approach is also applied in this work. Alternatively, a heterogeneous Neumann boundary condition (MAYRHOFER ET AL. (2013)) can be applied which models a variable heat flux depending on the temperature of the boundary

$$\mathbf{q}_{ext} = \mathbf{q}_b(T) \qquad on \qquad \Gamma_N. \tag{2.23}$$

This type of boundary condition is called Robin boundary and is used to model heat conduction in the non-discretized region behind the solid boundaries for a more natural cooling behavior and to reduce the numerical space. This boundary is applied for example by KHAIRALLAH ET AL. (2016) or WESSELS (2019). In this work the Robin boundary was not applied as its use introduces another parameter to model the substrate. Instead of this, the Dirichlet boundary temperature was applied what is common practice in literature (COOK & MURPHY (2019)). A criticism of this approach is that the boundary condition does not adapt to the environment and is therefore not able to represent a heating of the boundary. In section 6.2.2 a study is conducted, showing that from a certain depth, the melt pool becomes independent of the substrate depth. This critical depth is observed within the simulations and should be checked when changing thermodynamically relevant simulation parameters.

2.4 Constitutive equations

Constitutive equations are used to make material behavior, as well as complex processes, mathematically tangible. In this section, the relevant aspects for the momentum equation are introduced: the fluid stresses, the explicit Tait pressure equation and the recoil pressure. For the energy equation, the used heat source term for the laser heat source is presented, as well as the common heat loss terms based on recoil pressure, radiation and convection.

2.4.1 Fluid stresses

Incompressible viscous fluids are well-studied. Their material behavior is known to consist of a pressure and a viscous part,

$$\boldsymbol{\sigma} = -\mathbf{1}p + \boldsymbol{\tau}, \tag{2.24}$$

where $\boldsymbol{\tau}$ is the viscous stress tensor. For Newtonian incompressible fluids, the viscous stress tensor is proportional to the symmetrical strain rate tensor $\mathbf{d}$:

$$\boldsymbol{\sigma} = -\mathbf{1}p + 2\mu\mathbf{d}, \tag{2.25}$$

with μ being the dynamic viscosity. In the incompressible and weakly compressible regime, this simplified formulation is used. It is neglecting the influence of the bulk viscosity, as no bulk movement is expected based on the $\nabla \cdot \mathbf{v} = 0$ condition. In WCSPH, where small relative compressions occur, this leads to slight bulk-viscosity effects stabilizing the method. Anyways, due to compressions additional energy is dissipated, which can reduce the flowability compared to the incompressible solution. By inserting (2.25) into (2.9) one obtains:

$$\rho\frac{d\mathbf{v}}{dt} = \mathbf{b} - \nabla \cdot \mathbf{1}p + \nabla \cdot 2\mu\mathbf{d}. \tag{2.26}$$

Through reformulation of the equation the incompressible Navier-Stokes momentum equation is derived as

$$\frac{d\mathbf{v}}{dt} = -\frac{\nabla p}{\rho} + \nabla \cdot (\nu\nabla\mathbf{v}) + \mathbf{a}, \tag{2.27}$$

where ν and $\mathbf{a}$ are the kinematic viscosity (μ/ρ) and body accelerations ($\mathbf{b}/\rho$).

2.4.2 Tait equation

When calculating the pressures p resulting from a defined change of the density, the so-called Tait equation is commonly applied to model weakly compressible behavior (MONAGHAN & RAFIEE (2013)):

$$p(\rho) = \frac{\rho c_0^2}{\tau}\left(\left(\frac{\rho}{\rho_0}\right)^{\tau} - 1\right), \tag{2.28}$$

where c_0 and τ are the numerical speed of sound and the adiabatic exponent. The physical speed of sound would lead to the most physical, weakly compressible reaction of the fluid but bounds the computational time steps to very small numbers, based on the the Courant-Friedrichs-Lewy (CFL) Condition given in equation (4.15). Thus, the numerical speed of sound is applied, which is defined as ten times the maximum expected speed occuring in the simulation. With this numerical speed of sound, density variations within 1 $\%$ are achieved (BATCHELOR & BATCHELOR (1967)). The adiabatic exponent τ for weakly compressible fluids is taken to be 7 to give a sufficient strong reaction to compressions. For compressible fluids or gases, τ is often set as 1 or 1.4.

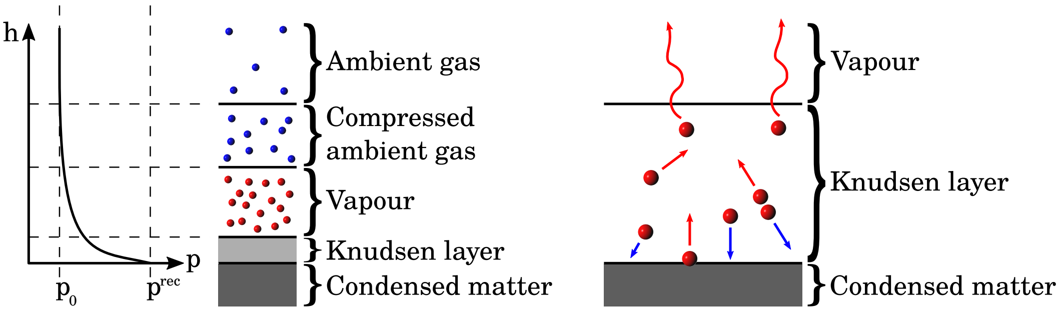

Figure 2.4. Left: Illustration of the layers resulting from vaporization in the subsonic case with the associated pressure; right: illustration of the vapor motion in the Knudsen layer with collisions and condensation, both according to KLASSEN (2018).

2.4.3 Recoil pressure

Whenever a substance is heated locally, a temperature gradient is created which can be of varying intensity based on the ratio of energy introduced and energy dissipated. In processes with low heat input due to low laser power, the cooling is dominated by heat conduction on the thermal side and by the surface tension and the associated Marangoni convection on the mechanical side. This modeling was applied in FÜRSTENAU ET AL. (2020b) to simulate the experimental results of YADROITSEV ET AL. (2010).

However, when the temperature gradient increases, as is common with today's SLM process parameters, there is local overheating that reaches evaporation. During evaporation, however, the evaporated material portions cannot move away from the liquid material surface unhindered, as they are bound by the surrounding medium (usually noble gas). In the process, this leads to a layering of gas and vapor as shown in figure 2.4 for the subsonic case according to KLASSEN (2018). The so-called Knudsen layer forms on the surface. In this thin layer, there is an imbalance between liquid and vapor, which leads to strong molecular movement resulting in a pressure gradient. In the Knudsen layer there are many molecular contacts, which cause parts of the evaporated material to be accelerated back to the surface and condense. When portions of material leave the Knudsen layer, they can escape into free space almost unhindered and lead to a displacement of the process medium. For the mechanics of this work, the so-called recoil pressure is of importance. This is the pressure caused by the particle movement in the Knudsen layer, which affects the liquid material normally to the surface. The vapor pressure resulting from the discontinuity between liquid and gaseous material is described by the Clausius-Clapeyron equation:

$$\frac{dp}{dT} = \frac{\Delta H_m^v}{\Delta V_m^v T}, \tag{2.29}$$

where ΔH_m^v and ΔV_m^v are the molar vaporization enthalpy of the material and the molar volumetric expansion ratio between liquid and vapor. By integrating the Clausius-Clapeyron equation one can obtain the pressure associated with a given temperature. This is done under the assumption that the ratio between expansion and evaporation enthalpy remains constant over the period considered, which is a common assumption (LEE ET AL. (2002)).

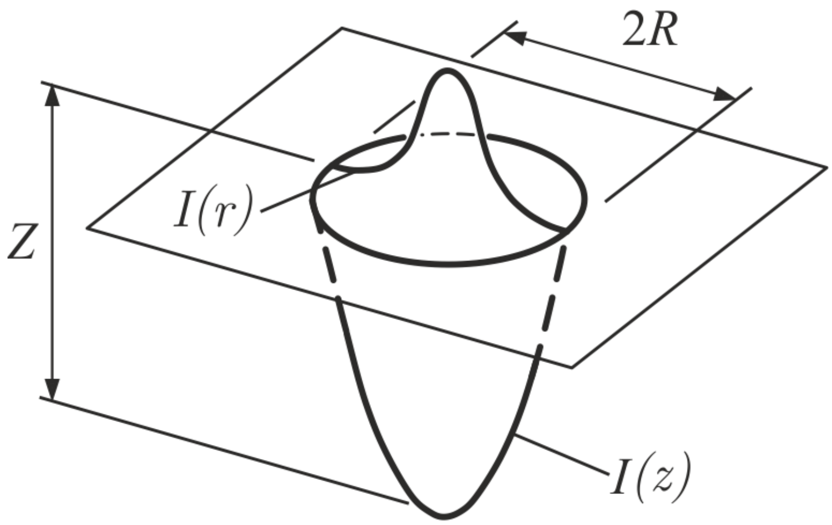

Figure 2.5. Illustration of the intensity function depending on the depth and the radius according to WESSELS ET AL. (2019).

The resulting approximate version reads

$$p(T) \approx p_0 \exp\left(\frac{\Delta H_m^v}{R}\frac{(T-T^v)}{TT^v}\right) = p_0 \exp\left(\frac{\Delta H_m^v}{R}\left(\frac{1}{T^v}-\frac{1}{T}\right)\right), \tag{2.30}$$

with R, p_0 and T^v as the gas constant, atmospheric pressure and vaporization temperature. The first variant is used in the publications of VON ALLMEN & BLATTER (1995), LEE ET AL. (2002) or CHO ET AL. (2009), while in recent publications the latter notation is used, e.g. by KHAIRALLAH ET AL. (2016), HU ET AL. (2016) or VOLKOV & ZHIGILEI (2017). Regarding the recoil pressure due to evaporation of metals, the following formulation has become generally accepted:

$$p^{rec}(T) = 0.54\, p_0 \exp\left(\frac{\Delta H_m^v}{R}\frac{(T-T^v)}{TT^v}\right). \tag{2.31}$$

Here the factor 0.54 results from the highest possible evaporation rate of the gaseous metal under the assumption that the gas molecules move at (sub)sonic speed (LEE ET AL. (2002); VON ALLMEN & BLATTER (1995)). It is to see, that the recoil pressure acts at every temperature but increases drastically when approaching the vaporization temperature. This is because micro vaporization is a process permanently happening. The partial vaporization comes together with a loss of thermal energy which is introduced in the next section.

2.4.4 Heat source modeling

To model the essential laser heat source for the SLM process, in this thesis a volumetric intensity distribution is assumed. This distribution consists of two parts being multiplied:

$$I(r,z) = I_0 e^{-\zeta z} e^{-2r^2/r_{laser}^2}, \tag{2.32}$$

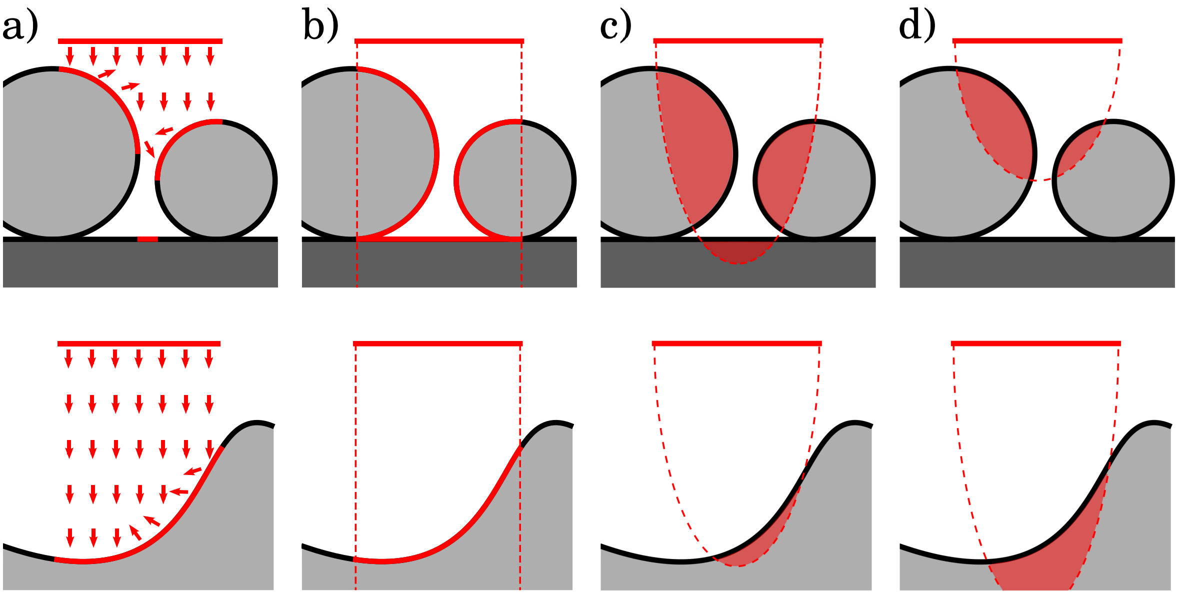

Figure 2.6. Illustration of the typical laser heat source representations in two representative cases highlighting the typical inaccuracies; a) Ray tracing algorithm with partial reflection; b) Gaussian flat heat source applied to free surfaces; c) volumetric heat source without adaptive depth correction; d) volumetric heat source with adaptive depth correction.

where r is the radial distance between the center of the laser and each particle, ζ is the extinction coefficient, r_{laser} is the laser radius and z is the vertical distance to the center of the laser. An illustration of the form of the intensity function is given in Fig. 2.5. The energy distribution is normalized over the volume within the radius and the depth

$$I_0 = \frac{2P_{laser}}{\pi r_{laser}^2}\frac{\zeta}{1-e^{-\zeta Z}}. \tag{2.33}$$

The parameters of this model are laser power P_{Laser}, laser penetration depth Z, laser radius r_{laser} and the extinction coefficient ζ of the powder bed which is calculated according to GUSAROV & KRUTH (2005) as

$$\zeta = \frac{3(1-\delta_p)}{2\delta D}, \tag{2.34}$$

where δ_p is the porosity of the powder bed and D the average particle diameter.

As mentioned before, the use of a ray tracing algorithm is a possible improvement at the cost of simulation runtime and the simulable number of particles (as the memory on a GPU is limited). The reason why a ray tracing algorithm is advantageous compared to a simple volumetric heat source can be found in figure 2.6. With a ray tracing algorithm (figure 2.6 (a)) the physically moving and reflecting rays grant a reasonable energy input. This applies to the sketched surface of the powder bed [top] and to the melt pool border [bottom]. In this thesis, tests have been conducted with a superficial heat source model and the described volumetric heat source model. The superficial heat source (figure 2.6 (b)) applies laser power to free surfaces within the laser radius. Although this leads to a reasonable energy distribution in the lower example, the energy input in the upper example would be clearly overestimated compared to ray tracing. The reason for this is that such an algorithm is not able to reproduce the shadow casted by the geometry by itself, which is automatically represented by the ray tracing algorithm. The heat source described above corresponds to the illustration in (figure 2.6 (c)). Due to the constant volumetric energy distribution, the energy applied differs significantly between the powder bed and the edge of the melt pool, unless corrected. Also from this heat source, undercuts cannot be represented, and the actual effective area of the laser depends on the height of the material. These restrictions lead to an uneven heat input, which is described in section 6.2.3. In this thesis two corrections are applied to overcome the restrictions of a volumetric laser heat source:

- A simple correction of the laser power is the calculation of a scalar correction factor that scales the intensity based on the filling of the 'laser volume' c_I:

  $$I_0^* = \frac{I_0}{c_I} \qquad with \qquad c_I = \sum_i e^{-\zeta z_i} e^{-2r_i^2/r_{laser}^2} V_i \tag{2.35}$$

  This correction guarantees a constant energy input regardless of the number of irradiated particles. But when the volume is small like in figure 2.6 (c) [bottom], the energy immediately vaporizes the few irradiated particles leading to instabilities.

- To overcome the problems of a too large or too small laser volume, the penetration depth Z of the laser must be controlled adaptively. This is performed based on the laser correction from (2.35):

  $$Z^{n+1} = \begin{cases} 0.95 \cdot Z^n, & c_I > c_I^{max}; \\ 1.05 \cdot Z^n, & c_I < c_I^{min}; \\ Z^n, & c_I^{min} < c_I < c_I^{max}. \end{cases} \tag{2.36}$$

  The iteration can be carried out within each time step, but can lead to a fluctuating laser depth. For this reason the penetration depth is only corrected once every time step. Due to the small time steps the deviations are always small. It was found that an uncorrected intensity of $0.5 \cdot I_0$ is desirable together with a tolerance of 5% leading to $c_I^{max} = 0.55$ and $c_I^{max} = 0.45$. A comparison of the uncorrected laser heat source with the two corrections is carried out in section 6.2.3. With this adaptive correction the two scenarios in figure 2.6 (d) can be solved in a more physical and stable way. Still the volumetric heat source is not able to reproduce casted shadows. Anyways, by decreasing and increasing the laser penetration depth the 'laser volume' can be controlled, and together with the scalar correction a constant heat input is realized.

2.4.5 Heat loss modeling

In addition to heat conduction through the substrate, there are three types of energy loss in the SLM process, which are listed here according to their contribution: evaporative cooling, radiative cooling and cooling by free convection. Forced convection does not take place because an active ventilation would stir up the powder bed. First of all, it should be noted that the thermal boundary conditions that represent the heat losses are generally representing a heat flow on a surface (see e.g. COOK & MURPHY (2019)). In SPH for superficial boundary conditions usually the CSF model by MORRIS (2000) is applied, which is introduced in section 3.2.1. The application of this model is only possible for vectorial quantities such as a heat fluxes $\mathbf{q}_{ext}$. The losses in the following equations are given as scalar values, which excludes the use of the CSF model. Instead, it is common practice in the literature (see e.g. ALSHAER ET AL. (2017)) to apply the scalar losses directly to the particles at the very top layer. The total dissipated energy can be calculated approximately by summing it over the associated area of the particles dx^2.

The evaporative cooling goes back to the Hertz-Knudsen model describing the mass flux on a surface in the context of evaporation (VON ALLMEN & BLATTER (1995); SHAH & VOLKOV (2019)). The resulting value J is the molar mass flux (unit $mol/m^2 \cdot s$):

$$J(T) = \frac{\phi p^{rec}(T)}{\sqrt{2\pi m_m RT}}, \tag{2.37}$$

where ϕ and m_m are the evaporation (or sticking) coefficient and the molar mass. The evaporation coefficient ϕ is commonly applied as 0.82 which can be derived from the maximum speed of the vapor (KLASSEN ET AL. (2014)). A coefficient of 0.82 suggests, that $82\ \%$ are accelerated away from the surface and $18\ \%$ are reflected back and condense again. To conduct the heat loss from evaporation, the molar enthalpy of evaporation ΔH_m is taken into account (see e.g. KHAIRALLAH ET AL. (2016)):

$$r^{rec}(T) = \frac{\phi \Delta H_m^v p^{rec}(T)}{\sqrt{2\pi m_m RT}}. \tag{2.38}$$

When the enthalpy of evaporation is not given in $[J/mol]$ but instead in $[J/kg]$ the term can be extended by the molar mass m_m giving an alternative form, which is e.g. applied by VOLKOV & ZHIGILEI (2017):

$$r^{rec}(T) = \frac{\phi \Delta H^v p^{rec}(T)}{\sqrt{2\pi RT/m_m}}. \tag{2.39}$$

When whole particles reach the vaporization temperature the particles are deleted or transformed in vapor particles. However, due to the strong cooling by partial evaporation the amount of vaporized particles was quiet low compared to the molten ones.

The other two cooling effects are orders of magnitude lower as seen in figure 2.7 but are implemented for the sake of completeness. The stronger cooling in the SLM process is resulting from the radiation outgoing from the glowing material below the laser. To model the cooling a standard approach is commonly used according to COOK & MURPHY (2019):

$$r^{rad} = \sigma\epsilon(T^4 - T_0^4). \tag{2.40}$$

Herein, σ is the Stefan-Boltzmann constant, ϵ the surface emissivity, which is assumed to be 0.1 (KHAIRALLAH ET AL. (2016)), and T_0 is the reference temperature. The least effective cooling is the convective cooling resulting from the free convection of the gas surrounding the powder bed. Since an active cooling cannot be realized, as the ventilation would whirl

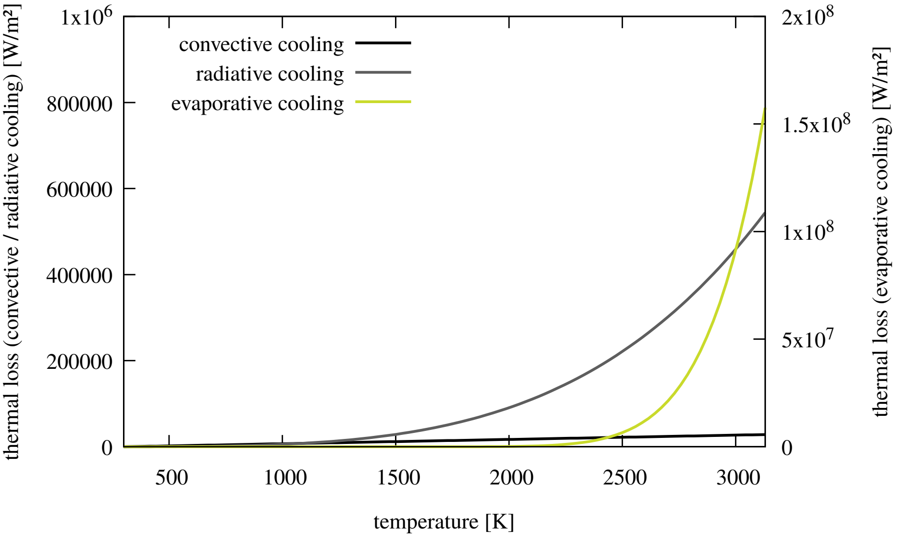

Figure 2.7. Plot of the thermal losses for S316L (WESSELS (2019)), note that the convective cooling and the radiative cooling use the left y-axis and the evaporative cooling uses the right one. One can see, that up to vaporization, the evaporative cooling is at least 2 orders of magnitude larger than the radiative cooling.

up the powder bed, only free convection occurs. For the convective cooling also a standard term can applied:

$$r^{con} = h_c(T - T_0), \tag{2.41}$$

where h_c and T_0 are the heat transfer coefficient between metal and gas and the reference temperature. As noted in COOK & MURPHY (2019) there is a large band of heat transfer coefficients from 10 to 100 $W/(m^2 \cdot K)$. The higher values are explained with other missing cooling phenomena. Since in this work all relevant cooling phenomena are included a low value of 10 $W/(m^2 \cdot K)$ is applied. It shall be noted, that all three cooling effects are only applied at the very surface of the fluid designated by equation (3.57).

2.5 Order of magnitude analysis

To get an idea of the main driving forces in SLM, an order of magnitude analysis is performed. The relative impact of surface tension, Marangoni and gravity forces as well as recoil pressure is assessed. The momentum equation (2.27) including the Neumann boundary conditions (2.19) writes in integral form:

$$\begin{aligned} \int_\Omega \rho \, \frac{d\mathbf{v}}{dt} \, dv = & \int_\Omega \left(-\nabla p + \rho \, \nu \, \nabla^2 \mathbf{v} + \rho \, \mathbf{f} \right) dv \\ & + \int_\Gamma \left(\gamma \, \kappa \, \mathbf{n} + \nabla_S \gamma + p^{rec} \, \mathbf{n} \right) da. \end{aligned} \tag{2.42}$$

A single sphere with a radius of $r = 13.5\ \mu m$ according to the distribution of KHAIRALLAH ET AL. (2016) is considered.

Surface tension

With the curvature $\kappa = r^{-1}$, the surface tension coefficient at the melting point $\gamma = 1.769\ N/m$ and the spherical surface $da = 4\pi r^2$, surface tension is estimated to be of the order $\mathcal{O}_{surf}\,(10^{-4}\ N)$:

$$\gamma\,\kappa\,|\mathbf{n}|\,da = 1.769\,\frac{N}{m}\cdot\frac{1}{r}\,4\pi r^2 \approx 3\cdot 10^{-4}\ N. \tag{2.43}$$

Marangoni effect

For the Marangoni force, a linear dependency of the surface tension coefficient γ on temperature as stated in e.g. WESSELS ET AL. (2018) is assumed (see appendix B). The tangential gradient of γ can be derived using the chain rule:

$$\begin{aligned}\int_\Gamma |\nabla_S\gamma| da &= |\frac{\partial\gamma}{\partial T}\nabla_S T|\,4\pi r^2\\ &\approx 2\cdot 10^{-12}\,\frac{Nm}{K}|\nabla_S T|.\end{aligned} \tag{2.44}$$

Depending on the magnitude of the temperature gradient, the Marangoni force may reach an order of magnitude similar to the surface tension force.

Recoil pressure

The recoil pressure is evaluated at the boiling point T_v, where the exponential in (2.31) equals one. With the ambient pressure $p^a = 10^5$ Pa, the order of magnitude is in the range $\mathcal{O}_{recoil}\,(10^{-4}\text{N})$:

$$\int_\Gamma p^{rec} da = 0.54\,p^a\,4\,\pi\,r^2 \approx 2\cdot 10^{-4}\ N. \tag{2.45}$$

Gravity and buoyancy

Since density decays with increasing temperature, the gravity force has its maximum at the initial ambient temperature prior to laser heating. Assuming $\rho = 7900\ kg/m^3$, a gravity acceleration g of $10\ m/s^2$ and substituting the volume integrand by $dv = (4/3)\,\pi r^3$ yields for the gravitational force an order of $\mathcal{O}_{grav}\,(10^{-10}\ N)$:

$$\rho\,|\mathbf{g}|\,dv = 7900\,\frac{kg}{m^3}\cdot 10\,\frac{m}{s^2}\cdot\frac{4}{3}\pi r^3 \approx 8\cdot 10^{-10}\ N \tag{2.46}$$

The comparison suggests that surface tension, Marangoni effect and recoil pressure are equally important to the SLM process. Gravity forces and related buoyancy phenomena are outnumbered by these effects by five orders of magnitude.

Chapter 3

Smoothed Particle Hydrodynamics

Initially SPH was developed in the field of astrophysics where large empty spaces have to be modeled as well as densely packed spaces which resemble astronomical objects. Naturally, the conservation of mass and momentum plays an important role in this field. This is where Lagrangian methods show superiority above Eulerian mehtods. In SPH the spatial discretization consists of an ansatz function, the so-called kernel. These kernels are spanned around every particle resembling a portion of matter, which is why in SPH the discretization follows the mass. To model physical phenomena and to guarantee the conservation of momentum, consistent spatial derivatives have to be established. In this chapter, firstly SPH is characterized and the kernel function is introduced. Based on the kernel function and its derivatives the physical models are illustrated to realize the balance equations from section 2.2. The chapter finalizes with details on the numerical implementation.

3.1 SPH - the basic ideas

SPH is a continuous, particle-based method represented in Lagrangian description. In the following section, the meaning behind this sentence and the distinction from other methods is explained. Afterwards, the essence of SPH namely the kernel function is derived and explained.

3.1.1 Lagrangian and Eulerian desription

When approaching numerical simulations of mechanics, the first question to be asked is for the spatial representation. The two basic descriptions are the Eulerian and the Lagrangian approach (see Fig. 3.1).

The **Eulerian approach** was introduced by D'ALEMBERT (1752) to describe the motion of bodies from the viewpoint of a fixed frame. This fixed frame usually comes together with a mesh which has to be introduced. In a mesh based method, the simulation space is geometrically filled with interpolation points, so-called nodes. These nodes are to see in figure 3.1 as the intersection points of the grid lines. They form elements available in diverse shapes. In an element, the form of the shape is known as much as its belonging nodes and

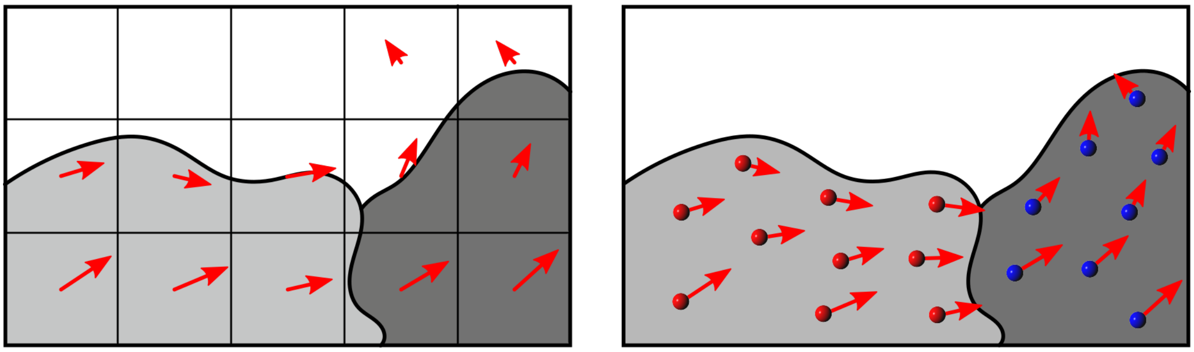

Figure 3.1. Cell-based Eulerian (e.g. FV) [left] and Lagrangian description [right] of a velocity field (red arrows) for a multi phase problem with free surfaces.

the neighboring elements. The motion of a body passing by is described calculating the amount and velocity of the body, traveling through the element. This description established in fluid simulations, where the simulation domain is fully filled and only the flow variables are changing in space (and time). As long as the grid is keeping its initial geometry, the computation of the fluid motion is comparatively simple. The underlying mesh is not bound to have a uniform size or form, what makes it easy to refine areas in which a higher resolution of flow phenomena shall be applied. This is commonly done when describing wall flows or eddies. A disadvantage of the method is that additional values must be introduced for several phases, which describe the quantity of each phase in each cell. This indirect description of the phases does not provide sufficient data to describe interfaces. To create a clear interface between two phases, additional surface tracking techniques such as Volume of Fluid (VoF) must be introduced. This also extends to the representation of free surfaces.

In the **Lagrangian approach**, which was introduced by EULER (1762), either mesh-based or particle-based (mesh-less) methods are commonly applied. The Lagrangian approach describes the motion by tracking points on the moving body. This means, that the discretization points are moving with the body representing a certain portion of mass or volume. The performed motion includes relative motion between the points. This relative motion of the discretizing frame adds complexity to the topic of body description. Calculating the physical behavior independently from the deforming numerical frame reasons a whole topic in continuum mechanics. The upside of this representation is that the description of surfaces and interfaces can be maintained without additional effort. A calculation of the surfaces from the distribution of the interpolation points is possible either in mesh-based and particle-based methods.

A third option is the **Arbitrary Lagrangian Eulerian** representation by HUGHES ET AL. (1981), where the deformation of the numerical frame is possible as much as the convection of matter and information relative to the frame. The framework used by KHAIRALLAH ET AL. (2016) for the simulation of the SLM process is based on this representation.

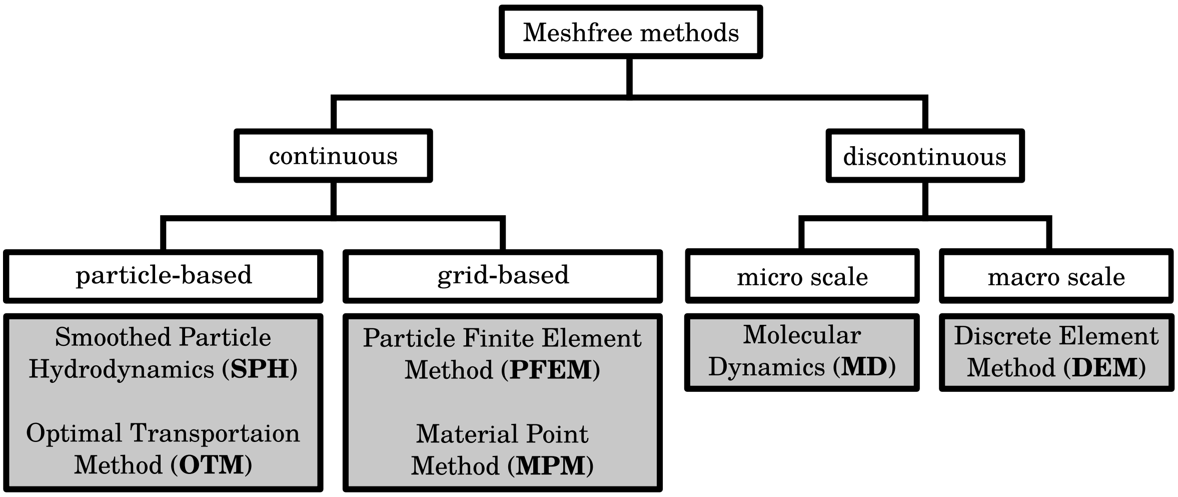
Meshfree methods
continuous
discontinuous
particle-based
grid-based
micro scale
macro scale
Smoothed Particle Hydrodynamics (**SPH**)
Optimal Transportaion Method (**OTM**)
Particle Finite Element Method (**PFEM**)
Material Point Method (**MPM**)
Molecular Dynamics (**MD**)
Discrete Element Method (**DEM**)

Figure 3.2. Distinction of mesh-less methods based on continuity, grid presence and scale.

3.1.2 Particle-based methods

Not all mesh-less methods are in fact particle-based but they are the majority. This is why, both descriptions are often mixed up. First of all, a mesh-less method does not depend on a mesh. This means in detail, that there is no fixed connectivity telling the particles to belong together. Simple particle methods like SPH or DEM are not meant to be aware of the global geometry. The particles move freely, having changing neighborhoods of particles resulting in certain forces. Then there are particle-based methods which constantly generate or deform grids, like the Particle Finite Elements Method (PFEM) by Oñate et al. (2004). The existing meshes in these methods do not necessarily last throughout the whole simulation. As one can see it is hard to draw the line between such more complex particle-based methods and mesh-based methods with remeshing techniques like the Deforming-Spatial-Domain/Space-Time (DSD/ST) procedure by Tezduyar et al. (1992). An overview of the common methods in literature can be found in figure 3.2.

The **benefits of particle-based methods** manifest in multiple features. First of all particles must not be present everywhere in the simulation space. This reduces the necessary resources and explains the initial application of SPH in astrophysics by Gingold & Monaghan (1977) and Lucy (1977). When simulating astrophysical phenomena, the mass is clustered in certain spaces while the vast surrounding space is empty. In particle-based methods the empty space can be ignored, Price (2011) calls this: 'resolution follows mass'. Secondly the particles allow for smooth surfaces and interfaces between interacting bodies. In comparison to this, the dynamic generation of matching meshes between two phases is more demanding. In the third place, the particle interactions are rather simple, making it easy to maintain force symmetry and thus momentum conservation.

A definitive **downside of particle based methods** is, that refinement and coarsening of the particles is comparatively complex. While the refinement is rather simple, the coarsening requires to collect several particles to generate coarse ones. Both processes suffer from physical errors, regarding volume and momentum conservation. This drawback renders SPH problematic for classical CFD problems which require mesh refinement. Further information on the topic can be found in VACONDIO ET AL. (2013). A further disadvantage of particle-based methods is that the changing neighborhoods lead to an increased numerical effort for the calculation of the interaction partners. With a mesh-based method, where the connectivity does not change, this additional effort is omitted. For this reason, mesh-based methods developed faster to maturity than particle-based methods, which initially required a higher computing power.

In this work the upsides of particle-based methods can be utilized for the simulation of SLM. The gaseous phase above the powder bed is not described to make use of the particle-based discretization advantage. The natural and smooth description of the surfaces by SPH stabilizes the approach, giving correct surface normals and curvatures for stable simulations. In the used DualSPHysics framework by CRESPO ET AL. (2015) the computations were massively parallelized to run on GPUs for a high simulation pace. Since the melt pool needs a high resolution in general and the flow in the pool is expected to be laminar (COOK & MURPHY (2019)) a further, local refinement is not necessary.

3.1.3 SPH kernel interpolation

The central idea of the SPH method is to introduce a kernel interpolant W to evaluate a field quantity A at a certain point in space $\mathbf{r}$ (GINGOLD & MONAGHAN (1977),LUCY (1977)) analytically by integrating around the point

$$A(\mathbf{r}) = \int_{\Omega} A(\mathbf{r}')W(\mathbf{r} - \mathbf{r}')dv, \tag{3.1}$$

where $\mathbf{r}'$ is the position vectors of volume increments in the neighborhood around the point $\mathbf{r}$. To fulfill partition of unity the kernel must satisfy the condition

$$\int_{\Omega} W(\mathbf{r} - \mathbf{r}')dv = 1, \tag{3.2}$$

which tells the kernel integral over the volume to be equal to one. With the kernel radius, the so-called smoothing length h, approaching zero, the kernel function converges towards the Dirac delta δ function. The method follows the principles of the Monte Carlo method (HAMMERSLEY & HANDSCOMB (1964)), which tells that a function can be approximated by randomly distributing points:

$$\langle A(\mathbf{r}_i)\rangle = \frac{1}{n_j}\sum_{j}^{n_j} A(\mathbf{r}_j)W(\mathbf{r}_i - \mathbf{r}_j). \tag{3.3}$$

Note that throughout this work the indices $\bullet_i$ and $\bullet_j$ represent the particle of interest i and all its variables, respectively its neighboring particles j. This formulation converges as the number of neighboring particles n_j goes towards infinity. To acquire the field values, particles of constant mass are distributed in the simulation domain and move with the flow. They carry the field quantities of the fluid. This way, on one hand each particle represents an amount of matter, moving in space, while on the other hand it represents an interpolation support for its neighbors. As the field values and their evaluated derivatives are defined on the same points, the method is called a collocation method. Since the particles with prescribed mass represent the disretization points the method is mass-resolved and mass conserving (PRICE (2011)). To the contrary, most mesh-based methods are volume-resolved and thus volume conserving. To integrate numerically using equation (3.3), the condition (3.2) is applied:

$$\langle A(\mathbf{r}_i)\rangle = \sum_j V(\mathbf{r}_j)A(\mathbf{r}_j)W(\mathbf{r}_i - \mathbf{r}_j), \tag{3.4}$$

with V_j being the volume of the neighboring particles. This way the the method is made independent from the number of neighboring particles, which is necessary to evaluate more/less populated areas as a physical effect. To receive the standard SPH approximation the variable volume is described depending on the mass $V = m/\rho$:

$$\langle A(\mathbf{r}_i)\rangle = \sum_j \frac{m_j}{\rho(\mathbf{r}_j)}A(\mathbf{r}_j)W(\mathbf{r}_i - \mathbf{r}_j), \tag{3.5}$$

In this equation, the variable density ρ is the most important property of the fluid in any SPH algorithm (PRICE (2012)), since it is needed for the calculation of all further field values. For a better overview the field values are rewritten as $A(\mathbf{r}_i) = A_i$ in the following and the kernel function $W(\mathbf{r}_i - \mathbf{r}_j)$ between i and j is abbreviated to W_{ij}.

Kernel function

The not yet specified kernel function has to fulfill at least three essential criteria to represent the Dirac delta, drafted by LUCY (1977):

- strict positive weighting (within specified borders), monotonically decreasing from $\mathbf{r}$ with smooth derivatives,
- point symmetry with respect to $\mathbf{r}$,
- a flat peak close to $\mathbf{r}$ to reduce local effects.

The original function used by GINGOLD & MONAGHAN (1977) to discretize SPH is the Gaussian kernel. According to Monaghan's 'golden rule' (MONAGHAN (1992)), this kernel should always be used for the physical interpretation of SPH. The disadvantage of the Gaussian kernel is that it does not have a compact support but converges to zero in infinite distance. Many functions were designed to resemble the Gaussian kernel with a compact support. Possible representations are polynomials and B-splines. One of the most commonly used kernels for SPH computations is the fifth order Wendland-C2 kernel from WENDLAND (1995), which can be derived continuously twice:

$$W_{ij} = \frac{7}{4\pi h^2}\begin{cases} \left(1 - \frac{r_{ij}}{2h}\right)^4\left(\frac{2r_{ij}}{h} + 1\right) & \text{for } r_{ij} \le 2h \\ 0 & \text{for } r_{ij} > 2h \end{cases} \tag{3.6}$$

where r_{ij} is the scalar particle distance delimited to a radius of $2h$. The graphical representation of the Wendland-C2 kernel and its first and second derivative can be found in figure 3.3. This kernel is a compromise between sufficient accuracy for most applications and minimal computational effort. Recently in CHOW ET AL. (2018) a quintic spline kernel was applied giving better results for ISPH. Nevertheless, for 3D systems the Wendland kernel had to be used because of its lower computational effort. The only free parameter of the kernel is the smoothing length h, which defines the radius of influence of the kernel ($2h$ for Wendland-C2). The smoothing length has a decisive influence on the simulation and is therefore a parameter that should not be chosen arbitrarily. First of all for an increase of the smoothing length leads to an increase of neighbors (quadratic in 2d, cubic in 3d), which results in an increased computational effort. On the physical side, the smoothing length has an influence on the smoothness and width of the transition regions resulting from jumps in the field values to be discretized. In processes such as pressure shock tubes or at phase boundaries in multi-phase simulations, the transition region and thus the smoothing length should be as small as possible. However, a minimal smoothing length is often the source of instability at such jumps. In this thesis the sufficiently smooth description of the curvature of the surface represents the lower limit for the smoothing length. Section 6.1.2 shows that a smoothing length of 1.7 dx is necessary for a stable simulation of the SLM process using the WCSPH and ISPH approach. With such smoothing lengths, the occurrence of the so-called pairing or clumping instability is an issue that also appears in this work and is also discussed in section 6.1.2. The pairing instability occurs when the particles come closer than the minimum of the first derivative of the kernel (see figure 3.3). With the Wendland-C2 kernel this minimum is located at 0.5 r/h. With a smoothing length of 1.7 dx this results in a minimum distance of the particles of 0.85 dx. While on a regular lattice this value is not undergone, the motions of the fluid can lead to such compressions and thus to this instability. At this point the particles are bound together due to the pressure forces and tend to collapse into each other. This instability is discussed for example in PRICE (2012), who proposes a smoothing length h of 1.2 dx based on the instability. In contrast, VIOLEAU (2012) suggests the following numbers of neighbors per particle: 30-50 in 2D and 80-200 in 3D. The applied smoothing length of 1.7 dx results in a total of 170 neighboring particles on a regular grid in 3D and thus follows Violeau.

Kernel correction

The kernel itself takes the particle distribution into account, since it should primarily calculate the density which is meant to be distribution dependent. This step is carried out between (3.3) and (3.4), where the division through the number of neighbors is replaced by multiplying the volume. Thus, the calculated value by a kernel reduces when there are fewer particles in the influence radius or when the particle distances are increasing. While this behavior is desired for variables like the density, it means that the kernel itself is not zeroth order consistent. In other words it does not fulfill the partition of unity, which is a crucial property of numerical methods and which is automatically fulfilled by mesh-based methods like the FEM or the FV method. To correct the kernel a normalization is proposed by SHEPARD

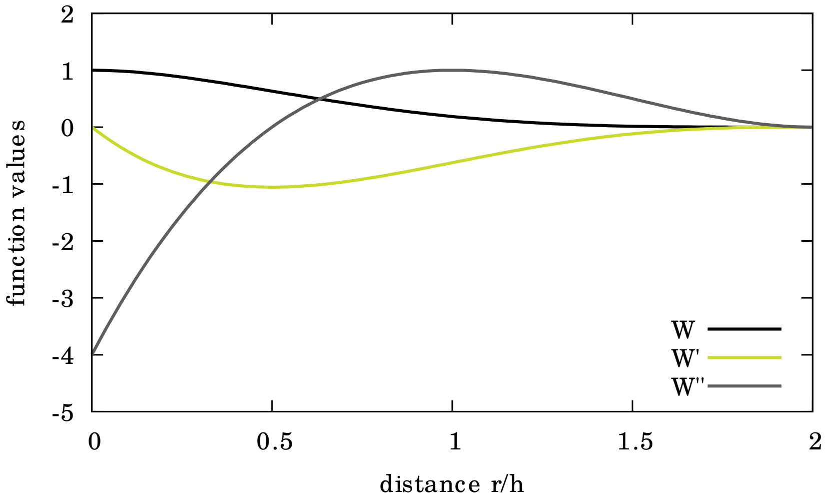

Figure 3.3. Representation of the Wendland kernel, as much as its first and second derivative.

(1968), being a common correction called Shepard filter today:

$$\tilde{A}_i = \sum_j V_j A_j \tilde{W}_{ij} \qquad with \qquad \tilde{W}_{ij} = \frac{W_{ij}}{\sum_j V_j W_{ij}}. \tag{3.7}$$

With this correction, the kernel is zeroth order consistent and can be used for arbitrary particle distributions, granting partition of unity. For a detailed overview of kernel properties and its corrections see Li & Liu (2007). It shall be noted, that corrected values will be described by $(\tilde{\bullet})$ throughout this work.

3.1.4 First Order Derivative

The most straight forward way of taking the spatial derivative is by applying the gradient directly to the kernel:

$$\begin{aligned} \nabla A(\mathbf{r}) &= \int_\Omega \nabla A(\mathbf{r}')W(\mathbf{r}-\mathbf{r}')dv \\ &= \int_\Omega \nabla[A(\mathbf{r}')W(\mathbf{r}-\mathbf{r}')]dv - \int_\Omega A(\mathbf{r}')\nabla W(\mathbf{r}-\mathbf{r}')dv \end{aligned} \tag{3.8}$$

With the Gaussian theorem the left term can be replaced with a surface integral and based on the symmetry of the kernel and its gradient the sign of the right term can be turned (Violeau (2012)):

$$\nabla A(\mathbf{r}) = \int_\Gamma A(\mathbf{r}')W(\mathbf{r}-\mathbf{r}')\mathbf{n}(\mathbf{r}')da + \int_\Omega A(\mathbf{r}')\nabla W(\mathbf{r}-\mathbf{r}')dv. \tag{3.9}$$

Later it is assumed, that the kernel is equal to zero in the surface integral, which is valid as long as the kernel does not interact with boundary conditions. Commonly this is avoided by using particles to represent solid boundaries and by transforming surface forces into volumetric forces, like performed in this work. This way the boundary conditions are treated in a volumetric way making use of the second term. On the other hand, this means that the standard boundary conditions in (2.7) respectively (2.19) can not be applied directly. These derivations and assumptions lead to the standard discretization for the first spatial derivative:

$$\nabla A(\mathbf{r}) = \int_{\Omega} A(\mathbf{r}')\nabla W(\mathbf{r}-\mathbf{r}')dv. \tag{3.10}$$

Discretized, this term is represented as:

$$\langle \nabla A_i \rangle = \sum_j \frac{m_j}{\rho_j} A_j \nabla W_{ij}. \tag{3.11}$$

Symmetrization

The resulting gradient from equation (3.11) is not zeroth order consistent, meaning that the gradient of a constant field not being zero. To correct this, a correction term is taken into account, generating the symmetric variant of the first derivative which is widely used within the SPH community. This is derived according to the (later formulated) golden rule of MONAGHAN (1992), which says that the density is to be taken within the derivations. By applying the product rule (LUCY (1977)) the identity is constructed as

$$\nabla \cdot \mathbf{A} = \left(\nabla \cdot (\rho \mathbf{A}) - \mathbf{A} \cdot \nabla \rho\right)/\rho. \tag{3.12}$$

Following this approach a symmetric representation of the divergence can be derived

$$\begin{aligned} \langle \nabla \cdot \mathbf{A}_i \rangle &= \frac{1}{\rho_i} \sum_j \frac{m_j}{\rho_j} \rho_j \mathbf{A}_j \cdot \nabla W_{ij} - \frac{\mathbf{A}_i}{\rho_i} \cdot \left(\sum_j \frac{m_j}{\rho_j} \rho_j \nabla W_{ij} \right) && (3.13) \\ &= \sum_j \frac{m_j}{\rho_i} \left(\mathbf{A}_j - \mathbf{A}_i\right) \cdot \nabla W_{ij}. && (3.14) \end{aligned}$$

The same procedure can be applied to the gradient:

$$\langle \nabla A_i \rangle = \sum_j \frac{m_j}{\rho_i} \left(A_j - A_i\right) \nabla W_{ij}. \tag{3.15}$$

In PRICE (2012) the same formulation is derived by applying a Taylor expansion to the gradient and incorporating the first term as a correction. For pressure forces this correction was found to result in instabilities when the difference becomes negative. The result is a clumping of the particles which has to be tackled with correction techniques. This approach is mostly used within ISPH formulations (like in LIND ET AL. (2012)), where corrections have to be applied anyways. The resulting formulation fulfills zeroth order consistency but does not strictly conserve linear momentum.

The majority in the literature applies another symmetric gradient based on the opinion that conservation of momentum has a higher priority than zeroth order consistency (MONAGHAN (1982); PRICE (2011)). The reason for this judgment is, that while correct kernels offer lower error in the kernel evaluation, a momentum conserving formulation offers long term stable results and thus a higher accuracy.

A momentum conserving gradient for the pressure was derived, making use of the quotient rule

$$\nabla\left(\frac{A}{\rho}\right) = \frac{\nabla A\rho}{\rho^2} - \frac{A\nabla\rho}{\rho^2}. \tag{3.16}$$

By pulling the gradient of the density from the right hand side to the left, the gradient ∇A can be discretized as follows:

$$\left\langle\frac{\nabla A_i}{\rho_i}\right\rangle = \sum_j \frac{m_j}{\rho_j}\frac{A_j}{\rho_j}\nabla W_{ij} + \frac{A_i}{\rho_i^2}\sum_j \frac{m_j}{\rho_j}\rho_j\nabla W_{ij} \tag{3.17}$$

$$= \sum_j m_j\left(\frac{A_j}{\rho_j^2} + \frac{A_i}{\rho_i^2}\right)\nabla W_{ij}. \tag{3.18}$$

This way the symmetry of forces is granted in all cases resulting in the conservation of momentum. For multi-phase simulations MONAGHAN & RAFIEE (2013) derived the following formulation from the Lagrangian:

$$\left\langle\frac{\nabla p_i}{\rho_i}\right\rangle = \sum_j m_j\frac{p_i + p_j}{\rho_i\rho_j}\nabla W_{ij}. \tag{3.19}$$

This formulation reduces instabilities between phases of different density while still conserving linear momentum like (3.18). Anyways, both formulations do not grant zeroth order consistency.

Gradient Correction

The calculation of the corrected gradient is state of the art in the field of ISPH as it is a necessity for most systems of equations implicitly calculating the pressure. In WCSPH it is rather uncommon, as the correction comes together with high computational effort. Nevertheless, gradient correction is applied in this work on both approaches, ISPH and WCSPH. The reason for this is the calculation of the curvatures, which is demanding the correction for physical and stable values (FÜRSTENAU ET AL. (2020a)). The gradient correction applied in this work originates from RANDLES & LIBERSKY (1996). The correction is applied for a gradient or divergence of a field to fulfill first order completeness. For the kernel gradient correction a renormalization is performed, starting from the fulfillment of the first oder completeness condition

$$\sum_j V_j\mathbf{r}_{ij} \otimes \tilde{\nabla}W_{ij} = \begin{pmatrix} 1 & 0 \\ 0 & 1 \end{pmatrix}, \tag{3.20}$$

with $\tilde{\nabla}W_{ij} = \mathbf{L}_i\nabla W_{ij}$, the resulting two-dimensional correction matrix $\mathbf{L}_i$ can be explicitly calculated as:

$$\mathbf{L}_i = \left(\sum_j V_j\mathbf{r}_{ij} \otimes \nabla W_{ij}\right)^{-1}. \tag{3.21}$$

Applying the corrected divergence, (3.14) can be evaluated independently from the particle distribution, giving the exact result for a linear field. The only drawback is, through the gradient correction the symmetry of the gradient $\nabla W_{ij} = -\nabla W_{ji}$ is lost. This is the reason why in this thesis the corrected gradient is not applied onto terms being important for the energy and momentum balance (pressure, viscous force and heat conduction). Here, the corrected gradient is only applied to the calculation of curvature in equation (3.39) and its gradient (3.46), the pressure-Poisson equation (PPE) in equation (3.52), and its source term (3.53), which clearly benefit from the correction in terms of stability and accuracy. In LI & LIU (2007) further correction techniques for SPH are presented. Among others, the Moving Least Squares (MLS) correction from LI & LIU (1996) and LIU ET AL. (1997) is mentioned. Their approach corrects the kernel by solving a system of equations per particle. This method leads to a first order consistent kernel and gradient. However, the solution results in much higher computational effort than the applied corrections and is therefore rejected. The corrected gradient of the corrected kernel by BONET & LOK (1999) was tested against the used corrected gradient in a previous work (FÜRSTENAU ET AL. (2018)) and was found to give no significant improvement besides its higher computational effort.

3.1.5 Second Order Derivative

When solving CFD in the strong form, second order derivatives are needed to model several terms based on the Laplacian, namely the viscosity term, the PPE for ISPH and the heat conduction term. In the early days of SPH it was found that the application of the second derivative in the same way as the first derivative

$$\langle \nabla^2 A_i \rangle = \sum_j \frac{m_j}{\rho_j} \left(A_j - A_i \right) \nabla^2 W_{ij} \tag{3.22}$$

is not giving satisfying results (BROOKSHAW (1985); MONAGHAN (1988)). Instead of this representation two different approaches emerged. The most popular approach is the finite difference based one introduced by BROOKSHAW (1985) achieved by expanding the formulation for isotropic heat conduction $\nabla \cdot (k \nabla T)$ by a Taylor series. The most commonly used form is the one introduced by CLEARY (1998):

$$\langle \nabla \cdot (k \nabla T_i) \rangle = \sum_j \frac{2m_j}{\rho_j} \frac{2k_i k_j}{k_i + k_j} \left(T_j - T_i \right) \frac{\mathbf{r}_{ij} \cdot \nabla W_{ij}}{\mathbf{r}_{ij}^2 + \eta^2}. \tag{3.23}$$

Herein η is a factor keeping the formulation from diverging in case of particles getting too close. η is chosen to be $0.01\ h$ according to CLEARY (1998). For the correction of the finite difference based second derivative, the correction matrix from equation (3.21) can be applied. This approach is commonly used in the literature for thermal conductivity, viscosity and the PPE. The alternative is to calculate the gradient of the temperature first and then calculate its divergence (3.14):

$$\langle \nabla \cdot (k \nabla T_i) \rangle = \sum_j \frac{m_j}{\rho_j} \left(k_j \nabla T_j - k_i \nabla T_i \right) \cdot \nabla W_{ij}. \tag{3.24}$$

This approach is referred to as nested sum or double summation derivative. For the gradient and the divergence several representations can be applied, like explained in section 3.1.4. This approach is the only one of the three presented approaches that offers the possibility to directly apply Neumann boundaries. It is used e.g. for modeling thermal conductivity (see BIRIUKOV & PRICE (2018)) or as a correction for ISPH as performed by HU & ADAMS (2009). Additionally the Implicit Incompressible SPH (IISPH) approach by IHMSEN ET AL. (2014) is based on this derivative. In this ISPH approach, the PPE is set up entirely based on the double summation approach, which is solved in a matrix-free way. In literature oftentimes it is observed, that the double derivative tends to oscillations like in FATEHI ET AL. (2008).

In an earlier study (see FÜRSTENAU ET AL. (2017)) it was found found that all three mentioned approaches are able to model incompressible free-surface flows in stable manner. It was concluded, that the instabilities were not occurring as the higher oder kernel from (3.6) was used. In a lid-driven cavity flow the double derivative approach behaved too stiff, leading to total stop of the motion, while the direct second derivative was constantly underestimating the pressures. For this reason the difference-based approach was used throughout this work. Anyways, the application of the IISPH approach is a topic of interest as it can lower the numerical effort for incompressible SPH drastically. BIRIUKOV & PRICE (2018) showed that the double derivative representation of the Laplacian gives stable results when using higher order kernels like the M6 quintic spline kernel. In their work several approaches were tested for thermodynamical simulations.

3.2 Modeling of the balance equations

In this section the modeling of the balance equations from section 2.2 is presented. The section starts with the balance of momentum, with an additional subsection about the treatment of surface forces, which are both identical for weakly compressible and incompressible SPH. Afterwards, the continuity equation follows, divided into two subsections for WCSPH and ISPH separately. The section is finalized by the discretization of the energy equation, which is again identical for WCSPH and ISPH. It should be noticed, that in the following, when the current density ρ is used, for ISPH the reference density ρ_0 is applied instead, since the ρ is constant in the incompressible case.

3.2.1 Balance of momentum

To start with the modeling first the Navier-Stokes equation (2.27) on the particle of interest i is evaluated. This reads as follows:

$$\frac{d\mathbf{v}_i}{dt} = -\frac{\nabla p_i}{\rho_i} + \nabla \cdot (\nu_i \nabla \mathbf{v}_i) + \mathbf{a}_i^g + \mathbf{a}_i^S, \tag{3.25}$$

where $\mathbf{a}_i^S$ and $\mathbf{a}_i^g$ are the particle accelerations due to surface effects and gravity. While the accelerations in the Navier-Stokes equation indicate volumetric forces, in SPH also Neumann boundary conditions from (2.18) are represented as volumetric forces following the concept of the Continuous Surface Force (CSF) from BRACKBILL ET AL. (1992). An explanation of this approach follows in section 3.2.2.

First, the pressure term is implemented as introduced in (3.19):

$$\left\langle \frac{\nabla p_i}{\rho_i} \right\rangle = \sum_j m_j \frac{p_i + p_j}{\rho_i \rho_j} \nabla W_{ij}. \tag{3.26}$$

This equation shows the most stable results and is widely used, especially for multiphase flows (see e.g. COLAGROSSI & LANDRINI (2003); MONAGHAN & RAFIEE (2013); HIRSCHLER ET AL. (2017)). For single phase flows like applied in this work, also the single-phase approach from equation (3.18) could be applied, while the difference for incompressible and weakly compressible flow is negligible. For the calculation of the viscous forces several formulations are featured in the literature, most of them based on the second order derivative by BROOKSHAW (1985). In this work the viscosity based on (3.23) by CLEARY (1998) is applied:

$$\langle \nabla \cdot (\nu_i \nabla \mathbf{v}_i) \rangle = \sum_j \frac{\xi m_j}{\rho_i \rho_j} \frac{4 \mu_i \mu_j}{\mu_i + \mu_j} \frac{(\mathbf{v}_j - \mathbf{v}_i) \cdot \mathbf{r}_{ij}}{r_{ij}^2 + \eta^2} \nabla W_{ij}. \tag{3.27}$$

In this formulation ξ is a calibration factor which was calibrated by CLEARY (1998) with a Couette flow, resulting in a value of $\xi = 4.96333$. This result was tested in the lid-driven cavity flow test in Sec. 5.1, giving satisfying results. Like the pressure term, this equation is able to handle varying densities and viscosities and could thus be used for multi-phase flows as well. Since both terms are also applied in an uncorrected manner (resulting in $\nabla W_{ij} = -\nabla W_{ji}$), both terms conserve linear momentum. Due to the fact, that the direction of both, the pressure and the viscous force, is governed by the gradient of the kernel, both terms also conserve angular momentum according to PRICE (2012). While this is common for the pressure description, there exist some viscosity formulations like in SZEWC ET AL. (2012), where the direction of the viscous force is governed by the relative velocity between the particles. These approaches do not conserve angular momentum.

In the external body accelerations $\mathbf{a}$, two forces are introduced in the discretized momentum equation. First of all, in this term the gravity appears as a constant acceleration affecting every fluid particle. For the expansion based buoyancy, commonly the Boussinesq approximation is applied (COOK & MURPHY (2019)). This approximation accounts for the temperature dependent density of materials

$$\rho(T) = \rho_0 + \rho'(T) = \rho_0 - \rho_0 \beta T', \tag{3.28}$$

where β and T' are the thermal expansion coefficient and the temperature deviation from the reference temperature T_0. Under the assumption of a divergence-free velocity field and by linearization, the resulting gravitational force term reads

$$\mathbf{a}_i^g = \mathbf{g} \left(1 - \beta \left[T_i - T_0\right]\right). \tag{3.29}$$

Details of the Boussinesq approximation and the full modeling of the non-Bussinesq regime are outlined and analyzed in a SPH framework in SZEWC ET AL. (2011). The second external body acceleration $\mathbf{a}^S$ consists of the surface tension effects and the recoil pressure based on the Neumann boundaries from equation (2.19). These boundary forces are reformulated into volumetric forces, following the concept of CSF, explained in the following section.

Resolution	2D	3D
10 μm	0.906	0.928
8 μm	0.968	0.932
6 μm	0.977	1.011
4 μm	0.937	0.891
2 μm	1.076	0.877

Table 3.1. Particle normals integrated over the discretization perpendicular to the normal surface.

3.2.2 Surface Forces

The CSF model was initially designed for the contact of two fluids. Between the two fluids, a sharp jump in material properties occurs resulting in surface tension. The first part of the CSF model according to BRACKBILL ET AL. (1992) introduces a transition region. This way the surface force $\mathbf{F}_S$ is represented by a volumetric force $\mathbf{f}_S$ which is applied within the transition region denoted by δ_S

$$\mathbf{F}_S = \int_\Gamma \mathbf{f}_S da = \int_\Omega \mathbf{f}_S \delta_S dv. \tag{3.30}$$

Assuming that $\mathbf{f}_S$ is identical in both formulations, which is true for thin films, the line can be shortened by the term $\int_{\partial A} \mathbf{f}_S da$, since the surface is also identical. Following MORRIS (2000) and assuming $\delta_S := |\mathbf{n}|$ the formulation reads then:

$$1 = \int_{\partial \Gamma_\perp} |\mathbf{n}| ds_\perp. \tag{3.31}$$

This means, that the integral of the normals perpendicular to the surface in the finite band over the particles has to be equal to the unit normal. This way the rest of the formulation can stay untouched and does not need a volumetric reformulation. Brackbill claims that with this formulation numerical instabilities for surface tension can be avoided demanding $\kappa s < 1$, where s is the transition region width. The requirement from (3.31) was tested in an example simulation where the normals and curvatures of converging bubbles were calculated. Plots of the calculated normal magnitudes can be found in figure 3.4. To check for the integral value five equidistant particles of each discretization were taken, summed up and multiplied with the discretization length to integrate the normal length in normal direction. The resulting normal length ranges from 0.877 to 1.076 resulting from the irregular distribution of the particles (see table 3.1). On a regular lattice the normal magnitudes result in much lower divergence from the analytical value.

The second part of the model is the weighting of the normals in the transition region. This is done by a color function

$$c(\mathbf{x}) = \begin{cases} c_1, & \text{in fluid 1;} \\ c_2, & \text{in fluid 2;} \\ \langle c \rangle = (c_1 + c_2)/2, & \text{at the interface.} \end{cases} \tag{3.32}$$

To realize this each fluid particle is given the color of its belonging fluid. Due to a lack of interface particles this system is binary for two phase flows. Based on this color distribution a smoothed color function $\tilde{c}$ can be computed

$$\langle \tilde{c_i} \rangle = \sum_j \frac{m_j}{\rho_j} c_j W_{ij}. \tag{3.33}$$

The formulation can be used to recognize the interface region but more importantly the gradient of the color function is used to calculate the interface normals in the interface region based on equation (3.15)

$$\langle \mathbf{n}_i \rangle = \sum_j \frac{m_j}{\rho_j} (c_j - c_i) \nabla W_{ij}. \tag{3.34}$$

This gradient is applied for the contact of two fluids with a unit jump between the color functions. For multiple fluids the formulation becomes more complex, as normals and curvatures have to be calculated independently for every phase pairing (see KUNZ ET AL. (2018)). As one can see, the normal in the equation vanishes when two particles have the same color and is thus generated by the particles of the other fluid. For single phase flows with free surfaces, like applied in this work, the other fluid is not explicitly modeled. For this reason the gradient is altered, following HIRSCHLER ET AL. (2017), based on the simple SPH gradient (3.11):

$$\langle \mathbf{n}_i \rangle = \sum_j \frac{m_j}{\rho_j} \nabla W_{ij}. \tag{3.35}$$

As the non-modeled particles cannot contribute to the surface normals, only the particles of the same fluid are incorporated in the formulation. The normal on the one hand describes the free surface based on the fluid particles with a weighting based on the distance from the surface, fulfilling (3.31). It was found that for a smooth transition of the normals and thus of the curvature κ a smoothing of the normals has to be performed, which was suggested by HIRSCHLER ET AL. (2017). The smoothing is performed using (3.7)

$$\tilde{\mathbf{n}}_i := \frac{\sum_j \mathbf{n}_j W_{ij}}{\sum_j W_{ij}}. \tag{3.36}$$

Alternatively the color function can be smoothed following SZEWC ET AL. (2012). The final formulation for the smoothest and most physical normals (fulfilling (3.31)) consists of three steps:

- calculate normals $\mathbf{n}$ by (3.35);
- cut off normals with $|\mathbf{n}| < 0.1/h$;
- smooth normals $\tilde{\mathbf{n}}$ by (3.36).

The cutoff is made necessary to account for erroneous normals occurring within the continuum body for irregular particle distributions. This type of cutoff is always necessary to reduce small normals (see e.g. COLAGROSSI & LANDRINI (2003); HU & ADAMS (2006)) but has to be increased for single phase flows using equation (3.35).

Based on the CSF model the Neumann boundary conditions from (2.19) can be applied to a finite layer of particles resulting in a physical force, despite the fact that the boundary

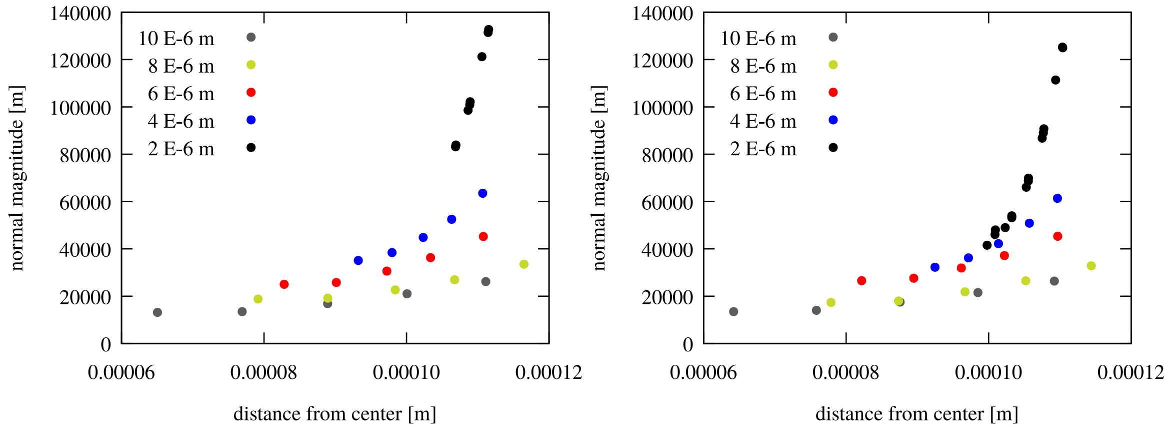

Figure 3.4. 3D representation of the surface normal length of a set of surface particles of converged bubbles; left: bubble in 2D with an analytical radius of 122 μm; right: bubble in 3D with an analytical radius of 112 μm.

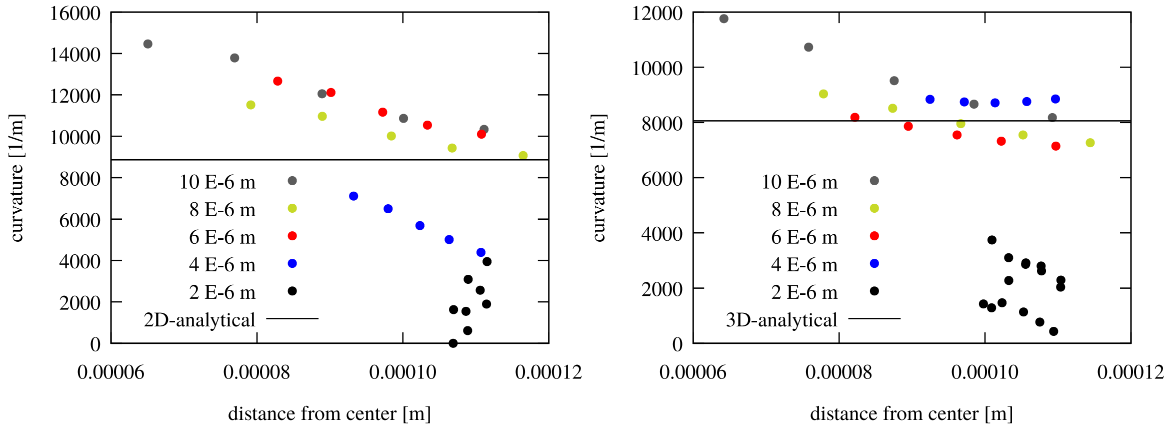

Figure 3.5. 3D representation of the curvatures of a set of surface particles of converged bubbles; left: bubble in 2D with an analytical radius of 112 μm; right: bubble in 3D with an analytical radius of 122 μm.

condition is not only applied on the surface. The surface forces are included in the external accelerations $\mathbf{a}$ in (2.27)

$$\mathbf{a}_i^S = \left(-\gamma_i \kappa_i \hat{\mathbf{n}}_i + \nabla_S \gamma_i + p_i^{rec} \hat{\mathbf{n}}_i\right) \frac{|\mathbf{n}_i|}{\rho_i}. \tag{3.37}$$

While the inclusion of the recoil pressure can be performed by calculating the pressure by (2.31) and its multiplication with the unit normal, the surface tension effects have to be explained in more detail. For free surface tension particular attention has to be paid on a stable force distribution, as there is no second phase that can damp oscillations. The smoothed normal is one key ingredient for this stable force. Additionally the curvature has to be treated with special care. For 2D simulations, the curvature can be calculated in the well known way applying (3.14) to calculate the divergence of the normalized smoothed normals $\hat{\hat{\mathbf{n}}}$

$$\langle \kappa_i \rangle = V_0 \sum_j \left(\hat{\hat{\mathbf{n}}}_j - \hat{\hat{\mathbf{n}}}_i \right) \cdot \tilde{\nabla} W_{ij}. \tag{3.38}$$

In this formulation the use of the corrected gradient (3.21) is mandatory. Also the correction and the curvature have to be calculated, based on particles with an existing smoothed normal $\tilde{\mathbf{n}}$. This procedure by HIRSCHLER ET AL. (2017) leads to stable physical curvatures in 2D which can be tested by comparing them to the analytical curvature of a sphere which was carried out FÜRSTENAU ET AL. (2020a). For 3D simulations it was found that, the calculation with (3.38) leads to an overestimation of the curvature. In FÜRSTENAU ET AL. (2020a) a method was introduced to calculate the physical curvature in 3D, based on the principal curvatures. To do so, first of all a curvature tensor is calculated as the gradient of the normalized smoothed normals

$$\langle \mathbf{K}_i \rangle = V_0 \sum_j \hat{\hat{\mathbf{n}}}_{ij} \otimes \tilde{\nabla} W_{ij}. \tag{3.39}$$

Here again the corrected gradient has to be calculated for physical curvature values. Like usual with particle based methods, the values of $\mathbf{K}$ are described in terms of a global Cartesian coordinate system. To calculate the principal curvatures, the curvature tensor has to be transformed to a local coordinate system based on the normal and tangential vectors. The first tangent vector is constructed based on the normal and the global coordinate axes

$$\mathbf{t}_i^1 := \begin{cases} \hat{\hat{\mathbf{n}}}_i \times (0,1,0) & if \quad ||\hat{\hat{\mathbf{n}}}_i \times (0,1,0)|| > 0.01 \\ \hat{\hat{\mathbf{n}}}_i \times (1,0,0) & \qquad else \end{cases}. \tag{3.40}$$

The choice of the axes is arbitrary, a distinction is just necessary to avoid tangent vectors with zero length. In order to get a local Cartesian coordinate system, the tangent vector has to be normalized. With the first tangent, the second one is calculated from

$$\hat{\mathbf{t}}_i^2 := \hat{\hat{\mathbf{n}}}_i \times \hat{\mathbf{t}}_i^1. \tag{3.41}$$

To rotate the curvature tensor into the local coordinate system, the bases of the tensor have to be transformed by multiplication with the transformation tensor $T_{ij} = \mathbf{G}_i \cdot \mathbf{L}_j$ from both sides. Here, $\mathbf{G}$ are the Global basis vectors which form a unit matrix and $\mathbf{L} = (\hat{\mathbf{n}}, \hat{\mathbf{t}}^1, \hat{\mathbf{t}}^2)$ are the local basis vectors (described in Einstein's summation convention):

$$K_{kl} = T_{ki}^T K_{ij} T_{jl}. \tag{3.42}$$

After the transformation, the matrix is reduced to a two dimensional one based on the tangent vectors. This is done by deleting the row and the column depending on the normal vector, in our case the first one each. Through the reduction, a 2x2 matrix is left which is fully populated, as the tangent vectors were arbitrarily chosen. Now the principal curvatures κ_1 and κ_2 are calculated, which is equal to the calculation of the eigenvalues of a matrix. When the principal curvatures were calculated the mean curvature is computed as

$$\kappa_i = \frac{1}{2}(\kappa_1 + \kappa_2). \tag{3.43}$$

With either the curvature from (3.38) for 2D cases or from (3.43) for 3D cases, the curvature is smoothed again by applying the Shepard filter (3.7)

$$\tilde{\kappa}_i := \frac{\sum_j \kappa_j W_{ij}}{\sum_j W_{ij}}. \tag{3.44}$$

The additional smoothing is only carried out between particles with an existing smoothed normal to achieve a constant distribution of curvature over the surface region without widening the transition region. The smoothed curvature $\tilde{\kappa}$ is plugged into (3.37).

The calculated curvatures for the converging bubbles can be seen in figure 3.5. In the figures two things become obvious. The curvatures in 3D are converging much better towards the analytical value. This was also observed in FÜRSTENAU ET AL. (2020a) where the novel approach was tested against the one from equation 3.38. Here the standard approach showed a slightly better average value but a higher scattering. The scattering can also be an issue in the plots, since only very few particles are plotted for better visibility. The second observation is, that for the 2D curvature the two highest resolutions seem to underestimate the curvature as much as the highest curvature in 3D. This phenomenon was observed whenever the resolution is very fine compared to the represented geometrical features. For the bubbles, this critical value between discretization length and bubble diameter was achieved at a ratio of 56 in 2D and 122 in 3D. In the SLM cases these values are not reached since the largest powder particles have a diameter of 38 μm and the smallest simulated discretization is 1 μm. Most of the simulations are carried out with 3 μm resolution, leading to a ratio around 13.

The last term to be modeled is the Marangoni convection $\nabla_S \gamma$. To calculate the surface gradient of the surface tension coefficient, the simplest procedure is

$$\nabla_S \gamma_i = \nabla \gamma_i - \left(\nabla \gamma_i \cdot \hat{\tilde{\mathbf{n}}}_i \right) \hat{\tilde{\mathbf{n}}}_i. \tag{3.45}$$

Herein, the gradient of the surface tension coefficient is calculated

$$\langle \nabla \gamma_i \rangle = \sum_j \frac{m_j}{\rho_j} (\gamma_j - \gamma_i) \cdot \tilde{\nabla} W_{ij}. \tag{3.46}$$

Afterwards the normal part is subtracted to form the purely tangential gradient. A further smoothing of γ is not necessary, as the appearing gradients are not steep.

3.2.3 Continuity equation - WCSPH

The continuity equation in weakly compressible SPH is handled in an explicit way, like the whole algorithm. Following the modeling of the DualSPHysics framework, the density starts from reference density at $t = 0\ s$ and is integrated in time via

$$\left\langle \frac{d\rho_i}{dt} \right\rangle = \sum_j m_j \left(\mathbf{v}_j - \mathbf{v}_i\right) \cdot \nabla W_{ij}. \tag{3.47}$$

The formulation is based on the symmetrized variant of the divergence (3.14). The time integration of the density shows a higher stability than the direct evaluation of the particle distribution at each time step for a direct evaluation of the density (see e.g. HU & ADAMS (2009)). The reason for this is the quadratic time integration (see section 4.1.1), which results in a smoother evolution of the density and is less susceptible to disturbances. Based on the current density ρ_i the pressure is calculated based on the Tait equation (2.28):

$$p_i(\rho_i) = \frac{\rho_i c_0^2}{\tau} \left(\left(\frac{\rho_i}{\rho_0} \right)^{\tau} - 1 \right). \tag{3.48}$$

The Tait equation for weakly compressible materials ($\tau = 7$) penalizes small density deviations with an exponential increase in pressure. Through the strong reaction of the pressure only slight deviations of the density around 1 % are occurring (VIOLEAU (2012)).

3.2.4 Continuity equation - ISPH

In an incompressible framework, the continuity equation is based on the assumption of a constant density ($\rho(t) = \rho_0$), which leads to the fact that the velocity field is divergence-free (see equation (2.4)). In mesh-based CFD, this condition is met by ensuring that all the inflows and outflows of each cell are in equilibrium (except for sinks and sources). Since the connectivity and the cell faces are known and usually do not change over time, the resulting system of equations is set up once. In SPH, the zero-divergence condition results in the criterion that for each particle, the adjacent particle velocities pointing towards and away from the particle of interest add up to zero. The velocities in the system of equations are weighted with their distance to the particle of interest (by the kernel gradient). This means that the system of equations has to be set up anew in every time step, because the neighborhoods and particle distances are constantly changing. In mesh-based schemes oftentimes a monolithic approach is used, where the velocity is solved with the zero-divergence condition (2.4) and the Dirichlet (2.17) and Neumann boundary conditions (2.18) are applied directly onto the velocity. From this system of equations the pressure can be extracted as a side product. This approach did not settle in the SPH community. Instead of that a predictor-corrector procedure developed by CUMMINS & RUDMAN (1999) is commonly applied. When a new time step is calculated first an intermediate position of the particles $\mathbf{r}^*$ is calculated, which is advantageous compared to using the end-position of the last time step $\mathbf{r}^t$ according to RIDER (1995). This intermediate position is of pure numerical nature and serves as predictor step. The non-pressure forces are evaluated based on the intermediate position and the velocities of the old time step leading to a velocity field which does not fulfill the zero divergence criterion. To correct the velocity field, its divergence can be expressed as

$$\nabla \cdot \mathbf{v}^{t+\Delta t} = 0 = \nabla \cdot \left(\mathbf{v}^t + \left(-\frac{\nabla p^{t+\Delta t}}{\rho} + \nabla \cdot \left(\nu \nabla \mathbf{v}^t \right) + \mathbf{a}^t \right) \Delta t \right). \tag{3.49}$$

The term of the unknown pressures can be separated from the non-pressure terms by reordering. Since the non-pressure forces are calculated explicitly, this method is not truly implicit but of an explicit type with an implicit pressure calculation. For this reason the term semi-implicit is more suitable. Through the reordering the resulting formulation reads

$$\nabla \cdot \left(\frac{\nabla p^{t+\Delta t}}{\rho} \right) \Delta t = \nabla \cdot \left(\mathbf{v}^t + \left(\nabla \cdot \left(\nu \nabla \mathbf{v}^t \right) + \mathbf{a}^t \right) \Delta t \right). \tag{3.50}$$

For a better readability the current velocity $\mathbf{v}^t$ and the non-pressure accelerations are combined into the so-called intermediate velocity $\mathbf{v}^*$ which is part of the predictor step like the intermediate position $\mathbf{r}^*$. With this simplification the equation

$$\nabla \cdot \left(\frac{\nabla p^{t+\Delta t}}{\rho} \right) = \frac{\nabla \cdot \mathbf{v}^*}{\Delta t}, \tag{3.51}$$

can be identified as the Pressure-Poisson Equation (PPE) which has to be solved. For the discretization of the left hand side several approaches appear in the literature. Basically they can be summed up in two different groups, depending on the type of the second derivative (see 3.1.5). The largest group is applying the second derivative according to CLEARY (1998) in several variations. Examples for this are LIND ET AL. (2012) or HIRSCHLER ET AL. (2017). The second group applies the double derivative shown in (3.24) like IHMSEN ET AL. (2014) or HU & ADAMS (2009), where Hu&Adams are using both derivatives within one time step to make use of both approaches advantages. In this work the PPE is discretized by applying the first approach from equation (3.23) for the PPE

$$\left\langle \nabla \cdot \left(\frac{\nabla p_i}{\rho_i} \right) \right\rangle = \sum_j \frac{4 m_j}{\rho_j} \frac{p_j - p_i}{\rho_i + \rho_j} \frac{\mathbf{r}_{ij} \cdot \tilde{\nabla} W_{ij}}{\mathbf{r}_{ij}^2 + \eta^2}. \tag{3.52}$$

The discretization of the source term follows the commonly used symmetrized divergence from equation (3.14):

$$\left\langle \frac{\nabla \cdot \mathbf{v}_i^*}{\Delta t} \right\rangle = \sum_j \frac{m_j}{\rho_j} (\mathbf{v}_j - \mathbf{v}_i) \cdot \tilde{\nabla} W_{ij} \tag{3.53}$$

Boundary conditions

Since the PPE only has the pressure as primary variable, the boundary conditions from equation (2.19) can not be applied. For this reason new boundary conditions have to be constructed. The standard boundary condition for ISPH approaches is to apply a Dirichlet boundary at the free surface yielding $p_b = 0$. It was found that, when accounting for surface tension the use of this boundary condition is not sufficient. In the literature two approaches were found for modeling ISPH with surface tension according to HIRSCHLER ET AL. (2017) and NAIR & TOMAR (2014). The approach of HIRSCHLER ET AL. (2017) was implemented and tested in FÜRSTENAU ET AL. (2020a), where it showed to be prone to instabilities in our implementation. Due to its higher complexity the the approach according to NAIR & TOMAR (2014) was not tested but appears to be a promising alternative. In FÜRSTENAU ET AL. (2020a) a novel boundary condition was constructed, which is explained in the following. The new pressure boundary is based on the balance of linear momentum at an interface between two fluids (LANDAU & LIFŠIC (1987)):

$$(p_1 - p_2 + \gamma\kappa)\hat{\mathbf{n}} = (\boldsymbol{\sigma}_1 - \boldsymbol{\sigma}_2) \cdot \hat{\mathbf{n}} + \nabla_S \gamma. \tag{3.54}$$

The index denotes the different phases. For the case of incompressible fluids, the left hand side represents an equilibrium of volumetric stresses and the right hand side represents an equilibrium between the different stresses. Since $\boldsymbol{\sigma}$ depends only on the viscosity, which is expected to be zero in normal direction for incompressible flows, there is no interference between the two sides. Therefore, the formulation is simplified to the Laplace formula, representing uniaxial conservation (BRACKBILL ET AL. (1992))

$$p_2 - p_1 = \gamma\kappa. \tag{3.55}$$

To account for the recoil pressure, its term is added onto the right hand side. Such effect was not covered in the initial formulation but its addition appears legit. If the explicit modeling of the second phase is not desired, the pressure jump can be explicitly applied onto the free surface

$$p_b = \gamma\kappa + p^{rec}. \tag{3.56}$$

If recoil pressure is not intended, constant atmospheric pressure can be applied instead. For the recognition of the free surface, the divergence of the particle distribution is calculated

$$\langle \nabla \cdot \mathbf{r}_i \rangle := \sum_j \frac{m_j}{\rho_j} \mathbf{r}_{ij} \cdot \nabla W_{ij}. \tag{3.57}$$

This value is then compared to the divergence of a fully filled Cartesian grid:

$$\langle \nabla \cdot \mathbf{r} \rangle_i \geq 0.9 \, \langle \nabla \cdot \mathbf{r} \rangle_{grid} \, . \tag{3.58}$$

This formulation showed the best results for the recognition of the free surface. To account for the solid boundaries, the PPE is not treated with Neumann boundary conditions, as there is no natural influence from boundaries on the pressure. Instead, the solid boundary is modeled with particles contributing to the PPE like fluid particles. The only difference is, that their velocity is prescribed. Through the continuous description, the incompressibility condition is treated in the same way near the boundary like in the continuum. This approach is producing stable results but resulting in a comparatively high numerical effort, as several layers of boundary particles near the fluid have to be simulated to fill the kernel of the fluid particles. Recently BAND ET AL. (2018) presented a pressure extrapolation method, enhancing the approach of ADAMI ET AL. (2012). In their approach the pressures of the boundary particles is not solved within the PPE. Instead of this, the pressure of the boundaries is calculated after the PPE is solved, with the goal to satisfy the no-penetration condition based on the pressures and velocities of the fluid particles. This way the numerical effort can be reduced while the stability shall be further increased.

Source term

When permanent surface forces (such as ambient pressure or surface tension) are applied, numerical errors add up, leading to permanent compressions. These compressions are apparently not sufficiently counteracted by the velocity divergence source term in equation (3.51). This phenomenon has been described in ALY ET AL. (2013). To overcome the unwanted compressibility, an additional source term based on the intermediate density is introduced. This source term is derived from the density of the new time step, which is expected to be equal to the initial density $\rho^{t+\Delta t} = \rho_0$. The density is divided into two parts. First an intermediate density ρ^*, which corresponds to the evaluation of the particle distribution $\rho_i^* = \sum_j m_j W_{ij}$ at the intermediate position $\mathbf{r}^*$. Just like the intermediate position, the intermediate density just corresponds to the predictor step. Second, the change in density, following equation (3.47), caused by the pressure accelerations in the corrector step is calculated:

$$\rho^{t+\Delta t} = \rho_0 = \rho^* - \rho \nabla \cdot \left(\frac{\nabla p}{\rho} \right) \Delta t^2. \tag{3.59}$$

After reformulation of the expression, a different right hand side is derived for the PPE.

$$\nabla \cdot \left(\frac{\nabla p}{\rho} \right) = \frac{\rho_0 - \rho^*}{\rho_0 \Delta t^2}. \tag{3.60}$$

In this source term, compressions have a permanent effect, which leads to expansion pressures. However, IHMSEN ET AL. (2014) showed that the use of a purely density-based source term leads to unphysical damping at the surface and to a reduction of the spattering behavior, for which a source term correction is applied. ALY ET AL. (2013)) instead suggests a combination of the velocity and density based source term for long term stable simulations

$$\nabla \cdot \left(\frac{\nabla p}{\rho} \right) = \alpha_{\mathbf{v}} \frac{\nabla \cdot \mathbf{v}^*}{\Delta t} + \alpha_\rho \frac{\rho_0 - \rho^*}{\rho_0 \Delta t^2} \tag{3.61}$$

After intensive numerical tests, the combination of $\alpha_{\mathbf{v}} = 1$ and $\alpha_\rho = 0.1$ is used. This combination leads to the expected fluid behavior with a small corrective term, penalizing lasting compressions which were not prohibited by the zero divergence condition. IHMSEN ET AL. (2014) uses a more complex approach for the intermediate density, comprising of the particle distribution and the divergence of the velocity. In this work the simpler term is used as the intermediate density is only a corrective term and the velocity already appears in the main source term.

3.2.5 Energy equation

The discretized energy equation in this work consists of heat conduction, a heat source of the laser and thermal losses by partial evaporation, radiation and convection. Since the source and loss terms were introduced in section 2.4.4 and 2.4.5, only the heat conduction term will be introduced here to complete the formulation. More important in this section is the energy based modeling of phase changes, which differs from the description of similar publications.

For the discretization of the heat conduction term $-\nabla \cdot (k\nabla T)$ in the energy equation (2.16), the approach according to CLEARY (1998) from equation (3.23) is applied:

$$\left\langle \rho_i \frac{du_i}{dt} \right\rangle = \sum_j \frac{4m_j}{\rho_j} \frac{k_i k_j}{k_i + k_j} (T_j - T_i) \frac{\mathbf{r}_{ij} \cdot \nabla W_{ij}}{r_{ij}^2 + \eta^2} + I_i - r_i^{rec} - r_i^{rad} - r_i^{con}. \tag{3.62}$$

It shall be noted, that in this term, the kernel gradient is not corrected with equation (3.21). The reason for this is that the correction matrix must be recalculated for the correction, because the thermal calculation is applied at the new particle position $\mathbf{r}^{t+\Delta t}$, which means additional calculation effort. Furthermore, the symmetry of the energy balance $\mathbf{r}_{ij} \cdot \nabla W_{ij} = \mathbf{r}_{ji} \cdot \nabla W_{ji}$ is given more importance than the independence of the particle distribution, since only the former ensures energy conservation throughout many time steps (PRICE (2011)).

Phase change

While the most common approach to represent phase changes in the SPH community is the apparent heat approach based on the temperature T by HASHEMI & SLIEPCEVICH (1967) (see i.e. HU & EBERHARD (2017); RUSSELL ET AL. (2018)), in this work the internal energy was chosen to be the primary variable instead of the temperature. In FÜRSTENAU ET AL. (2020b) it was found that the use of the apparent heat approach in combination with the short heating cycle and explicit time stepping can lead to unphysical behavior. To calculate the temperature from the internal energy a mapping is performed. This way, the calculation of the temperature and the stored latent heat is more exact.

The melting of the solid material and its resolidification are the most important phenomena to be modeled when simulating the SLM process. In this work, the solid phase is not further modeled as pointed out before. Particles belonging to the solid phase are modeled as fluid particles with zero velocity and acceleration (just like zero velocity boundaries). When the melting temperature is reached, the particles receive accelerations and velocities from the balance equations. The mapping between internal energy and temperature is visualized in figure B.1 in appendix B. As one can see, at the melting and vaporization point, the temperature stays constant, while the energy is used to perform the phase change. When cooling down, the temperature stays constant again, while the phase change happens. The same mapping appears at vaporization temperature. Above vaporization temperature, the particles are deleted, as they are treated as totally vaporized. The mushy behavior of partly molten particles is not covered in this work. Particles start to move, when the latent heat is completely absorbed and the melting temperature is reached.

Chapter 4

Implementation Details

In this section, the schemes for the temporal integration of the particle variables are explained. Afterwards the time step criteria are given, which have to be satisfied for stable simulations.

4.1 Time stepping schemes

For the temporal integration a couple of schemes have established in the SPH community. While the majority of researchers is using a simple quadratic time stepping scheme for WCSPH, for problems of higher complexity like astrophysical applications researchers have focused on higher order Runge-Kutta procedures. This thesis introduces the Verlet time integration scheme for WCSPH, which is implemented in the used DualSPHysics framework (CRESPO ET AL. (2015)). For ISPH, the majority of researchers use the quadratic predictor-corrector technique introduced by CUMMINS & RUDMAN (1999). Instead, some researchers applied a linear time-stepping scheme (e.g., IHMSEN ET AL. (2014)), which was tested in the process of this work. Finally, the standard approach was chosen because of its superior robustness with little additional computational effort.

4.1.1 WCSPH

For weakly compressible simulations the Verlet time integration scheme according to CRESPO ET AL. (2015) is applied. In this scheme, the velocities, positions and densities of the new time step are calculated in the following manner

$$\mathbf{v}^{n+1} = \mathbf{v}^{n-1} + 2\Delta t \left(\frac{d\mathbf{v}}{dt}\right)^n, \tag{4.1}$$

$$\mathbf{r}^{n+1} = \mathbf{r}^n + \Delta t \mathbf{v}^n + \frac{1}{2}\Delta t^2 \left(\frac{d\mathbf{v}}{dt}\right)^n, \tag{4.2}$$

$$\rho^{n+1} = \rho^{n-1} + 2\Delta t \left(\frac{d\rho}{dt}\right)^n. \tag{4.3}$$

To prevent the integrated values from diverging, every N steps the variables are integrated in a linear way:

$$\mathbf{v}^{n+1} = \mathbf{v}^n + \Delta t \left(\frac{d\mathbf{v}}{dt}\right)^n, \tag{4.4}$$

$$\mathbf{r}^{n+1} = \mathbf{r}^n + \Delta t \mathbf{v}^n + \frac{1}{2}\Delta t^2 \left(\frac{d\mathbf{v}}{dt}\right)^n, \tag{4.5}$$

$$\rho^{n+1} = \rho^n + 2\Delta t \left(\frac{d\rho}{dt}\right)^n. \tag{4.6}$$

This corrective step is suggested to be performed every ≈ 50 steps, which was also applied here. The advantage of this method is a second order time integration scheme, except when the linear step is done, with only little more overhead than a linear time integration scheme.

4.1.2 ISPH

The standard ISPH approach is based on the splitting scheme according to CUMMINS & RUDMAN (1999). According to this method the pressure accelerations are separated from the rest of the accelerations resulting in a fractal time step. At first an intermediate configuration is calculated by integrating the old velocities in time

$$\mathbf{r}^* = \mathbf{r}^t + \mathbf{v}^t \Delta t. \tag{4.7}$$

In the intermediate configuration the intermediate velocity is calculated, based on all non-pressure accelerations (see equation (3.25)) according to the position $\mathbf{r}^*$ and velocity $\mathbf{v}^t$

$$\mathbf{v}^* = \mathbf{v}^t + (\frac{1}{\rho}\nabla \cdot (\mu \nabla \mathbf{v}^t) + \mathbf{a}^g + \mathbf{a}^S)\Delta t, \tag{4.8}$$

To get the full, divergence-free, time step the unknown pressure part has to be added onto the intermediate velocity

$$\mathbf{v}^{t+\Delta t} = \mathbf{v}^* - \frac{1}{\rho}\nabla p^{t+\Delta t}\Delta t. \tag{4.9}$$

To calculate the unknown pressures the PPE discussed in section 3.2.4 has to be solved based on the intermediate variables ($\mathbf{r}^*$, $\mathbf{v}^*$ and ρ^*). With the obtained pressures, $\mathbf{v}^{t+\Delta t}$ can be calculated. The new velocity is then used to advance the particle positions in time in a quadratic manner

$$\mathbf{r}^{t+\Delta t} = \mathbf{r}^t + \frac{\mathbf{v}^t + \mathbf{v}^{t+\Delta t}}{2}\Delta t. \tag{4.10}$$

By the use of this splitting scheme, the velocity is calculated explicitly and only the pressure is left as the primary variable in the system of equations. Thus, the number of unknowns in the system of equations can be reduced from four ($\mathbf{v}$ and p) to one. Through the utilization of the intermediate time step, a full pressure projection is performed, being independent of the pressures from the last time step. This method has been found to be beneficial in mesh-based methods, avoiding the accumulation of errors, according to RIDER (1995).

4.1.3 Energy equation

The evolution of the internal energy is calculated after the calculation of the new positions by integrating (3.62) with a simple Euler-forward time integration

$$u^{t+\Delta t} = u^t + \Delta t \left(\frac{du}{dt}\right)^t . \tag{4.11}$$

This leads to an integration of the old temperature and temperature dependent variables on the new configuration $\mathbf{r}^{t+\Delta t}$. Surely the explicit linear integration of the energies will lead to an error compared to the quadratic integration for position and density. However, since the time steps for the simulated cases are very small and the heat conduction was implemented in an energy conserving way (see section 3.2.5), the resulting errors are likely to be small. For both approaches, ISPH and WCSPH, the time integration of the other variables could have been adapted. However, this idea was not pursued to obtain an identical time integration for both approaches.

4.1.4 Time step limitations

For the calculation of the maximum time step size several criteria have to be satisfied, which differ between WCSPH and ISPH. For this reason first the mutual time step criteria are summarized, going into the differentiating details afterwards. When simulating surface tension and heat conduction, static time step criteria have to be introduced, depending on the material parameters. This way the first two time step criteria can be constructed:

$$\Delta t_\gamma = \sqrt{\frac{h^3 \rho}{2\pi\gamma}} \tag{4.12}$$

based on the surface tension (ADAMI ET AL. (2010)) and

$$\Delta t_k = \frac{h^2 \rho c}{2k} \tag{4.13}$$

based on the heat conductivity (CLEARY & MONAGHAN (1999)). The third common time step criterion is based on the maximum acceleration within the time step

$$\Delta t_a = \sqrt{\frac{h}{|\mathbf{a}_{max}|}}. \tag{4.14}$$

WCSPH

For the weakly compressible approach, the viscous and the Courant criterion are combined according to (MONAGHAN & KOS (1999)):

$$\Delta t_C = \frac{h}{c_0 + \max\left(\frac{h\mathbf{v}_{ij}\cdot\mathbf{r}_{ij}}{\mathbf{r}_{ij}^2+\eta^2}\right)}. \tag{4.15}$$

Herein it should be noted again, that the numerical speed of sound c_0 has to be chosen an order higher than the maximum velocity in the system. This condition reduces the maximum time step size in WCSPH for the most. The maximum time step is then calculated as:

$$\Delta t_{WCSPH} = \alpha \min(\Delta t_\gamma, \Delta t_k, \Delta t_a, \Delta t_C), \tag{4.16}$$

where α is the Courant number, which has to be chosen between 0 and 1. In SPH values between 0.1 and 0.3 are common. In this work, 0.25 is chosen if not stated differently. The check of the maximum time step is performed after the calculation of the total accelerations and before the time integration. This way no iterations are necessary.

ISPH

For ISPH, the viscous and the Courant criterion are split. Because of its semi-implicit nature, the speed of sound is not used. Instead, the Courant criterion is based on the maximum velocity in the system

$$\Delta t_v = \frac{h}{|\mathbf{v}_{max}|}. \tag{4.17}$$

This increases the critical time step by around one order. The viscous time step criterion is simply based on the viscosity (HIRSCHLER ET AL. (2017))

$$\Delta t_\nu = \frac{h^2}{2\nu}. \tag{4.18}$$

The maximum time step in ISPH is then calculated as:

$$\Delta t = \alpha \min(\Delta t_\gamma, \Delta t_k, \Delta t_a, \Delta t_v, \Delta t_\nu) \tag{4.19}$$

The check is performed at the beginning and the end of every time step, rewinding the whole time step, when one of the time step criteria is violated. The rewind is necessary, as the pressures and final velocities are depending on the intermediate positions (4.7), which have to be recalculated for a changed time step size.

4.1.5 Shifting

In ISPH, maintaining an isotropic particle spacing is of utmost importance. To achieve this, the use of the density-based source term from the equation (3.61) helps in the continuum but fails at the free surface. Here the density is greatly reduced by truncation of the kernel. If the density source term is activated at the surface, it leads to a contraction of the fluid and thus to pairing and hence to numerical instability. The use of the shifting method according to LIND ET AL. (2012) keeps the particles at the surface at a distance because it is not based on density and is not affected by kernel truncation. The basic ideas from XU ET AL. (2009) were applied to closed fluid systems like the Taylor-Green vortices, vortex spin-down or the lid-driven cavity flow tests. In their work Xu et al. found, that for the observed simulations, particles follow the streamlines and do change their spacing due to this occasion. They found that the use of the velocity based source term 3.53 in combination with their shifting algorithm is the most exact and the computationally cheapest method to solve closed fluid systems accurately. The main part of this shifting algorithm is the shifting vector

$$\delta \mathbf{r}_i = C|\mathbf{v}_{max}|\Delta t \mathbf{R}_i, \tag{4.20}$$

where C and $\mathbf{R}_i$ are the shifting constant (0.01-0.1) and the shifting direction. After the shift has been carried out, the conservation variables must be corrected to adapt them to the new particle distribution. This is done by calculating the gradient of each variable according to equation (3.15) and multiply it with the shfting vector. In this work this is done for the velocity, which is crucial for the stability:

$$\mathbf{v}_i' = \mathbf{v}_i^{t+\Delta t} + \delta \mathbf{r}_i \cdot \nabla \mathbf{v}_i^{t+\Delta t}. \tag{4.21}$$

The correction could also be carried out for the temperature, but was omitted for performance reasons. In LIND ET AL. (2012) on the one hand, a new shifting direction was introduced which is applied in this work as

$$\mathbf{R}_i = \sum_j V_j \left(1 + 0.2 \left(\frac{W_{ij}}{W(dx)} \right)^4 \right) \nabla W_{ij}, \tag{4.22}$$

where $W(dx)$ is the kernel value of the initial particle distance. On the other hand, the shifting algorithm was extended to free surface flows, since the original algorithm by XU ET AL. (2009) would lead to an expansion of the fluid due to the kernel truncation at the free surface. The correction of the shifting vector is carried out by a surface correction, similar to the calculation of the Marangoni convection in equation (3.45):

$$\delta \mathbf{r}_i = C|\mathbf{v}_{max}|\Delta t \left[\mathbf{R}_i - (\mathbf{R_i} \cdot \mathbf{n}_i)\mathbf{n}_i \right]. \tag{4.23}$$

Lind et al. also added a corrective term to allow for some shifting perpendicular to the surface to counteract contractions. This term is not shown here, since it was not found necessary in this thesis to maintain the volume of the fluid (due to the density source term in (4.25)). The algorithm is completed by applying the shifting constant as $C = 0.1h$ (like implemented in DualSPHysics V4). This way the shifting constant becomes independent of the problem and can stay at 0.1 throughout all simulated cases. MOKOS ET AL. (2017) applied the shifting algorithm to his WCSPH approach as well. Since the weakly compressible approach in this thesis is already slower than the incompressible one, the additional calculations were avoided here. Furthermore, the shifting algorithm is generally only used for the ISPH approach in the literature.

4.2 GPU programming details

When programming on GPU, the architecture differs from the well known CPU architecture. The CPU on the one hand is the general-purpose core of the computer, built to do all kind of jobs, which the operating system and the user demand it to do. On the other hand the GPU is a specialized device, built to process and display the images visible on the computers

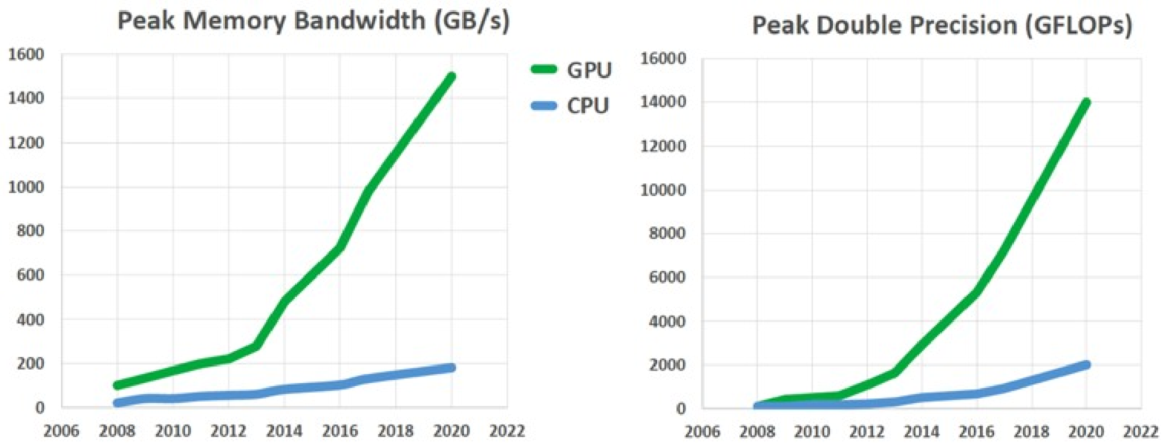

Figure 4.1. Graphic by NATOLI (2019) showing the maximum memory bandwidth and peak performance of the best-in-class GPU and CPU models of every year from 2008 to 2020. The values for 2020 were extrapolated from preliminary specifications. Courtesy of Dr. Vincent Natoli.

monitor. Driven by the gaming industry, GPUs have developed in a much faster way than CPUs in the last decade. While this development was not usable beside visualization, in 2007 NVIDIA published the first version of their Compute Unified Device Architecture (CUDA) Toolkit (NVIDIA CORPORATION (2020a)). With this programming language for GPUs, which is based on C++ and can also be combined with Fortran, the possibility was given to use GPUs as a General Purpose GPU (GPGPU) similar to a CPU. From this point on, the development of double precision performance became important, which until then was not relevant for GPUs. Since 2007, the double precision performance increased significantly compared to CPU double precision performance as seen in figure 4.1. A reason for this can be found in the recent introduction to the field of computations as much as in its specialized architecture which does not need to satisfy the general-purpose demands of a CPU.

The specialization of the GPU leads to some differences between programming on a GPU and classic CPU programming and its parallelization via OpenMP. The latter is comparable to programming on a single GPU, as it is done in this thesis. In this section, details are given about the particular type of GPU programming, taking into account the architecture and memory. The section concludes by explaining the generation and filling of the equation system for the PPE and its efficient implementation on GPU.

4.2.1 Programming basics

For programming on GPU, it is first necessary to know the differences between the architectures, which can be seen in figure 4.2. While a CPU has only a few cores (e.g. up to 28 in the Intel Xeon Platinum 8180), a GPU contains several thousand stream processors (e.g. up to 5120 in the NVIDIA Quadro GV100). A direct comparison between stream processor and CPU core is not possible, because stream processors can only perform smaller and more specialized tasks than CPU cores. But if such jobs need to be computed and both the CPU and GPU core can be utilized at 100 % load, one can estimate the amount of instructions to

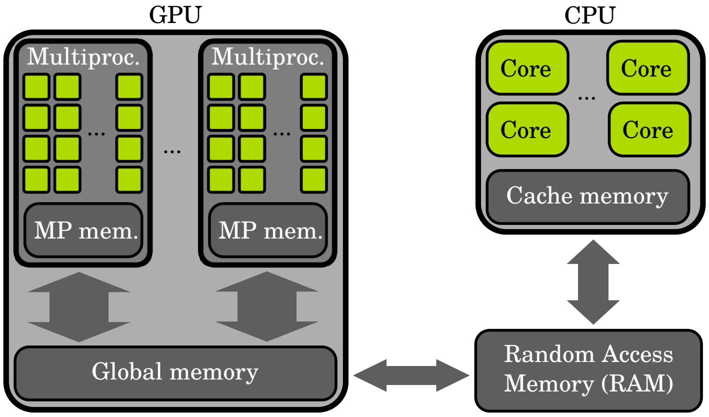

Figure 4.2. Principal representation of a GPU (left) and a CPU (right) with their belonging memory and memory interactions as arrows (scaled according to memory throughput). The green cores of the GPU are called stream processors, arranged in multiprocessors.

be computed. For the CPU mentioned above, there are 28 cores that operate at a maximum turbo clock speed of 3,800 megahertz. This means that a maximum of 106,400 million instructions can be processed within one second. For the GPU, 5,120 stream processors work with a maximum turbo clock frequency of 1,530 megahertz. This means that a theoretical maximum of 7,833,600 million instructions can be processed within one second, which corresponds to an almost 74 fold increase in performance. Certainly this example is very hypothetical because there are several other factors that influence performance, but it gives an idea of why calculations are translated/designed for GPUs.

What is also visible in figure 4.2 is that the stream processors are not working independently but are grouped in multiprocessors. In case of the mentioned top GPU the 5,120 stream processors are bundled in 80 multiprocessors, thus there are 64 stream processors available per multiprocessor. When a job (called kernel) is sent to the GPU a multiprocessor is addressed, which passes the sub-jobs (called threads) to the stream processors. These threads have to be identical, just varying the pointers to the working set of data. Thus, only applications with a highly repetitive character can be parallelized this way, like numerical simulations where the same process is repeated node by node or particle by particle. The name of the underlying procedure is called SIMT (Single Instruction Multiple Threads) and is opposing to the CPU parallelization.

To utilize the GPU and make use of SIMT, the threads are bundled to thread blocks which are again bundled to a grid (see figure 4.3). The optimal grid and block sizes can be computed automatically by the compiling software, depending on the complexity of the threads and the number of multiprocessors and stream processors. When the grid is sent to the GPU the blocks are assigned to a multiprocessor each. Within the multiprocessor, the thread blocks are split up into warps consisting of 32 threads. Each warp occupies 32 stream processors and is the minimum lot of threads to be handled. This means if a block with only 1 thread is sent, it takes as much time to compute as 32 threads, as the other 31 processors will idle in the processing time.

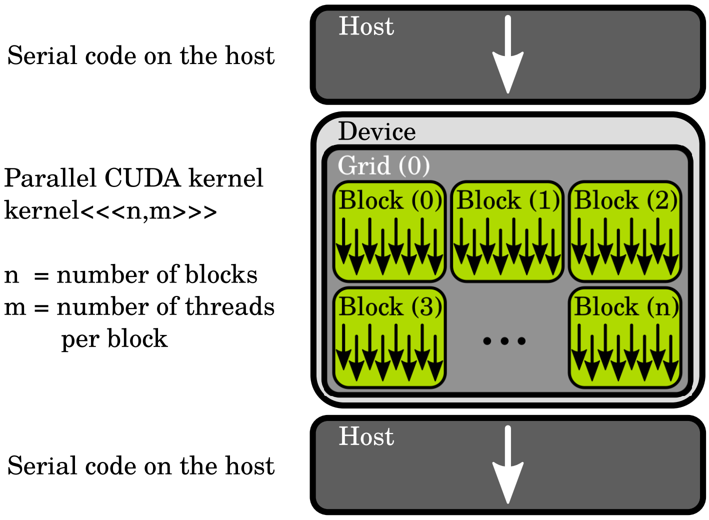

Figure 4.3. Use of GPU inside a CUDA code, with the serial part of the code being handled on CPU and the parallel part handled on the GPU. Arrows represent single threads.

At this point it must be made clear that not every program can be executed faster on GPU than on CPU. Besides the condition that there must be enough threads and thread blocks of low complexity to use the entire GPU, memory interactions are the biggest challenge for efficient programming. To understand this point, it must be mentioned that the GPU cannot execute code on its own. The host, i.e. CPU and RAM, must deliver the jobs and data to the GPU. For example, when data is read from a file, it resides in the RAM of the CPU. To make the data available to the GPU threads, the data must be copied to the GPU RAM. After the data has been calculated, the results usually have to be copied back into the CPU RAM to make them readable or plotable. This means that the memory interactions for input and output are expensive. Comparing the theoretical memory throughput, the top GPUs with HBM2 RAM have a maximum throughput of 870 GB/s, which is high compared to today's top DDR4 RAM with peak performance of 25.6 GB/s. However, when data needs to be transferred to the GPU, it must pass through the PCIE3 port, which provides a maximum throughput of 15.8 GB/s. This results in much longer processing times when there is a high level of data exchange between host and device (CUDA internal term for GPU). Then the memory interaction time can exceed the computing time, making GPU computing slower than CPU computing. For this reason, memory interactions between CPU and GPU must be minimized and if possible performed asynchronously.

When a warp is processed within one multiprocessor, the necessary data is called from the GPU RAM (called global memory). This is not performed variable by variable but in a grouped way. The first thread calls for a specific number within a data array and all following threads are delivered with the succeeding data. This means when thread 0 demands the density of particle 0, the following tasks automatically receive the densities of particles 1, 2 ... 31. This way the memory interactions are accelerated but it demands the threads to use the data in an organized way. Calling the memory in an unorganized way on GPUs will lead to a performance decrease by a factor of 32 while on the CPU the performance loss will be insignificant. For this reason, in a GPU code, everything should be numbered and handled in a linear way, resulting in a minimum amount of memory calls. That is why the developers of DualSPHysics store the particles in a Verlet list, sorted according to their spatial position. The calls within the GPU routines are then organized by their thread number to associate the particles. This means that for every particle, a thread is doing all the interactions with its neighboring particles which is the same basic task for every thread.

When a grid of threads is sent to the GPU the load balancing is performed automatically. In the first place it means that the blocks are dynamically queued between the multiprocessors, to reduce the total computation time. While each multiprocessor is only able to work actively on a single block, the GPU can assign multiple blocks to a single multiprocessor at once to work on. This procedure is called latency hiding and gives a speedup in the following manner. When a task is executed, the process can be described in cycles. A cycle is a single command to be executed on a multiprocessor. For example an addition or a multiplication are one cycle while a division or a square root equals 6 cycles for single precision floating point variables. When a new block is started, the multiprocessor requests all the needed data for the first warp from the global memory in the first place. This is done as the global memory has a comparatively large latency of 200-400 cycles (NVIDIA CORPORATION (2020b)). Since there is no work to do in the current warp, the processor performs a context switch and starts the next warp, requesting the belonging memory. This way, the processor only has an idle time during the first memory call and can then work continuously. This way several warps and even blocks can be started at the same time. The only bound for the amount of concurrent warps/blocks is the needed amount of internal memory on the multiprocessor. When more variables are needed per warp, the processor can cache less warps, which probably leads again to waiting times. To do all the multi tasking, the GPU needs to know the exact amount of memory per thread, which is calculated on compilation level and can also be outputted by the NVIDIA compiler/profiler. To do so in a reliable way, the compiler has to follow each if-else statement and tests each outcome, which turns the compilation process of GPU code more lengthy compared to the CPU compilation process.

The if-else statements are not only of importance during the compilation process. The entire efficiency of the stream processors is based on the assumption, that the processors are doing exactly the same task with different data portions. An if-else statement can disturb this coalescence. During computation the multiprocessor checks if all the streams have the same outcome. If this is not the case or the code is too complex to evaluate the result in the very beginning of the kernel, all possible outcomes are calculated for each thread. If the results differ in their complexity, i.e. outcome A has some hundred lines of code while outcome B is just one line, this type of double calculation has a high additional effort. In this case it can be useful to sort the streams according to the condition and to execute two separate kernels. Surely, this treatment is not feasible to be done for several conditions simultaneously, as the overhead for the recurring sorting would be high. More details on performance optimizations can be found in the 'Programming' and 'Best Practice' guides in NVIDIA CORPORATION (2020b).

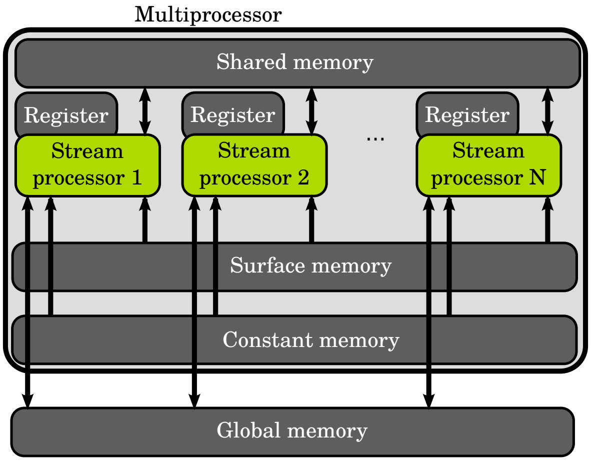

Figure 4.4. Principal representation of a multiprocessor inside a GPU with its belonging memories and possible memory interactions.

4.2.2 Memory usage

As mentioned earlier there are several types of memory on the GPU. In comparison, on the host there is only the RAM which is explicitly used by the programmer. When the data is transferred to the CPU, it is stored in the cache on at least two levels. Anyways, this storage usually is not directly addressed by the programmer but assigned by the CPU in run time. On the GPU the data to be handled is mostly stored in the global memory, which is equal to the hosts RAM. But there are several aspects about the global memory which have to be cared about and special cases in which the global memory performs badly. For this reason specialized memory types have been developed to be used instead of the global memory in certain cases. In this section first the global memory and the registers are discussed followed by the specialized constant memory, the texture memory and the shared memory. A schematic view of the memories within the GPU is provided in figure 4.4.

Global memory

Like stated earlier, the global memory is the main and largest memory available on the GPU. It is available on the device level, which means, that it can be accessed by all multiprocessors and is the exchange memory for the communication with the host. The global memory is also the largest memory on the GPU with a current maximum of 32 GB in the NVIDIA Quadro GV100. It was also mentioned that the memory has a rather high latency, when servicing read or write requests. When called, the multiprocessors receive the memory block-wise for their threads, where the variables are called in 32, 64 or 128 bit blocks. For this reason variables in the GPU code should be sized accordingly. This means that floats (single precision variables) with a size of 8 bits are grouped as Float4 to reach 32 bits while doubles (double precision variables) with a size of 16 bits are grouped as 2 to fill 32 bits. When saving a boolean (8 bits in C++) or a single precision symmetric matrix with 6 entries (48 bits) or a full single precision matrix with 9 entries (72 bits) are called in the memory, the rest of their belonging 32, 64 or 128 bit blocks remains empty. For this reason in the code there exist constructions like $(\mathbf{v}, \rho)$ or $(\hat{\mathbf{n}}, |\mathbf{n}|)$ to make use of the block sizes and to simplify the code by e.g. saving the magnitude of a vector separately. To avoid the losses due to 1 bit booleans, they can be used as a template at function call if the argument is the same for a grid. This way the argument is evaluated outside the multiprocessor and does not have to be loaded into the registers.

Registers

When the data is called from the global memory it is forwarded to the registers which are the fastest memory available on multiprocessor level. On this level the latency is lower by 2 orders of magnitude and the transfer speed is higher by one order of magnitude. In the registers all the variables used are automatically stored and can be manipulated quickly. However, the variables are not automatically updated globally but have to be written explicitly to the global memory to reduce memory traffic. The number of free registers also limits the number of warps and blocks to be processed simultaneously. Since CUDA Compute Capability 3.0 (around 2012), the maximum number of registers per multiprocessor is fixed to 65,536 resulting in a maximum of 262,144 single precision variables per multiprocessor. Still the maximum number of registers per block is limited to 255 resulting in 1020 single precision variables. If this number is exceeded, the variables are called from the 'local memory', which is basically a mapping to the global memory. Through this redirection the speed of the whole process is depending on the high latency of the global memory again. For good parallelization only some hundreds of variables should be called per thread.

Constant memory

The global memory and the registers are made for single calls. When multiple threads try to access the same register at the same time, they are queued. For a warp this means up to 31 cycles of waiting. Because in every code, there are constants to be used, the constant memory is utilized. Constant memory consists of structures with fixed sizes at compilation time, which values can be set at run time. When all the threads of a warp are trying to access a variable of the constant memory, they are all served in the same cycle. This kind of memory is used in DualSPHysics for several material constants. The maximum size of constant memory is also 65,536 Bytes which is equal to 16,384 single precision floating point variables.

Texture memory

It was discovered that when handling multiple materials the use of constant memory is not applicable, as the amount of materials and thus constants is not known at compilation time. For this reason the texture memory was implemented into the framework. In the texture memory variables can be placed in a 1-, 2- or 3-dimensional vector. For multiple materials vectors with the length of the number of materials were generated, which are then called to get the material properties. In the later work, several variables were meant to be temperature dependent. In these cases a two dimensional texture was build with the material defining one axis and the temperature defining the other axis. The same procedure is done when mapping the temperature from the internal energy. For the mapping the textures are able to interpolate the values between two points linearly. As there is no interpolation wanted between the materials, the resulting mapping is performed only on the temperature level being denoted by a floating point variable while the fluid coordinate always takes discrete integer numbers, this is then called a 1D-layered texture. This way 2,048 different 1D-mappings can be saved with 16,384 interpolation points each. Optimal performance can be reached here when all mappings of one warp are close to each other. In the texture memory no issues occur from multiple accesses on the same element.

Shared memory

The shared memory is not directly implemented in this work but it is part of every linear equation system solver (like the used PARALUTION library by LUKARSKI & TROST (2014)) and mentioned here for completeness. Shared memory is available on multiprocessor level and can be shared between threads and blocks. While constant and texture memory are read-only memory, the shared memory is also writable. For this reason it is used for matrix computations like in linear equation system solvers and pre-conditioners. The read and write accesses on shared memory can be performed within one cycle but multiple accesses cause waiting times to avoid two processes writing the same variable at once. The maximum amount of shared memory per multiprocessor is between 48 and 112 kilo Bytes (equals 12,288 to 28,672 single precision floating point variables).

4.2.3 Matrix assembly

The simulation of incompressible SPH on the GPU is a rare topic as the number of solvers implemented on GPU is low. Recently CHOW ET AL. (2018) published details about their implementation of ISPH into DualSPHysics. In their work they use pre-conditioners and solvers from the ViennaCL library by RUPP ET AL. (2016). For their simulations they used either a Jacobi or an Algebraic Multi-Grid (AMG) pre-conditioner together with a Bi-Conjugate Gradient Stabilized (BiCGStab) solver. In this work, the solution of the system of equations is performed by the PARALUTION library by LUKARSKI & TROST (2014), which offers a variety of parallel solvers and pre-conditioners, mostly programmed for CPU and GPU. For the simulations performed in this thesis, various linear equation system solvers of the PARALUTION library were tested. The most important limitation in the search for a suitable solver was, that non-symmetric systems of equations have to be solved. These asymmetric systems of equations occur due to the correction of the gradients, which is indispensable for the stability of the system of equations. The most common solutions for asymmetric systems of equations are the BiCGStab and the Generalized Minimal Residual Method (GMRES) algorithms (see e.g. SAAD (2003)), both of which are available in the library and have been tested. Finally, the combination of the Induced Dimension Reduction (IDR) solver of SONNEVELD & VAN GIJZEN (2009) with the simple Jacobi pre-conditioner (see e.g. SAAD (2003)) was used, since this combination converged in all simulations and showed the lowest computational time.

For an efficient solution of the system of equations, the resulting matrix is stored in the Compressed Sparse Row (CSR) format. While a fully filled matrix has $n \times n$ entries the

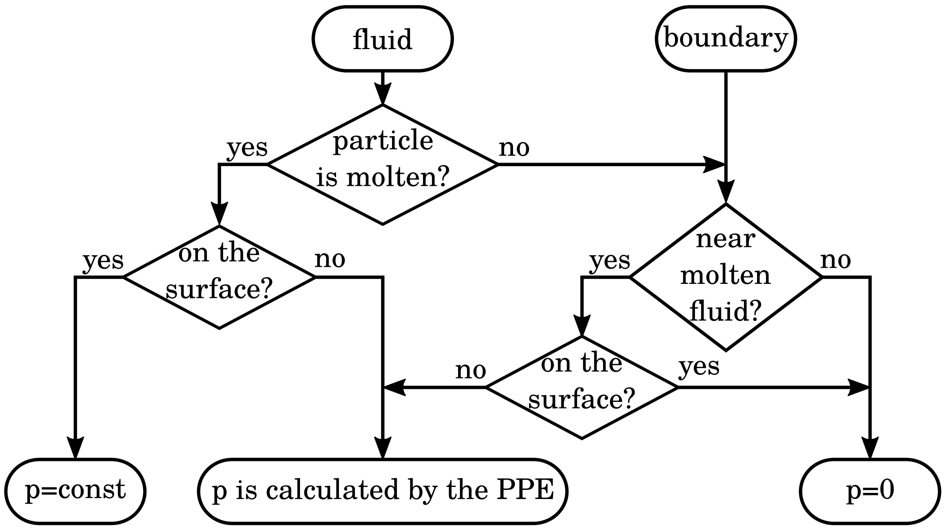

Figure 4.5. Flow diagram of the distinction if a particles pressure is calculated by the PPE.

CSR format only fills non-zero entries, where n is the total number of degrees of freedom. For a typical situation in a SLM simulation there were 17,034 degrees of freedom, occupying a total of 3,323,596 entries in the CSR matrix. With a full matrix description there would have been 290,157,156 entries, e.g. the infill was 1.1 $\%$. Through an overhead to address the variables the memory consumption of the CSR in this case was 2.2 $\%$ of the full matrix format.

The biggest drawback of the ISPH equation system is that it has to be set up every time step anew, as the neighboring particles are constantly changing. On CPU, vectors can be used in C++, which can have a variable length. With this method the matrix can be set up easily, although not very efficiently. On GPU, vectors with variable length are not an option, as the GPU needs to know exactly the size of each vector being constructed. To generate a vector of known size at first, a matrix calibration step is performed. For the calibration the information has to be known, for which particles the pressure has to be computed. The decision process is done while calculating the non-pressure accelerations and can be found in figure 4.5.

When the decisions are made, every particle either has its pressure pre-calculated (p^0) or is set to have its pressure calculated from the PPE. In the matrix calibration for every particle with non-fixed pressure the number of neighboring particles belonging to the system of equations is stored. For the CSR format the number of entries per row is summed up successively along the vector to address the entries of the matrix. The final amount of entries is then used to allocate the needed memory for the matrix. In the matrix assembly the system of equations ($\mathbf{A} \cdot \mathbf{p} = \mathbf{b}$) is computed. The left hand side is filled in by the use of the address vector from the matrix calibration based on equation (3.51):

$$A_{ii} = \sum_j A_{ij} \qquad \text{with} \qquad A_{ij} = \frac{4m_j}{\rho_i \rho_j} \frac{1}{\rho_i + \rho_j} \frac{\mathbf{r}_{ij} \cdot \nabla W_{ij}}{\mathbf{r}_{ij}^2 + \eta^2}, \tag{4.24}$$

where A_{ij} is the matrix entry of row i and column j. The source term is calculated using

(3.61) including the fixed pressures at the free surface from (3.56):

$$b_i = \alpha_{\mathbf{v}} \frac{\nabla \cdot \mathbf{v}_i^*}{\Delta t} + \alpha_\rho \frac{\rho_0 - \rho_i^*}{\rho_0 \Delta t^2} - \sum_j A_{ij} p_j^0. \tag{4.25}$$

With the assembled system of equations in CSR format and the source term vector the system can be solved with every standardized linear equation system solver capable of solving asymmetric matrices.

4.3 Post-processing

A big drawback of particle-based methods is the output of the data especially when comparing the data with mesh-based methods. The standard output of the SPH simulations is a point cloud like shown in figure 4.6. In two dimensions, this representation is sophisticating but in three dimensions the points offer no indicator for depth and thus give a representation that is hard to understand. The simplest solution to add a 3D-effect is to apply the glyph filter of Paraview (AYACHIT (2020)) onto the points. This way every point is surrounded by a sphere resulting in a picture that is easier to understand (see figure 4.6 [right]). Unfortunately, the glyph filter is very expensive in terms of computational effort, resulting in a couple of tenthousand particles to be represented with the glyph filter depending on CPU-performance and RAM of the displaying system. Also, the contour plots or streamlines frequently used in CFD cannot be generated on the basis of the point cloud data, because the connectivity between the particles is missing to generate a continuous representation.

For this reason a post-processing tool was developed, based on the post-processing tools inside the DualSPHysics framework, to generate a continuous grid. The desired values from the particles are projected onto the grid using the usual SPH method (3.5). Depending on the amount of data produced and the desired resolution, the grid resolution should be set between 1-2 particle distances. The resulting grid can then be used to generate contour plots, stream lines or slices to analyze the flow like shown in figure 4.7.

In the current implementation, there is the drawback that the mesh is not adaptive in any way. The amount of data (which can become several gigabytes per output) and the runtimes of the post-processing could be reduced greatly if the mesh was only generated in areas with particles present. Also an adaptivity of the grid spacing could increase the quality of the results greatly.

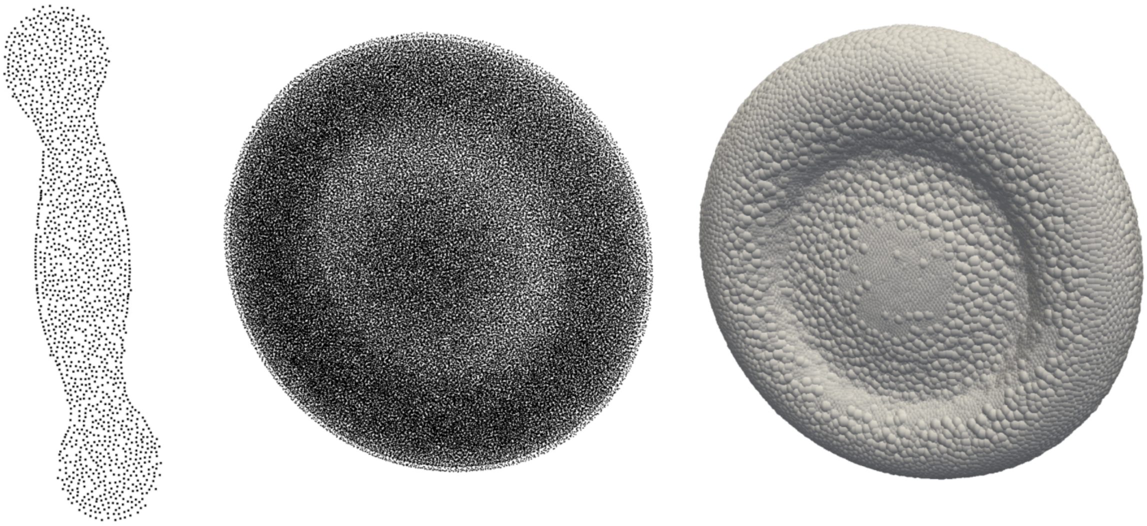

Figure 4.6. Representation of an SPH code output as a 2-dimensional [left] and 3-dimensional [middle] point cloud without coloring. The point clouds give no information about the depth and surface of the represented body. To generate a depth effect and a continuous surface, the particles can be used as the center of spheres for the post-processing [right], called Glyphs in Paraview (AYACHIT (2020)).

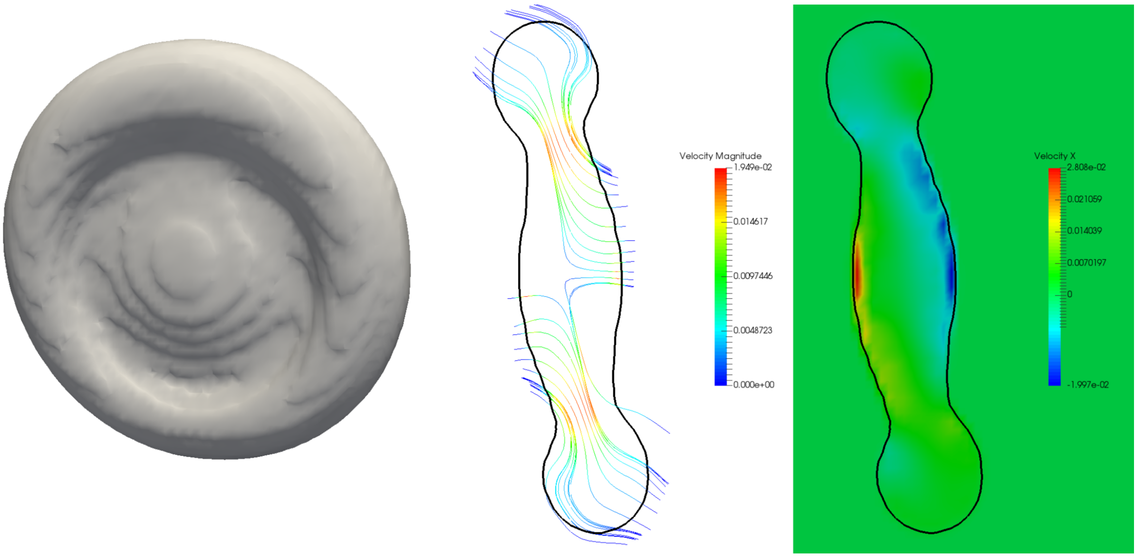

Figure 4.7. Possible representations of the particle data being projected on a continuous background grid: Contour plot to show the fluid surface in 3D [left]; streamline plot with contour in 2D [middle]; velocity colored slice plot with contour in 2D [right].

Chapter 5

CFD Validation

Two test cases are simulated to validate the flow properties shown. First, the test case of the lid-driven cavity flow is simulated to verify both the functionality of the incompressible approach and the viscous behaviour. Secondly, bubble collisions are calculated using the WCSPH and ISPH approaches to confirm the free surface tension modeling and to show the difference between the two approaches. Further tests on surface tension in combination with the ISPH approach are described in FÜRSTENAU ET AL. (2020a). For validation of the entire SLM process, a comparison with experimental results is given in 6.4.

5.1 Lid-driven cavity flow

The first validation test case is the well studied lid-driven cavity flow. This test case is a common validation for mesh-based methods, which can also be represented with SPH. In the test, both the viscous behavior and the modeling of the incompressibility are validated. For this reason it is a common test case simulated with ISPH. Due to its compressible nature, the WCSPH approach has difficulties to represent the test case in a stable way. While LEE ET AL. (2008) succeeded in simulating the lid-diven cavity with WCSPH, the WCSPH approach presented in this paper was not able to capture the resulting flow. It appears that more advanced correction techniques are necessary to achieve the results presented in LEE ET AL. (2008). However, Lee et al. have shown that the results of the WCSPH approach drastically underestimate the resulting flow rates compared to the ISPH approach. The reason for this is explained by pressure fluctuations in the particles, which result from the combination of the explicit, compressible approach of WCSPH combined with the closed system of the test case.

The lid-driven cavity flow test case consists of a two-dimensional box with three solid walls that apply a no-slip boundary condition to the fluid. The flow inside the cavity is driven at a certain velocity by the fourth wall, which is located on the top of the box (see figure 5.1). For comparison, the results of GHIA ET AL. (1982) are usually referenced.

The simulations can be carried out for several Reynolds numbers, which is recalled here for completeness:

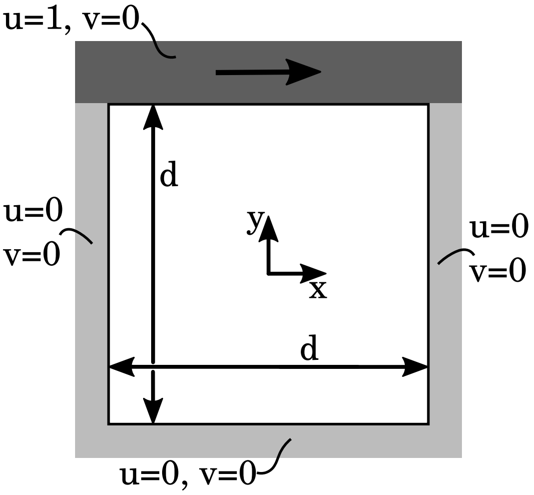

$\rho\ [kg/m^3]$	1000
$d\ [m]$	1
$\eta\ [Pas]$	0.01
$\lvert\mathbf{v}\rvert_{Re100}\ [m/s]$	0.001
$\lvert\mathbf{v}\rvert_{Re400}\ [m/s]$	0.004

Figure 5.1. Lid-driven cavity flow test case geometry [left]. Used set of parameters for lid-driven cavity flow test case [right].

$$Re = \frac{\rho|\mathbf{v}|d}{\eta}, \tag{5.1}$$

where d is the characteristic length. With higher Reynolds numbers the flow becomes more and more complex and demanding, especially in terms of spatial description. For particle-based methods, the exact simulation of this test case is more difficult to achieve with higher Reynolds numbers compared to mesh-based methods. This is due to the Lagrangian nature of particle-based methods. For this test case there is for example the 'geometric boundary condition' or 'mirror particle approach', which allows a more smooth and exact wall description (see e.g. VIOLEAU (2012)). This boundary condition, however, increases the computational effort considerably for irregular and changing boundaries, as is the case with the SLM simulations conducted. For this reason, the particle-based boundary condition from section 3.2.4 was used, which reproduces this type of boundary without additional effort. The aforementioned approach by BAND ET AL. (2018) can possibly overcome both downsides, as it is an analytical description, based on a particle representation. Also the movement of the particles in the closed system without voids is a problem for the incompressible approach. In FÜRSTENAU ET AL. (2017), for example, it was found that the double summation approach (3.24) was too incompressible for the PPE and did not allow any motion within the cavity at all. Therefore, a certain degree of compressibility has to be allowed for the particles to move according to their Lagrangian nature. The approach used for the PPE (3.23) allows this movement apparently, and therefore some compressions. With an Eulerian approach, with static cells, this problem is non-existent.

For the simulation of the lid-driven cavity flow, some changes had to be applied to the framework, as this test case is the only simulated case without a free surface. When there is no free surface in a simulation, the PPE has no Dirichlet boundary condition, which turns the system of equations to become unstable because of linear dependency. To overcome this problem, CUMMINS & RUDMAN (1999) correct the source term (4.25) by reducing it by the average of all source terms:

$$b_i' = b_i - \frac{1}{n_{eq}} \sum_j^{n_{eq}} b_j. \tag{5.2}$$

As the solid boundaries are not a key part of the proposed framework, a simple model was applied, treating the boundary particles similar to fluid particles by calculating their Part of the PPE by equation (3.52). Due to the linear dependence, the system of equations for this test case was still unstable and prone to simulation failures. To catch these instabilities the system of equations was altered by calculating the diagonal entry for fluid particles as

$$A_{ii}^{fluid} = 2\sum_j A_{ij}. \tag{5.3}$$

This procedure was adapted from BØCKMANN ET AL. (2012) who used the approach to stabilize free surface flows with ISPH. By increasing the diagonal components the system of equations becomes diagonally dominant, reducing its complexity. With these adaptations, the lid-driven cavity test case was run with the Reynolds numbers 100 and 400. With a box size of 1 m, a density of 1000 kg/m^3 and a dynamic viscosity η of 0.01 Pas the resulting lid speed is 0.001 m/s for Re 100 and 0.004 m/s for Re 400 respectively. The complete set of parameters for the test case is shown in figure 5.1 [right].

The comparison is oftentimes carried out over the horizontal and vertical velocities plotted over the x- and y-axis through the center of the cavity. First of all a plot of the stream lines is produced to show the correct distribution of velocity (see Fig. 5.3). These results can be seen in figures 5.2 and 5.4. The simulations were carried out with 50 x 50 and 250 x 250 particles. As a comparison, the simulations by Ghia et al. were performed with an equidistant mesh of 129 x 129 fluid cells. From the graphs it can be seen that the velocity distribution in the cavity agrees quite well with the mesh-based results. Only the minima and maxima are not quite reached, which is due to the indirect application of the boundary conditions and possibly also a slight overestimation of the viscosity as a result of discretization errors from the moving particles.

For the sake of completeness, Figure 5.3 and 5.5 show the streamline plots of Ghia et al. and from the low-resolution simulation, as well as the particle distribution. What becomes visible is that the secondary vortices in the lower corners are not visible in the performed simulations. Whether this is an error from the calculation or from the post-processing presented in section 4.3 is not clear. However, what is shown in figure 5.5 [right] shows an uneven resolution in the upper right corner of the cavity. This is caused by the fact that in the corner the largest pressure in the system is created by the movable wall, which destabilizes the system. This detachment near the wall becomes even stronger for a Reynolds number of 1000 and finally leads to a simulation failure. This problem can probably be remedied with a better boundary representation. However, since the lid-driven cavity (no free surface, solid walls) is very different from the objective of this thesis and all simulated SLM setups are in the range below $Re = 400$, this validation shall be regarded as fulfilled for the further simulations.

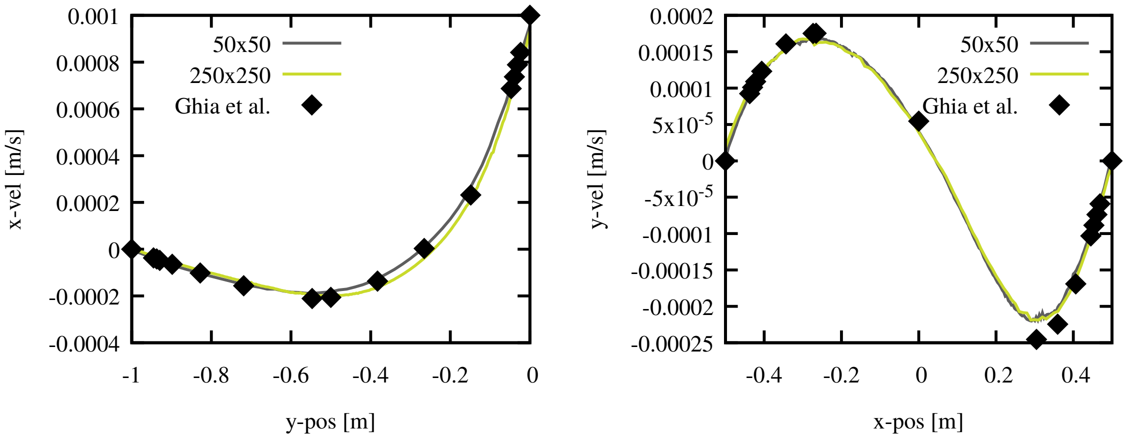

Figure 5.2. Velocity plots of the $Re = 100$ test. Left: horizontal velocity plotted over vertical position; right: vertical velocity plotted over horziontal position. Two resolutions are compared to the results of GHIA ET AL. (1982).

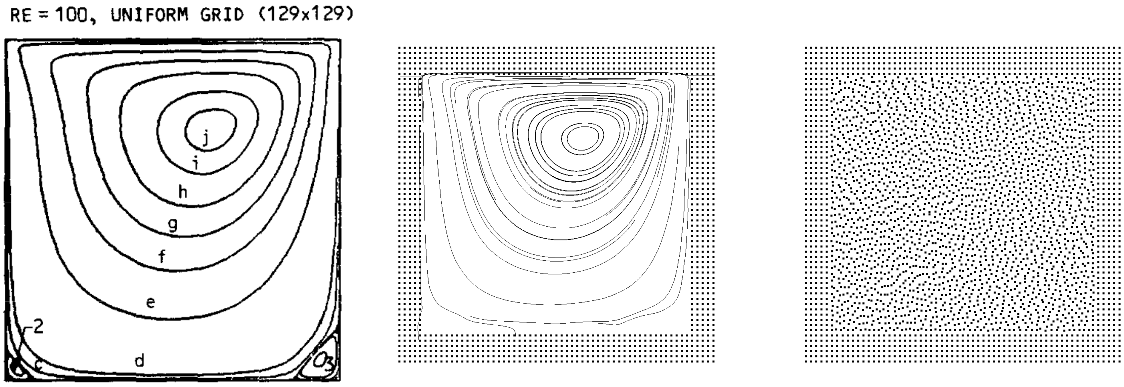

Figure 5.3. Results of the $Re = 100$ test. Left: representation of the streamlines in GHIA ET AL. (1982); middle: streamline results and particle distribution with the lowest resolution of 50 x 50 particles.

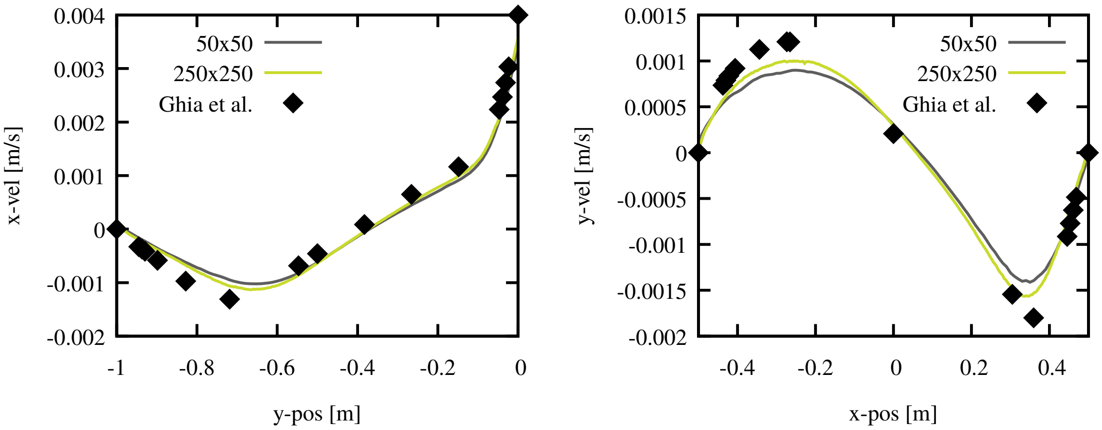

Figure 5.4. Velocity plots of the $Re = 400$ test. Left: horizontal velocity plotted over vertical position; right: vertical velocity plotted over horziontal position. Two resolutions are compared to the results of GHIA ET AL. (1982).

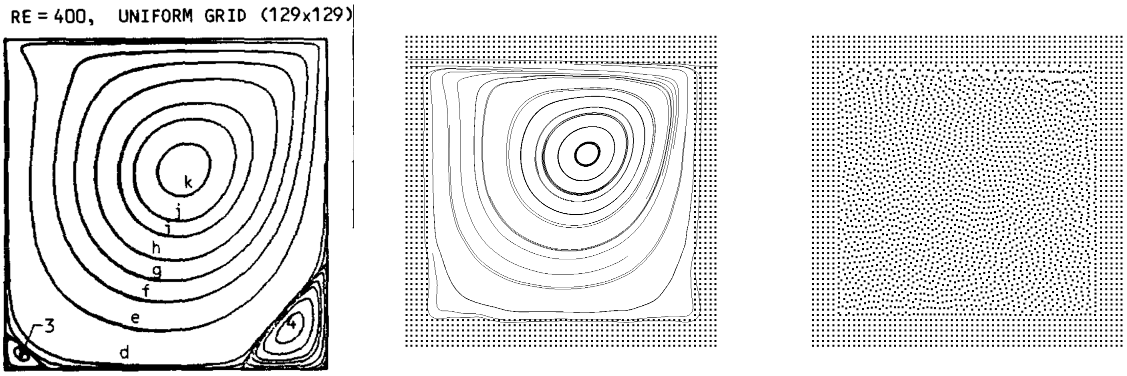

Figure 5.5. Results of the $Re = 400$ test. Left: representation of the streamlines in GHIA ET AL. (1982); middle: streamline results and particle distribution with the lowest resolution of 50 x 50 particles.

5.2 Bubble collision

After the validation of the general flow behavior of the framework with the lid-driven cavity flow test, the focus is now on the validation of the surface tension on free surfaces. For this simulation the experimental results of QIAN & LAW (1997) were used. In this section the validation is based on the experimental results, but this chapter also describes the point where the results of the ISPH and WCSPH approaches differ. Before starting to describe the experimental setup, it should be mentioned that the bubble collision domain contains complex physics. Although two bubbles of the same fluid collide, they behave very differently depending on the kinetic energy they carry and their surface-to-volume ratio. This relationship can be attributed to the ratio of inertia to surface tension. This ratio can be described by the Weber number:

$$We = \frac{\rho |\mathbf{v}|^2 d}{\gamma}, \tag{5.4}$$

The second variable needed to describe the bubble collision is the distance between the bubble centers b. For the sake of generality, this parameter is often referred to as the impact parameter B, by dividing it through the bubble radius:

$$B = b/r \tag{5.5}$$

Thus, when two bubbles collide, there are a total of five states that depend on the parameters We and B. These can be plotted in a diagram which can be seen in figure 5.6:

- In state I, the kinetic energy of the bubbles is so low that the bubbles unite immediately upon impact.
- In state II, the kinetic energy is higher and the bubbles bounce off each other as if they were made of immiscible fluids.
- In state III, the bubbles in turn have such a high kinetic energy that they no longer bounce against each other, but overcome the surface tension and unite. The viscous friction inside the united bubble reduces the kinetic energy until the united bubble is in equilibrium. In this area oscillations of the bubble take place, whose number depends on the Weber number.
- In states IV and V the bubbles unite and oscillate as in state III. However, the kinetic energy is so high that during oscillations the inertia overcomes the surface tension and the two bubbles separate again. In state IV, this is referred to as centric separation and in state V as eccentric separation.

It has been shown that in the transition areas between the described states, the behavior depends very much on the distinction by the kinetic energy. This can be captured and modeled analytically, what was done for example in HIRSCHLER ET AL. (2017) with a SPH approach or in PAN & SUGA (2005) with an ALE approach. However, since this distinction is a calibration requirement and not the declared goal of this work, situations were selected in which the behavior is unambiguously. These are the points B, F and P from QIAN & LAW (1997) which are also marked in Fig. 5.6:

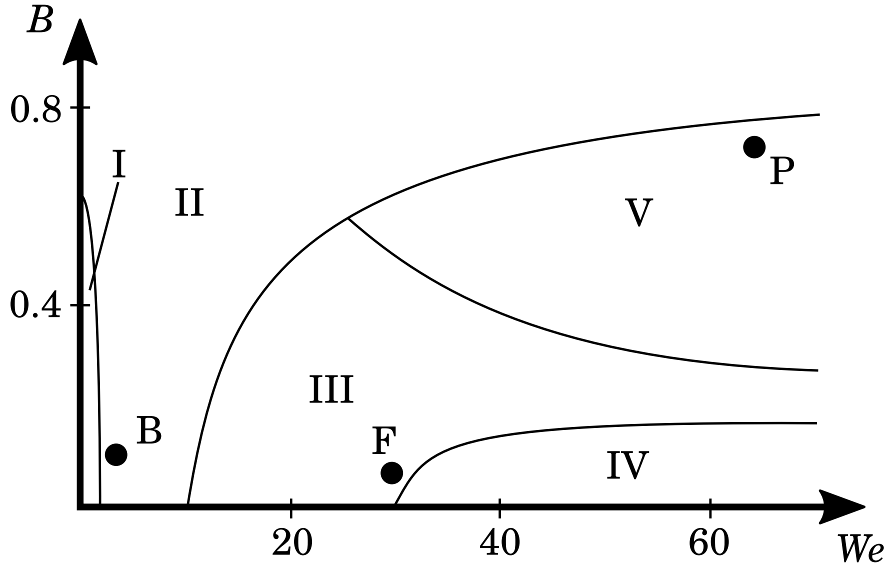

Figure 5.6. Bubble collision state diagram depending on We and B acoording to QIAN & LAW (1997) with simulated examples marked.

- In test case B a clear bouncing of the bubbles is occurring.
- In test case F the bubbles coalesce but due to the closeness to state IV, the bubble oscillates showing the interplay between viscosity and surface tension.
- In test case P, the kinetic energy is very high and the bubbles collide quiet eccentrically such that the common bubble is torn apart and splits up into several small ones.

The complexity of the motion increases from test case B over F to P. Thus, the importance of the stability of the free surface tension in combination with internal pressure and viscosity rises from case to case. Reason for this are the more violent motions on the surface which are demanding a stable calculation of the surface tension and the conservation of momentum.
The general setup of the test cases is outlined in figure 5.7 [left]. From the experiments of QIAN & LAW (1997) the measured Weber and Reynolds numbers were directly used as much as the bubble radii r and the collision parameter B. Additionally to the given parameters, the approximate density and viscosity of water were applied. This is in contrast to the work of Qian & Law who used bubbles of tetradecane in 1 atm nitrogen. Since the parameters of the liquid were not given in the work, the well studied parameters of water were used. Impact velocity and surface tension were then adjusted by calculation from the Weber and Reynolds number. The parameters can be found in figure 5.7 [right]. The comparison is done visually. The simulations were carried out with the WCSPH and ISPH algorithm. It shall be noted, that the characteristic length d in this setup is the bubble diameter and the characteristic speed $|\mathbf{v}|$ is the collision speed and thus twice as high as the calculated value.

Test case B

Test case B has a low Weber number of 0.5, which indicates a comparatively high influence of surface tension compared to inertia. Since the bubbles bounce off each other immediately

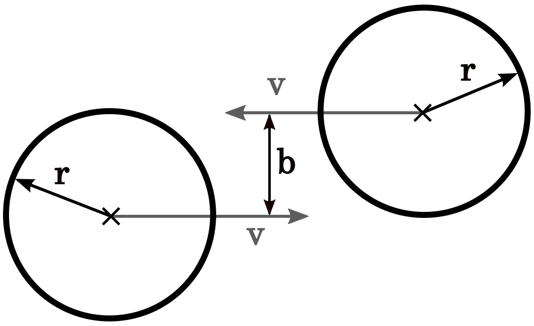

Qian & Law test case No.	B	F	P
We	0.5	32.8	64.9
Re	23.6	210.8	312.8
B	0.1	0.08	0.71
r $[\mu m]$	131	159	177
ρ $[kg/m^3]$	1000	1000	1000
η $[Pas]$	0.001	0.001	0.001
$\lvert\mathbf{v}\rvert$ $[m/s]$	0.045	0.331	0.442
γ $[mN/m]$	4.252	4.260	4.259

Figure 5.7. Left: Bubble collision test case geometry; right: bubble collision test case parameters for water-like bubbles (density, viscosity) in vacuum (bold parameters are taken directly from QIAN & LAW (1997).)

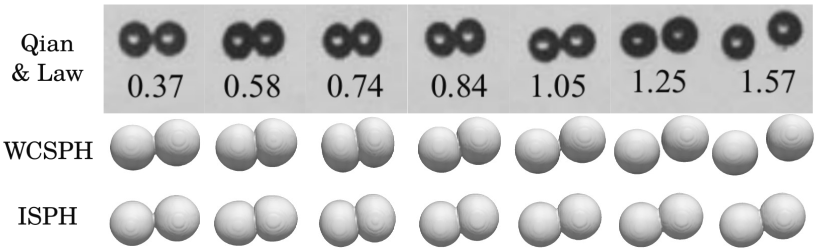

Figure 5.8. Bubble collision results of test case B simulated with the WCSPH and ISPH approach compared to the experimental results of QIAN & LAW (1997). The numbers below the experimental results represent the time in ms.

and no obvious cohesion effect between the bubbles is visible, both bubbles can be treated as different liquids during the simulation. The results of the simulations can be observed in Fig. 5.8.

The snapshots of the simulations show a good agreement of both simulative approaches compared to the experimental results. The visible effect of the common surface, which looks like adhesion, is merely a result of post-processing, since the algorithm described in section 4.3 does not distinguish between different fluids. Only between the incompressible approach and the experimental results there are obvious differences starting at about 1.05 ms. Here it can be seen that the bubbles do not separate from each other, as in reality and in simulation with the weakly compressible approach. This is due to the fact the two bubbles are considered as two different liquids for the surface tension but not for the calculation of the pressures with the PPE. The introduction of a second liquid for the surface tension can be easily modeled by using the original color function from equation (3.32). However, for the PPE, a common system of equations is generated for all particles when the two bubbles touch. This system of equations generates large negative pressures when the two bubbles separate because the incompressibility condition does not allow the particles to move apart. A similar effect would be expected for the weakly compressible approach, which however is not able to represent larger negative pressures via its equation of state. The large negative pressures are necessary

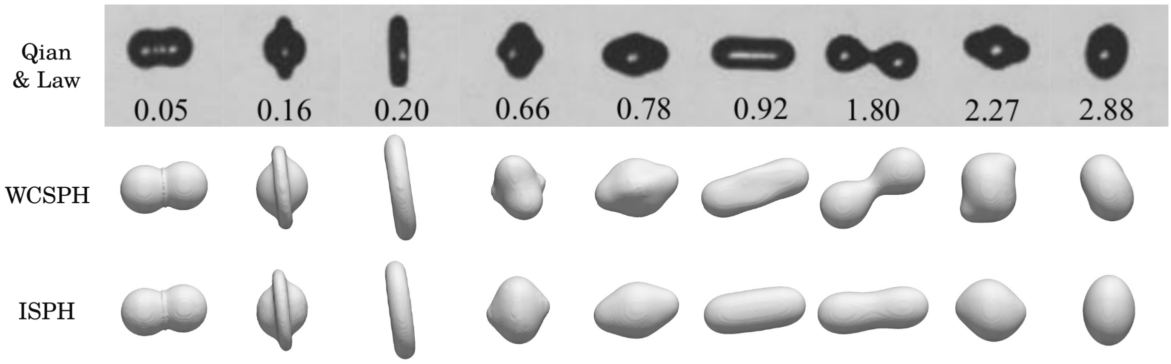

Figure 5.9. Bubble collision results of test case F simulated with the WCSPH and ISPH approach compared to the experimental results of QIAN & LAW (1997). The numbers below the experimental results represent the time in ms.

for test cases F and P because they hold the bubbles together under large deformations and thus reduce the kinetic energy. In both following test cases the deviations of the WCSPH approach are therefore greater. In order to overcome the problem of the negative pressures in ISPH, it is possible to solve separate systems of equations for the two fluids and to introduce a coupling term at the interface instead. A similar approach was applied by LIND ET AL. (2016) to couple an incompressible phase with a compressible phase. Since the representation of several phases is not essential for the SLM simulations in this work, the deviations in test case B were accepted.

Test case F

Test case F has an increased Weber number by a factor of 60 compared to test case B, which means a significantly less surface tension dominated reaction of the liquid bubbles. Since cohesive effects are visible in this test from the very beginning, a single fluid can be assumed. The results of the simulation can be found in Fig. 5.9.

The results of both approaches appear very close to the experimental ones up to 0.92 ms. Until then, the only visible deviation is a slightly higher rotation resulting from smaller errors in the angular momentum conservation. Starting at 1.8 ms, it can be seen that for the ISPH approach, the viscous damping is slightly higher, so that the lobes formed by the elongated bubble are significantly less pronounced. The WCSPH approach seem to fit the experimental results much better except for the rotation. However, it should be noted that with the standard parameters for the smoothing length ($h = 1.7\ dx$) and the physical value of the viscosity no useful results were obtained. For the shown results an extensive parameter study was necessary. At the end of this study the viscosity had to be increased by a factor of 2, and the smoothing length was reduced to 1.3 dx. The reason for this is, that the dissipation of kinetic energy in this case is not only based on the viscosity but also on the negative pressure forces. There are underestimated with the WCSPH approach and therefore had to be stabilized with higher viscosity. With the ISPH approach such a fitting was not necessary.

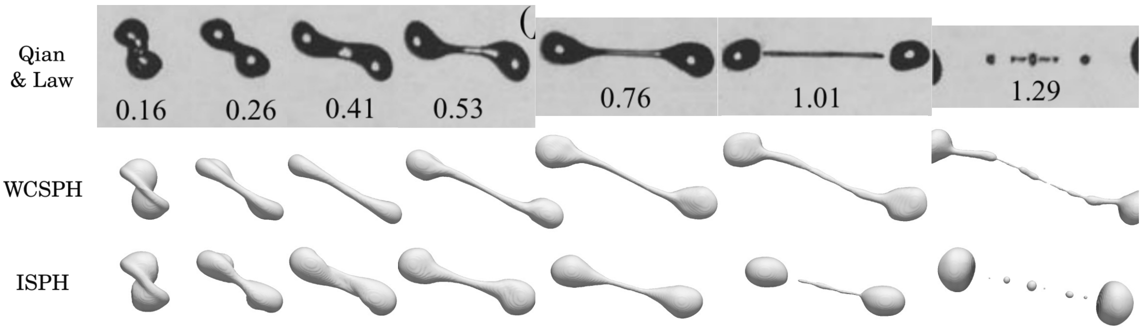

Figure 5.10. Bubble collision results of test case P simulated with the WCSPH and ISPH approach compared to the experimental results of QIAN & LAW (1997). The numbers below the experimental results represent the time in ms.

Test case P

In test case P the Weber number is again increased by a factor of 2 compared to test case F. Also the Reynolds number reaches its highest value with 312.8. In this case, cohesion effects occur from the first contact, so both bubbles are treated again as a single liquid. The results of the simulations are shown in Fig. 5.10.

In this test case, no realistic results could be achieved with the WCSPH approach despite an extensive parameter study. The results in the figure were achieved with the standard parameters, but show a clear deviation regarding the tearing of the deformed bubble. Not only the rotation of the bubble is drastically underestimated, also the elongation of the bubble is significantly higher than in the ISPH simulation and the experiment. The tearing of the bubble is delayed, and there is a clear difference in the pattern of bubbles that develop. The reason for the large differences is the inability of the WCSPH algorithm to correctly represent negative pressures. In both test case F and test case P, the negative pressures help the bubbles to maintain their shape and form the expected patterns. While the behavior in test case F could still be adjusted via the smoothing length and viscosity, this was no longer possible in test case P. In the ISPH approach, the simulation was carried out without parameter study and with the original parameters. Except for the rotational deviation already mentioned, a similar pattern is formed, which also includes the tearing of the bubble.

In general it could be shown that the algorithm applied is capable of representing the surface tension dominated bubble dynamics under large deformations. Deviations for the ISPH approach were found in case B, because this test case results in a kind of multi-phase problem, which cannot be solved with the single-phase approach of this thesis. For the WCSPH approach, major problems arose from the occurrence of negative pressures and the resulting deviations in the bubble formation. These are related to clumping or pairing instability, which is also discussed in the section 6.1.2 with regard to the SLM process.

Chapter 6

Selective Laser Melting

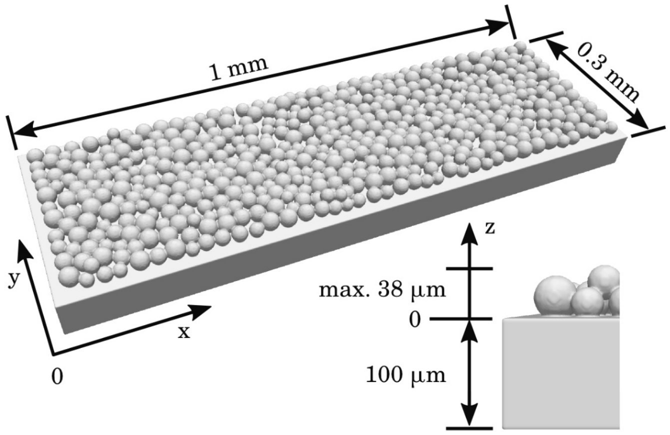

Figure 6.1. SLM test case particle distribution reproduced according to KHAIRALLAH & ANDERSON (2014) at highest resolution.

For the analysis of the SLM problems, this section first introduces the numerical data describing the test case. All following simulations are performed with the identical powder bed, so that geometrical effects (except for resolution) do not lead to any deviations here. Especially on the powder level, where a powder particle is about the size of the melt pool, the distribution of the particles can have a significant effect, which is suppressed by use of an identical powder bed. The powder bed was generated with an in-house DEM code, courtesy of Tobias Bode. In the DEM simulation, the particles were generated with a random size following a normal distribution with an average diameter of 27 μm and a standard deviation of $\approx$ 4.25 μm. This equals the distribution described in KHAIRALLAH & ANDERSON (2014). The resulting powder bed is displayed in figure 6.1. With the help of DEM simulations, the spreading process could also be carried out to ensure a more realistic distribution and compaction of the powder, as was done in FOUDA & BAYLY (2020). In this work, two different materials are used. The first is S316L like applied in WESSELS ET AL. (2018) and FÜRSTENAU ET AL. (2020b). The second is the material, used for the validation case according to TENG ET AL. (2017), a chromium-cobalt alloy. Their constant material parameters can be found in table 6. Some material parameters are known to have an important temperature

Material parameters according to	S316L [WESSELS ET AL. (2018)]	CoCr [TENG ET AL. (2017)]
Density ρ	7900 kg/m^3	8276 kg/m^3
Melting temperature T^m	1700 K	1690 K
Lat. heat of melting ΔH^m	270.33 kJ/kg	260 kJ/kg
Vap. temperature T^v	3130 K	2520 K
Lat. heat of vap. ΔH^v	6.09 MJ/kg	7.39 MJ/kg
Molar mass in g/mol	59.75 (LEE & ZHANG (2016))	110.93 (pure CoCr)*
Absorptivty	0.3	0.67*
Thermal conductivity k	variable (see App. B)	12.6 $W/(m \cdot K)$
Thermal capacity c_p	variable (see App. B)	462 $J/(kg \cdot K)$
Surface tension γ	variable (see App. B)	variable (see App. B)*

Table 6.1. Constant material parameters for the simulated test cases. *: the marked parameters were applied differently from TENG ET AL. (2017), see section 6.4 for more details.

dependency, namely surface tension γ, heat capacity c_p and thermal conductivity k. Their temperature dependent profiles can be found in appendix B. The Density ρ, which also temperature dependent, is applied as constant. Only the buoyancy term from equation 3.29 accounts for the decreasing density from thermal expansion with a slope of $1.5{\cdot}10^-5\ 1/K$ according to WESSELS (2019). Due to missing parameters this value was also used for CoCr, knowing that the effect of gravity and buoyancy is small anyway. The process parameters, which are not material dependent, are summarized in table 6.2 and are used throughout this section if not stated differently.

Before the simulation and evaluation of the SLM process is performed, inaccuracies and sources of uncertainty are identified. In section 6.1 the modeling of fluid dynamics is considered, including viscosity, resolution and smoothing length. In section 6.2 the modeling of thermal phenomena and the resulting inaccuracies are considered. This includes the conductivity of the powder, the substrate depth and the laser modeling. In these two sections the chosen parameters and modeling decisions are explained in order to proceed with the validation of the chosen approach on the experimental results of TENG ET AL. (2017) in section 6.4. The underlying experimental and simulative series is used to evaluate the processes and to generate a virtual process map.

6.1 Mechanical modeling

This section deals with the mechanical modeling of selective laser melting and matters of discretization. First the resolution is investigated, then the smoothing length and finally the influence of viscosity is analyzed.

Test case parameters	
Viscosity μ	0.1 Pas
Starting temperature	300 K
Laser power P_{laser}	600 W
Laser beam radius r_{laser}	35 μm
Laser penetration depth Z	38 μm
Laser start position (x,y)	0.1, 0.15 mm
Laser end position (x,y)	0.9, 0.15 mm
Laser speed v_{laser}	1.92 m/s
Numerical parameters	
Speed of sound	20 m/s
Smoothing length h	1.7 dx

Table 6.2. Constant parameters for the simulated test cases.

6.1.1 Resolution

The most important property of a simulation code for Selective Laser Melting, besides the models that can be represented, is the resolution. While most codes work with a resolution of about 5-3 μm (see e.g. RUSSELL ET AL. (2018); KHAIRALLAH ET AL. (2016)), the highest achieved resolution in literature is that of 1 μm found in KLASSEN ET AL. (2016) for a 2D case. Already in FÜRSTENAU ET AL. (2020b) it could be shown that a resolution of 5-4 μm is not sufficient to represent the powder bed in its initial configuration and thus the resulting dynamics (since the flow is also depending on the initial curvatures). From 3 μm the characteristics of the melt pool begin to stand out more clearly and become finer with higher resolution. It could also be shown that the resolution influences the width of the melt pool, because the increased resolution reduces the contact areas between the powder particles more and more, which influences the thermal conductivity. However, a clear difference was only visible when jumping from 2 to 1 μm. An analysis on the influence of resolution on thermal conductivity can be found in section 6.2.1.

In this section, the simulation results newly generated with the ISPH approach with resolutions of 5 to 2 μm are presented and compared with the results obtained with the WCSPH approach from FÜRSTENAU ET AL. (2020b) at 250 W laser power. The resolution of 1 μm could not be carried out with the ISPH approach, since the generated system of equations to solve the PPE leads to an overflow of the 6 GB of RAM of the used NVIDIA GTX 1660 Ti. The comparison was carried out with the already obtained results for the following reasons:

- The added models and features in the code increase the simulation time, especially compared to the computationally optimized approach in FÜRSTENAU ET AL. (2020b). This results in an increase of the computation time for the 1 μm case from 5 days to around 10 days for the WCSPH approach, leading to several weeks of additional computations.

- Due to the low energy input, this simulation shows many partial melts. These areas are particularly irregular and show the effect of the increased resolution much clearer

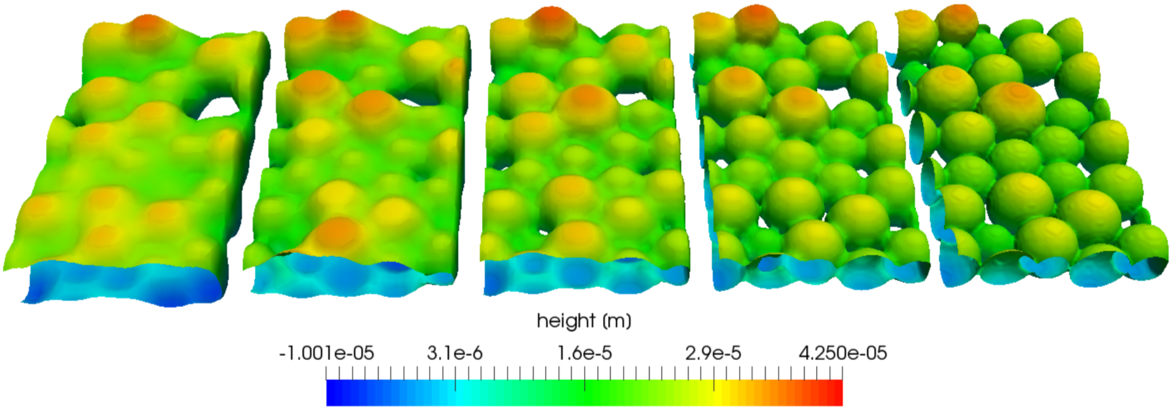

Figure 6.2. Contour plots of the initial powder distribution in a rectangular box of size 164 x 100 x 38 μm with increasing resolution from left to right.

Resolution	Particle volume	Number of particles	Particle volume fraction
5 μm	125 μm^3	3203	0.64
4 μm	64 μm^3	5963	0.61
3 μm	27 μm^3	13413	0.58
2 μm	8 μm^3	39584	0.51
1 μm	1 μm^3	287266	0.46

Table 6.3. Calculation of the particle volume fractions for the rectangular box from figure 6.2.

than the cases with higher laser power. Such a simulation was also carried out in the publication with 600 W laser power.

- Due to the low energy input, there is no effect of the recoil pressure, which is the biggest difference between the framework used in this thesis and that used in FÜRSTENAU ET AL. (2020b). So in this simulation, the added model does not cause a significant difference in the results.

Before the melt tracks are considered, the initial particle distribution at resolutions of 1-5 μm is examined. Figure 6.2 shows the contour of a section of the initial powder bed. As can be seen, the details increase from 5 to 1 μm and gaps are forming between the powder spheres. While the increase in detail is expected, the inaccuracy of the DualSPHysiscs proprietary meshing algorithm becomes apparent in the visibly decreasing particle volume. For the box visible in figure 6.2, the volume fraction occupied by the particles was evaluated, the results can be found in table 6.1.1. It can be seen that the particle volume decreases linearly with the increasing resolution. This effect can be counteracted by enlarging the spheres in the input file. The influence of the resolution on the heat conduction is referred to in section 6.2.1.
The final melt tracks of the WCSPH approach from FÜRSTENAU ET AL. (2020b) are shown in figure 6.4 and the newly simulated melt tracks are shown in figure 6.5. The WCSPH approach and the ISPH approach show similar structures, which become more detailed with increasing resolution. This underlines that for the results from FÜRSTENAU ET AL. (2020b)

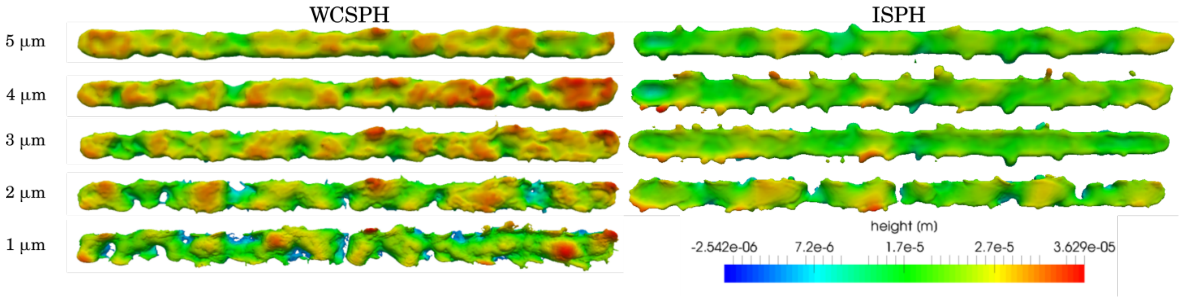

Figure 6.3. Comparative representation of the final melt pool geometries for the different resolutions.

the assumption that the recoil pressure plays a minor role for the applied laser power was correct. Direct comparison of the melt pools and their height profile in figure 6.3 shows, that the ISPH approach seems to result in a smaller melt pool with less details. In fact, the size of the melt pool is similar and the missing level of detail is resulting from a more even surface resulting from the ISPH approach. The roughness of the WCSPH approach results from the pairing instability, which is discussed in section 6.1.2. It is evident, that the incompressible melt pool tends to less small spikes and waves. The empty spaces at the sides of the pool and the discontinuities at a resolution of 2 μm of the incompressible approach are also present in the weakly compressible cases with 2 and 1 μm, as a result of the initial powder distribution. When looking at the side views of the melt pools (figure 6.6), again the increasing discontinuity of the melt pool is eminent. Especially for the resolution of 2 μm in the incompressible case the roughness of the bottom of the melt pool is more prominent than in the other cases. This is a result of the lowered thermal conductivity of the higher resolutions dealt with in section 6.2.1.

6.1.2 Smoothing length

A key question in any SPH simulation is the choice of a suitable smoothing length h. This is specified as a multiple of the particle distance dx. Basically the smoothing length should be as small as possible to be close to the Dirac delta property from section 3.1.3. Applied, a higher smoothing length means that phenomena are smeared over a larger area. To produce sharp gradients despite high smoothing lengths, the resolution must be increased. In practice, the smoothing length is chosen to be just as large as necessary for a stable simulation. This minimum length varies based on the phenomena to be modeled. In this thesis the phenomenon with the highest resolution requirements is the surface tension as found in FÜRSTENAU ET AL. (2020b), together with the corresponding Marangoni convection. From the literature there is a recommendation in the form of particles in the neighborhood, described in VIOLEAU (2012). Here 30-50 neighboring particles in 2D and 80-200 particles in 3D are recommended. This corresponds to a smoothing length of 1.3 - 1.8 for the selected kernel. In this study the smoothing length was varied in four steps: 1.2, 1.55, 1.7 and 2.05 dx. The values 1.5 and 2.0 were not used here, since these can lead to asymmetrical forces in the initial state of Cartesian meshing since the neighboring particles lay exactly on the border of the kernel.

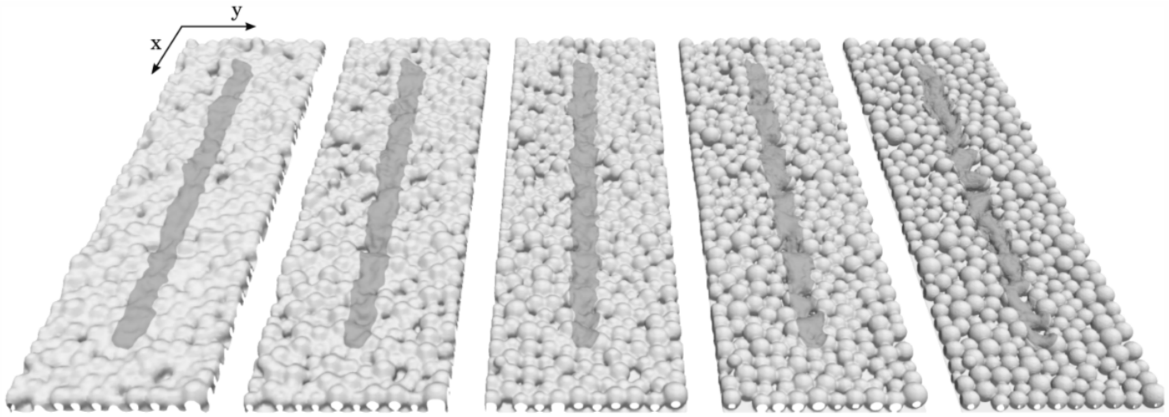

Figure 6.4. Plot of the final melting path simulated with the WCSPH approach with increasing resolution from 5 μm to 1 μm from left to right. The darker areas mark the resolidified pool.

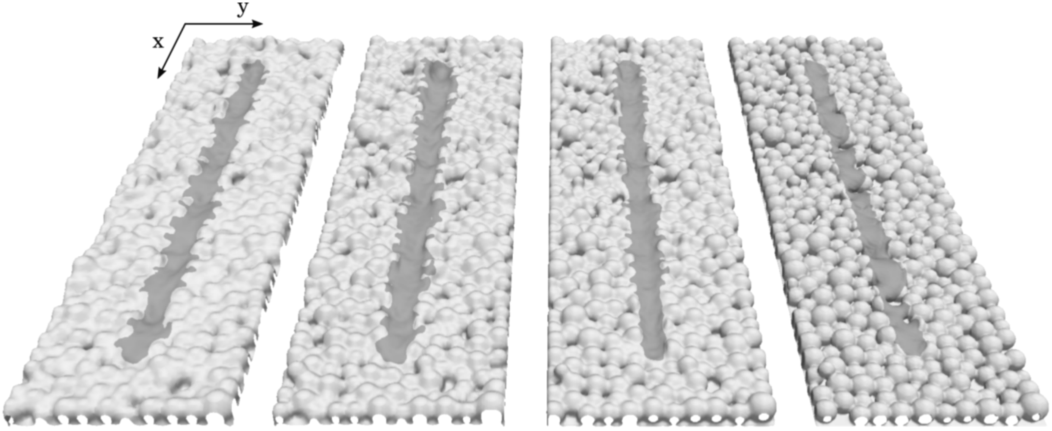

Figure 6.5. Plot of the final melting path simulated with the ISPH approach with increasing resolution from 5 μm to 2 μm from left to right.

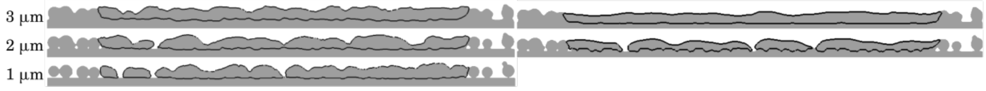

Figure 6.6. Slice of the final contours of the final melting path. The black contour marks the resolidified pool.

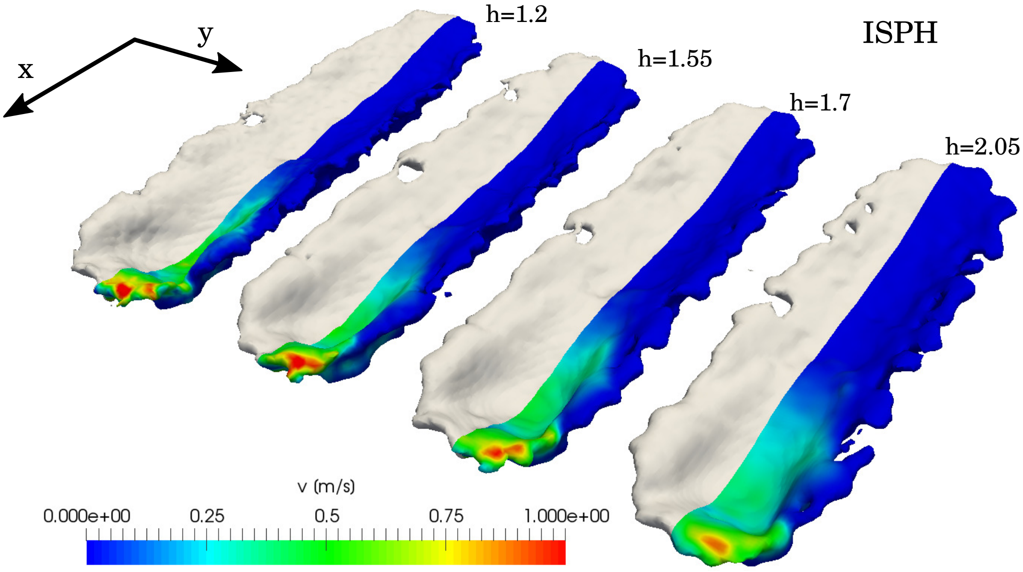

Figure 6.7. Plot of the melt pool contours of the smoothing length analysis simulated with the ISPH approach. Colored on one half in neutral color to examine the surface and on the other half with the surface velocity.

First the influence of the smoothing length is analyzed for the ISPH approach. For the comparison a shortened laser track of 0.4 mm was simulated as some of the tested setups are prone to instabilities and could not be calculated until resolidification. The results are shown in figure 6.7. The figure shows that changing the smoothing length does not change the flow features in the ISPH approach. Especially at the edges it can be seen that the macroscopic flow features do not differ in this study. Only the lowest smoothing length of 1.2 dx shows a slightly uneven surface of the melt pool. These optical differences are occurring, as the the smoothing length is also applied in the post processing to calculate the contour surface. Apparently, the ISPH setup of the SLM case is less sensitive to low smoothing lengths than the test cases from FÜRSTENAU ET AL. (2020a), where lower smoothing lengths resulted in unstable behavior. Reason for this can be a higher viscosity or the geometry, since the SLM case has a fixed ground and the tested cases in the publication were floating in a vacuum having no fix point to stabilize the motion. In summary, it can be said that the numerical stability of the ISPH approach applied onto the SLM process is not dependent on the smoothing length.

Secondly, the influence of the smoothing length on the weakly compressible approach is examined. Here the calculation of the same test case showed a completely different behavior. On the one hand, the simulations with the WCSPH approach and smoothing lengths of 1.2 and 1.55 dx are significantly less stable. The reason for this are oscillations of the particles at the surface of the melt pool these are caused by an instability of the surface tension algorithm, which was already observed to be the source of instability in FÜRSTENAU ET AL. (2020a). Increasing the smoothing length above 1.7 dx solved the problem there. When increasing the smoothing length to 1.7 or 2.05 dx, again the pairing instability becomes evident again. They occur in the form of a more compact melt pool in the powder plane as well as in its wavy surface. As introduced in section 3.1.3, pairing issues occur when the smoothing length

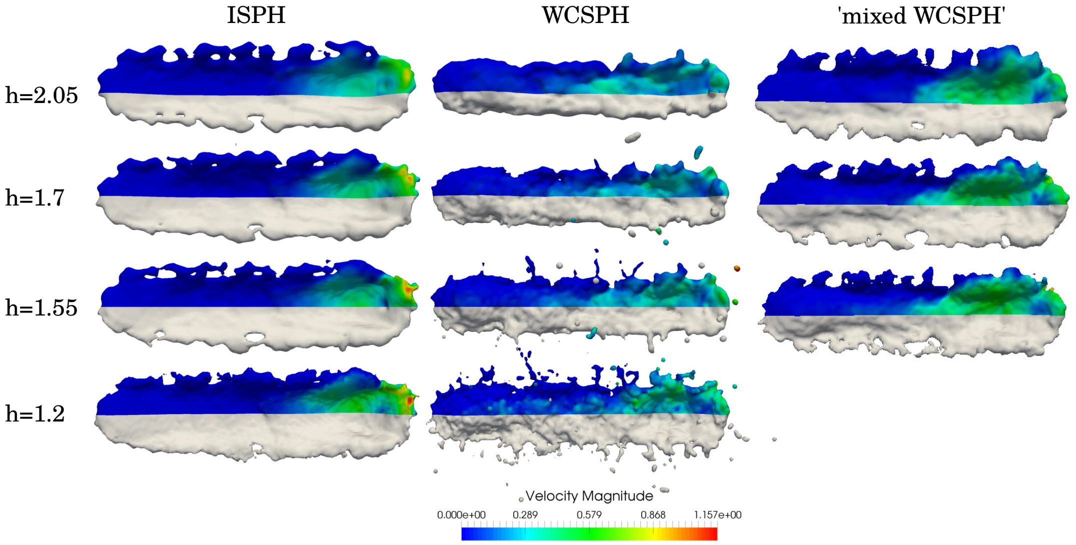

Figure 6.8. Top views of the melt pool contours of the smoothing length studies for the different used approaches. Left: ISPH; middle: WCSPH; right: WCSPH approach with mixed smoothing length.

is large and particles are getting too close compared to the kernel radius. PRICE (2011), who analyzed this problem found a solution by reducing the smoothing length for his used kernels to 1.2 dx. In this work, this results in the above mentioned instability of the surface tension. The resulting motion contours of the melt pool can be found in figure 6.8 [middle]. As one can see, the overall appereance of the WCSPH results for an h of 2.05 and 1.7 dx is very similar to the results achieved in FÜRSTENAU ET AL. (2020b), which were simulated with a smoothing length of 1.8 dx. These are very different from the results achieved with the ISPH approach. With smaller smoothing lengths, many spatters are accelerated out of the melt pool, which shows a strong form of instability of the surface tension. Apparently, with none of the four smoothing lengths trustworthy results comparable to the ISPH approach can be achieved if melt pool simulations with higher heat input (than in the previous publication) are to be modeled.

A solution to the problem was found by using two smoothing lengths like applied by RUSSELL ET AL. (2018). One smoothing length for the surface tension, which requires a larger one to calculate accurate and stable curvatures, and a smaller one for the rest to avoid clumping. With the 'mixed WCSPH' approach in figure 6.8 [right], using the variable smoothing length for the surface tension and a constant smoothing length of 1.2 dx for the other terms, similar results as with the ISPH approach could be achieved for all cases. In this test case, which was reduced in space and time, the application of the 'mixed WCSPH' approach also had a consistently positive effect on the simulation time and the number of time steps. This suggests the replacement of the WCSPH approach by the 'mixed WCSPH' approach. Unfortunately, this positive effect could not be reproduced in the complete test cases. For comparison, figure 6.39 shows a result with the material parameters from the validation section 6.4 that was solved with all three approaches. Here, the WCSPH results as much as the 'mixed WCSPH' results are very different from the ISPH results. Additionally, the resulting computing times show, that the use of the 'mixed WCSPH' approach did not lead to a more stable simulation while increasing the simulation time by a factor of 2.7 compared to the WCSPH approach. For this reason, the thermal sensitivity analyses in section 6.2 and the phenomena section 2.1, the ISPH approach will be used only, since the results of the WCSPH approach give no additional information compared to the ISPH results, and the 'mixed WCSPH' approach is too computational expensive while not stabilizing the simulation entirely.

6.1.3 Viscosity

For viscosity, one of the most fundamental phenomena of melt pool evolution, some authors in the literature accept a certain error by artificially raising the values. While authors using mesh-based methods such as KHAIRALLAH ET AL. (2016) usually apply the physical viscosity of molten steel ($0.00642\ Pas$), in mesh-free methods it is quiet rare like in HU & EBERHARD (2017). Here a smaller time step has to be accepted to produce stable results despite low viscosity. More often the viscosity is artificially increased, as for example in RUSSELL ET AL. (2018) ($0.01\ Pas$). In this work the viscosity was further increased as performed by HE ET AL. (2003) or WESSELS (2019) and also in the previous work (FÜRSTENAU ET AL. (2020b)). This allows for shorter calculation times with increased stability. However, it should be noted that an increase in viscosity by a factor of about 20 can have a significant influence on the melt pool geometry. This can also be expected by looking at the characteristic quantities that are used to characterize the melt pool behavior, like the Reynolds number, Weber number and several others. A detailed listing and explanation of these characteristic quantities can be found in YADROITSEV (2008). In this subsection the influence of viscosity on melt pool dynamics is considered. Viscosities of 0.0062, 0.01 and 0.1 Pas were used for the test. According to JAMSHIDINIA ET AL. (2012), this results in the Reynolds numbers according to the following formula:

$$Re = \frac{\rho v_{laser} r_{laser}}{\eta}, \tag{6.1}$$

meaning, that the characteristic length and velocity scale for the SLM process is set to be the laser radius and velocity. The resulting Reynolds numbers for the three test cases are shown in table 6.4. It is visible, that the increased viscosity lowers the Reynolds number, but still all calculated Reynolds numbers are below 100 resulting in a laminar flow behavior in the, well-represented area as seen in section 5.1.

Dynamic Viscosity $[Pas]$	0.1	0.01	0.00642
Reynolds number	5.53	55.3	86.1

Table 6.4. Dynamic viscosities and belonging Reynolds numbers for the viscosity analysis.

When comparing the simulated results, several details become apparent. First of all, with a look at the contours of the melt pool geometry. The representations of the final melt pool geometries can be found in figures 6.9 and 6.10. In the figures, it is first noticeable that a

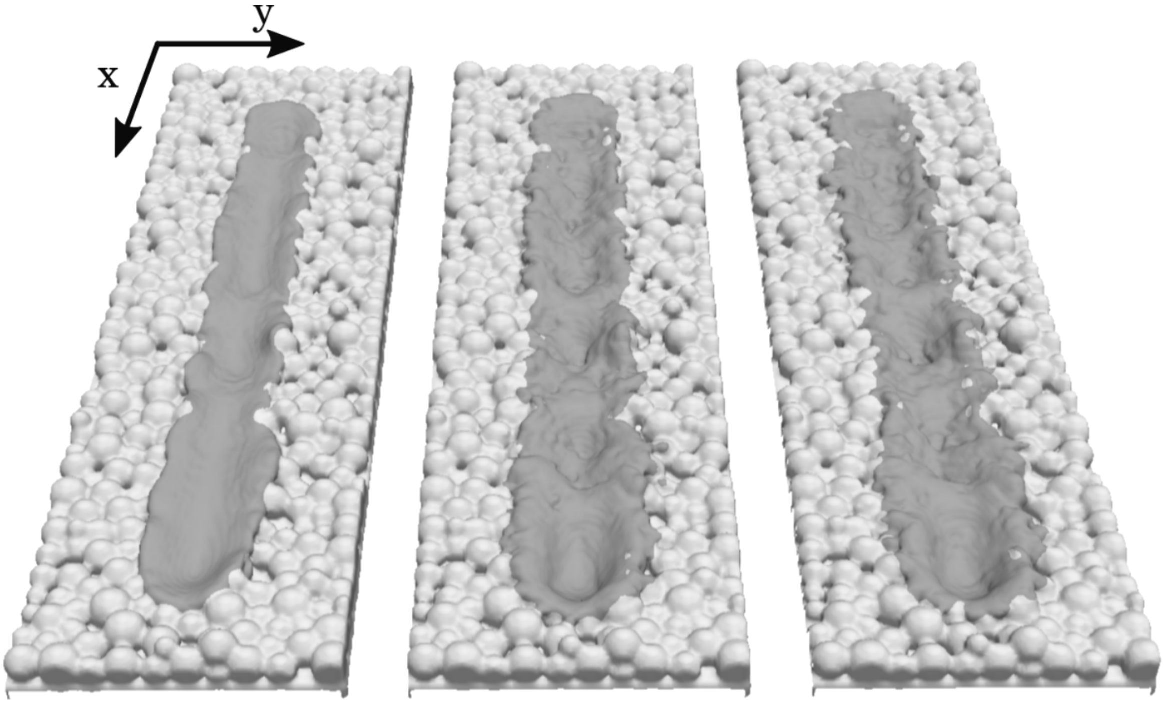

Figure 6.9. Final melt pool surface plots of the viscosity study with the ISPH approach. From left to right the viscosity decreases from 0.1 over 0.01 to 0.00642 Pas.

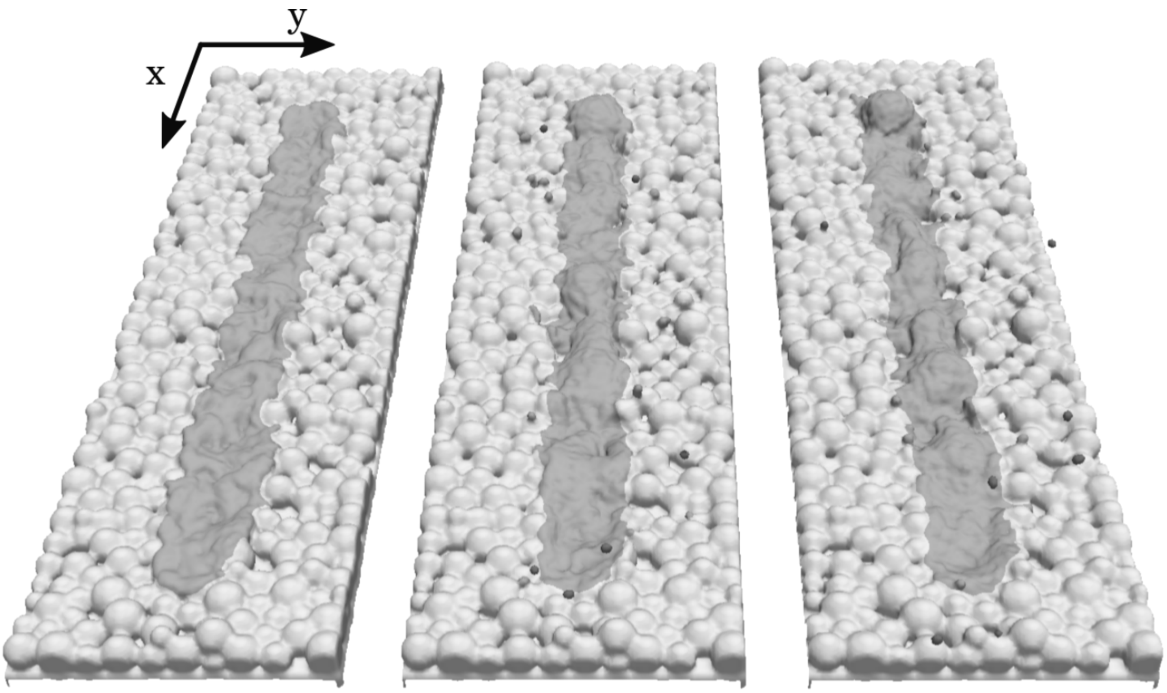

Figure 6.10. Final melt pool surface plots of the viscosity study with the WCSPH approach. From left to right the viscosity decreases from 0.1 over 0.01 to 0.00642 Pas.

reduction in viscosity in ISPH and WCSPH produces different effects. In the ISPH approach, the melt pool increases in width on the one hand, as the melt penetrates deeper into the solid powder to the sides. On the other hand, the melt pool becomes deeper due to the particles flowing off to the sides and the surface becomes more uneven. The latter effect is also visible with WCSPH approach, but to a greater extent. The formation of lumps at the beginning of the melt path and in the middle is particularly noticeable. In contrast to the ISPH approach, the WCSPH approach does not change the width of the melt pool. When searching for the reason of the effects, a look at the surface velocities during the simulations gives further insight (see figure 6.11):

- In the ISPH approach, the surface velocity approximately doubles, pointing away from the laser spot and increasing towards the melt pool boundary. On the one hand, this leads to a poor filling of the laser intensity function and thus to a lower energy input. On the other hand, the wider distribution of the molten particles leads to a more pronounced cooling of the pool, and ultimately to the uneven surface. The lower energy input can also be observed in Graph 6.13 [left], where the energy input decreases by about 20-25 % as the viscosity decreases. At the same time, the number of liquid particles in Graph 6.12 [left] decreases by about half, which is due to the stronger cooling. Due to these two effects, the melt pool does not have enough time to form an even surface and solidifies in its rough shape. The aspects of heat conduction are discussed in section 6.2.1 and a correction of the laser source is introduced in section 6.2.3 to eliminate these deviations.

- In the WCSPH approach, at low viscosities the surface velocity is even higher in the rear part of the melt pool, where at higher viscosity the velocity has already dropped to '0'. This is because the reduced viscosity further increases the effect of pairing (from section 6.1.2), resulting in poorer heat dissipation. The lumps of liquid particles move away from the hot laser source due to the Marangoni convection and finally lead to the visible peaks of the solidified melt pool. At the same time, it is visible that many spatters are accelerated from the melt pool, which is an extreme form of instability that was already noticed in section 6.1.2 due to surface tension instabilities. Apparently, lowering the viscosity has a similar destabilizing effect as decreasing the smoothing length. It is shown that the increased viscosity is necessary to stabilize the surface of the melt pool, because the numerical instability of the WCSPH approach is further increased by the real viscosity. VIOLEAU (2012) performed theoretical analyses on the stability of explicit SPH which help understanding the occurring instabilities. Summarized, the combination of small particle sizes, low viscosity and a low order explicit time integration scheme are a demanding combination to generate stable results. In the graphs 6.13 [right], hardly any reduction of energy absorption is visible, since clumping impedes Marangoni convection in this region. The number of liquid particles in graph 6.12 [right] also decreases only slightly and is significantly higher than with the ISPH approach.

As the last point the influence of the reduced viscosity on the calculation time is shown (see table 6.1.3). It can be seen that with the ISPH approach, the simulation time remains

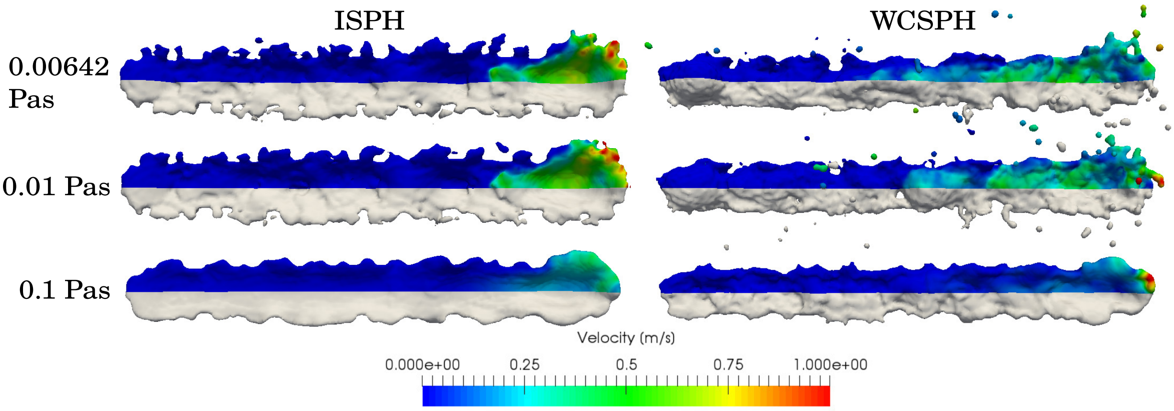
ISPH
WCSPH
0.00642 Pas
0.01 Pas
0.1 Pas
Velocity (m/s)
0.000e+00
0.25
0.5
0.75
1.000e+00

Figure 6.11. Plot of the melt pool contours of the viscosity analysis. Left: results of the ISPH approach; right: results of the WCSPH approach. Colored on one half in neutral color to examine the surface and on the other half with the surface velocity.

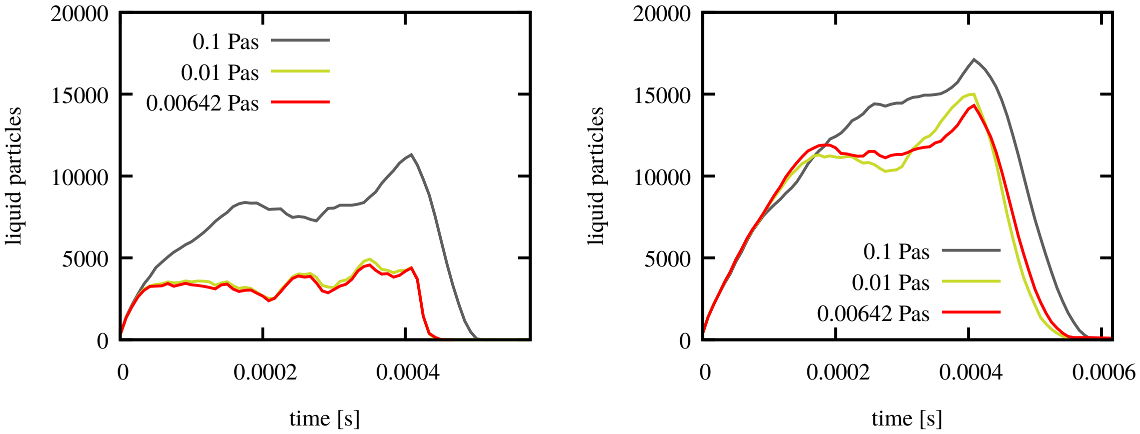

Figure 6.12. Graphs representing the number of liquid particles in the viscosity analyses over time. Left: results of the ISPH approach; right: results of the WCSPH approach.

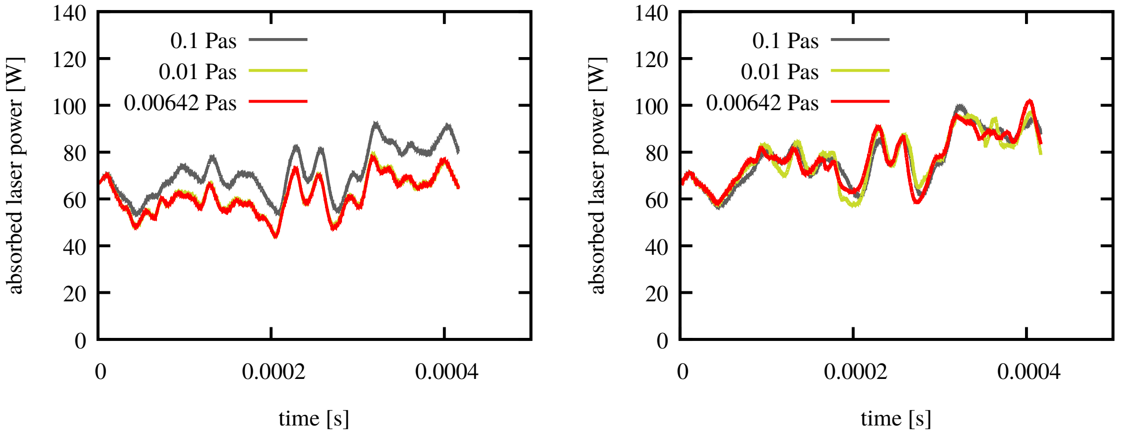

Figure 6.13. Graphs representing the absorbed laser power during the viscosity analyses over time. Left: results of the ISPH approach; right: results of the WCSPH approach.

	dynamic viscosity	simulation runtime	average time step size
ISPH	0.1 Pas	3 h 35 min	7.893 E-8 s
	0.01 Pas	3 h 31 min	7.892 E-8 s
	0.00642 Pas	3 h 31 min	7.890 E-8 s
WCSPH	0.1 Pas	6 h 24 min	2.281 E-8 s
	0.01 Pas	11 h 16 min	1.295 E-8 s
	0.00642 Pas	12 h 31 min	1.168 E-8 s

Table 6.5. Simulation run time and time stepping data of the viscosity analyses.

constant despite decreasing viscosity, whereas with the WCSPH approach, the calculation time increases significantly with decreasing viscosity. The reason for this lies in the average time step size. In the ISPH approach, the mean time step size remains almost constant because it is almost exclusively limited by the surface tension-based time step barrier from formula (4.12). In the WCSPH approach, the minimum time step is almost entirely limited by the CFL time step barrier from formula (4.15), which is mainly determined by the surface tension instability and the resulting high velocities.

In summary, the ISPH approach offers the possibility to simulate the physical viscosity. On the one hand, the effects that lead to deviations can be controlled by correcting the laser energy source and by adjusting the powder conductivity. This requires a fit of the surface temperature and if possible of the solidification rate. On the other hand, the reduction of the viscosity has no influence on the simulation speed. For the WCSPH approach the picture is different. The reduction of the viscosity further increases the numerical instability of the approach, which further limits the comparability of the results. Simulations with the 'mixed WCSPH' approach could probably solve these problems, but are currently too computationally intensive (see section 6.1.2).

Given a higher probability of spatters which can affect the numerical stability of the ISPH approach in a negative way for higher energy inputs and the increased simulation time of the WCSPH approach, the viscosity is kept at 0.1 Pas for the following simulations.

6.2 Thermal modeling

Following the consideration of the simulation conditions on the mechanical side, this section discusses the thermal influences on the SLM process. In TENG ET AL. (2016) and TENG ET AL. (2017) the sensitivities were considered and the largest influences on the width and depth of the melt pool could be identified at the following points:

- the consideration of the latent heat (sometimes called supercooling),
- the difference between powder and solid thermal conductivity,
- the laser penetration depth in powder and solid material,
- the packing density of the powder.

The first point has already been considered in FÜRSTENAU ET AL. (2020b). It could be shown that the negligence of the latent heat can lead to strong deviations, as well as the combination of a simple time stepping scheme with the apparent heat approach. The approach used in this thesis combines the correct representation by an internal energy-temperature mapping with a simple explicit time integration scheme (see section 3.2.5 or FÜRSTENAU ET AL. (2020b)). The second point, thermal conductivity, is discussed in section 6.2.1. Here the resolution of the powder and the heat conduction in the SPH method is discussed. In section 6.2.2 the necessary depth of the substrate is discussed, in order to be able to represent the solution independently of the boundary conditions. The third point deals with the heat source and its effective depth. In section 6.2.3 the uneven energy absorption already observed in section 6.1.3 is discussed and the two correction processes from section 2.4.4 are applied to allow a constant heat input and to achieve a stable solution without unphysical overheating. The last point, the dependence on the packing density, is not considered in this thesis, since all simulations are based on the same particle distribution.

6.2.1 Powder conductivity

Theoretical considerations on the thermal conductivity of the powder are difficult. In principle, the contact between the spherical particles is infinitely small. This means that when refining the discretization, the contact areas in the SPH simulation are becoming smaller and smaller, besides the volume loss found in section 6.1.1. Therefore the thermal conductivity should decrease with increasing discretization. However, the thermal conductivity in SPH is also dependent on the smoothing length, since particles on the surface and in contact can transfer heat even over a certain distance, which is desirable for the conduction over irregular particle distributions. Therefore, it is either necessary to apply an analytical contact algorithm such as Hertzian contact to calculate the thermal conductivity of the contact area, or to apply an SPH-based approach that makes conductivity independent of the resolution.

To test the thermal conductivity in the current approach, the powder bed was simulated without substrate, as shown in figure 6.14. To ensure a more defined heat input than by the laser, a bar with constant temperature was placed in front of the powder bed, the other end is thermally free. The temperature of the powder is set to 300 K and the bar set to 1700

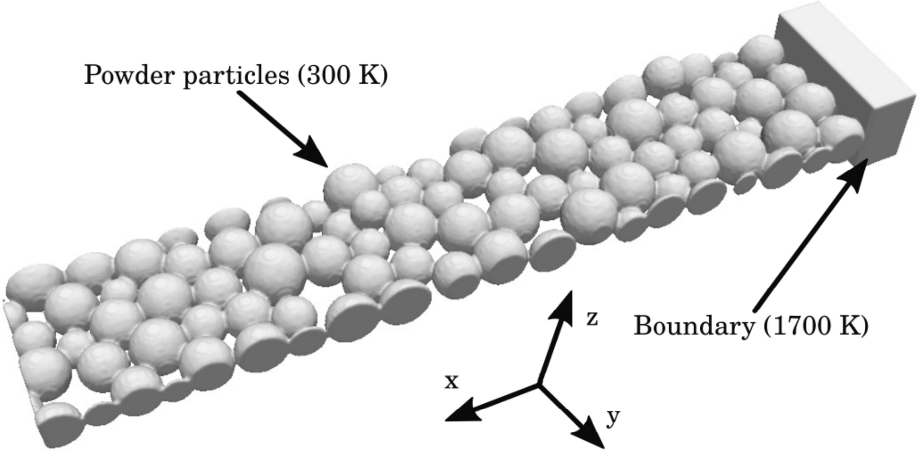

Figure 6.14. Geometry and boundary conditions for heat conduction test.

Resolution	Number of particles	Equivalent solid conductivity
5 μm	9,565	$\approx k/1.3$
4 μm	17,765	$\approx k/1.3$
3 μm	39,034	$\approx k/1.3$
2 μm	119,864	$\approx k/1.3$
1 μm	869,778	$\approx k/3$

Table 6.6. Additional details on the resolution test of the heat conduction test case and the fitted equivalent solid conductivities. Additional figures of the fitting can be found in appendix C.

K. The thermal conductivity of the bar was set to the same value as assumed for the base plate (20.9 $K/(m \cdot s)$), so that its thermal conductivity is not the bottleneck in terms of conductivity. To classify the thermal conductivity, simulations with resolutions from 1 to 5 μm and with a solid block of material were performed. This simple experimental setup leads to a transient heat propagation, which can be solved analytically for constant heat capacity and conductivity. This was done for example in FÜRSTENAU ET AL. (2017). However, an analytical solution is difficult here since in this work the simulations were carried out with a non-constant thermal conductivity and heat capacity.

For comparison, the temperatures averaged over the y-z-plane were plotted as a function of the x-coordinate in figure 6.15 [right], heat conductivity and capacity follow the curves in appendix B. It can be seen that over all resolutions but the finest of 1 μm the thermal conductivity is only slightly lower than that of the solid material. Therefore, the assumption that modeling the thermal conductivity via the spatial representation of the powder is not sufficient, at least for the SPH method. The results of the fitting carried out subsequently are shown in figure 6.15 [right]. The plots of the raw particle temperatures with fitted curves, as well as 3D-illustrations of the temperature over the particle distribution can be found in appendix C. For the fitting, the thermal conductivity function has been divided by a constant factor. The resulting factors can be found in 6.6. As can be seen, the values of thermal conductivity between resolution of 5 to 2 μm are very close to each other, and can

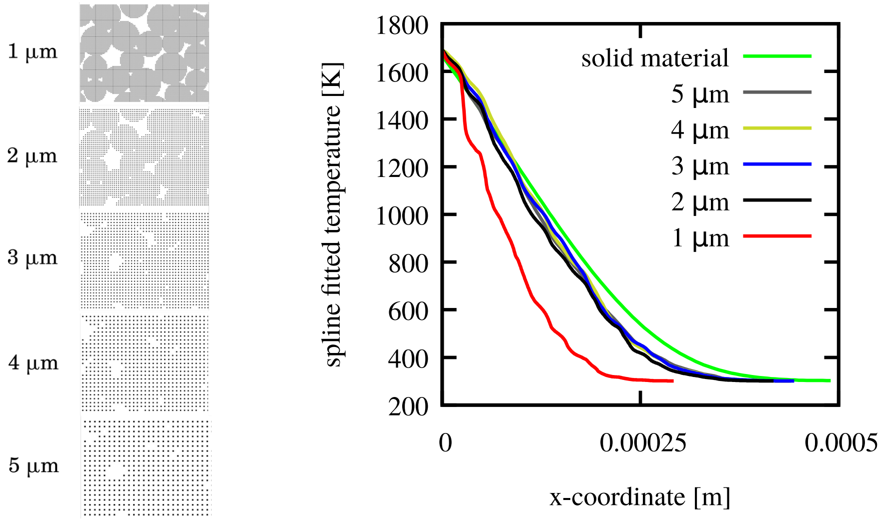

Figure 6.15. Left: Representations of the very same part of the powder in 2D view from the top with the five analyzed resolutions; right: spline-fits of the particle transient temperatures at 5 ms compared to the solid material conductivity.

be fitted by the solid conductivity divided by 1.3. Only the finest discretization of 1 μm has a significantly lower conductivity, equivalent to one third of the initial one on a solid block. A comparison of the same section and its discretization is shown in figure 6.15 [left], showing again the more sparse volume filling with increasing resolution. The temperature curves in appendix C also show that the deviations in temperature along the x-axis increase noticeably at 1 μm due to the smaller contact surfaces and larger gaps. This is because the powder spheres heat up at different rates based on their contact area.

Overall, the simulations show that the assumption of a discretized powder bed, automatically resulting in physically lower thermal conductions is wrong and requires a fit. To do so, the thermal conductivity of the powder spheres is reduced, following GUSAROV ET AL.

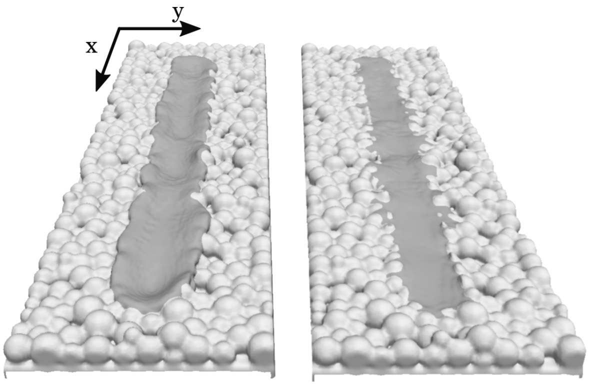

Figure 6.16. Representation of the final melt pool geometry of the heat conductivity analyses. Left: melt pool geometry ’without phase change’; right: melt pool geometry ’with phase change’.

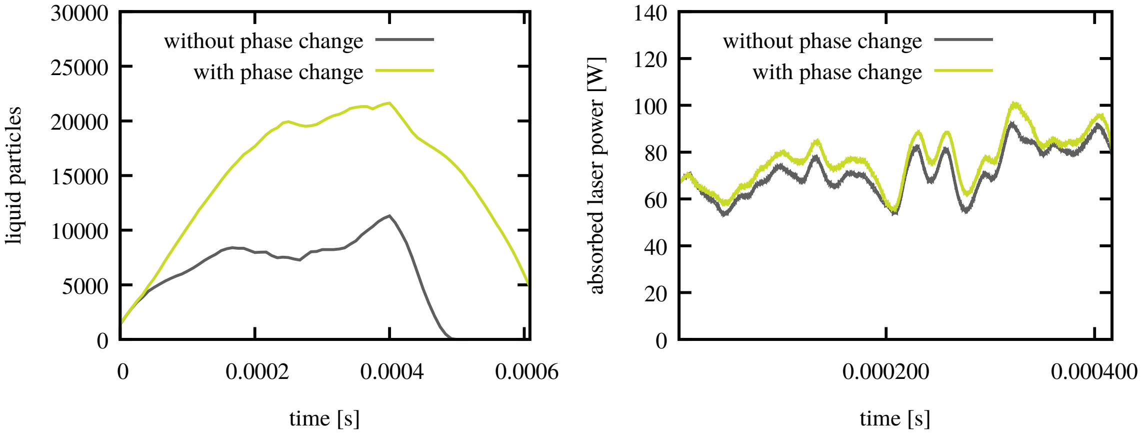

Figure 6.17. Left: graphs representing the number of liquid particles in the heat conductivity analyses over time (active laser time 0.417 ms); right: absorbed laser power in the heat conductiy analyses over time showing only a minor difference.

(2009), by a factor of 100. This is only a modeling approach, as in reality, the conductivity between the spheres should be reduced but inside every sphere it should be equal to the bulk conductivity. Such a modeling would be possible by applying something similar to a multi-phase approach, giving every powder particle a high internal thermal conductivity but only a small conductivity with other particles. To realize this a larger implementation in terms of thermal properties and multi-phase approach would be necessary, which is not followed here. Instead, two simplified simulations are carried out:

- In one simulation, the heat conductivity of the powder particles is lowered by a factor of 100 compared to the liquid and substrate particles. When a particle of the powder melts, it changes to the 'bulk phase' with increased conductivity and remains in this phase also after solidification. This simulation is referred to in the following as 'with phase change'.
- In the other simulation, the heat conductivity of all three parts, powder, substrate and molten particles, follows the same curve. This simulation is referred to in the following as 'without phase change'.

The results of both simulations show a clear influence of the thermal conductivity of the powder. Looking at the final melt pool geometries in figure 6.16, it can be seen that without the phase change, the melt pool becomes significantly wider and sinks in the middle, as the liquid particles are pulled towards the edges by Marangoni convection and solidify there because of the higher conductivity of the powder. In total, the melt pool appears somewhat wider and consists of 50,000 molten particles. With the phase change, the melt pool is very uniform and shows little sign of the Marangoni convection. In some places the melt oozes between the solid particles, as it cannot melt them. It is also visible that many particles at the edges of the melt pool are only partially melted, as their thermal conductivity is reduced. This phenomenon is less physical as the powder particles usually melt completely or remain completely solid due to the high thermal conductivity inside and the lower one between the

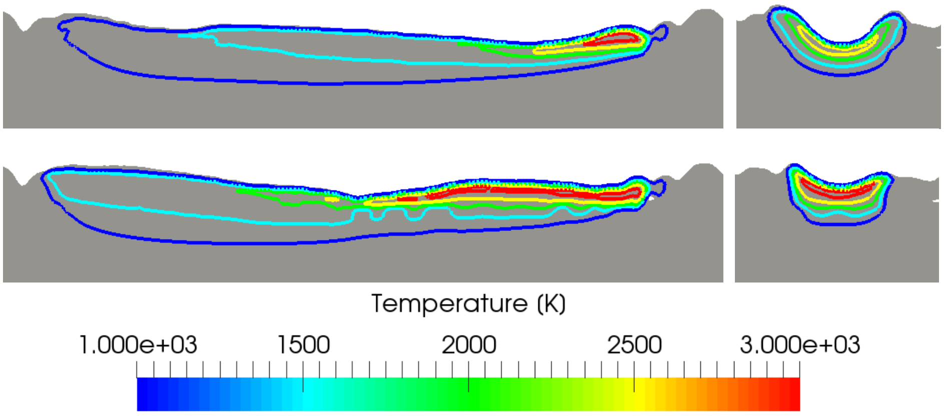

Figure 6.18. Melt pool slices during the SLM process showing the temperature profiles below the laser. Top: melt pool geometry 'without phase change'; bottom: melt pool geometry 'with phase change'.

particles. This effect could not be reproduced correctly here, as described above. The melt pool with phase change also appears to be somewhat narrower and contains only 45,000 molten particles, about 10 % less than without phase change. The number of liquid particles in figure 6.17 [left] gives the reason for the more even surface of the melt pool with phase change: by the lowered powder conductivity, the heat is kept longer in the pool, which leads to about two times more liquid particles throughtout the simualtion and to a way longer time for the pool to cool down, which generates a more even surface. In the right graphs it is also visible, that the absorbed laser power is nearly equal in both simulations, such that the energy input is not responsible for the differences in the number of molten and liquid particles. Finally, a look at the temperature distributions in the melt pool sections in figure 6.18 shows the propagation of the melt pool under the laser beam and along the path followed. It can be seen that with phase change, hardly any heat flows off to the sides of the melt pool, which leads to a smaller width and a higher temperature in the melt, whereas without phase change, the melt loses energy at the edges so quickly that the melt pool solidifies in an arc shape.

In summary, it can be said that the thermal conductivity has a great influence on the melt pool geometry and the solidification process. The assumption that the resolution of the powder geometry is sufficient for correct heat conduction could be refuted at least for the SPH approach. However, it was found that the thermal conductivity, although significantly higher than expected, differs only slightly between a resolution of 5 to 2 μm. In the comparative simulation of the SLM process a strong influence was shown while extreme values were tested. The reality is probably between these extreme values and a fit of the actual thermal conductivity of the powder seems reasonable. The following simulations are calculated without phase change, because it does not seem reasonable to use phase change because of its unrealistically high cooling times and the resulting flat melt pool. Also it does not seem reasonable to assume an arbitrary value for the thermal conductivity difference and make the results dependent on it.

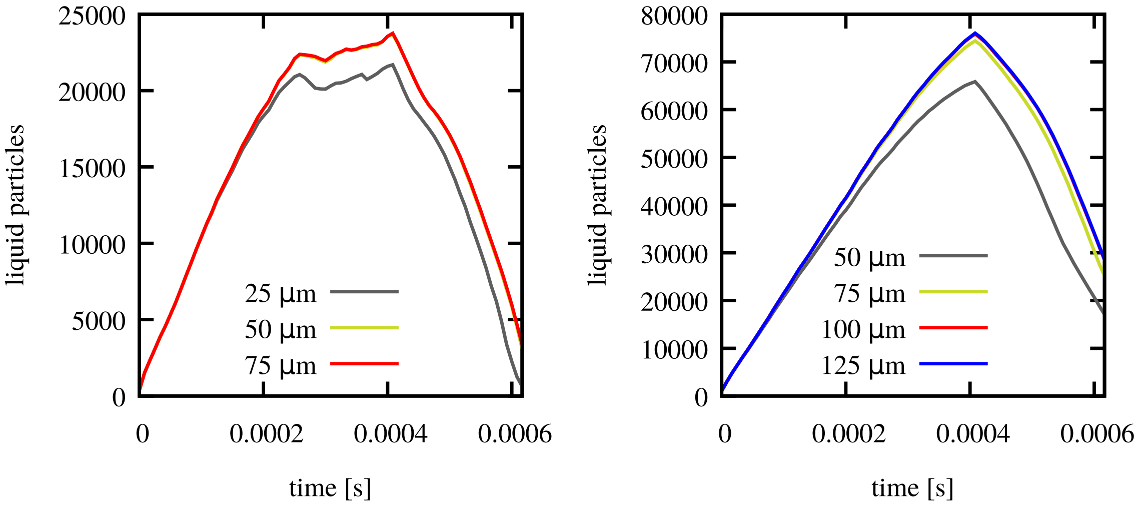

Figure 6.19. Graphs representing the number of liquid particles in the substrate depth analyses over time. Left: 600 W laser heat source; right: 900 W laser heat source.

6.2.2 Substrate depth

The question of the necessary substrate depth is more of numerical nature. In reality there is a comparably large substrate of solid steel, unmolten powder or solidified material below the powder bed, that drains the heat from the melt pool. While the near substrate is certainly melted by the laser, the distant substrate is hardly affected by it. During the process, a temperature gradient to the boundary condition is established in this area. For the Dirichlet boundary condition used in this work, room temperature is set as a fixed value. If the boundary condition described by this is too close to the melt pool, the temperature gradient becomes steeper and more heat is drained from the melt pool, which influences the melt pool geometry. If the boundary condition is further away from the melt pool, this has no effect on the melt pool, but increases the simulation time unnecessarily. For this reason, this section uses two series of simulations to determine the necessary substrate depth from which the melt pool geometry becomes independent of the distance between the pool and the boundary condition. Alternatively, it is possible to apply a Robin boundary condition as done in WESSELS (2019). This linear boundary condition is able to emulate the temperature gradient to a fixed point, making it possible to omit the distant substrate area. However, this approach has not been applied here, since the productive use of this approach requires a careful study of the expected melt pool depth, in order not to come too close to it.

The two series of simulations carried out are two printing processes with different laser power (600 and 900 W) at the speed of 1.92 m/s. To evaluate when the printing process becomes independent of the substrate depth, the number of molten particles is recorded at fixed times. The results of this study are shown in figure 6.19. For the first row, an independent result is obtained from 50 μm substrate depth, with a melt pool depth of 9.5 μm. For the second row, starting at 100 μm substrate depth, there is an independent result, at a melt pool depth of 37.8 μm. Figure 6.20 shows the two melt pools and the marking of the different melt pool depths. As can be seen, there is an independent result for both series starting from a distance

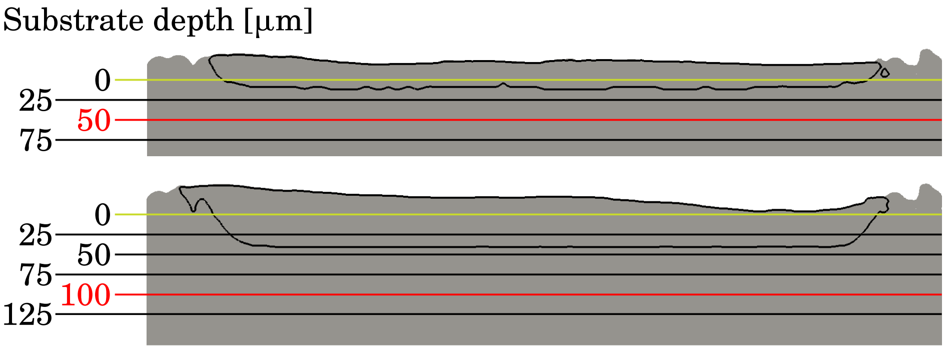

Figure 6.20. Final melt pool slices from the substrate depth analyses. Shown are the independent melt pool geometries (600 W [top] and 900 W [bottom]). The numbered marks represent the tested substrate depth, with the green mark as the substrate surface and the red line the critical substrate depth.

of about 40 μm for the lower energy case and 60 μm for the higher energy case between melt pool and boundary condition. This finding is taken into account in the further simulations so that the substrate zone is deep enough.

6.2.3 Laser modeling

As found in the previous simulations, an unreliable energy source for the SLM process represents a large uncertainty. In the simulations, differences and fluctuations in energy input of up to 20 % could be observed, while on average only 50-70 % of the laser power actually affected the material. This deviation is not acceptable for a reliable representation of the SLM process and therefore this section deals with the correction of the laser heat source.
As described in section 2.4.4, a volumetric heat source is used in this thesis. In previous simulations, the energy was introduced uncorrected, which led to large deviations. In this section, the two correction possibilities presented in section 2.4.4 are tested. To do so, a study with five laser variants is carried out:

- uncorrected laser,
- scalar corrected laser with the intensity correction from (2.35),
- three variants of adaptive laser correction with penetration depth correction (2.36) and intensity correction (2.35). For the three variants, the target laser intensity for the depth correction was set to 0.25, 0.5 and 0.75. This results in different laser penetration depths which are also investigated.

For the five simulations the laser power was reduced from 600 to 200 W and the laser speed from 1.92 to 1.5 m/s, as the scalar corrected and the adaptive heat source approach with a target laser intensity of 0.25 are tending to become unstable at higher laser powers due to local overheating. The reason for this is that in some occasions the laser power is focused on very small portions of particles. With the changed speed and power, the heat input is lower and the melt pool more stable, still giving information about the influence of the applied corrections.

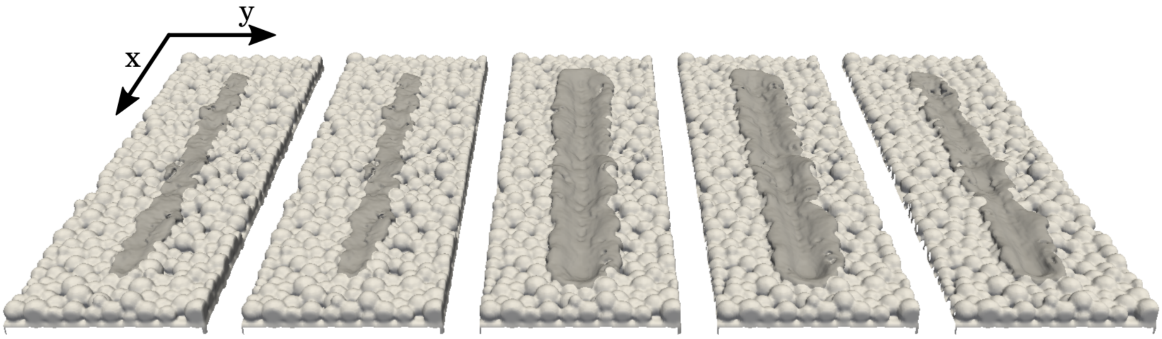

Figure 6.21. Representation of the final melt pool geometry of the laser correction analyses. From left to right: uncorrected laser heat source, scalar correction, adaptive correction: target intensity 0.25, 0.5 0.75.

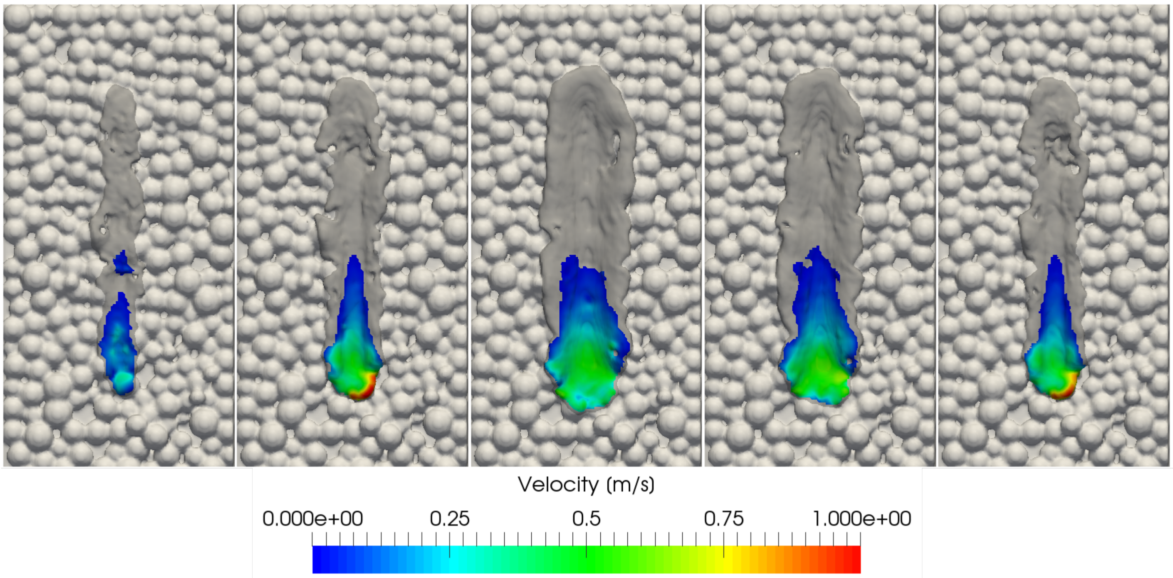

Figure 6.22. Representation of the final melt pool geometry of the laser correction analyses. From left to right: uncorrected laser heat source, scalar correction, adaptive correction: target intensity 0.25, 0.5 0.75.

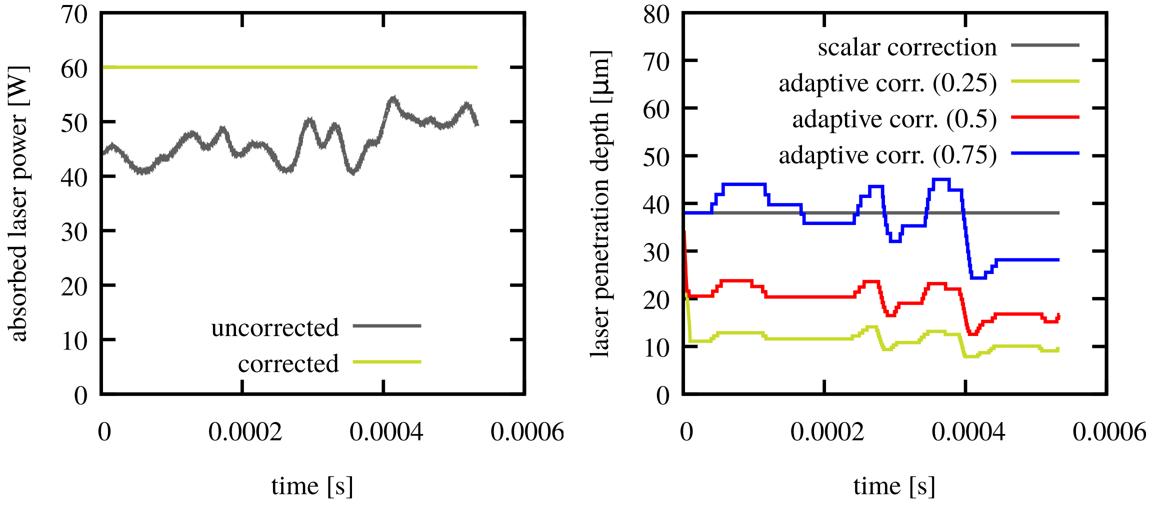

Figure 6.23. Left: graph of the uncorrected compared to the corrected absorbed laser power for a 200 W laser heat source with an absorptivity of 0.3; right: graphs of the laser penetration depth with the three different adaptive laser corrections.

Laser correction	Effective laser power	Average penetration depth	Molten particles	Vaporized particles
Uncorrected	46.5 W	38 μm	19,820 (100 %)	0
Scalar correction	60 W	38 μm	34,168 (172 %)	0
Adaptive corr. (0.25)	60 W	11.3 μm	46,091 (233 %)	2,001
Adaptive corr. (0.5)	60 W	19.8 μm	46,039 (232 %)	362
Adaptive corr. (0.75)	60 W	36.4 μm	35,363 (178 %)	2

Table 6.7. Additional information on the laser corection analyses, showing the total amount of molten and vaporized particles.

The resulting final melt pool contours are to be seen in figure 6.21. These initially show an increase in the melt pool width from the uncorrected laser source to the corrected one. The comparison of the uncorrected and corrected laser power in figure 6.23 [left] shows an average difference of 13.5 W (corresponding to 23 %), which explains the narrower melt pool.

Secondly, it is noticeable that the melt pools of the corrected laser sources also differ significantly. The second and the fifth melt pool (scalar correction and adaptive correction (0.75)) appear to be similarly narrow as the melt pool of the uncorrected heat source. In the top view in figure 6.22 the similarities become even more obvious. While the scalar correction and the adaptive correction (0.75) produce a wider melt pool than the uncorrected laser source, they do not reach the two adaptive corrections (0.25 and 0.5). The answer to this can be found in the graphs in figure 6.23 [right]. By correcting the laser penetration depth using formula 2.36 with different correction targets, very different penetration depths can be achieved.

The mean values of the laser penetration depth are also given in table 6.7. Here it can be seen that the depth correction with the intensity target of 0.75 with an average penetration depth of

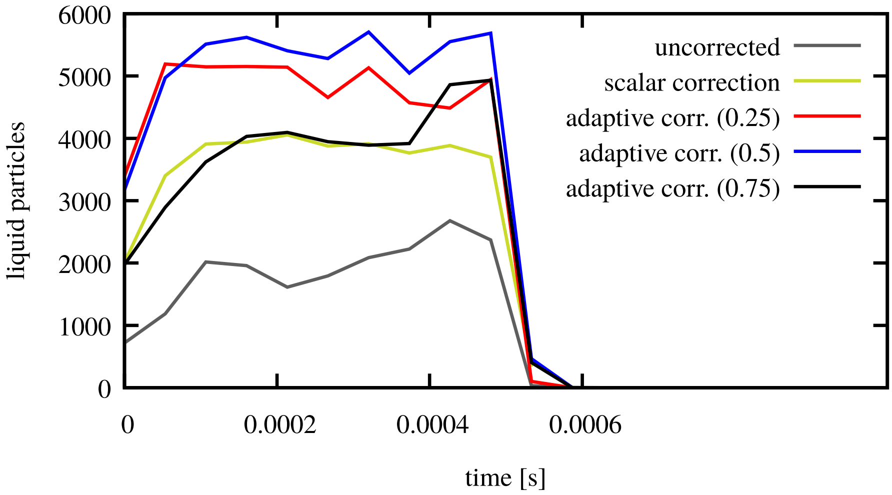

Figure 6.24. Graphs representing the number of liquid particles in the laser correction analysis over time (active laser time 0.53 ms).

36.4 μm hardly leads to a change of the penetration depth compared to the initial depth of 38 μm. This initial depth goes down to the substrate and distributes the heat to a large number of particles. With the intensity targets of 0.25 and 0.5, the mean penetration depth decreases to 19.8 and 11.3 μm, irradiating only half and one third of the powder bed, respectively. This more focused irradiation again significantly increases the number of molten particles. It is noticeable that the number of molten particles does not differ between the penetration depths of 19.8 and 11.3. Only the number of evaporated particles increases at the lowest penetration depth from 362 to 2001 particles. Here the penetration depth seems to make only a small difference. Whether this is due to the fact that convective heat dissipation takes place sufficiently quick or whether the majority of evaporating particles causes the additional heat to be dissipated faster is not clear at this point. What was visible in the calculations, however, is that with an intensity target of 0.25 the stability of the simulation is endangered and the simulations stop more often at higher laser powers. For this reason, the adaptive laser correction with an intensity target of 0.5 is used for the further simulations. Since the actual penetration depth is difficult to measure, the only way to fit this parameter would be to use ray tracing algorithm, similar to the study in KING ET AL. (2015b), to validate the heat distribution through the laser. Also a fitting based on analytical solutions for heat conduction and experiments based on thermal imaging could be a way to calibrate the laser heat input.

6.3 Physical phenomena

In this section the individual phenomena that are active in the liquid melt pool during the SLM process are considered. This separate consideration starts with the simplest representation of a viscous fluid under the influence of gravity and the temperature-based buoyancy and successively adds further models up to the final state of this work and examines the influences of the individual effects. The effects are ordered according to their complexity and the frequency of their occurrence in the literature. Finally, the additional heat losses due to

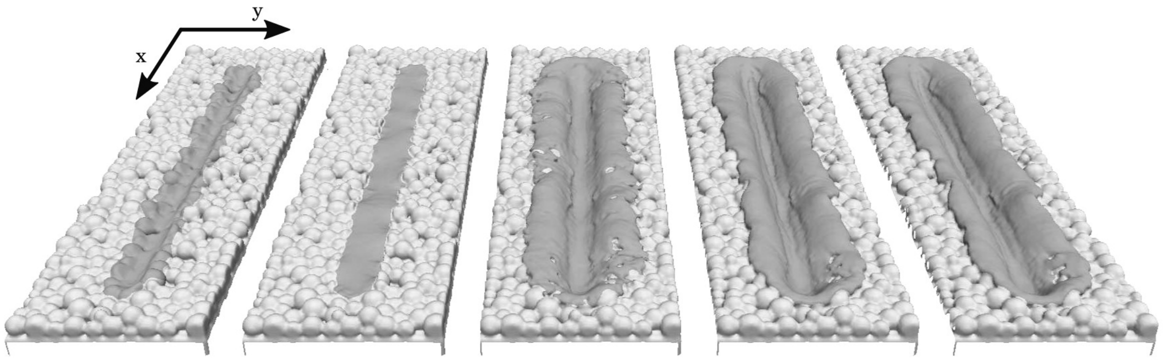

Figure 6.25. Representation of the final melt pool geometry of the phenomena study for temperature decreasing surface tension. From left to right: gravity and buoyancy, constant surface tension, Marangoni convection, recoil pressure and evaporative cooling, radiative and convective cooling.

radiation and convection are considered to show their magnitude compared to the energy loss due to evaporation. This results in the following order of phenomena in this study:

1. Gravity and temperature-based buoyancy force following equation (3.29),
2. Constant surface tension visualized in figure 2.2 [left],
3. Temperature-variable surface tension leading to the Marangoni convection represented in figure 2.2 [right],
4. Temperature dependent recoil pressure according to equation (2.31) together with the associated cooling effect from evaporation according to equation (2.38)
5. Including heat losses from radiation and convection.

Since in this section the energy input is corrected by the laser correction from section 6.2.3 (adaptive correction with intensity target 0.5), the absolute energy in the system is independent of the phenomena. Differences in the number of molten and vaporized particles result exclusively from the different distribution of the melt and heat dissipation.

In each of the following sections, the melt pool is first shown in side view, since the differences due to the increase in phenomena are on first sight visible on the surface of the melt pool. Further evaluations in comparative pictures with all simulations are shown at the end of this section.

1. Gravity and buoyancy

The first phenomenon presented in this study is gravity and thermal buoyancy (see figure 6.26). As a result, the melt pool becomes a pure viscous fluid which, when melted, moves downwards by gravity and possibly is mixed by the temperature-based buoyancy.

At first sight it is visible that under gravitational influence the majority of the melt pool section has hardly moved, although they have melted. This can be seen, as the original shape

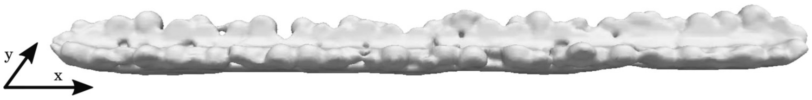

Figure 6.26. Side view of the melt pool under the influence of gravitational and buoyant forces according to equation 3.29.

Included models		No. molten particles		No. vaporized particles	
	1. Gravity	74,945	(100 %)	11,745	(100 %)
	2. Surface tension	77,979	(104 %)	7,342	(63 %)
temperature-decreasing surface tension	3. Marangoni Conv.	92,442	(123 %)	9,424	(80 %)
	4. Recoil pressure	99,006	(132 %)	9,085	(77 %)
	5. Additional cooling	98,968	(132 %)	9,109	(78 %)
temperature-increasing surface tension	3. Marangoni Conv.	96,807	(129 %)	5,484	(47 %)
	4. Recoil pressure	98,139	(131 %)	4,298	(37 %)
	5. Additional cooling	98,155	(131 %)	4,301	(37 %)

Table 6.8. Numbers of molten and vaporized particles during the phenomena analyses, comparing all five effects in the context of decreasing and increasing surface tension.

of the powder balls is still visible. Already in KHAIRALLAH & ANDERSON (2014) a comparison between the behavior of the melt pool under gravity and with surface tension was made, with very similar results. The only difference between the melt pool shown here and the results of Khairallah et al. is that in this work there is a distinct indentation in the middle of the melt pool. This results from the complete evaporation of the SPH particles at the moment when they have absorbed the complete evaporation energy. At this point, the particles are deleted in this work. Complete evaporation was considered neither in KHAIRALLAH & ANDERSON (2014) nor in KHAIRALLAH ET AL. (2016), so the comparison by Khairallah et al. shows deformed powder particles in the middle instead. The reason for the missing representation is probably that the mass of the particles cannot simply be deleted in mesh-based methods. Instead, a phase transition would have to occur, which is much more complex. A look at table 2.1 shows that the absolute number of molten particles under pure gravity is rather small compared to the other simulations, while the number of vaporized particles is the highest in all simulations. The reason for this is that the gravitational acceleration on the particles is very low, which is also shown in the order of magnitude analysis in section 2.5. Because of this low acceleration, the particles under the laser hardly move at all, so that particles located at the hottest points (in the middle on top of the powder particles) remain in the focus of the laser for a longer time until they vaporize. This causes the system to lose energy directly and the central area of the melt pool is completely vaporized.

2. Surface tension

The second phenomenon added onto the gravity is the surface tension (see figure 6.27). By adding a constant surface tension of 1.769 N/m^2 (maximum surface tension of S316L at the melting point), the melt pool becomes very flat. This type of behavior is observed in some publications, when the additional phenomena from this section are neglected (see e.g. KHAIRALLAH & ANDERSON (2014)).

Figure 6.27. Side view of the melt pool under the influence of gravitational, buoyant and surface tension forces.

With a look at the perspective view in figure 6.25 or at the height profile in figure 6.32, it becomes obvious that the pool is not totally flat but has some waves along the laser path which are pointing to unmolten powder spheres close to the sides of the melt pool. A behavior which was also exposed in KHAIRALLAH & ANDERSON (2014). Due to the undisturbed surface tension of the melt pool, an even surface forms very quickly under the laser. The rapid motion of the melt pool is also visible in figure 6.35 [top], where the velocity along the melt path of the molten particles is shown. The particles at the bottom of the bed that have recently melted move directly towards the melt pool as they are contracted by the surface tension force that minimizes the surface area. When comparing the melt pools in figure 6.35 it can be seen that the melt pool is the largest of all simulations, although the total amount of molten particles in table 2.1 is not the maximum. The reason for this is that the rapid movement of the freshly melted particles under the laser results in an even energy distribution between the particles, which also explains the lowest number of vaporized particles. Furthermore, the minimization of the surface area due to the constant surface tension leads to a minimization of the contact area with the surrounding powder. As a result, the heat in the melt pool is retained longer and the number of molten particles is the highest, which can also be seen in the graph in figure 6.33.

In summary, it can be said that the melt pool takes on a desirable shape when the surface tension is dominant. However, the heat is retained in the melt for a comparatively long time, which can have a negative effect on the process speed.

3. Marangoni convection

The third added phenomenon is the temperature dependent surface tension, which leads to Marangoni convection (see figure 6.28). In the work of ACHARYA ET AL. (2017) and HU & EBERHARD (2017) laser melting processes were also simulated with this combination of phenomena.

The material S316L according to WESSELS (2019) in this work has a surface tension decreasing with increasing temperature, shown in the material data given in appendix B. For the material, the surface tension decreases from the maximum value at the melting point (1.769 N/m) with constant slope (-0.89 $mN/(m \cdot K)$). Since there exist also materials, which have an increasing surface tension with increasing temperature, a second study is performed to show this effect too. In YADROITSEV (2008) the author gives as an example materials with sulfur content. In DUBBERSTEIN ET AL. (2015) a positive dependence of surface tension on temperature was measured for AISI 4142. In his thesis, YADROITSEV (2008) also names literature for materials that have both positive and negative dependencies

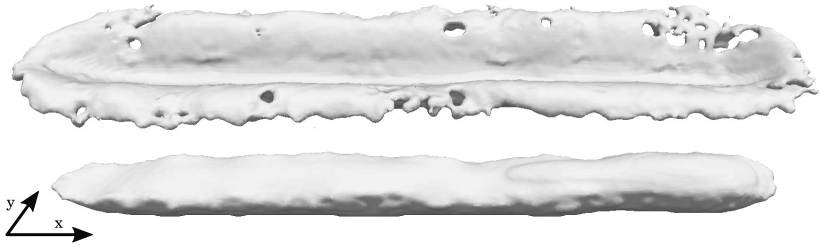

Figure 6.28. Side view of the melt pool under the influence of gravitational, buoyancy, surface tension and the Marangoni convection. Top: temperature decreasing surface tension; bottom: temperature increasing surface tension.

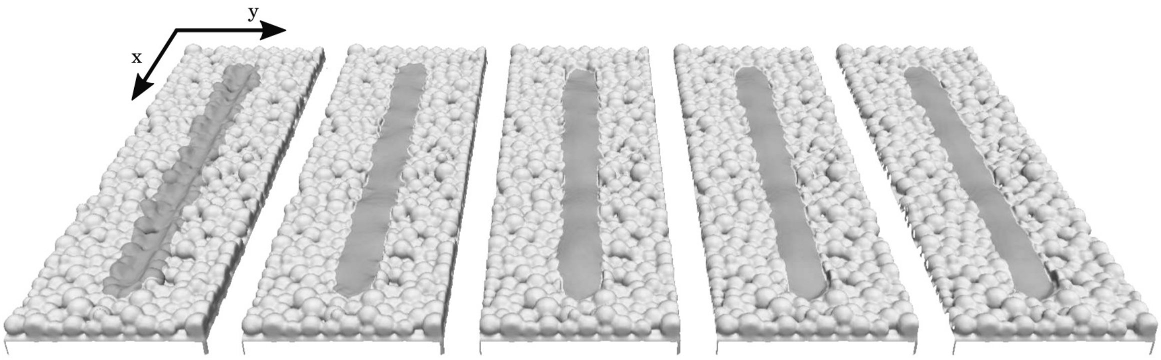

Figure 6.29. Representation of the final melt pool geometry of the phenomena study for temperature increasing surface tension. From left to right: gravity and buoyancy, constant surface tension, Marangoni convection, recoil pressure and evaporative cooling, radiative and convective cooling.

over different temperature ranges. The representation of such materials is also possible with the presented texture mapping (see section 4.2.2.)

In order to show the influence of surface tension increasing with increasing temperature, a simulation was carried out in which all parameters are identical except for the surface tension slope. The surface tension has its minimum value at the melting point (1.769 N/m^2) and increases with a constant gradient (0.89 $mN/(m^2 \cdot K)$).

When looking at the two solidified melt pools in figure 6.28, it can first be seen that the curvature of the melt pool surface increases due to the addition of Marangoni convection in both cases. With decreasing surface tension, the melt pool becomes arc shaped and the center of the melt sinks down to the substrate. With increasing surface tension the surface of the melt pool becomes slightly curved in comparison to constant surface tension. additionally a bump at the end zone of the laser track (right) becomes apparent. This results from the molten particles following the laser and solidifying when the laser is turned off.

For the decreasing surface tension the opening of the valley is an expected result. Similar processes are shown for example in KHAIRALLAH ET AL. (2016). However, it is unexpected that the valley does not close again after the laser passage. While in Khairallah et al. a reflux occurs after the laser passage, in the simulation shown the melt moves so far onto the unmelted powder material that it cools down and cannot flow back. The reasons for this deviation from the expected results can be various:

- The surface tension can be overestimated by SPH discretization. A common test to check the Marangoni force is not established yet,
- As found in section 6.2.1, the thermal conductivity of the powder has a great effect on the melt pool behavior. By lowering the thermal conductivity of the powder, the Marangoni convention is greatly reduced. As explained there, a thermal calibration of powder and melt could help to reduce the melt overflow.
- The treatment of melt and powder as one material in the single-phase approach used could be another reason for the deviation. By using a multi-phase approach with wetting mechanics, more complex interactions of the phases could be described as pointed out in section 2.1.3.

In figure 6.35 the fast propagation during the melting process can be recognized by high surface speeds. A wave of liquid material builds up in front and at the sides of the laser, which is visible in the velocity plots as surface velocities pointing away from the center of the laser. While in figure 6.33 a significant decrease in molten particles is visible over time, in table 6.8 it can be seen that the total number of molten particles increases by 20 %. The reason for this is that the molten particles come into contact with many solid powder particles at the edges of the melt pool. Some of these powder particles are melted by the contact, which causes the particles from the melt pool to lose energy and solidify faster.

For the increasing surface tension, the formation of a slight hill on the melt pool surface can be explained by the convection towards the hottest spots of the melt pool. In this simulation case, the laser speed is higher than the possible velocity of the melt surface. For this reason the melt generates a hill behind the hot spot. This hill follows the laser in this simulation with a velocity in x-direction of about 0.2 m/s as seen in figure 6.36 [top]. For the increasing surface tension, a higher number of vaporized particles is expected as the particles gather at the hot spot. A look at the particle numbers in the table 6.8 shows that the total number of molten particles is higher for increasing surface tension than for decreasing surface tension, while the number of vaporized particles is lower. This can be explained by mixing under the laser, as the particles from the sides of the hot spot that are constantly being added push the particles down, resulting in a more homogeneous distribution of heat. With respect to the graphs in figure 6.34 one can see that the Marangoni convection leads to a further increase of molten particles compared to the constant surface tension.

In summary, it is clear that the temperature-dependent surface tension has a decisive influence on the final melt contour. A major uncertainty in this consideration is the actual course of the surface tension as a function of temperature. The frequently used linear progression is only an extrapolation, since the surface tension can usually only be measured in a small temperature range above the melting point of the metal (see e.g. DUBBERSTEIN ET AL. (2015)). Also the modeling of melt and powder are a source of uncertainty here, leading to the overflow of the melt pool for the temperature decreasing surface tension.

4. Recoil pressure

The last key phenomenon is the recoil pressure. This phenomenon consists of two parts as described in sections 2.4.3 and 2.4.5. One is the pressure resulting from partial vaporization of the liquid matter and the resulting pressure rise at the surface. The other is the evaporative cooling which results from the partial vaporization of the high energetic portions of the material. The melt pools resulting from the combination of gravity, surface tension, Marangoni convection and recoil pressure can be seen in figure 6.30. Simulations of laser or electron beam melting processes with similar combinations can be found for example in the work of KHAIRALLAH ET AL. (2016), LEE & ZHANG (2016) or KLASSEN (2018).

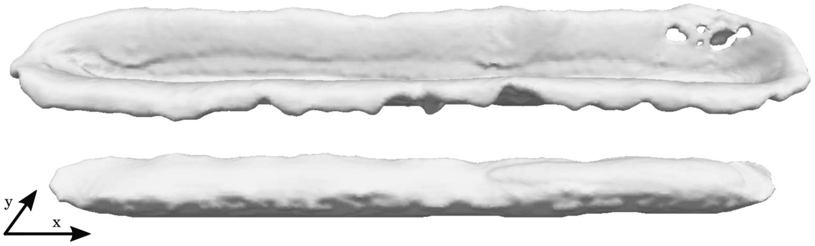

Figure 6.30. Side view of the melt pool under the influence of gravitational, buoyancy and surface tension forces, the Marangoni convection and the recoil pressure. Top: temperature decreasing surface tension; bottom: temperature increasing surface tension.

Again the analysis of the phenomenon of recoil pressure starts with the final melt pool surfaces in figure 6.30. For the decreasing surface tension, the comparison with the melt pool under the influence of Marangoni convection first of all shows, that more particles are moved to the sides of the melt pool. This results form the recoil pressure accelerating even more particles from the laser heat source to the sides, due to the shape of the melt indentation. In the direct comparison in figure 6.32 this effect is visible even better, in form of a more continuous overflow pattern to the sides of the melt pool. With a look at the velocity plots in figure 6.35, the recoil pressure slightly increases the flow in negative x-direction, flowing away from the laser heat source. As a result of the activated recoil pressure, the size of the molten material is slightly reduced compared to pure Marangoni convection. Lastly, the valley in figure 6.25 becomes a little deeper and more pointed. In this study, the effect of the evaporative cooling is rather low when looking at the temporal progression of the molten particles in figure 6.33. Since the evaporative cooling mainly takes place in areas with the highest energy content, the evaporative cooling is expected to reduce the vaporization. A slight reduction of vaporized particles is visible in table 6.8 but this is less conspicuous than then increase of the total number of molten particles by about 9 %. A possible reason for this is the smoothing of the melt pool resulting from the recoil pressure, resulting in a reduced distribution of the heat by the moving melt.

For the increasing surface tension a smoothing of the melt pool is visible in figure 6.29. In figure 6.32 the effect is visible more clearly. The recoil pressure smooths the sink at the laser start point and the hill at the laser end point. In contrast, the number of molten particles increases over time (see figure 6.34). This is accompanied by a slight increase in molten particles and a decrease in vaporized particles of 10 % compared to Marangoni convection (see

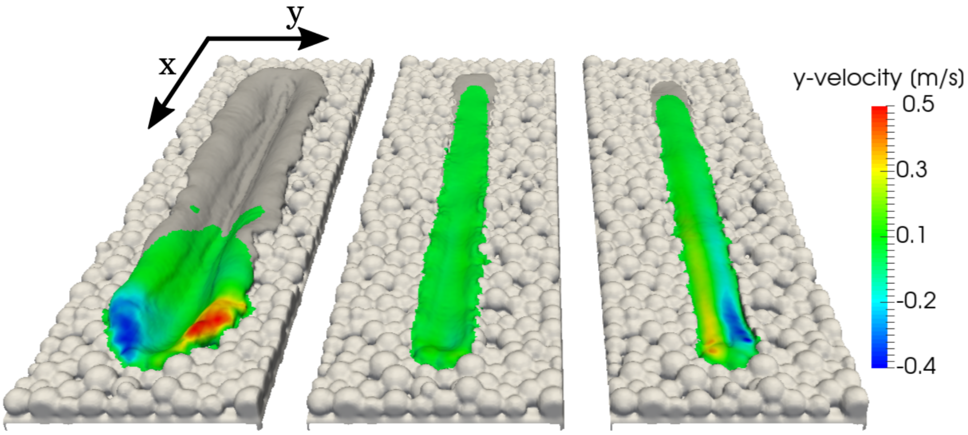

Figure 6.31. Melt track at the end of the laser path during the phenomena study. Solidified areas are colored in dark gray and liquid areas are colored with their velocity. Simulations under surface tension and recoil pressure; from left to right: temperature decreasing surface tension, constant surface tension, temperature increasing surface tension.

table 6.8). The conclusion is obvious that evaporative cooling is more efficient in preventing the complete evaporation of the particles, than having an effect on the number of molten particles. Furthermore, the recoil pressure, which is the strongest under the laser, seems to support the mixing by Marangoni convection in the case of temperature increasing surface tension.

Overall, the effect of the recoil pressure on the melt pool seems to be rather small even at this increased laser power (of 600 W). An effect that often occurs in reality, the formation of spattered particles that are accelerated from the melt pool, only appears to a very small extent in the simulations, and the particles lost in this way remain far behind the vaporized ones. The question arises whether the actual vaporization of particles is a useful effect here or whether this effect is unphysical and artificially reduces the actual effect of the recoil pressure. Also the artificially increased viscosity has an effect on the formation of spatter particles as shown in section 6.1.3. However, further studies are needed to classify this deviation.

Finally, figure 6.31 shows a comparison of the effect of surface tension and recoil pressure. In the perspective view, the lateral velocity of [from left to right] decreasing, constant and increasing surface tension under recoil pressure are displayed. It can be seen that even without Marangoni convection only a small deformation of the melt pool occurs at the edges and the surface velocity is significantly lower than in the cases with Marangoni convection.

5. Radiative and convective cooling

The last two phenomena added in this section are the radiative and convective cooling. As described in section 2.4.5 the energy losses of these phenomena are at least 2 orders of magnitude lower than the evaporative cooling. For this reason their influence on the SLM process were tested. In the simulations it was found that not only the resulting melt pools appear exactly as the melt pools from the recoil pressure simulations (see figures 6.25 and 6.29). Also

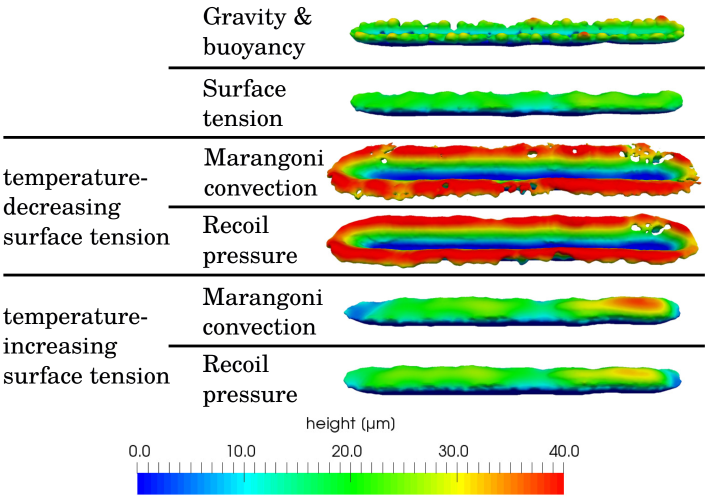
Gravity &
buoyancy
Surface
tension
temperature-
decreasing
surface tension
Marangoni
convection
Recoil
pressure
temperature-
increasing
surface tension
Marangoni
convection
Recoil
pressure
height (μm)
0.0
10.0
20.0
30.0
40.0

Figure 6.32. Side view of the solidfied melt pools from the phenomena study, colored with height above substrate.

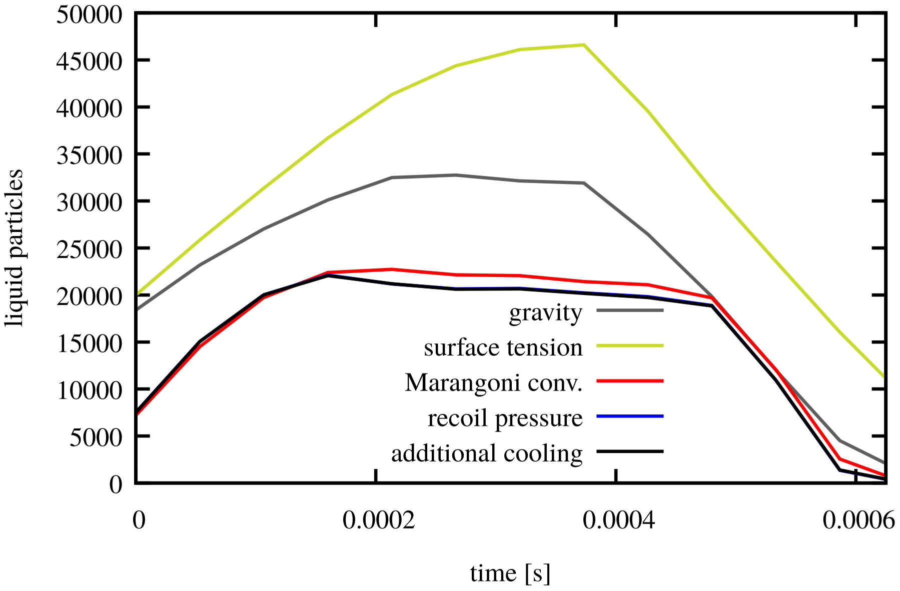

Figure 6.33. Plot of the molten particles over time for the decreasing surface tension phenomena series.

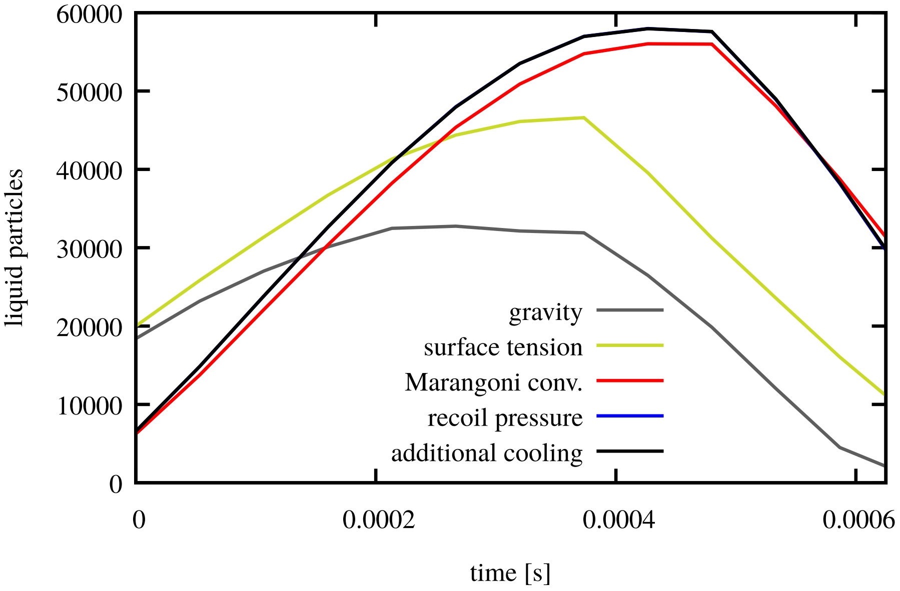

Figure 6.34. Plot of the molten particles over time for the increasing surface tension phenomena series.

the numbers of molten particles, in table 6.8 only differ by the last 2 digits. For this reason the influence of the radiative and convective cooling seems negligible compared to the evaporative cooling and the conductivity of the melt pool. This observation is supported by GUSAROV ET AL. (2009) and KHAIRALLAH ET AL. (2016).

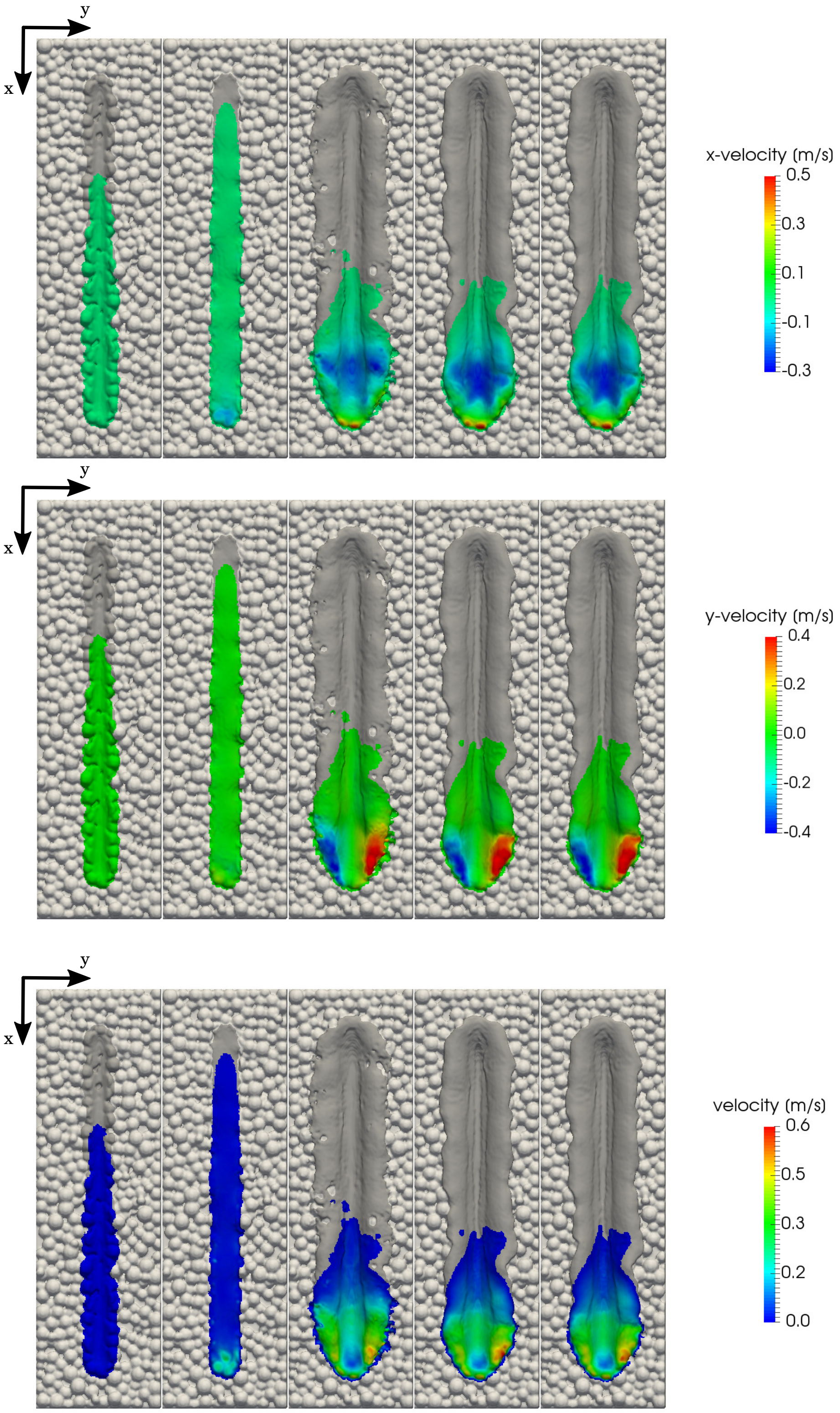
y
x
x-velocity (m/s)
0.5
0.3
0.1
-0.1
-0.3
y
x
y-velocity (m/s)
0.4
0.2
0.0
-0.2
-0.4
y
x
velocity (m/s)
0.6
0.5
0.3
0.2
0.0

Figure 6.35. Representation of the melt track at the end of the laser path for the decreasing surface tension phenomena series. Solidified areas are colored in darker gray and liquid areas are colored with their velocity. From left to right: gravity and buoyancy, constant surface tension, Marangoni convection, recoil pressure and evaporative cooling, radiative and convective cooling.

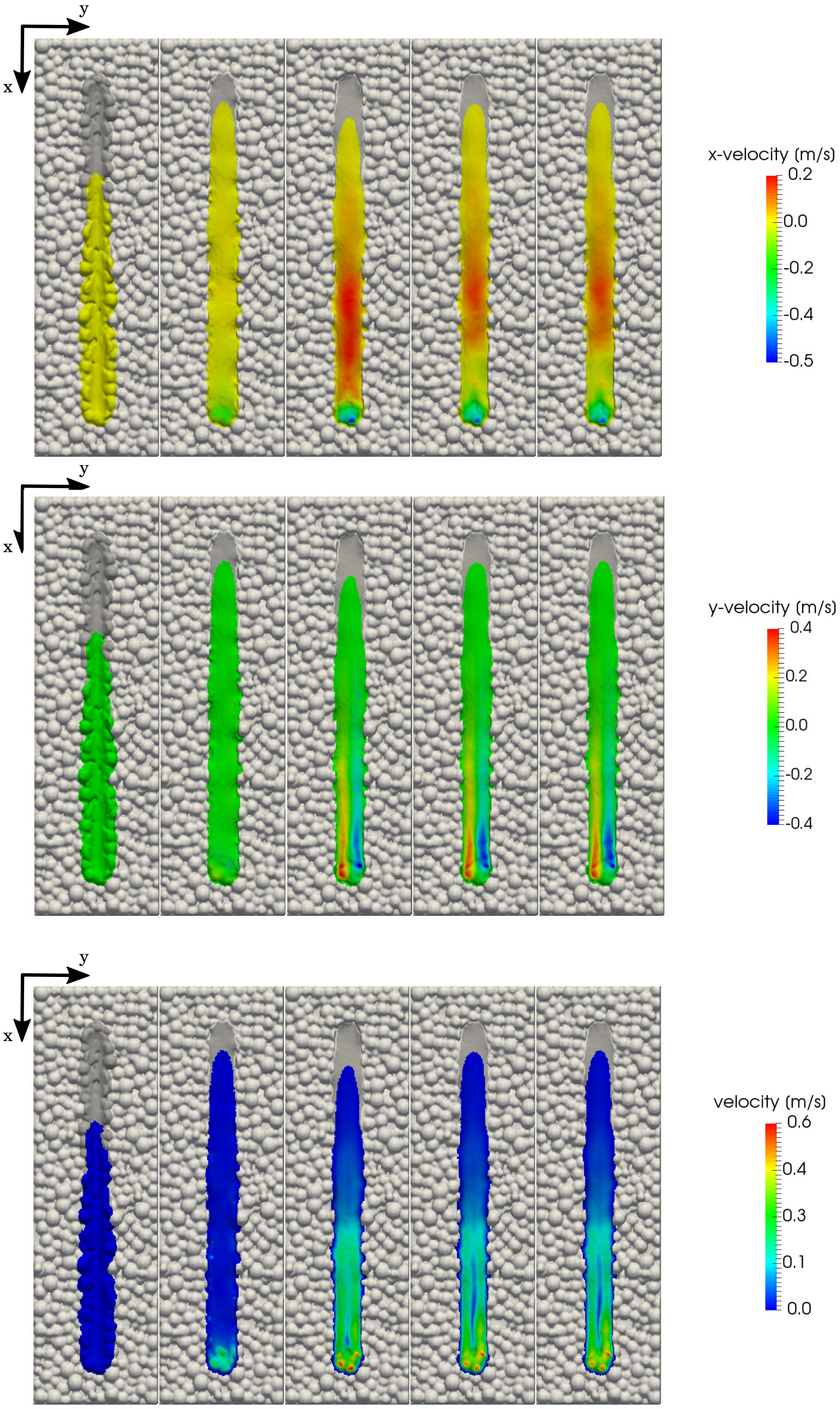
y
x
x-velocity (m/s)
0.2
0.0
-0.2
-0.4
-0.5
y
x
y-velocity (m/s)
0.4
0.2
0.0
-0.2
-0.4
y
x
velocity (m/s)
0.6
0.4
0.3
0.1
0.0

Figure 6.36. Representation of the melt track at the end of the laser path for the increasing surface tension phenomena series. Solidified areas are colored in darker gray and liquid areas are colored with their velocity. From left to right: gravity and buoyancy, constant surface tension, Marangoni convection, recoil pressure and evaporative cooling, radiative and convective cooling.

6.4 Validation / Simulation Series

In this last section two things are to be presented:

- On the one hand, the melt pool behavior is to be compared with experimental results to validate the underlying algorithm.
- On the other hand, ways to use simulation to optimize the SLM process and to save time consuming experiments are to be highlighted.

The publication of TENG ET AL. (2017) is used as a validation case. In contrast to the validation case from FÜRSTENAU ET AL. (2020b), the single track experiments of YADROITSEV ET AL. (2010), the experiments of Teng et al. represent a recent process area with respect to laser power and laser speed. In FÜRSTENAU ET AL. (2020b) the focus was on validation results where no influence of recoil pressure is to be expected, therefore a test case with low energy density E_V was explicitly used. Here the focus is on the representability of state-of-the-art process parameters where recoil pressure cannot be avoided. Unfortunately, no publication could be found in this context that provides sufficient experimental results on S316L, therefore another material was used for this comparison: a chromium-cobalt alloy. This alloy is often used for dental prosthetics. The data for the alloy can be found in table 6.2. Please note that a constant value is given for both thermal conductivity and heat capacity, which applies to the entire material. In TENG ET AL. (2017) two absorption values were given for the powder and the melt pool (0.74 (powder) / 0.4 (pool)). Since in this work the absorptivity is implemented as a laser property, a common value had to be found. By fitting of the melt pool width for the combination of 330 W laser power and 1.6 m/s laser speed, an absorptivity of 0.67 was selected. This value is equal to the modeling of TENG ET AL. (2017) if 80 $\%$ of the material below the laser consists of unmolten powder. Due to the differences in laser modeling and physics this simple fit seems legit. The absorptivity was fitted together with the laser spot diameter, which was not given in the publication. A diameter of 100 μm showed good agreement together with the chosen absorptivity. Furthermore, the publication did not apply surface tension or recoil pressure, which is why the data on molar mass and surface tension are missing. For the molar mass the value of a pure CrCo molecule was used. In a short test it was also shown that the molar mass, which is almost twice as high as for S316L, has only a small influence on the melt pool contour. The lack of information about surface tension is a major problem, because this effect is very important, as described in section 2.1. Since neither constant nor temperature-dependent surface tension parameters could be found, a substitute value had to be used. It turned out that besides S316L also AISI 4140/4142 steels belong to the more frequently used materials in additive manufacturing. In contrast to S316L these steels have a surface tension that increases with temperature, which lead to the domed single tracks observed in TENG ET AL. (2017) and avoids the seemingly overestimated Marangoni convection for S316L from section 2.1. Since this temperature dependent surface tension is documented in detail in DUBBERSTEIN ET AL. (2015), a linear relationship could be extrapolated from this as for S316L. This can be found in appendix B. For validation in TENG ET AL. (2017) results for 5 laser speeds and 4 laser powers are presented. For all 20 experiments sectional images are shown in the publication, which were measured and compared with simulated results of Teng et al. The melt pools in figure 6.43

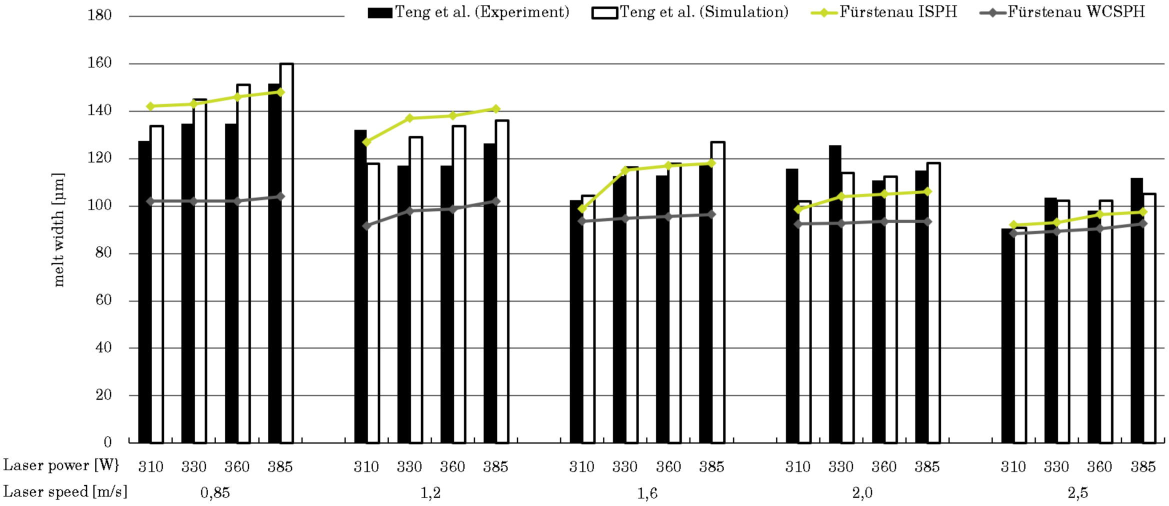

Figure 6.37. Graphs of the melt pool width from the validation case. Results consisting of experimental and simulative results of TENG ET AL. (2017) and own results simulated with ISPH and WCSPH approach.

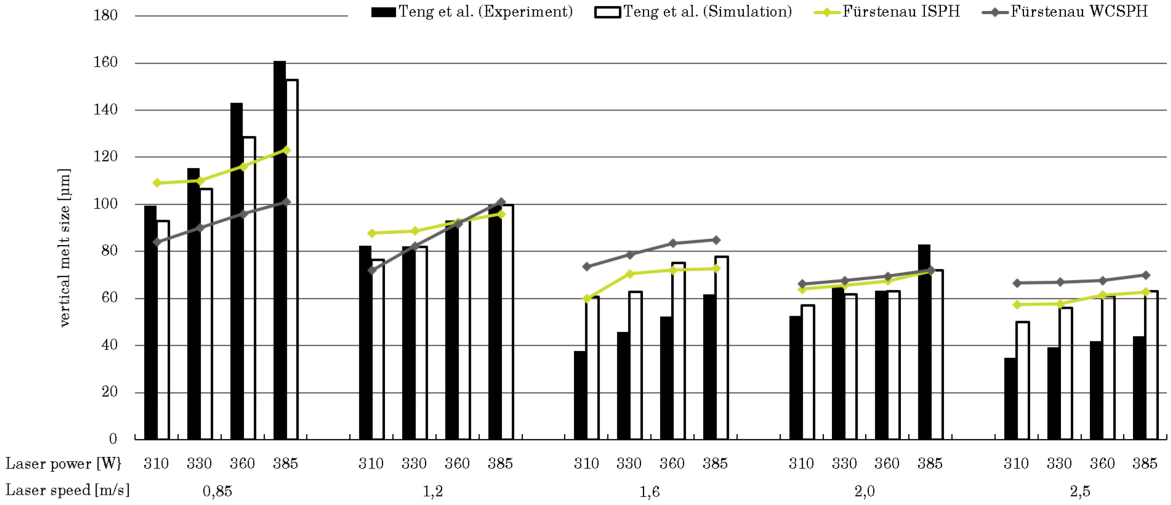

Figure 6.38. Graphs of the vertical melt pool size from the validation case. Results consisting of experimental and simulative results of TENG ET AL. (2017) and own results simulated with ISPH and WCSPH approach.

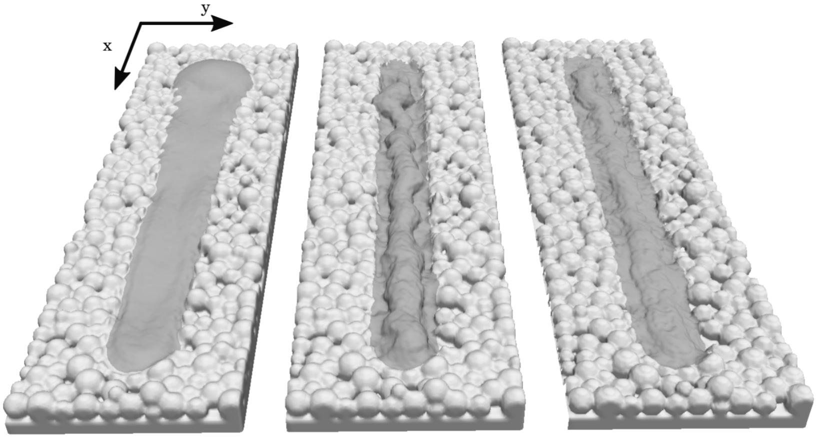

Figure 6.39. Comparison of the final melt pool geometries for the validation case with 330 W laser power and 1.6 m/s laser speed. From Left to right: ISPH approach, WCSPH approach, 'mixed WCSPH' approach from section 6.1.2. The simulation times for the case were: ISPH: 5.7 h; WCSPH: 8.8 h; 'mixed WCSPH': 24.4 h.

show that a wide range of melt pool depths and widths were achieved, covering almost the complete process spectrum. More details on this spectrum can be found in the progress of this section. To validate the simulated results, all 20 experiments were re-simulated with the ISPH and WCSPH approach. The WCSPH approach did not use the mixed smoothing length from section 6.1.2. The reason for this is that the 'mixed WCSPH' approach leads to significantly higher computational effort and the stabilizing effect was also significantly lower than observed in section 6.1.2. A comparative test between the ISPH approach, the WCSPH approach and the 'mixed WCSPH' approach for the used parameters can be found in figure 6.39. While the ISPH approach needed 6.4 h to compute the case (330 W, 1.6 m/s), the WCSPH approach with constant smoothing length needed 8.8 h and the 'mixed WCSPH' approach 24.4 h.

The melt pool width and the melt pool depth are used as comparative values. In this work the term depth is used differently from TENG ET AL. (2017). While Teng et al. use the melt pool depth to describe the distance between the highest point of the melt pool and the lowest melted point in the substrate, in this work the depth describes the distance of the lowest point to the zero line of the substrate and the height the highest elevation above the zero line. In experiments this line is often not clearly recognizable and is therefore not evaluated separately. To avoid confusion, the distance between the highest and lowest point is referred to here as the vertical melt size.

When comparing the melt width and the vertical melt size, the graphs in figures 6.37 and 6.38 show four series of measurements plotted against laser power and laser speed: the experimental measurements and simulated results according to TENG ET AL. (2017) and the results of the ISPH and WCSPH simulation. Additionally, the simulated contours of the melt pool can be seen in figure 6.43.

The comparative consideration of the melt pool width in figure 6.37 shows a good agreement between the experimental and simulative results of Teng et al. and the results calculated in this thesis. Especially the ISPH results in the range of 1.6 to 2.5 m/s show very small deviations. However, it is noticeable that the measured values show some outliers here. Teng et al. also emphasize this in their publication and justify it with high deviations in the experimental single tracks, which makes averaging over several microsgraphs necessary. However, it was not possible to make more microsgraphs because the resulting effort per graph is high. In all areas except for the measurements below 0.85 m/s an identical course of the ISPH approach can be seen as in the simulated results of Teng et al. At the lowest speed the tendency of the simulations is significantly lower. The reason for this was found in the fact that at this speed the melt pool depth drops from 80 μm at 310 W to 105 μm at 385 W (see figure 6.40). At a substrate depth of 130 μm, the increased heat dissipation due to a too low substrate depth from section 6.2.2 becomes apparent here. Since these simulations were already among the most computationally expensive (longest simulated time and highest amount of molten particles) and the increase of the substrate depth further increases the computing time, a repetition of these simulations was omitted. The results of the WCSPH approach show everywhere larger deviations but for 2.5 m/s. On the one hand, the tendencies with increasing laser power are clearly underestimated by this approach as well as the increase of the melt pool width by reducing the laser speed. The reason for this is the unstable behavior of the WCSPH melt pool under positive surface tension. While the ISPH approach produces a uniform smooth melt, the WCSPH approach produces unstable distortions on the surface due to the paring instability. These are shown in the sections in figure 6.43 and on the sample surface in figure 6.39. This leads to increased evaporation of particles as seen in figure 6.41. The increase evaporation results in a higher energy loss and thus to a lower molten mass. This effect increases with increasing energy density E_V, i.e. with increasing laser power or decreasing laser speed.

The vertical melt size shows a slightly different picture. Here, larger deviations between the simulations and experimental results (also those of Teng et al.) are shown. While in the range of 1.6 to 2.5 m/s the ISPH results agree very well with the simulated results of Teng et al. the experimental results show a volatile behavior in absolute heights as well as in the tendencies over the laser power. Again, the ISPH results show a better overall agreement than the WCSPH results. Only at 0.85 m/s the deviation is larger again due to the missing substrate depth. The increasing deviation of the WCSPH approach with increasing energy input, which was found for the melt pool width, is not so noticeable here, since the vertical melt size at 1.6 to 2.5 m/s is initially overestimated. Only at 0.85 and 1.2 m/s, when the noted evaporation comes into play, increased deviation is occurring again. The reason for the initial overestimation is currently unknown. Based on a sensitivity study in TENG ET AL. (2016) suggest that the deviations in vertical melt size happen due to the laser penetration depth. These and the latent heat were tuned in TENG ET AL. (2017) to fit the results.

In summary, it could be shown that the melt pool behavior as well as the tendencies due to changes in laser power and speed can be represented within a similar tolerance frame as the simulated results of TENG ET AL. (2017). It should also be noted that the results of TENG ET AL. (2017) are preceded by extensive preliminary studies. The most influential factors identified were the ratio of thermal conductivity between powder and solid, the powder packing density, the melting temperature with latent heat and the laser penetration depth. These parameters were calibrated for CoCr and the results of the sensitivity study were summarized in TENG ET AL. (2016).

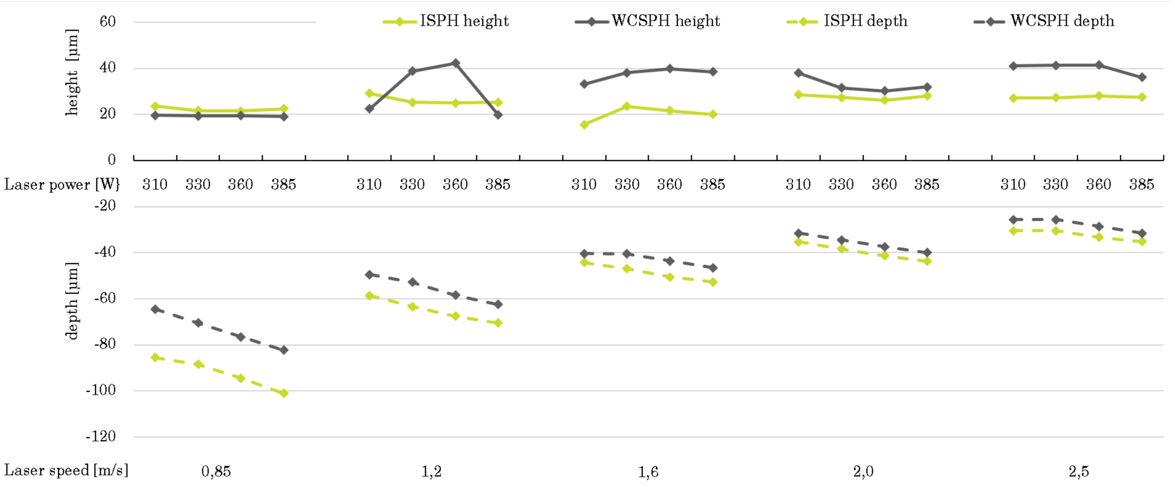

Figure 6.40. Graphs showing the melt depth and height from the validation case according to TENG ET AL. (2017).

In the further course of this section further evaluation possibilities are presented, which are based on the validation simulation series. For this purpose it is helpful to remember the aims of optimizing the SLM process:

- melting of the desired layer thickness and width,
- production of an even and dense layer,
- production of a good connection to the lower layers via the melt depth,
- generation of a flat surface and straight melt pool edges to reduce the need for post-treatment,
- avoid unnecessary evaporation to increase energy efficiency and reduce spatter and porosity,
- achieving a uniform cooling process.

Based on these diverse and difficult-to-measure boundary conditions, it is possible to create process maps for certain parameter combinations, e.g. powder material, grain size, layer thickness and process temperature. This allows to select useful parameter combinations of laser speed and power for the single track, which form a so-called process window. For two-dimensional prints the so-called hatch spacing has to be considered, which defines the distance between two laser tracks to create a continuous surface. There are several definitions and limitations for the process windows in the literature, which are briefly outlined below.
A rough limitation is given in YADROITSEV (2008). Roughly incorrect process parameters in the SLM process result in superficially visible errors. On the one hand, the balling effect for very low energy densities E_V, which leads to partial melting and ball formation on the powder bed without connection to the substrate. On the other hand there is the track distortion, which results from very high energy densities and leads to high spattering rates. These

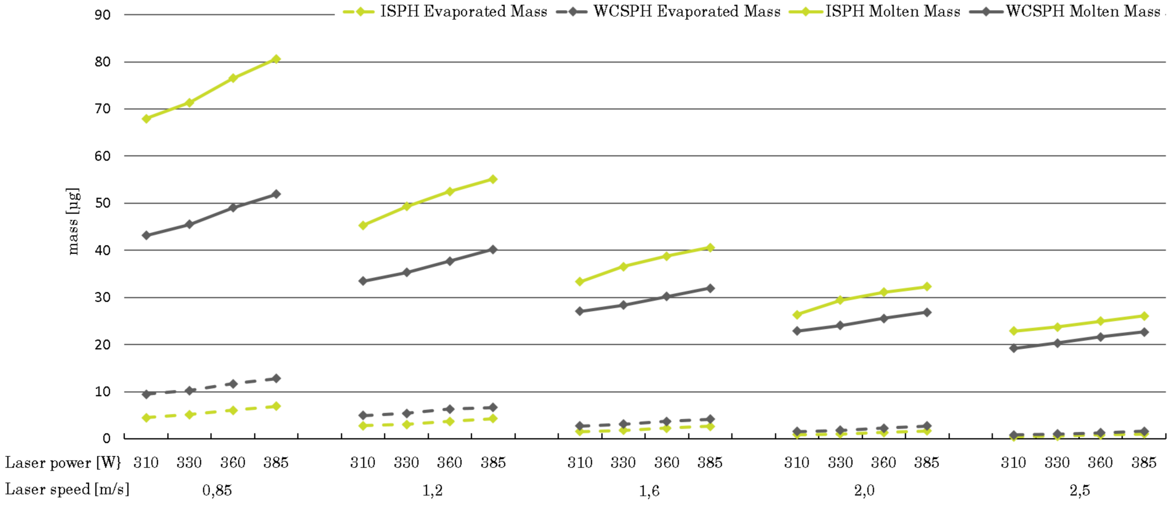

Figure 6.41. Graphs showing the molten and vaporized masses from the validation case according to TENG ET AL. (2017).

spatters and the triggering effect of recoil pressure leads to high material and energy losses in the melt pool and thus to uneven and therefore unusable melt tracks. These limitations are very rough, because poor melting tracks are also created in between these boundaries, which are not distinguishable from the outside. These poor melt tracks appear either in high or low melt depths, which are documented in SEEDE ET AL. (2020). Too low energy densities result in a low melting depth, which compromises the connection to the underlying layers and thus weakens the component. Too high energy densities result in excessive melt depths. They are an indication of increased recoil effects. These cause the melt pool to undergo large movements (similar to those in section 2.1), which promote the formation of entrapped gas bubbles and pores, when the reflux closes the melt valley again. These two types of melt pools are rightly pointed out as unusable in SEEDE ET AL. (2020), while the surfaces of such melt pools are inconspicuous. The only way to identify these defects is to take cross-sections, perform stress tests or density measurements.

There are various opinions in the literature on the identification of process windows, which certainly also differ due to the use of different powders and other process parameters. KING ET AL. (2015b) describes the optimal process as the region in which the melt pool depth is comparable with the layer thickness of the new layer. For SEEDE ET AL. (2020) this range already belongs to scrap. Overall, Seede et al. establish a very defined process window. The upper one towards too high energy densities is defined by:

$$\text{Melt pool depth} \geq \frac{\text{melt pool width}}{2.2}, \tag{6.2}$$

as from this value increased pore formation due to keyholing / recoil pressure can be expected. The lower limit towards too low energy densities is defined as:

$$\text{Melt pool depth} \leq \text{layer height}, \tag{6.3}$$

as from this point in time a lack of fusion with the substrate is to be expected. This lower limit value would represent the optimum operating point for King et al. Instead, Seede et al.

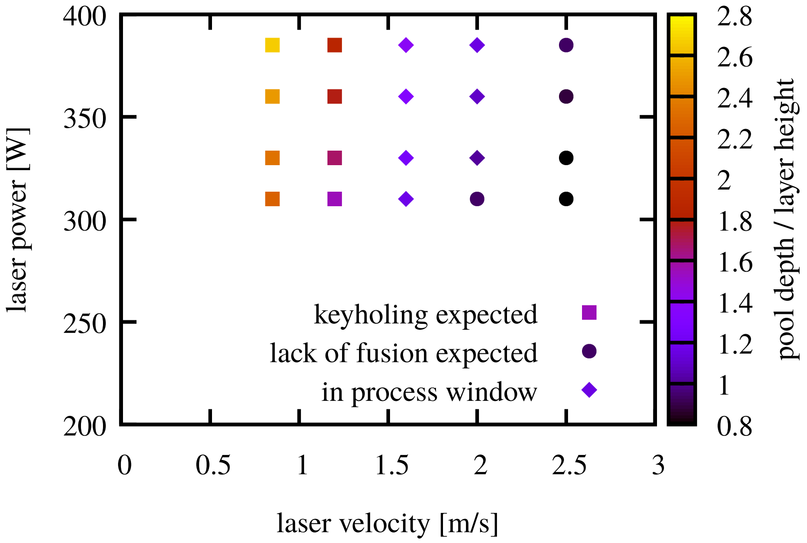

Figure 6.42. Process map derived from the simulative results from the validation simulation series. For the process map the ISPH results are used.

define the optimal operating point as

$$\text{Melt pool depth} = 1.5x \text{ layer height.} \tag{6.4}$$

The values simulated with the ISPH method were used to generate such a process map. The melt pool depths are shown in figure 6.40 and the derived process map in figure 6.42. Since the generation of the necessary measured values for such a process map is only possible by the complex production of micrographs, it is advisable to first carry out simulations for new process points. Of course this requires a well calibrated model.

Another question that arises when operating an SLM system is energy efficiency. Since only the energy used to melt the powder can be used, the observation of energy losses can be of interest. Since evaporation and spattering can draw large amounts of mass and energy from the melt pool, the simulation offers the possibility to observe the mass of molten, evaporated, and spatter particles. In figure 6.41 this was done for the molten and evaporated masses. Here it can be seen that the evaporated mass for which the velocities of 1.2 and 0.85 m/s are significantly increased, which potentially reduces the useable energy and thus the mass of molten particles. One aspect that was not dealt with in the simulations is the heating of the build chamber (here: T_0 =300 K), which should be mentioned in connection with energy efficiency. Although heating and tempering the build chamber results in additional energy consumption, the heating of the particles can reduce the required laser power and can thus improve the melt quality (in terms of shape, depth and inner structure). This is possible because with reduced laser power, local overheating is prevented. This causes the extensive recoil pressure and thus spatter and evaporation. For further test tests heating should be taken into consideration as it is state of the art.

In summary, it could be shown in this section that the simulations performed in this thesis can provide correct trends and acceptable errors for the process of SLM. In addition, possibilities were shown how information can be obtained from the simulations which cannot be generated with experimental methods or which can be generated with great effort. Beyond these results, the underlying calculations could be performed in relatively short computation times from 3.5 to 11.3 hours with the ISPH and from 5.6 to 17.7 hours with the WCSPH approach on a desktop computer with an average consumer graphics card (NVIDIA GTX 1660 Ti). Additional data on the simulations can be found in tabular form in appendix C.

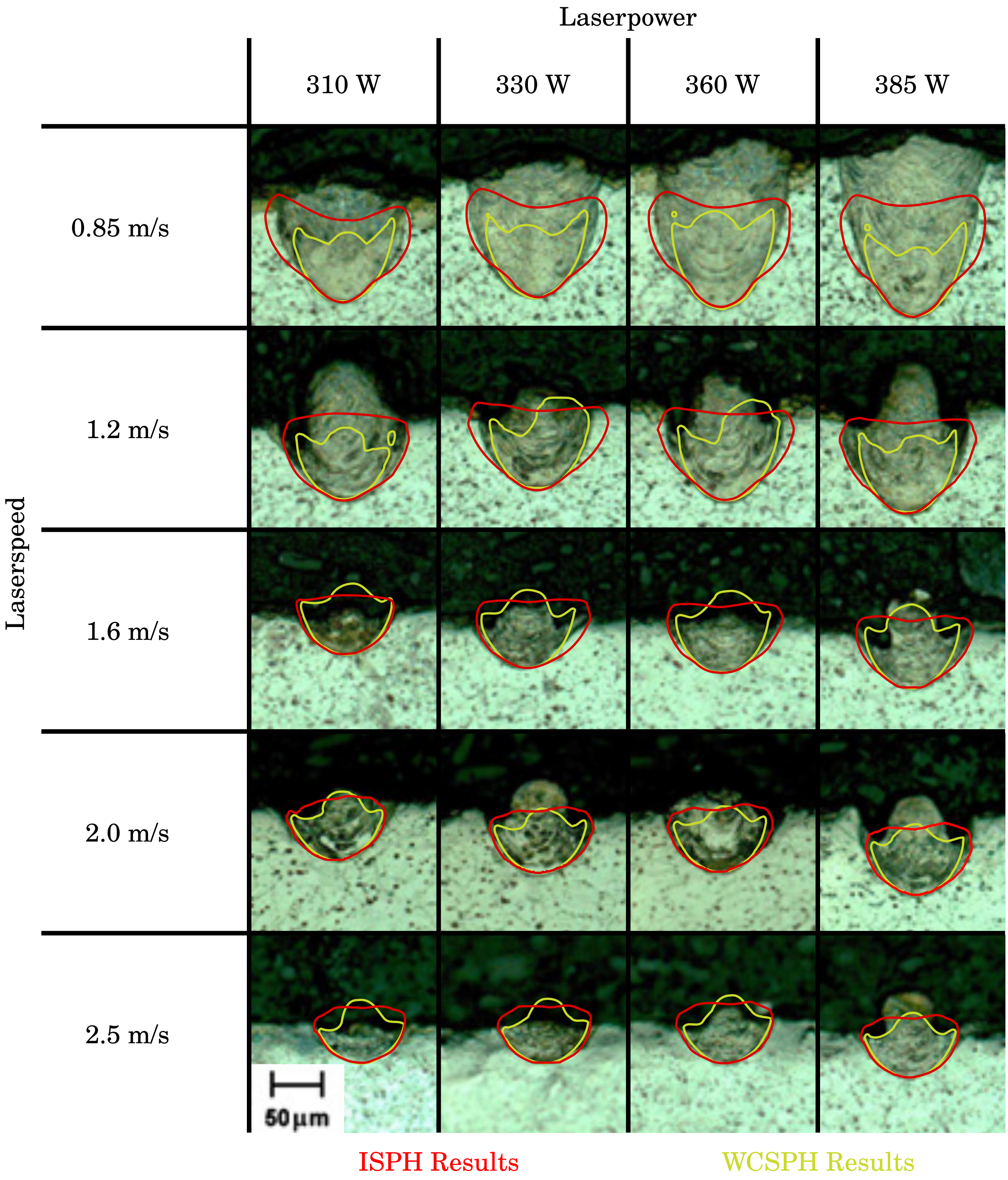
Laserpower
310 W
330 W
360 W
385 W
Laserspeed
0.85 m/s
1.2 m/s
1.6 m/s
2.0 m/s
2.5 m/s
50µm
ISPH Results
WCSPH Results

Figure 6.43. Tabular compilation of experimental melt pool slices from the validation examples by TENG ET AL. (2017). The green melt pool geometries are simulated with the WCSPH approach and the red ones with the ISPH approach. The simulated melt pools are always oriented at the experimental melt pool ground for clarity.

Chapter 7

Conclusions

In this thesis the incompressible SPH approach (ISPH) and to some extent the weakly compressible SPH approach (WCSPH) could be successfully applied to the simulation of the melt pool dynamics of the selective laser melting (SLM) process. For these simulations it is advantageous that the SPH method, in a pseudo single phase approach, does not require the surrounding gas above the powder bed or the solid phase to be represented mechanically. This saves a large part of the simulation effort compared to Eulerian or arbitrary Lagragian Eulearian (ALE) methods. The application of the ISPH approach in this thesis is one of the first applications to address three-dimensional, non-academic problems. Due to the complex physical processes, the application of the ISPH approach has not only a qualitative but also a computational advantage over the WCSPH approach in terms of performance. This is because the additional physical models require various additional loops that increase the computational effort per time step. Because the ISPH approach allows for a time step that is at least three times larger than the WCSPH time step, this results in a performance advantage (as observed in the carried out simulations). Furthermore, the ISPH approach does not cause any pairing instabilities that could not be eliminated for the WCSPH approach here and that other authors (e.g. RUSSELL ET AL. (2018)) eliminate by accepting significantly smaller time steps and thus higher computation times. With the following phenomena, the most important physical influences on the melt pool seem to be reproduced, so that this approach corresponds to the state of the art at the modeling level (see e.g. COOK & MURPHY (2019)):

- controlled energy absorption by depth-adaptive, volumetric laser heat source,
- consideration of latent heat with internal energy as primary variable,
- representation of the heat losses due to heat conduction, evaporation, convection and radiation,
- modeling of temperature dependent thermal conductivity and heat capacity for powder and melt,
- stable representation of high surface tension with temperature dependent Marangoni convection,

- depiction of partial and complete evaporation with resulting recoil pressure, mass and energy loss.

For the discretization of the SLM process with WCSPH and ISPH, new models for the evaluation of the curvature (see section 3.2.2) and for the realization of the pressure boundary condition in ISPH were developed (see section 3.2.4). These models were published in FÜRSTENAU ET AL. (2020b) and FÜRSTENAU ET AL. (2020a) and are discussed in this thesis. Additionally, a depth-adaptive correction of the laser heat source was applied and tested in this work (see sections 2.4.4 and 6.2.3), which has not yet been published elsewhere.

The first step on the way to this thesis was the examination of the incompressible SPH approach and the development of an own implementation (FÜRSTENAU ET AL. (2016)) based on the weakly compressible DualSPHysics framework (CRESPO ET AL. (2015)). The equation solver was first implemented on CPU (FÜRSTENAU ET AL. (2017)) and was gradually extended from a direct to an iterative equation solver until it finally came to its current form with an iterative, GPU-parallelized equation solver from the PARALUTION library (LUKARSKI & TROST (2014)).

The gradient correction plays an important role in the solution of the pressure Poisson equation in order to obtain stable and at the same time reliable results. For this reason the influence of correction techniques in the SPH method was worked out and compared, what was shown in FÜRSTENAU ET AL. (2018) using a simple thermal example. The results are part of the ISPH approach and the applied model of the surface tension.

The treatment of surface tension on free surfaces in an ISPH framework is still a challenge today. Important publications on this topic are HIRSCHLER ET AL. (2016) or NAIR & TOMAR (2014). While the approach according to Nair et al. has not been tested, the approach of Hirschler et al. showed unstable results in the formulation of the SLM process, which often caused the calculations to be aborted. For this reason, an own description of the surface tension was developed for the ISPH method, which was compared in FÜRSTENAU ET AL. (2020a) with the method according to HIRSCHLER ET AL. (2016). This method showed stable and consistent results. With this method, the complete SLM process with surface tension, Marangoni convection and recoil pressure could be modeled with ISPH.

The possibilities of simulating the SLM process in a WCSPH framework were shown in FÜRSTENAU ET AL. (2020b). While some elements of this thesis are missing in the publication, e.g. the recoil pressure and the laser correction, it was shown that the advantages of the Lagrangian SPH method described at the beginning of this section allow for simulations of the SLM process at comparatively low computation times. This makes the method suitable for simulation series in order to create virtual process maps or to carry out optimizations and predictions on the quality of melt tracks.

In the first stage of the performed SLM simulations, the main sources of uncertainty on the fluid-dynamic side (6.1) and on the thermal side (see section 6.2) were identified and answered as far as possible. However, some of the modeling issues and uncertainties, such as the pairing instability for the WCSPH approach, could not be solved conclusively here and require further investigations. Nevertheless, the preferred ISPH approach works without obvious instabilities with all tested process parameters and this in about 63 % simulation time of the WCSPH approach (see appendix C). Also some parameters and modeling approaches, e.g. the thermal conductivity of the powder bed, require experimental adjustments, which were not carried out in this thesis. In the second stage of the simulations (section 6.3), the used models were added step-by-step in order to consider the influences of the individual physical effects independently. This way it was possible to show, for example, how large the influence of the Marangoni convection is compared to the recoil pressure. However, it was also found that if the surface tension is negatively dependent on the temperature, the reflux is lower than expected, which has an unphysical effect on the melt pool. This phenomenon requires closer examination, for example using the real viscosity of the melt, or a sensitivity study of the heat conductivities. It could also be shown how small the influence of radiation and convective cooling is, so that these contributions can be neglected. In the last stage of the simulations (section 6.4) the presented simulation approach was validated by experiments. This is based on a study consisting of experimental and simulative results from TENG ET AL. (2017). Here, similarly accurate results could be obtained as with the mesh-based approach from the study. The study revealed, above all, the lack of parameter sets for the temperature-dependent parameters such as surface tension, heat capacity and conductivity, which are often assumed to be constant or are widely extrapolated. In order to obtain better data sets or to carry out experiments for their determination, a cooperation with an experimentally oriented institute or company seems to be inevitable.

This observation leads directly to the first point of the outlook. For a higher quality simulation study, a fully documented experiment with a characterized material would have to be recalculated in cooperation with such an institute or company. Such a study would provide much better information about the accuracy of the method used.

When modelling the SLM process, some additional phenomena could be included in the framework presented. For example the correct representation of the contact angles between powder and melt (see e.g. KUNZ ET AL. (2018)), which increases the level of detail of the pseudo-single phase simulation, and also makes it possible to simulate multi-phase alloys. The current formulation also does not allow for the trapping of gases or the formation of voids in the melt pool. Their simulation would require the representation of a multi-phase system or require the mechanical simulation of the solid particles (see e.g. HU & EBERHARD (2017); RUSSELL ET AL. (2018)). However, both approaches are equivalent to a significantly increased numerical effort.

This increased effort can not only be tackled with better hardware, since even current top GPUs have only about three times as much computing power as the GPU used and DualSPHysics in its current form is a single-GPU framework. Rather, improved numerical approaches should be pursued to accelerate the simulations. As mentioned, the more stable and preferred approach is the ISPH method. In the simulations carried out, between 20 and 65 pressure iterations per time step were necessary. Together with the assembly of the system of equations in each time step, this results in a significant effort. This problem could be improved by enhanced solvers, such as the Algebraic Multi-Grid (AMG) solvers, or by using a completely matrix-free approach, as in IHMSEN ET AL. (2014). Additionally, targeted profiling and more efficient algorithms can certainly achieve significantly higher performance compared to this thesis.

Appendix A

Solution Procedures

In this appendix, the entire solution procedures, for the weakly compressible SPH (WCSPH) framework and the incompressible SPH (ISPH) framework are summarized in detail. In the algorithms, every major equation is referred to.

A.1 Weakly compressible SPH

```
Surface tension;
forall fluid particles $i$ do
    calculate surface normals (3.35)*;
    cut off small normals with $|\mathbf{n}| < 0.1/h$;
end
forall fluid particles $i$ with $|\mathbf{n}_i| > 0$ do
    smooth surface normals (3.36)*;
    calculate correction tensor (3.21)*;
    calculate curvature (3.39)*;
end
Forces;
forall fluid particles $i$ do
    calculate the change of density (3.47)*;
    calculate pressure forces (3.48, 3.26);
    calculate viscous forces (3.27);
    if $|\mathbf{n}_i| > 0$ then
        smooth curvature (3.44);
        calculate surface forces (3.37);
    end
end
forall boundary particles $i$ do
    calculate the change of density (3.47);
end
```

Algorithm 1: Weakly Compressible SPH time stepping (Part 1)

```
Energy;
forall fluid particles $i$ do
    calculate the change of the internal energy (3.62)*;
end
Verlet time step;
forall fluid particles $i$ with $T \geq T_{melt}$ do
    advance density in time (4.6);
    advance velocity in time (4.4);
    advance particle positions in time (4.5);
end
forall boundary particles $i$ do
    advance density in time (4.6);
end
```

Algorithm 2: Weakly Compressible SPH time stepping (Part 2)

A.2 Incompressible SPH

```
Advance particles to intermediate position;
forall fluid particles $i$ do
    move particle according to (4.7);
end
Surface tension;
forall fluid particles $i$ with $T \geq T_{melt}$ do
    calculate surface normals (3.35)*;
    cut off small normals with $|\mathbf{n}| < 0.1/h$;
end
forall fluid particles $i$ with $|\mathbf{n}_i| > 0$ do
    smooth surface normals (3.36)*;
    calculate correction tensor (3.21)*;
    calculate curvature (3.39)*;
end
Forces;
forall fluid particles $i$ do
    calculate viscous forces (3.27)*;
    recognize surface particles (3.58) (see figure 4.5);
    if $|\mathbf{n}_i| > 0$ then
        smooth curvature (3.44);
        calculate surface forces (3.37);
    end
end
```

Algorithm 3: Incompressible SPH time stepping (Part 1)

```
Matrix calibration;
forall fluid particles $i$ with $T_i < T_{melt}$ do
    calculate if non-surface liquid particle is in kernel radius (see figure 4.5);
end
forall boundary particles $i$ do
    calculate if non-surface liquid particle is in kernel radius (see figure 4.5);
end
forall non-surface fluid particles $i$ with $T \geq T_{melt}$ do
    calculate necessary line size of matrix*;
end
forall non-surface fluid particles $i$ with $T \leq T_{melt}$ and all boundary particles with
  non-surface liquid particles in kernel radius do
    calculate necessary line size of matrix
end
Matrix Population;
forall active fluid particles $i$ do
    calculate gradient correction (3.21)*;
    calculate matrix entries (3.52)*;
    calculate source and fixed value entries (4.25);
end
forall active boundary particles $i$ do
    calculate gradient correction (3.21)*;
    calculate matrix entries (3.52);
    calculate source and fixed value entries (4.25);
end
Solving the system of equations with Paralution (IDR + Jacobi);
Time integration;
forall fluid particles $i$ do
    calculate pressure accelerations (3.26)*;
end
forall fluid particles $i$ with $T \geq T_{melt}$ do
    calculate final velocitites (4.9);
    calculate final positions (4.10);
end
forall fluid particles $i$ do
    calculate the change of the internal energy (3.62)*;
end
Shifting algorithm;
forall fluid particles $i$ with $T \geq T_{melt}$ do
    shift particle positions (4.20)*;
    correct particle velocities (4.21);
end
```

Algorithm 4: Incompressible SPH time stepping (Part 2)

Appendix B

Temperature Variable Material Parameters

In this appendix the used temperature variable process parameters for S316L and CoCr are given in a tabular and graphical way. The material parameters for S316L are applied according to WESSELS ET AL. (2018). For the material parameters of CoCr, the mapping between internal energy and temperature is applied according to the thermal capacities from TENG ET AL. (2017). The temperature dependent surface tension coefficient was applied according to DUBBERSTEIN ET AL. (2015), who measured AISI 4142 with a positive temperature dependency. This positive dependency is leading to similar shapes of melt pools like the observed ones in TENG ET AL. (2017), who did not apply surface tension at all.

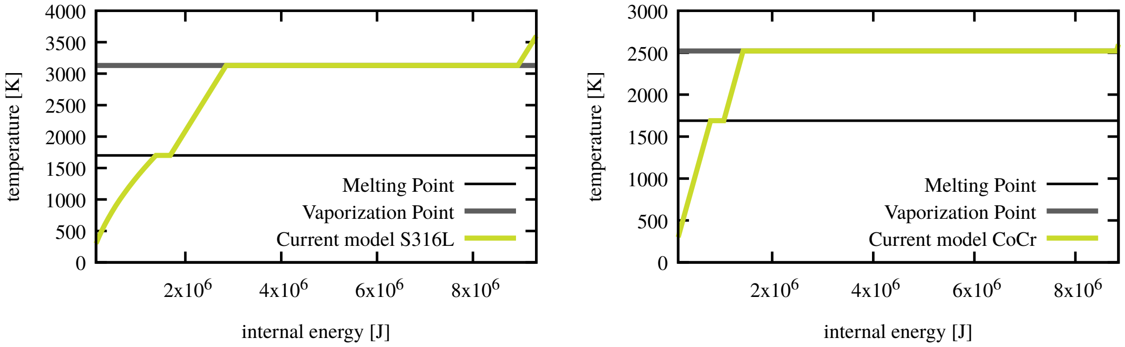

Figure B.1. Plot of the applied internal energy - temperature mapping with the latent heat of melting and vaporization explicitly modeled. Left: mapping for S316L (WESSELS ET AL. (2018)); right: mapping for CoCr (TENG ET AL. (2017)).

internal energy $[J]$	temperature $[K]$
136141.8	300
191842.4	400
252703	500
318723.6	600
389904.2	700
466244.8	800
547745.4	900
634406	1000
726226.6	1100
823207.2	1200
925347.8	1300
1032648.4	1400
1145109	1500
1262729.6	1600
1385510.2	1700
1684510.2	1700
2849950	3130
8939950	3130
9323000	3600

temperature $[K]$	thermal conductivity $[W/(m \cdot K)]$
300	9.35
1700	32.4
3600	32.4

temperature $[K]$	heat capacity $[J/(kg \cdot K)]$
300	376.4
1700	815
3600	815

temperature $[K]$	surface tension coefficient $[N/m^2]$
300	1.769
1700	1.769
3600	0.078

Table B.1. Tabular overview of temperature dependant variables for S316L (Wessels et al. (2018)).

internal energy $[J]$	temperature $[K]$
138600	300
780780	1690
1040780	1690
1424240	2520
8814240	2520
8851200	2600

temperature $[K]$	surface tension coefficient $[N/m^2]$
300	1.212
1700	1.212
2520	1.723

Table B.2. Tabular overview of temperature dependant variables for CoCr. Internal energy - temperature mapping based on Teng et al. (2017) and surface tension according to Dubberstein et al. (2015).

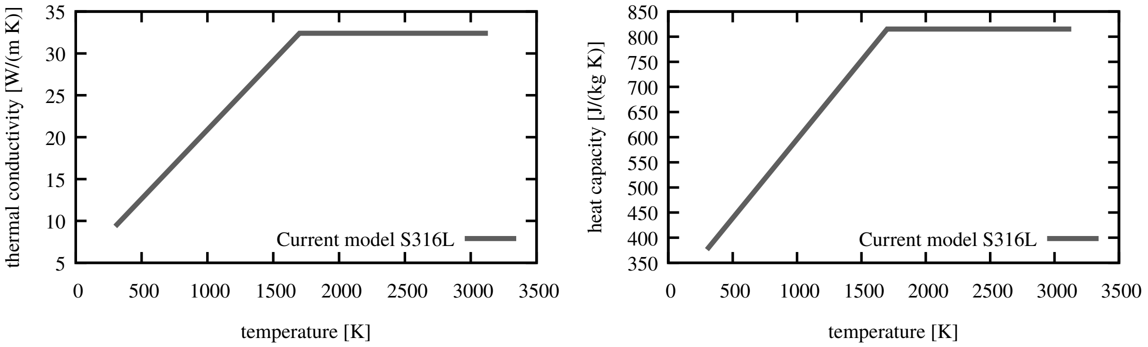

Figure B.2. Thermal conductivity [left] and heat capacity [right] plotted over the temperature for S316L (WESSELS ET AL. (2018)).

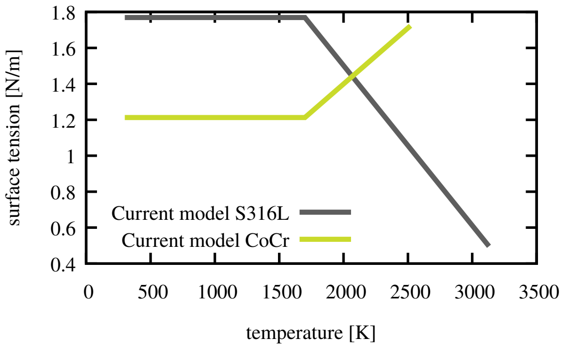

Figure B.3. Surface tension coefficient plotted over the temperature for S316L (WESSELS ET AL. (2018)) and for CoCr (DUBBERSTEIN ET AL. (2015), measured for AISI 4142).

Appendix C

Supplementary Test Data

This appendix gives additional information on the performed simulations in in chapter 6. This data is not found directly in the thesis, as it does not provide entirely new data but can help understanding the simulations.

C.1 Powder conductivity

In the powder conductivity section 6.2.1, the conductivity of unmolten spheres was simulated and fitted with thermal conductivities on a solid block. These fittings are shown in this section. Besides the decreasing conductivity with resolution, one can see the higher amount of deviations from the mean conductivity with increasing resolution, as the air gaps between the spheres open up wider and generate a more inhomogeneous conductivity.

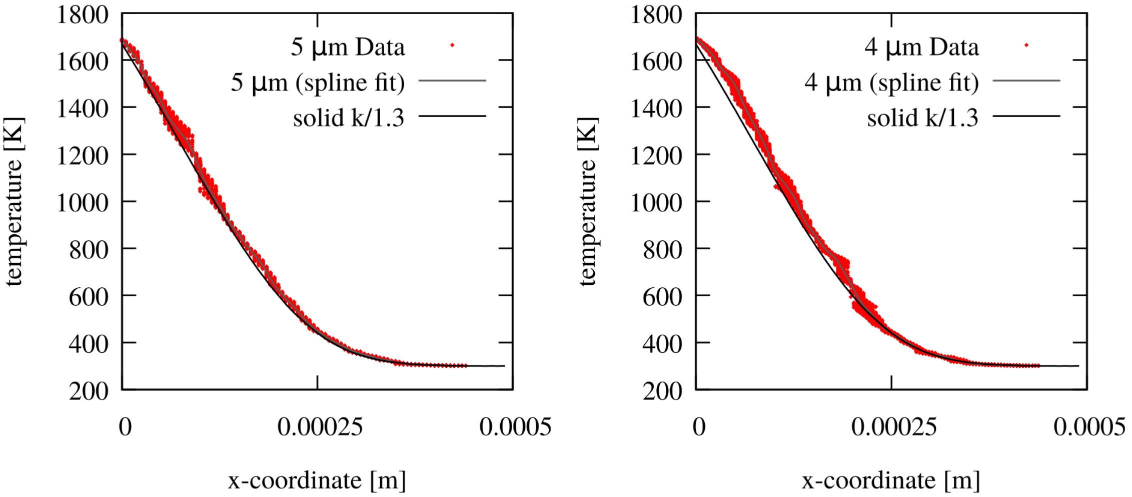

Figure C.1. Geometry and boundary conditions for heat conduction test for 5 and 4 μm resolution.

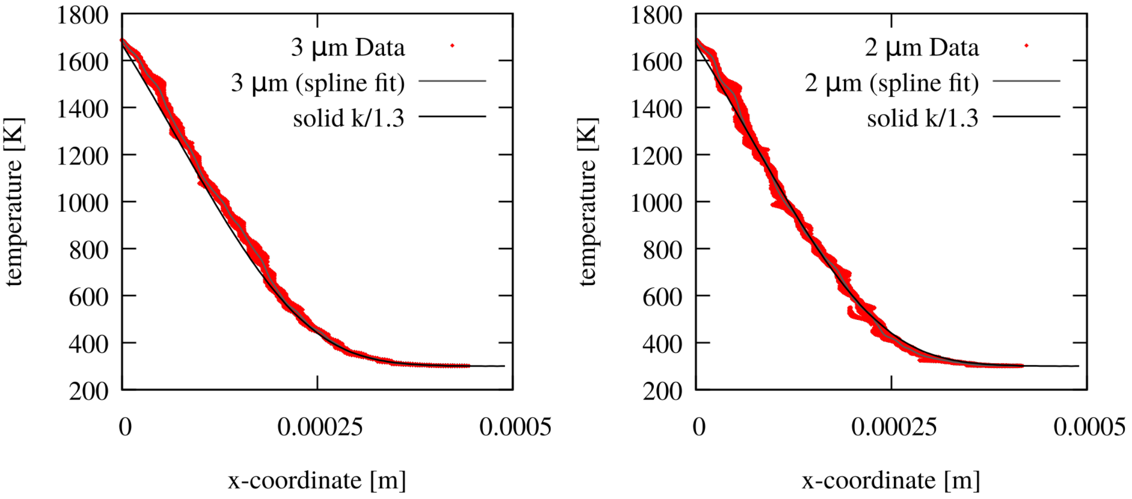

Figure C.2. Geometry and boundary conditions for heat conduction test for 3 and 2 μm resolution.

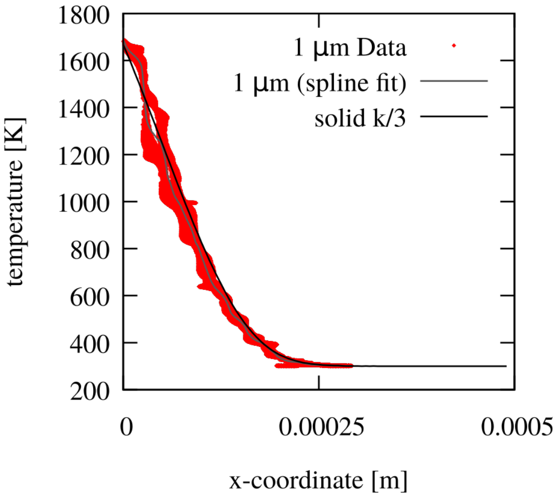

Figure C.3. Geometry and boundary conditions for heat conduction test for 1 μm resolution.

C.2 Laser modeling

In the following figures, slices of the laser modeling test (section 6.2.3) are presented. It is visible, how the uncorrected laser heat source drastically underestimates the applied energy. Additionally the temperature distribution of the scalar correction and the adaptive correction with a target intensity of 0.75 appear similar, while a lower depth correction parameter turns the melt pool to be more shallow. This also affects the final geometry, which changes from a deeper penetration with slight overhangs on the sides to a flat U shape, for lower target laser intensities.

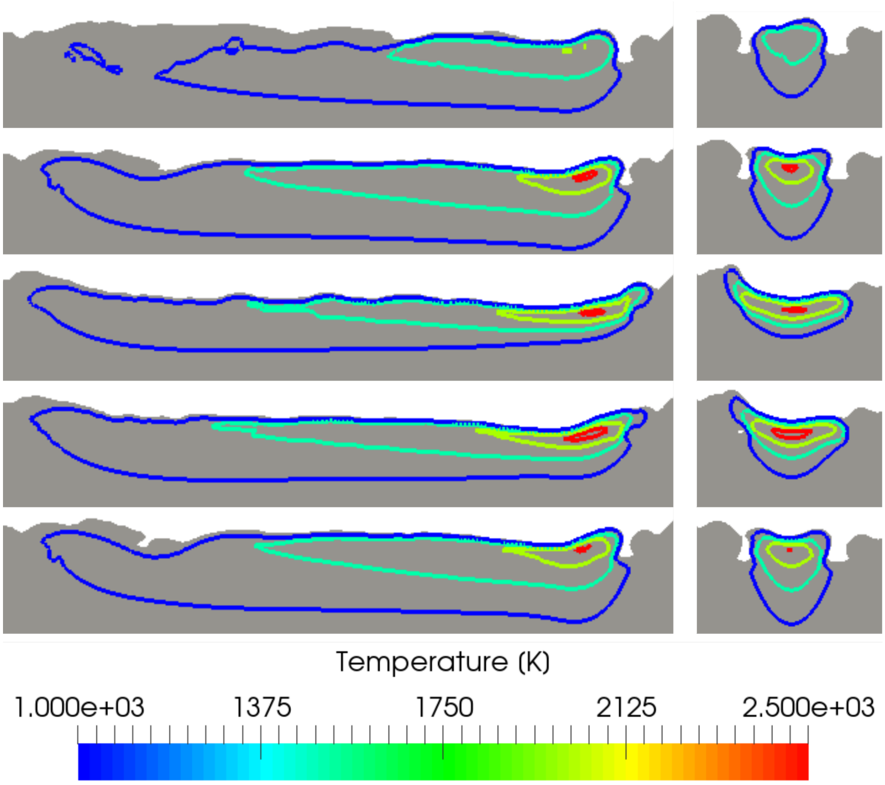

Figure C.4. Representation of melt pool slices with temperature contour lines during the laser correction analyses. From top to bottom: uncorrected laser heat source, scalar correction, adaptive correction: target intensity 0.25, 0.5 0.75.

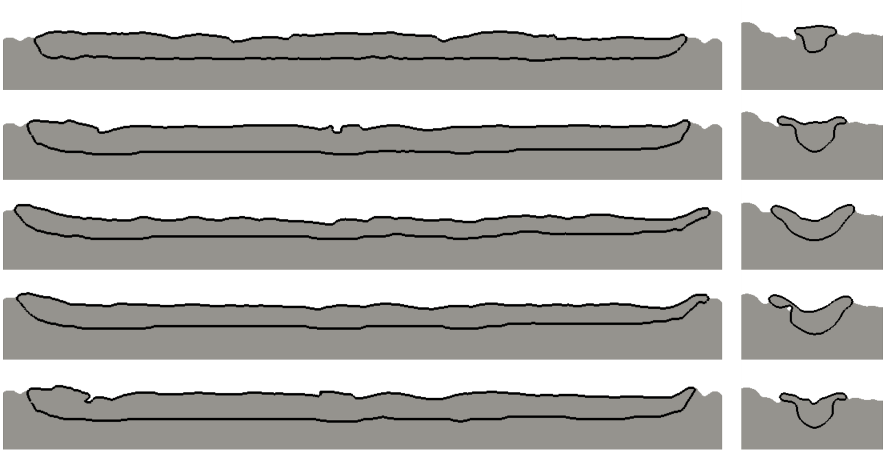

Figure C.5. Representation of melt pool slices of the final melt pool geometry of the laser correction analyses. From top to bottom: uncorrected laser heat source, scalar correction, adaptive correction: target intensity 0.25, 0.5 0.75.

C.3 Validation / Simulation series

In this last part, the data from the validation section 6.4 is given in tabular form. This can be used to do further analytics on the simulated and experimental results of this work and the remeasured values from TENG ET AL. (2017).

Process parameters			Width [μm]		Vertical size [μm]	
Speed [m/s]	Power [W]	E_V [$\mu J/\mu m^3$]	Teng et al. Experiment	Teng et al. Simulation	Teng et al. Experiment	Teng et al Simulation
0.85	310	0.192	127.5	133.7	99.4	92.9
0.85	330	0.204	134.6	144.9	115.4	106.5
0.85	360	0.223	134.6	151.1	143.1	128.5
0.85	385	0.238	151.6	160.0	161.0	152.9
1.2	310	0.136	132.0	117.8	82.5	76.5
1.2	330	0.145	117.0	128.9	82.1	82.0
1.2	360	0.158	117.0	133.8	93.2	93.1
1.2	385	0.169	126.5	136.1	99.8	99.6
1.6	310	0.102	102.5	104.2	37.6	60.7
1.6	330	0.109	112.7	116.2	45.9	62.9
1.6	360	0.118	112.8	117.9	52.4	75.2
1.6	385	0.127	117.2	126.9	61.9	77.8
2	310	0.082	115.9	102.0	52.5	57.0
2	330	0.087	125.7	113.9	65.4	61.9
2	360	0.095	110.9	112.2	63.3	63.0
2	385	0.101	115.0	118.0	83.0	72.0
2.5	310	0.065	90.6	90.8	34.7	50.0
2.5	330	0.069	103.5	102.1	39.1	56.0
2.5	360	0.076	98.1	102.2	41.8	60.9
2.5	385	0.081	111.9	105.2	44.0	63.1

Table C.1. Remeasured geometry data of the melt pool for the experimental and simulated melt pool geometry from the work of TENG ET AL. (2017) in text format.

Process parameters			Width [μm]		Vertical size [μm]		Depth [μm]		Height [μm]	
Speed [m/s]	Power [W]	E_V [$\mu J/\mu m^3$]	ISPH	WCSPH	ISPH	WCSPH	ISPH	WCSPH	ISPH	WCSPH
0.85	310	0.192	142	102	109	84	-85.5	-64.5	23.7	19.6
0.85	330	0.204	143	102	110	89.9	-88.5	-70.5	21.7	19.4
0.85	360	0.223	146	102	116	95.9	-94.5	-76.5	21.5	19.5
0.85	385	0.238	148	104	123	101	-101	-82.3	22.5	19.1
1.2	310	0.136	127	91.7	87.8	71.9	-58.6	-49.5	29.1	22.5
1.2	330	0.145	137	97.9	88.7	82.2	-63.4	-52.8	25.3	38.8
1.2	360	0.158	138	98.6	92.5	91.7	-67.5	-58.5	25	42.3
1.2	385	0.169	141	102	95.8	101	-70.5	-62.5	25.2	19.7
1.6	310	0.102	98.8	93.6	59.9	73.5	-44.3	-40.4	15.6	33.1
1.6	330	0.109	115	94.8	70.4	78.6	-46.9	-40.5	23.5	38.1
1.6	360	0.118	117	95.5	72.1	83.4	-50.5	-43.6	21.6	39.8
1.6	385	0.127	118	96.5	72.7	84.9	-52.7	-46.5	20.1	38.5
2	310	0.082	98.5	92.4	63.9	66.1	-35.3	-31.5	28.6	38
2	330	0.087	104	92.7	65.6	67.6	-38.3	-34.5	27.4	31.6
2	360	0.095	105	93.5	67.5	69.4	-41.3	-37.4	26.2	30.2
2	385	0.101	106	93.5	71.7	72	-43.7	-40	28.1	32
2.5	310	0.065	92	88.4	57.4	66.5	-30.4	-25.6	27.1	41
2.5	330	0.069	93.1	89.3	57.7	66.9	-30.4	-25.6	27.3	41.3
2.5	360	0.076	96.4	90.5	61.4	67.6	-33.3	-28.6	28.1	41.4
2.5	385	0.081	97.5	92.6	62.8	70	-35.2	-31.5	27.6	36.1

Table C.2. Melt pool geometry data from validation test simulations in text format of the validation test case according to TENG ET AL. (2016).

Process parameters			Molten particles		Evaporated particles		Simulation runtime [h]	
Speed $[m/s]$	Power $[W]$	E_V $[\mu J/\mu m^3]$	ISPH	WCSPH	ISPH	WCSPH	ISPH	WCSPH
0.85	310	0.192	294777	156472	20691	43790	11.2	17.7
0.85	330	0.204	307397	163728	23823	47599	11.1	16.6
0.85	360	0.223	326951	173444	28241	54172	11.2	16.7
0.85	385	0.238	342078	181757	32175	59342	11.3	17.0
1.2	310	0.136	197595	132511	12775	22886	7.6	12.2
1.2	330	0.145	214719	138678	14036	25063	7.6	12.1
1.2	360	0.158	226529	145706	17194	29301	7.7	12.2
1.2	385	0.169	235987	155721	19964	30900	7.7	12.2
1.6	310	0.102	147771	113225	7151	12483	5.6	8.9
1.6	330	0.109	161226	117434	8366	14352	5.6	8.9
1.6	360	0.118	169485	122942	10549	17298	5.7	8.8
1.6	385	0.127	176219	129132	12408	19249	5.6	9.0
2	310	0.082	118370	99157	3963	7132	4.4	7.4
2	330	0.087	131581	103113	4863	8406	4.5	7.1
2	360	0.095	137993	108021	6365	10553	4.5	7.4
2	385	0.101	141937	112187	7895	12475	4.5	7.1
2.5	310	0.065	104384	85497	1919	3807	3.5	5.8
2.5	330	0.069	107404	89569	2666	4615	3.5	5.7
2.5	360	0.076	111971	94494	3881	6029	3.5	5.6
2.5	385	0.081	116357	97723	4671	7430	3.6	5.6

Table C.3. Numbers of molten and vaporized particles as much as simulation run times of the validation test case according to TENG ET AL. (2016).

Bibliography

ABOULKHAIR N.T., EVERITT N.M., ASHCROFT I. & TUCK C. Reducing porosity in alsi10mg parts processed by selective laser melting. *Additive Manufacturing*, 1 (2014): 77–86.

ACHARYA R., SHARON J.A. & STAROSELSKY A. Prediction of microstructure in laser powder bed fusion process. *Acta Materialia*, 124 (2017): 360–371.

ADAMI S., HU X. & ADAMS N. A new surface-tension formulation for multi-phase sph using a reproducing divergence approximation. *Journal of Computational Physics*, 229 (2010) (13): 5011–5021.

ADAMI S., HU X. & ADAMS N.A. A generalized wall boundary condition for smoothed particle hydrodynamics. *Journal of Computational Physics*, 231 (2012) (21): 7057–7075.

ALSHAER A.W., ROGERS B. & LI L. Smoothed particle hydrodynamics (sph) modelling of transient heat transfer in pulsed laser ablation of al and associated free-surface problems. *Computational Materials Science*, 127 (2017): 161–179.

ALY A.M., ASAI M. & SONDA Y. Modelling of surface tension force for free surface flows in isph method. *International Journal of Numerical Methods for Heat & Fluid Flow*, 23 (2013) (3): 479–498.

AMMER R., MARKL M., LJUNGBLAD U., KÖRNER C. ET AL. Simulating fast electron beam melting with a parallel thermal free surface lattice boltzmann method. *Computers & Mathematics with Applications*, 67 (2014) (2): 318–330.

AYACHIT U. *The paraview guide*, volume 366. Kitware Inc, New York, 2020.

BAND S., GISSLER C., PEER A. & TESCHNER M. Mls pressure boundaries for divergence-free and viscous sph fluids. *Computers & Graphics*, 76 (2018): 37–46.

BATCHELOR C.K. & BATCHELOR G. *An introduction to fluid dynamics*. Cambridge university press, Cambridge, 1967.

BIRIUKOV S. & PRICE D.J. On second derivatives in sph. In *Proceedings of the 13th International SPHERIC Workshop, Galway, Ireland, June*, pages 255–262. 2018.

BØCKMANN A., SHIPILOVA O. & SKEIE G. Incompressible sph for free surface flows. *Computers & Fluids*, 67 (2012): 138–151.

BONET J. & LOK T.S. Variational and momentum preservation aspects of smooth particle hydrodynamic formulations. *Computer Methods in applied mechanics and engineering*, 180 (1999) (1-2): 97–115.

BRACKBILL J., KOTHE D.B. & ZEMACH C. A continuum method for modeling surface tension. *Journal of computational physics*, 100 (1992) (2): 335–354.

BROOKSHAW L. A method of calculating radiative heat diffusion in particle simulations. *Publications of the Astronomical Society of Australia*, 6 (1985) (2): 207–210.

CHILDS T., HAUSER C. & BADROSSAMAY M. Selective laser sintering (melting) of stainless and tool steel powders: experiments and modelling. *Proceedings of the Institution of Mechanical Engineers, Part B: Journal of Engineering Manufacture*, 219 (2005) (4): 339–357.

CHO J.H., FARSON D.F., MILEWSKI J.O. & HOLLIS K.J. Weld pool flows during initial stages of keyhole formation in laser welding. *Journal of Physics D: Applied Physics*, 42 (2009) (17): 175 502.

CHOW A.D., ROGERS B.D., LIND S.J. & STANSBY P.K. Incompressible sph (isph) with fast poisson solver on a gpu. *Computer Physics Communications*, 226 (2018): 81–103.

CLEARY P.W. Modelling confined multi-material heat and mass flows using sph. *Applied Mathematical Modelling*, 22 (1998) (12): 981–993.

CLEARY P.W. & MONAGHAN J.J. Conduction modelling using smoothed particle hydrodynamics. *Journal of Computational Physics*, 148 (1999) (1): 227–264.

COLAGROSSI A. & LANDRINI M. Numerical simulation of interfacial flows by smoothed particle hydrodynamics. *Journal of Computational Physics*, 191 (2003) (2): 448–475.

COOK P.S. & MURPHY A.B. Simulation of melt pool behaviour during additive manufacturing: Underlying physics and progress. *Additive Manufacturing*, (2019): 100 909.

CRESPO A.J., DOMÍNGUEZ J.M., ROGERS B.D., GÓMEZ-GESTEIRA M. ET AL. Dualsphysics: Open-source parallel cfd solver based on smoothed particle hydrodynamics (sph). *Computer Physics Communications*, 187 (2015): 204–216.

CUMMINS S.J. & RUDMAN M. An sph projection method. *Journal of computational physics*, 152 (1999) (2): 584–607.

D'ALEMBERT J.L.R. *Essai d'une nouvelle théorie de la résistance des fluides*. David l'aîné, Paris, 1752.

DIN 8580. *Fertigungsverfahren – Begriffe, Einteilung*, volume 8588. Beuth, Berlin, 2003.

DUBBERSTEIN T., HELLER H.P., KLOSTERMANN J., SCHWARZE R. ET AL. Surface tension and density data for fe–cr–mo, fe–cr–ni, and fe–cr–mn–ni steels. *Journal of materials science*, 50 (2015) (22): 7227–7237.

EULER L. *Lettre de M. Euler à M. de la Grange*. Joseph Louis Lagrange, Turin, 1762.

FATEHI R., FAYAZBAKHSH M. & MANZARI M. On discretization of second-order derivatives in smoothed particle hydrodynamics. In *Proceedings of World Academy of Science, Engineering and Technology*, volume 30, pages 243–246. Citeseer, 2008.

FLEISSNER F. Pasimodo v1. 9.3, software package and template files. *Inpartik & ITM University of Stuttgart, Tübingen*, (2012).

FLOW SCIENCE, INC. Flow-3d additive manufacturing (2017). `https://www.flow3d.com/products/flow3d-am/` (accessed: 15.08.2020).

FOUDA Y.M. & BAYLY A.E. A dem study of powder spreading in additive layer manufacturing. *Granular Matter*, 22 (2020) (1): 10.

FÜRSTENAU J.P., AVCI B. & WRIGGERS P. A semi-implicit multi-fluid sph algorithm suitable for gpu. *Proceedings in Applied Mathematics and Mechanics*, 16 (2016) (1): 593–594.

FÜRSTENAU J.P., AVCI B. & WRIGGERS P. A comparative numerical study of pressure-poisson-equation discretization strategies for sph. In *Proceedings of the 12th International SPHERIC Workshop, Ourense, Spain, June*, pages 67–74. 2017.

FÜRSTENAU J.P., WEISSENFELS C. & WRIGGERS P. Examining errors and correction techniques for sph. *Proceedings in Applied Mathematics and Mechanics*, 18 (2018) (1): e201800 081.

FÜRSTENAU J.P., WEISSENFELS C. & WRIGGERS P. Free surface tension in incompressible smoothed particle hydrodynamcis (isph). *Computational Mechanics*, 65 (2020a) (2): 487–502.

FÜRSTENAU J.P., WESSELS H., WEISSENFELS C. & WRIGGERS P. Generating virtual process maps of slm using powder-scale sph simulations. *Computational Particle Mechanics*, 7 (2020b) (4): 655–677.

GANERIWALA R. & ZOHDI T.I. A coupled discrete element-finite difference model of selective laser sintering. *Granular Matter*, 18 (2016) (2): 21.

GEBHARDT A. *Additive Fertigungsverfahren*. Carl Hanser Verlag, München, 2016, 5 edition.

GHIA U., GHIA K.N. & SHIN C. High-re solutions for incompressible flow using the navier-stokes equations and a multigrid method. *Journal of computational physics*, 48 (1982) (3): 387–411.

GIESEKE M., ALBRECHT D., NÖLKE C., KAIERLE S. ET AL. Laserbasierte technologien. In *3D-Druck beleuchtet*, pages 19–30. Springer, 2016.

GINGOLD R.A. & MONAGHAN J.J. Smoothed particle hydrodynamics: theory and application to non-spherical stars. *Monthly Notices of the Royal Astronomical Society*, 181 (1977) (3): 375–389.

GUSAROV A. & KRUTH J.P. Modelling of radiation transfer in metallic powders at laser treatment. *International Journal of Heat and Mass Transfer*, 48 (2005) (16): 3423–3434.

GUSAROV A.V., YADROITSEV I., BERTRAND P. & SMUROV I. Model of radiation and heat transfer in laser-powder interaction zone at selective laser melting. *Journal of Heat Transfer*, 131 (2009) (7): 072 101.

HAMMERSLEY J.M. & HANDSCOMB D.C. *Monte Carlo Methods*. Methuen&Co, London, 1964.

HASHEMI H. & SLIEPCEVICH C. A numerical method for solving two-dimensional problems of heat conduction with change of phase. In *Chemical Engineering Progress Symposium Series*, volume 63, pages 34–41. 1967.

HE X., FUERSCHBACH P.W. & DEBROY T. Heat transfer and fluid flow during laser spot welding of 304 stainless steel. *Journal of Physics D: Applied Physics*, 36 (2003) (12): 1388–1398.

HIRSCHLER M., KUNZ P., HUBER M., HAHN F. ET AL. Open boundary conditions for isph and their application to micro-flow. *Journal of Computational Physics*, 307 (2016): 614–633.

HIRSCHLER M., OGER G., NIEKEN U. & LE TOUZÉ D. Modeling of droplet collisions using smoothed particle hydrodynamics. *International Journal of Multiphase Flow*, 95 (2017): 175–187.

HODGE N.E., FERENCZ R.M. & SOLBERG J.M. Implementation of a thermomechanical model for the simulation of selective laser melting. *Computational Mechanics*, 54 (2014) (1): 33–51.

HODGE N.E., FERENCZ R.M. & VIGNES R.M. Experimental comparison of residual stresses for a thermomechanical model for the simulation of selective laser melting. *Additive Manufacturing*, 12 (2016): 159–168.

HU H. & EBERHARD P. Thermomechanically coupled conduction mode laser welding simulations using smoothed particle hydrodynamics. *Computational Particle Mechanics*, 4 (2017) (4): 473–486.

HU H., FETZER F., BERGER P. & EBERHARD P. Simulation of laser welding using advanced particle methods. *GAMM-Mitteilungen*, 39 (2016) (2): 149–169.

HU X. & ADAMS N. A constant-density approach for incompressible multi-phase sph. *Journal of Computational Physics*, 228 (2009) (6): 2082–2091.

HU X.Y. & ADAMS N.A. A multi-phase sph method for macroscopic and mesoscopic flows. *Journal of Computational Physics*, 213 (2006) (2): 844–861.

HUGHES T.J., LIU W.K. & ZIMMERMANN T.K. Lagrangian-eulerian finite element formulation for incompressible viscous flows. *Computer methods in applied mechanics and engineering*, 29 (1981) (3): 329–349.

IHMSEN M., CORNELIS J., SOLENTHALER B., HORVATH C. ET AL. Implicit incompressible sph. *IEEE Transactions on Visualization and Computer Graphics*, 20 (2014) (3): 426–435.

JAMSHIDINIA M., KONG F. & KOVACEVIC R. Temperature distribution and fluid flow modeling of electron beam melting (ebm). In *ASME 2012 International Mechanical Engineering Congress and Exposition*, pages 3089–3101. American Society of Mechanical Engineers Digital Collection, 2012.

KHAIRALLAH S.A. & ANDERSON A.T. Mesoscopic simulation model of selective laser melting of stainless steel powder. *Journal of Materials Processing Technology*, 214 (2014) (11): 2627–2636.

KHAIRALLAH S.A., ANDERSON A.T., RUBENCHIK A. & KING W.E. Laser powder-bed fusion additive manufacturing: Physics of complex melt flow and formation mechanisms of pores, spatter, and denudation zones. *Acta Materialia*, 108 (2016): 36–45.

KING W., ANDERSON A., FERENCZ R., HODGE N. ET AL. Overview of modelling and simulation of metal powder bed fusion process at lawrence livermore national laboratory. *Materials Science and Technology*, 31 (2015a) (8): 957–968.

KING W.E., ANDERSON A.T., FERENCZ R.M., HODGE N.E. ET AL. Laser powder bed fusion additive manufacturing of metals; physics, computational, and materials challenges. *Applied Physics Reviews*, 2 (2015b) (4): 041 304.

KLASSEN A. *Simulation of Evaporation Phenomena in Selective Electron Beam Melting*. Ph.D. thesis, Friedrich-Alexander-Universität Erlangen-Nürnberg, Erlangen (2018).

KLASSEN A., FORSTER V.E. & KÖRNER C. A multi-component evaporation model for beam melting processes. *Modelling and Simulation in Materials Science and Engineering*, 25 (2016) (2): 025 003.

KLASSEN A., SCHAROWSKY T. & KÖRNER C. Evaporation model for beam based additive manufacturing using free surface lattice boltzmann methods. *Journal of Physics D: Applied Physics*, 47 (2014) (27): 275 303.

KUNZ P., HASSANIZADEH S. & NIEKEN U. A two-phase sph model for dynamic contact angles including fluid–solid interactions at the contact line. *Transport in Porous Media*, 122 (2018) (2): 253–277.

LANDAU L.D. & LIFŠIC E.M. *Course of theoretical physics. vol. 6: Fluid mechanics*. Heinemann, Oxford, 1987.

LEE E.S., MOULINEC C., XU R., VIOLEAU D. ET AL. Comparisons of weakly compressible and truly incompressible algorithms for the sph mesh free particle method. *Journal of Computational Physics*, 227 (2008) (18): 8417–8436.

LEE J.Y., KO S.H., FARSON D.F. & YOO C.D. Mechanism of keyhole formation and stability in stationary laser welding. *Journal of Physics D: Applied Physics*, 35 (2002) (13): 1570.

LEE Y. & ZHANG W. Modeling of heat transfer, fluid flow and solidification microstructure of nickel-base superalloy fabricated by laser powder bed fusion. *Additive Manufacturing*, 12 (2016): 178–188.

LI S. & LIU W.K. Moving least-square reproducing kernel method part ii: Fourier analysis. *Computer Methods in Applied Mechanics and Engineering*, 139 (1996) (1-4): 159–193.

LI S. & LIU W.K. *Meshfree particle methods*. Springer, Berlin and New York, 2007, corr. print edition.

LIND S., XU R., STANSBY P. & ROGERS B. Incompressible smoothed particle hydrodynamics for free-surface flows: a generalised diffusion-based algorithm for stability and validations for impulsive flows and propagating waves. *Journal of Computational Physics*, 231 (2012) (4): 1499–1523.

LIND S.J., STANSBY P. & ROGERS B.D. Incompressible–compressible flows with a transient discontinuous interface using smoothed particle hydrodynamics (sph). *Journal of Computational Physics*, 309 (2016): 129–147.

LIU W.K., LI S. & BELYTSCHKO T. Moving least-square reproducing kernel methods (i) methodology and convergence. *Computer Methods in Applied Mechanics and Engineering*, 143 (1997) (1-2): 113–154.

LUCY L.B. A numerical approach to the testing of the fission hypothesis. *The Astronomical Journal*, 82 (1977): 1013.

LUKARSKI D. & TROST N. Paralution project (2014). `http://www.paralution.com` (accessed: 15.08.2020).

MAYRHOFER A., ROGERS B.D., VIOLEAU D. & FERRAND M. Investigation of wall bounded flows using sph and the unified semi-analytical wall boundary conditions. *Computer Physics Communications*, 184 (2013) (11): 2515–2527.

MEINERS W., WISSENBACH K. & GASSER A. Shaped body especially prototype or replacement part production. *DE Patent*, DE 19649865 (1998-02-12).

MOKOS A., ROGERS B.D. & STANSBY P.K. A multi-phase particle shifting algorithm for sph simulations of violent hydrodynamics with a large number of particles. *Journal of Hydraulic Research*, 55 (2017) (2): 143–162.

MONAGHAN J.J. Why particle methods work. *SIAM Journal on Scientific and Statistical Computing*, 3 (1982) (4): 422–433.

MONAGHAN J.J. An introduction to sph. *Computer Physics Communications*, 48 (1988) (1): 89–96.

MONAGHAN J.J. Smoothed particle hydrodynamics. *Annual Review of Astronomy and Astrophysics*, 30 (1992) (1): 543–574.

MONAGHAN J.J. & KOS A. Solitary waves on a cretan beach. *Journal of Waterway, Port, Coastal, and Ocean Engineering*, 125 (1999) (3): 145–155.

MONAGHAN J.J. & RAFIEE A. A simple sph algorithm for multi-fluid flow with high density ratios. *International Journal for Numerical Methods in Fluids*, 71 (2013) (5): 537–561.

MORRIS J.P. Simulating surface tension with smoothed particle hydrodynamics. *International Journal for Numerical Methods in Fluids*, 33 (2000) (3): 333–353.

NAIR P. & TOMAR G. An improved free surface modeling for incompressible sph. *Computers & Fluids*, 102 (2014): 304–314.

NATOLI V. A decade of accelerated computing augurs well for gpus (2019). `https://www.nextplatform.com/2019/07/10/a-decade-of-accelerated-computing-augurs-well-for-gpus/` (accessed: 15.08.2020).

NEUGEBAUER F., KELLER N., FEUERHAHN F. & KOEHLER H. Multi scale fem simulation for distortion calculation in additive manufacturing of hardening stainless steel. *International Conference on Thermal Forming and Welding Distortion*, (2014).

NVIDIA CORPORATION. Cuda toolkit archive (2020a). `https://developer.nvidia.com/cuda-toolkit-archive` (accessed: 15.08.2020).

NVIDIA CORPORATION. Cuda toolkit documentation (2020b). `https://docs.nvidia.com/cuda/cuda-c-programming-guide/` (accessed: 15.08.2020).

OÑATE E., IDELSOHN S.R., DEL PIN F. & AUBRY R. The particle finite element method: An overview. *International Journal of Computational Methods*, 01 (2004) (02): 267–307.

PAN Y. & SUGA K. Numerical simulation of binary liquid droplet collision. *Physics of Fluids*, 17 (2005) (8): 082 105.

PRICE D.J. Smoothed particle hydrodynamics: things i wish my mother taught me. *arXiv preprint arXiv:1111.1259*, (2011).

PRICE D.J. Smoothed particle hydrodynamics and magnetohydrodynamics. *Journal of Computational Physics*, 231 (2012) (3): 759–794.

QIAN J. & LAW C.K. Regimes of coalescence and separation in droplet collision. *Journal of Fluid Mechanics*, 331 (1997): 59–80.

RANDLES P.W. & LIBERSKY L.D. Smoothed particle hydrodynamics: some recent improvements and applications. *Computer Methods in Applied Mechanics and Engineering*, 139 (1996) (1-4): 375–408.

RIDER W.J. Approximate projection methods for incompressible flow: Implementation, variants and robustness. In *LANL UNCLASSIFIED REPORT LA-UR-94-2000*. Los Alamos National Laboratory, Los Alamos, 1995.

RIEDLBAUER D., SCHAROWSKY T., SINGER R.F., STEINMANN P. ET AL. Macroscopic simulation and experimental measurement of melt pool characteristics in selective electron beam melting of ti-6al-4v. *The International Journal of Advanced Manufacturing Technology*, 88 (2017) (5-8): 1309–1317.

RUPP K., TILLET P., RUDOLF F., WEINBUB J. ET AL. Viennacl—linear algebra library for multi-and many-core architectures. *SIAM Journal on Scientific Computing*, 38 (2016) (5): S412–S439.

RUSSELL M.A., SOUTO-IGLESIAS A. & ZOHDI T.I. Numerical simulation of laser fusion additive manufacturing processes using the sph method. *Computer Methods in Applied Mechanics and Engineering*, 341 (2018): 163–187.

SAAD Y. *Iterative methods for sparse linear systems*. Society for Industrial and Applied Mathematics, Philadelphia, 2003.

SEEDE R., SHOUKR D., ZHANG B., WHITT A. ET AL. An ultra-high strength martensitic steel fabricated using selective laser melting additive manufacturing: Densification, microstructure, and mechanical properties. *Acta Materialia*, 186 (2020): 199–214.

SHAH D. & VOLKOV A.N. Combined smoothed particle hydrodynamics-ray tracing method for simulations of keyhole formation in laser melting of bulk and powder metal targets. In *ASME 2019 International Mechanical Engineering Congress and Exposition*. American Society of Mechanical Engineers Digital Collection, 2019.

SHEPARD D. A two-dimensional interpolation function for irregularly-spaced data. In *Proceedings of the 1968 23rd ACM national conference*, pages 517–524. ACM, 1968.

SLM SOLUTIONS GROUP AG. Slm auf einen blick (2016). `https://www.slm-solutions.com/fileadmin/user_upload/downloads/de/210DE180424-03-BLICK_WEB.pdf` (accessed: 15.08.2020).

SMITH J., XIONG W., CAO J. & LIU W.K. Thermodynamically consistent microstructure prediction of additively manufactured materials. *Computational Mechanics*, 57 (2016) (3): 359–370.

SONNEVELD P. & VAN GIJZEN M.B. Idr (s): A family of simple and fast algorithms for solving large nonsymmetric systems of linear equations. *SIAM Journal on Scientific Computing*, 31 (2009) (2): 1035–1062.

SZEWC K., POZORSKI J. & TANIERE A. Modeling of natural convection with smoothed particle hydrodynamics: non-boussinesq formulation. *International Journal of Heat and Mass Transfer*, 54 (2011) (23-24): 4807–4816.

SZEWC K., TANIÈRE A., POZORSKI J. & MINIER J.P. A study on application of smoothed particle hydrodynamics to multi-phase flows. *International Journal of Nonlinear Sciences and Numerical Simulation*, 13 (2012) (6): 383–395.

TENG C., ASHBY K., PHAN N., PAL D. ET AL. The effects of material property assumptions on predicted meltpool shape for laser powder bed fusion based additive manufacturing. *Measurement Science and Technology*, 27 (2016) (8): 085 602.

TENG C., GONG H., SZABO A., DILIP J. ET AL. Simulating melt pool shape and lack of fusion porosity for selective laser melting of cobalt chromium components. *Journal of Manufacturing Science and Engineering*, 139 (2017) (1).

TEZDUYAR T.E., BEHR M., MITTAL S. & LIOU J. A new strategy for finite element computations involving moving boundaries and interfaces-the deforming-spatial-domain/space-time procedure: Ii. computation of free-surface flows, two-liquid flows, and flows with drifting cylinders. *Computer Methods in Applied Mechanics and Engineering*, 94 (1992) (3): 353–371.

VACONDIO R., ROGERS B., STANSBY P., MIGNOSA P. ET AL. Variable resolution for sph: a dynamic particle coalescing and splitting scheme. *Computer Methods in Applied Mechanics and Engineering*, 256 (2013): 132–148.

VIOLEAU D. *Fluid mechanics and the SPH method: theory and applications*. Oxford University Press, Oxford, 2012.

VOLKOV A.N. & ZHIGILEI L.V. Melt dynamics and melt-through time in continuous wave laser heating of metal films: Contributions of the recoil vapor pressure and marangoni effects. *International Journal of Heat and Mass Transfer*, 112 (2017): 300–317.

VON ALLMEN M. & BLATTER A. *Laser-beam interactions with materials: physical principles and applications*. Springer, Berlin, 1995.

WELLMANN C., LILLIE C. & WRIGGERS P. Homogenization of granular material modeled by a three-dimensional discrete element method. *Computers and Geotechnics*, 35 (2008) (3): 394–405.

WENDLAND H. Piecewise polynomial, positive definite and compactly supported radial functions of minimal degree. *Advances in Computational Mathematics*, 4 (1995) (1): 389–396.

WESSELS H., BODE T., WEISSENFELS C., WRIGGERS P. ET AL. Investigation of heat source modeling for selective laser melting. *Computational Mechanics*, 63 (2019) (5): 949–370.

WESSELS H., WEISSENFELS C. & WRIGGERS P. Metal particle fusion analysis for additive manufacturing using the stabilized optimal transportation meshfree method. *Computer Methods in Applied Mechanics and Engineering*, 339 (2018): 91–114.

WESSELS M.S.H. *Thermo-mechanical modeling for selective laser melting*. Ph.D. thesis, Leibniz Universität Hannover (2019).

WIKIMEDIA COMMONS: BIONERD. Pouring liquid mercury (2008). File: Pouring_liquid_mercury_bionerd.jpg (accessed: 15.08.2020).

WOHLERS T., CAMPBELL I., DIEGEL O. ET AL. *Wohlers Report 2018*. Wohlers Associates, Fort Collins, 2018.

XU R., STANSBY P. & LAURENCE D. Accuracy and stability in incompressible sph (isph) based on the projection method and a new approach. *Journal of Computational Physics*, 228 (2009) (18): 6703–6725.

YADROITSEV I. *Selective laser melting: Direct manufacturing of of 3D objects by selective laser melting of metal powders*. Ph.D. thesis, ENISE, Saint-Etienne (2008).

YADROITSEV I., GUSAROV A., YADROITSAVA I. & SMUROV I. Single track formation in selective laser melting of metal powders. *Journal of Materials Processing Technology*, 210 (2010) (12): 1624–1631.

YAKOUT M., ELBESTAWI M. & VELDHUIS S.C. A study of thermal expansion coefficients and microstructure during selective laser melting of invar 36 and stainless steel 316l. *Additive Manufacturing*, 24 (2018): 405–418.

YAN W., GE W., QIAN Y., LIN S. ET AL. Multi-physics modeling of single/multiple-track defect mechanisms in electron beam selective melting. *Acta Materialia*, 134 (2017): 324–333.

YAN W., SMITH J., GE W., LIN F. ET AL. Multiscale modeling of electron beam and substrate interaction: A new heat source model. *Computational Mechanics*, 56 (2015) (2): 265–276.

List of Figures

1.1 Basic components of a SLM machine, visualizing the SLM process. Adapted from GIESEKE ET AL. (2016). 2

1.2 Left: inner and outer geometry of a classic hydraulic block, manufactured as a solid component with connected bores; right: inner and outer geometry of a flow-optimised hydraulic block, manufactured as an additive metal component. Courtesy of S.M.I.L.E. - FEM GmbH. 3

2.1 left: Photograph of mercury being poured onto a glas surface at room temperature by WIKIMEDIA COMMONS: BIONERD (2008). The strong effect of surface tension is visible, being still smaller than molten steel by a factor around 3.5; right: Photograph of the first line of a new layer being irradiated in the SLM process. The spatter of molten particles caused by vaporization is clearly visbile. Courtesy of Gorden Reh, Institute of Product Development (IPeG), Leibniz Universität Hannover. 12

2.2 left: visualization of the molecular forces forces inside a fluid body (solid arrow) and the apparent surface tension force (dotted arrows); right: visualization of the Marangoni convection. The red particles have a higher temperature and thus a lower cohesive force than colder blue particles (arrow thickness). The dotted arrow shows the apparent Marangoni force. 14

2.3 Visualization of the wetting effect; left: the low adhesive force (arrow thickness) between fluid particles (red) and substrate particles (blue) results in an acute contact angle; right: the higher adhesive force leads to an obtuse contact angle. 15

2.4 Left: Illustration of the layers resulting from vaporization in the subsonic case with the associated pressure; right: illustration of the vapor motion in the Knudsen layer with collisions and condensation, both according to KLASSEN (2018). 25

2.5 Illustration of the intensity function depending on the depth and the radius according to WESSELS ET AL. (2019). 26

2.6 Illustration of the typical laser heat source representations in two representative cases highlighting the typical inaccuracies; a) Ray tracing algorithm with partial reflection; b) Gaussian flat heat source applied to free surfaces; c) volumetric heat source without adaptive depth correction; d) volumetric heat source with adaptive depth correction. 27

2.7 Plot of the thermal losses for S316L (WESSELS (2019)), note that the convective cooling and the radiative cooling use the left y-axis and the evaporative cooling uses the right one. One can see, that up to vaporization, the evaporative cooling is at least 2 orders of magnitude larger than the radiative cooling. 30

3.1 Cell-based Eulerian (e.g. FV) [left] and Lagrangian description [right] of a velocity field (red arrows) for a multi phase problem with free surfaces. . . 34
3.2 Distinction of mesh-less methods based on continuity, grid presence and scale. 35
3.3 Representation of the Wendland kernel, as much as its first and second derivative. 39
3.4 3D representation of the surface normal length of a set of surface particles of converged bubbles; left: bubble in 2D with an analytical radius of 122 μm; right: bubble in 3D with an analytical radius of 112 μm. 47
3.5 3D representation of the curvatures of a set of surface particles of converged bubbles; left: bubble in 2D with an analytical radius of 112 μm; right: bubble in 3D with an analytical radius of 122 μm. 47

4.1 Graphic by NATOLI (2019) showing the maximum memory bandwidth and peak performance of the best-in-class GPU and CPU models of every year from 2008 to 2020. The values for 2020 were extrapolated from preliminary specifications. Courtesy of Dr. Vincent Natoli. 60
4.2 Principal representation of a GPU (left) and a CPU (right) with their belonging memory and memory interactions as arrows (scaled according to memory throughput). The green cores of the GPU are called stream processors, arranged in multiprocessors. 61
4.3 Use of GPU inside a CUDA code, with the serial part of the code being handled on CPU and the parallel part handled on the GPU. Arrows represent single threads. 62
4.4 Principal representation of a multiprocessor inside a GPU with its belonging memories and possible memory interactions. 64
4.5 Flow diagram of the distinction if a particles pressure is calculated by the PPE. 67
4.6 Representation of an SPH code output as a 2-dimensional [left] and 3-dimensional [middle] point cloud without coloring. The point clouds give no information about the depth and surface of the represented body. To generate a depth effect and a continuous surface, the particles can be used as the center of spheres for the post-processing [right], called Glyphs in Paraview (AYACHIT (2020)). 69
4.7 Possible representations of the particle data being projected on a continuous background grid: Contour plot to show the fluid surface in 3D [left]; streamline plot with contour in 2D [middle]; velocity colored slice plot with contour in 2D [right]. 69

5.1 Lid-driven cavity flow test case geometry [left]. Used set of parameters for lid-driven cavity flow test case [right]. 72

5.2 Velocity plots of the $Re = 100$ test. Left: horizontal velocity plotted over vertical position; right: vertical velocity plotted over horziontal position. Two resolutions are compared to the results of GHIA ET AL. (1982). 74
5.3 Results of the $Re = 100$ test. Left: representation of the streamlines in GHIA ET AL. (1982); middle: streamline results and particle distribution with the lowest resolution of 50 x 50 particles. 74
5.4 Velocity plots of the $Re = 400$ test. Left: horizontal velocity plotted over vertical position; right: vertical velocity plotted over horziontal position. Two resolutions are compared to the results of GHIA ET AL. (1982). 75
5.5 Results of the $Re = 400$ test. Left: representation of the streamlines in GHIA ET AL. (1982); middle: streamline results and particle distribution with the lowest resolution of 50 x 50 particles. 75
5.6 Bubble collision state diagram depending on We and B acoording to QIAN & LAW (1997) with simulated examples marked. 77
5.7 Left: Bubble collision test case geometry; right: bubble collision test case parameters for water-like bubbles (density, viscosity) in vacuum (bold parameters are taken directly from QIAN & LAW (1997).) 78
5.8 Bubble collision results of test case B simulated with the WCSPH and ISPH approach compared to the experimental results of QIAN & LAW (1997). The numbers below the experimental results represent the time in ms. 78
5.9 Bubble collision results of test case F simulated with the WCSPH and ISPH approach compared to the experimental results of QIAN & LAW (1997). The numbers below the experimental results represent the time in ms. 79
5.10 Bubble collision results of test case P simulated with the WCSPH and ISPH approach compared to the experimental results of QIAN & LAW (1997). The numbers below the experimental results represent the time in ms. 80

6.1 SLM test case particle distribution reproduced according to KHAIRALLAH & ANDERSON (2014) at highest resolution. 81
6.2 Contour plots of the initial powder distribution in a rectangular box of size 164 x 100 x 38 μm with increasing resolution from left to right. 84
6.3 Comparative representation of the final melt pool geometries for the different resolutions. 85
6.4 Plot of the final melting path simulated with the WCSPH approach with increasing resolution from 5 μm to 1 μm from left to right. The darker areas mark the resolidified pool. 86
6.5 Plot of the final melting path simulated with the ISPH approach with increasing resolution from 5 μm to 2 μm from left to right. 86
6.6 Slice of the final contours of the final melting path. The black contour marks the resolidified pool. 86
6.7 Plot of the melt pool contours of the smoothing length analysis simulated with the ISPH approach. Colored on one half in neutral color to examine the surface and on the other half with the surface velocity. 87

6.8 Top views of the melt pool contours of the smoothing length studies for the different used approaches. Left: ISPH; middle: WCSPH; right: WCSPH approach with mixed smoothing length. 88

6.9 Final melt pool surface plots of the viscosity study with the ISPH approach. From left to right the viscosity decreases from 0.1 over 0.01 to 0.00642 Pas. 90

6.10 Final melt pool surface plots of the viscosity study with the WCSPH approach. From left to right the viscosity decreases from 0.1 over 0.01 to 0.00642 Pas. 90

6.11 Plot of the melt pool contours of the viscosity analysis. Left: results of the ISPH approach; right: results of the WCSPH approach. Colored on one half in neutral color to examine the surface and on the other half with the surface velocity. 92

6.12 Graphs representing the number of liquid particles in the viscosity analyses over time. Left: results of the ISPH approach; right: results of the WCSPH approach. 92

6.13 Graphs representing the absorbed laser power during the viscosity analyses over time. Left: results of the ISPH approach; right: results of the WCSPH approach. 93

6.14 Geometry and boundary conditions for heat conduction test. 95

6.15 Left: Representations of the very same part of the powder in 2D view from the top with the five analyzed resolutions; right: spline-fits of the particle transient temperatures at 5 ms compared to the solid material conductivity. 96

6.16 Representation of the final melt pool geometry of the heat conductivity analyses. Left: melt pool geometry 'without phase change'; right: melt pool geometry 'with phase change'. 96

6.17 Left: graphs representing the number of liquid particles in the heat conductivity analyses over time (active laser time 0.417 ms); right: absorbed laser power in the heat conductiy analyses over time showing only a minor difference. 97

6.18 Melt pool slices during the SLM process showing the temperature profiles below the laser. Top: melt pool geometry 'without phase change'; bottom: melt pool geometry 'with phase change'. 98

6.19 Graphs representing the number of liquid particles in the substrate depth analyses over time. Left: 600 W laser heat source; right: 900 W laser heat source. 99

6.20 Final melt pool slices from the substrate depth analyses. Shown are the independent melt pool geometries (600 W [top] and 900 W [bottom]). The numbered marks represent the tested substrate depth, with the green mark as the substrate surface and the red line the critical substrate depth. 100

6.21 Representation of the final melt pool geometry of the laser correction analyses. From left to right: uncorrected laser heat source, scalar correction, adaptive correction: target intensity 0.25, 0.5 0.75. 101

6.22 Representation of the final melt pool geometry of the laser correction analyses. From left to right: uncorrected laser heat source, scalar correction, adaptive correction: target intensity 0.25, 0.5 0.75. 101
6.23 Left: graph of the uncorrected compared to the corrected absorbed laser power for a 200 W laser heat source with an absorptivity of 0.3; right: graphs of the laser penetration depth with the three different adaptive laser corrections. 102
6.24 Graphs representing the number of liquid particles in the laser correction analysis over time (active laser time 0.53 ms). 103
6.25 Representation of the final melt pool geometry of the phenomena study for temperature decreasing surface tension. From left to right: gravity and buoyancy, constant surface tension, Marangoni convection, recoil pressure and evaporative cooling, radiative and convective cooling. 104
6.26 Side view of the melt pool under the influence of gravitational and buoyant forces according to equation 3.29. 105
6.27 Side view of the melt pool under the influence of gravitational, buoyant and surface tension forces. 106
6.28 Side view of the melt pool under the influence of gravitational, buoyancy, surface tension and the Marangoni convection. Top: temperature decreasing surface tension; bottom: temperature increasing surface tension. 107
6.29 Representation of the final melt pool geometry of the phenomena study for temperature increasing surface tension. From left to right: gravity and buoyancy, constant surface tension, Marangoni convection, recoil pressure and evaporative cooling, radiative and convective cooling. 107
6.30 Side view of the melt pool under the influence of gravitational, buoyancy and surface tension forces, the Marangoni convection and the recoil pressure. Top: temperature decreasing surface tension; bottom: temperature increasing surface tension. 109
6.31 Melt track at the end of the laser path during the phenomena study. Solidified areas are colored in dark gray and liquid areas are colored with their velocity. Simulations under surface tension and recoil pressure; from left to right: temperature decreasing surface tension, constant surface tension, temperature increasing surface tension. 110
6.32 Side view of the solidfied melt pools from the phenomena study, colored with height above substrate. 111
6.33 Plot of the molten particles over time for the decreasing surface tension phenomena series. 111
6.34 Plot of the molten particles over time for the increasing surface tension phenomena series. 112
6.35 Representation of the melt track at the end of the laser path for the decreasing surface tension phenomena series. Solidified areas are colored in darker gray and liquid areas are colored with their velocity. From left to right: gravity and buoyancy, constant surface tension, Marangoni convection, recoil pressure and evaporative cooling, radiative and convective cooling. 113

6.36 Representation of the melt track at the end of the laser path for the increasing surface tension phenomena series. Solidified areas are colored in darker gray and liquid areas are colored with their velocity. From left to right: gravity and buoyancy, constant surface tension, Marangoni convection, recoil pressure and evaporative cooling, radiative and convective cooling. 114
6.37 Graphs of the melt pool width from the validation case. Results consisting of experimental and simulative results of TENG ET AL. (2017) and own results simulated with ISPH and WCSPH approach. 116
6.38 Graphs of the vertical melt pool size from the validation case. Results consisting of experimental and simulative results of TENG ET AL. (2017) and own results simulated with ISPH and WCSPH approach. 116
6.39 Comparison of the final melt pool geometries for the validation case with 330 W laser power and 1.6 m/s laser speed. From Left to right: ISPH approach, WCSPH approach, 'mixed WCSPH' approach from section 6.1.2. The simulation times for the case were: ISPH: 5.7 h; WCSPH: 8.8 h; 'mixed WCSPH': 24.4 h. 117
6.40 Graphs showing the melt depth and height from the validation case according to TENG ET AL. (2017). 119
6.41 Graphs showing the molten and vaporized masses from the validation case according to TENG ET AL. (2017). 120
6.42 Process map derived from the simulative results from the validation simulation series. For the process map the ISPH results are used. 121
6.43 Tabular compilation of experimental melt pool slices from the validation examples by TENG ET AL. (2017). The green melt pool geometries are simulated with the WCSPH approach and the red ones with the ISPH approach. The simulated melt pools are always oriented at the experimental melt pool ground for clarity. 123

B.1 Plot of the applied internal energy - temperature mapping with the latent heat of melting and vaporization explicitly modeled. Left: mapping for S316L (WESSELS ET AL. (2018)); right: mapping for CoCr (TENG ET AL. (2017)). 133
B.2 Thermal conductivity [left] and heat capacity [right] plotted over the temperature for S316L (WESSELS ET AL. (2018)). 135
B.3 Surface tension coefficient plotted over the temperature for S316L (WESSELS ET AL. (2018)) and for CoCr (DUBBERSTEIN ET AL. (2015), measured for AISI 4142). 135

C.1 Geometry and boundary conditions for heat conduction test for 5 and 4 μm resolution. 137
C.2 Geometry and boundary conditions for heat conduction test for 3 and 2 μm resolution. 138
C.3 Geometry and boundary conditions for heat conduction test for 1 μm resolution. 138

C.4 Representation of melt pool slices with temperature contour lines during the laser correction analyses. From top to bottom: uncorrected laser heat source, scalar correction, adaptive correction: target intensity 0.25, 0.5 0.75. 139

C.5 Representation of melt pool slices of the final melt pool geometry of the laser correction analyses. From top to bottom: uncorrected laser heat source, scalar correction, adaptive correction: target intensity 0.25, 0.5 0.75. 139

List of Tables

2.1 List of representable phenomena in powder and partial scale. Phenomena that can be represented on a certain scale are marked with 'X'. Phenomena that cannot be displayed are marked with a '/'. The representability of phenomena marked with '(X)' is limited. The table is based on FÜRSTENAU ET AL. (2020b). 12

3.1 Particle normals integrated over the discretization perpendicular to the normal surface. 45

6.1 Constant material parameters for the simulated test cases. *: the marked parameters were applied differently from TENG ET AL. (2017), see section 6.4 for more details. 82
6.2 Constant parameters for the simulated test cases. 83
6.3 Calculation of the particle volume fractions for the rectangular box from figure 6.2. 84
6.4 Dynamic viscosities and belonging Reynolds numbers for the viscosity analysis. 89
6.5 Simulation run time and time stepping data of the viscosity analyses. 93
6.6 Additional details on the resolution test of the heat conduction test case and the fitted equivalent solid conductivities. Additional figures of the fitting can be found in appendix C. 95
6.7 Additional information on the laser corection analyses, showing the total amount of molten and vaporized particles. 102
6.8 Numbers of molten and vaporized particles during the phenomena analyses, comparing all five effects in the context of decreasing and increasing surface tension. 105

B.1 Tabular overview of temperature dependant variables for S316L (WESSELS ET AL. (2018)). 134
B.2 Tabular overview of temperature dependant variables for CoCr. Internal energy - temperature mapping based on TENG ET AL. (2017) and surface tension according to DUBBERSTEIN ET AL. (2015). 134

C.1 Remeasured geometry data of the melt pool for the experimental and simulated melt pool geometry from the work of TENG ET AL. (2017) in text format. 140

C.2 Melt pool geometry data from validation test simulations in text format of the validation test case according to TENG ET AL. (2016). 141
C.3 Numbers of molten and vaporized particles as much as simulation run times of the validation test case according to TENG ET AL. (2016). 142

Curriculum vitae

Jan-Philipp Fürstenau (born Haun)
born March 31, 1989 in Gehrden, Germany

Professional Experience

since 05.2019	Business Development Manager ROCKY DEM, CADFEM GmbH, Hannover
05.2014 - 04.2019	Research assistant at the Institute of Continuum Mechanics, Leibniz Universität Hannover
09.2012 - 02.2017	Lectureship Engineering Mechanics III, Hochschule Hannover

Education

04.2012 - 04.2014	Leibniz Universität Hannover Mechanical Engineering Focus: Mechanics, Contact Mechanics, Automotive Engineering Degree: M. Sc.
08.2008 - 02.2012	Hochschule Hannover Mechanical Engineering (as dual education) Focus: Construction Technology Degree: B. Eng.
09.2008 - 06.2010	Volvo Construction Equipment, Hameln Apprenticeship as Industrial Mechanic (as dual education)
2001 - 2008	Secondary education at Otto-Hahn Gymnasium, Springe
1999 - 2001	Elementary education at Orientierungsstufe Nord, Springe and
1995 - 1999	Grundschule Bennigsen